Theoretical models for ultracold atom-ion collisions in confined geometries

Srihari Srinivasan

To cite this version:

Srihari Srinivasan. Theoretical models for ultracold atom-ion collisions in confined geometries. Other [cond-mat.other]. Université de Rennes, 2015. English. NNT : 2015REN1S036 . tel-01229627

HAL Id: tel-01229627
https://theses.hal.science/tel-01229627

Submitted on 17 Nov 2015

N^o d'ordre : **ANNÉE 2015**

THÈSE / UNIVERSITÉ DE RENNES 1
sous le sceau de l'Université Européenne de Bretagne
pour le grade de
DOCTEUR DE L'UNIVERSITÉ DE RENNES 1
Mention : Physique
Ecole Doctorale Science de la Matière
présentée par

Srihari Srinivasan

préparée à l'unité de recherche UMR CNRS 6251
Institut de Physique de Rennes

Theoretical Models for Ultracold Atom-Ion Collisions In Confined Geometries

Thèse soutenue à Rennes
le 30 mars 2015 à 14h00
devant le jury composé de :

Thierry STOECKLIN
Directeur de Recherche, l'Institut des Sciences Moléculaire, UMR CNRS 5255, Université de Bordeaux 1 / rapporteur

Pascal HONVAULT
Professeur, Institut UTINAM, UMR CNRS 6213, Université de Franche-Comté / rapporteur

Robert GEORGES
Professeur, Institut de Physique de Rennes UMR CNRS 6251, Université de Rennes 1 / examinateur

Andrea SIMONI
Maître de Conférences, Institut de Physique de Rennes UMR CNRS 6251, Université de Rennes 1 / examinateur

Grégoire GUILLON
Maître de Conférences, Laboratoire Interdisciplinaire Carnot de Bourgogne, UMR CNRS 6303, Université de Bourgogne / examinateur

ॐ पूर्णमदः पूर्णमिदम् पूर्णात् पूर्णमुदच्यते ।
पूर्णस्य पूर्णमादाय पूर्णमेवावशिष्यते ।।

Om Pūrṇamadaḥ pūrṇamidaṃ pūrṇāt pūrṇamudachyate |
Pūrṇasya pūrṇamādāya pūrṇamevāvaśiṣyate ||

That is infinite, This is infinite; from that infinite this infinite as risen |
From the infinite, even if the whole is taken away, what remains again is the infinite ||

- Bṛhadāraṇkaya Upaniṣad
around 700 BCE

In loving memory of my grand father
A. S. Rajagopal.

Abstract

Ultracold atom-ion systems have been a topic of interest for atomic physicists studying chemical reactions and since recently, the cold ion community (ion trap quantum computation and simulation). They have been looking at the possibility of using an ultracold atom gas to sympathetically cool ions since intrinsic motional modulation i.e micromotion is an inherent cause of decoherence in coherent applications of cold ions. Interest is also piqued by the possibility of using this hybrid system for studying impurity physics and to better understand ion-neutral reactions aimed at creation of molecular ions.

In this thesis, we aim to study the effect of ion micromotion in atom-ion collision. As a prelude, we treat the 1D collision of a particle in a harmonic trap (ion) and a free particle (atom) using different numerical schemes. This system is of interest in its own right due to the mixed 0D-1D dimensionality. Atom-ion potential is simplified to a zero range potential all through out the work. Next we deal with a similar problem but with the trapped particle in a time dependent harmonic trap identical to an ion Paul trap. Finally we extend the study of micromotion to a model system in 3D with an ion in a 3D spherical Paul trap and a heavy atom at the trap centre. We discuss the effect micromotion has on potential applications of such a system, like a quantum phase gate.

Résumé

Les systèmes composeś d'atomes et d'ions ultrafroids one étés un sujet d'interet pour les physiciens atomiques et, plus récemment, pour la communauté des ions froids (simulation et calcul quantique avec des ions piègés). Ils sont considéré la possibilité d'utiliser un gaz d'atomes ultrafroids pour refroidir sympathetiquement les ions car la modulation intrinsèque du movement, le micromouvement, représente une source de décohérence dans les applications des ions froids. L'interet envers ce système mixte est aussi movité par l'étude de la physique d'impuretés et par une meilleure comprehension des réactions entre espèces ioniques et neutre ayant pour but la création d'ions moléculaires.

Cette thèse a pour objectif d'étudier les effets du micromouvement dans les collisions atome-ion. Nous traitons au préalable les collisions à 1D d'une particule dans un piège harmonique (un ion) et d'un particule libre (une atome) en utilisant différentes approches numériques. Ce système est intéressant en soi en raison de la dimensionnalité miste 0D-1D. Le potentiel atome-ion est modélisé par une interaction à portèe nulle tout au cours de ce travail. Par la suite, nous traitons un problème similaire mais dans le cas d'une particule dans un piège harmonique décrivant un piège de Paul. Enfin, nous généralisons l'étude du micromouvement à un système modèle 3D avec un ion dans un piège de Paul sphérique 3D et un atome lourd au centre du piège. Nous discutons de l'influence du micromouvement en vue d'applications potentielles de ce système telle que la porte logique de phase.

Acknowledgements

I would like to express my utmost gratitude and appreciation to my thesis advisors Prof.Jean-Michel LAUNAY and Dr.Andrea SIMONI for their immense patience, generosity, guidance and support during the PhD. They have always made themselves available for help at all times and provided unassuming advice and suggestions through out my PhD.

I would also like to thank our group, the erstwhile 'Groupe SIMPA' for the very warm and welcoming atmosphere. I would especially like to thank the group cluster technician and engineer Guillaume Raffy for maintaining a very good and efficient cluster facility. I appreciate his help all throughout my PhD in sorting out issues with the cluster usage, programming and data management. I would also like to thank his other colleagues Gilles Bourhis and Jeremy Gardais for their help every time I approached them. I would be remiss if I do not thank Dr.Kevin Dunseath for a lot of help and suggestions regarding parallel programming, cluster use, F90 and particularly for giving me his very efficient, highly parallelized version of the Johnson-Manolopoulos Log Derivative propagation routine.

My gratitude also goes out to my colleagues over the years Dr.Markku Leino, Dr.Gregoire Guillon, Dr.Manuel Lara, Hugo Terrier and especially Dr.Olivier Vieuxmaire and Dr.David Dell'Angelo for the frequent outings, discussions and companionship. I also would like to thank Guillaume Raffy again, Dr.Brice Arnaud, Dr.Marie Postic and Dr.Véronique Vié for the very enjoyable weekly badminton sessions.

My deepest gratitude also goes out to my mother and sister for constant support through tough times and disappointment. My gratitude also goes to Dr. Hema Ramachandran for being a mentor I could look up to during testing times. One aspect of life in Rennes that will be sorely missed are the weekly cricket sessions, with some wonderful times spent playing saturday afternoon cricket, come winter, summer, rain or wind. I would like to thank Kamal, Charles, Karthik, Suresh, Yogesh, Ajay, Prasad, Kalyan, Saravana, Mani, Sumeet, Sentamizhan, Bhaskar and others for the some great times playing cricket. I thank Pathi, Vijay, Kumar, Xavier and Saurabh for companionship and some good times.

Lastly but certainly not the least, I would not just want to thank but also be thankful for having Somi, my wife. Caring, loving, understanding and by my side through thick and thin, she has made it worthwhile to go through life's crests and troughs alike, for the joy of her presence makes all bearable. Thank you for that!

I would also like to thank the administration at IPR, Rennes, the Ecole Doctorale-SDLM of Université de Rennes-1 for their cooperation during times of need. My work was financially supported by a grant from the regional ministry, bourse ministériel- région Bretagne, for three years and the ANR grant, for eight months.

Contents

List of Figures

Chapter 0

Résumé en Français

L'avènement de mélasses optique et du refroidissement par laser, le développement ultime des pièges magnéto-optiques (MOT) servant à piéger et à refroidir les atomes ont suscité énormément d'intérêt dans plusieurs domaines de la physique. En effet, ces avancées ont mis en perspective le fait de piéger un nombre presque déterministe d'atomes ou d'ions par des champs électromagnétiques afin d'étudier leur comportement quantique. Dès lors, le domaine de la physique des atomes froids s'est enrichi d'applications potentielles et de tests de physique fondamentale allant de la métrologie aux communications quantiques, permettant la simulation de phénomènes fondamentaux repoussant ainsi les frontières du calcul quantique et même la simulation quantique de phénomènes de haute énergie. Le domaine de la physique des atomes froids englobe l'étude de différents systèmes comprenant des atomes, des molécules, des ions, des ions moléculaires, des photons, les mélanges de différents atomes et également d'atomes et d'ions. Le système hybride atome-ion a suscité énormément d'intérêt puisqu'il était quasi-inexploré jusqu'à une époque récente. Depuis peu, des propositions et des mises en œuvre de systèmes hybrides de ce type émergent, couvrant un large variété d'applications et de champs d'études.

Motivation

La plupart des propositions d'étude des systèmes hybrides atome-ion exploitent le potentiel de polarisation à longue portée et la richesse de la physique qui sous-tend son utilisation. Il existe aussi des propositions de mise au point de l'équivalent atomique d'une sonde de balayage afin de détecter les propriétés locales des atomes ultra-froids [1,2]. La forte interaction atome-ion porte en elle la possibilité d'échange de charge au sein du système hybride [3,4], et de ce fait ont été étudiées par ailleurs les transitions de phases entre des états isolant et conducteur [5]. L'utilisation de systèmes ultra-froids pour simuler la physique d'autres systèmes a toujours attiré l'attention et à cette fin il a été proposé d'utiliser des systèmes hybrides atome-ion pour simuler la physique de l'état solide, en faisant interagir un gaz ultra-froid avec un cristal ionique linéaire [6]. Peut-être que l'une des premières idées consistant à utiliser un système hybride atome-ion a émergé de l'exigence en calcul quantique des pièges ioniques de trouver des moyens de réduire la décohérence. Le domaine des pièges ioniques dépend par nature étroitement du temps et n'est pas conservatif, ce qui pose des problèmes à ceux qui souhaitent utiliser des états cohérents d'ions pour effectuer des opérations logiques quantiques. Les idées consistaient initialement à utiliser un nuage d'atomes ultra-froids comme un réfrigérateur pour refroidir les ions [7, 8]. La communauté des spécialistes en atomes froids est en général très attachée à essayer de comprendre les systèmes condensés hétérogènes et comment les impuretés dans les systèmes ultra-froids peuvent être utilisées à des fins utiles. Dans ce but, de nombreuses expériences ont été réalisées, démontrant l'introduction d'impuretés contrôlées dans de la matière ultra-froide via l'immersion d'un atome neutre [9–11] dans un Condensat de Bose-Einstein, mais également d'un ion [27, 28]. De nombreux découvertes théoriques ont vu le jour ainsi que des propositions d'expériences au sujet des impuretés ioniques dans les gaz dégénérés [12–16]. L'idée d'insérer une impureté de forte interaction dans un gaz homogène ultra-froid va naturellement motiver l'étude des polarons dans les gaz ultra-froids [17–20]. Il y a eu également des propositions de mise en œuvre de porte quantique atome-ion utilisant la phase accumulée par la particule durant un transfert adiabatique selon des croisements évités [38–40] dans des systèmes liés accordables [37].

Ions pièges et micro-mouvements

Les pièges à particules chargées sont des systèmes non-conservatifs dépendant du temps, qui reposent sur une localisation basée sur un temps moyenné de l'ion entraînant le piègeage. Cette particularité inhérente au piège est sujette à des micro-mouvements de haute fréquence de la trajectoire de l'ion sur la partie supérieur de l'orbite lent. Ce mouvement est entraîné par un champ de radio-fréquences permettant un piègeage dynamique. Les micro-mouvements peuvent être réduits mais pas supprimés totalement. Bien que dans la plupart des calculs et simulations théoriques l'impact de ces micro-mouvements soit négligé, en pratique il n'est pas négligeable. Dans le meilleur des cas les expérimentateurs s'assurent que l'ion est refroidi et que son micro-mouvement est réduit [103, 104] avant de continuer à utiliser l'ion pour des applications cohérentes. Les systèmes atome-ion sont particulièrement intéressants à cause de la présence d'un potentiel d'attraction à grande distance qui évolue en $-C_4/(2r^4)$ et la présence de micro-mouvements, un artefact intrinsèque aux champs de confinement dynamique utilisés pour l'ion. Les expériences impliquant un ion interagissant avec des gaz ultra-froids rapportent des détails essentiels au sujet des effets des micro-mouvements, des sections efficaces pour les collisions avec des potentiels de si longue portée, des échanges inélastiques d'énergie entre les atomes et les ions, des échanges de charge, etc.

Bien que de nombreux aspects de la collision entre atomes et ions aient été étudiés dans les régimes froid et ultra-froid [42-46], l'intérêt d'un travail théorique se penchant sur les effets des micro-mouvements n'a été suscité que récemment. Aussi, bien que les mises en œuvre expérimentales aient fait état d'effets dus aux micro-mouvements, il existe relativement peu de littérature disponible au sujet du traitement quantique complet des micro-mouvements dans les systèmes hybrides atome-ion, excepté les travaux de Nguyen et al. [48] et de Krych et al. [47]. Dans [48], l'effet réel des micro-mouvements est moyenné sur la période de la radio-fréquence utilisée, selon l'approximation harmonique fournie par Cook et al. [51]. Ceci dans le but de réduire le mouvement de l'ion à une oscillation harmonique efficace dont on se référera comme étant nommée séculaire dans cette thèse. Cette méthode offre ainsi une relative facilité de calcul numérique et une base de comparaison par rapport à un oscillateur statique, isolant en un certain sens l'effet des micro-mouvements. Ils rapportent la possibilité de mise en œuvre d'une porte de phase quantique en utilisant des passages adiabatiques. Krych et al. [47] quant à eux fournissent une description complète des micro-mouvements et modélisent l'interaction d'un ion et d'un condensat de Bose-Einstein. Les paramètres a et q du piège à ion (Cf. Appendice.A.1) qui déterminent les con-

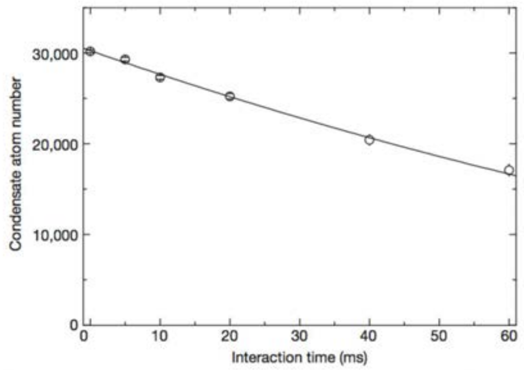

Figure 2 | Atom loss from a Bose–Einstein condensate due to collisions with a single ion. The solid line is a fit using a theoretical model (Methods) and is used to determine σ_{al}, the cross-section for neutral-atom loss. Each data point is averaged over approximately 40 repetitions of the experiment and the standard error is given. The bare atom loss rate, that is, the loss rate without the ion present, has been subtracted.

the loss of neutral atoms (Fig. 2) and is shown as a function of the interaction time in Fig. 4a. We observe a linear increase in the ion loss

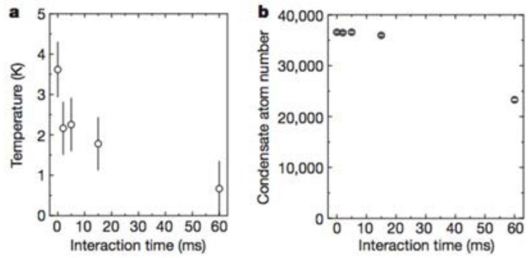

Figure 3 | Time-resolved sympathetic cooling of a single ion. **a,** Temperature decrease as a function of interaction time. The temperature is measured by laser fluorescence and the standard deviation of the maximum-likelihood estimate is shown. **b,** Atom loss during sympathetic cooling. While the ion is hot, atom losses are small and the cooling rate approaches 1,000 vibrational quanta per collision. When the ion cools, it localizes inside the region of higher density and the atom loss rate increases. The standard errors are shown. Each data point is averaged over approximately 200 repetitions of the experiment.

Figure 1: Pertes d'atomes du condensat et refroidissement sympathique de l'ion, d'après Zipkes et al. [27].

finements statique et dynamique sont utilisés comme paramètres d'entrée. Ils ne rapportent pas de refroidissement de l'ion, excepté dans le cas où le piège opère à la limite de la zone de stabilité, là où l'effet des micro-mouvements est prononcé. D'autre travaux détaillent l'effet des micro-mouvements sur la collision entre un atome et un ion en utilisant des approches classiques ou semi-classiques [49, 50]. Cetina et al. [49] effectuent un calcul classique dynamique afin d'estimer le travail du champ sur l'ion. Ils incluent le potentiel réel atome-ion dans le problème et postulent que l'interaction du potentiel de polarisation de longue portée avec le champ radio-fréquence de piègeage provoque le déplacement de l'ion du centre du

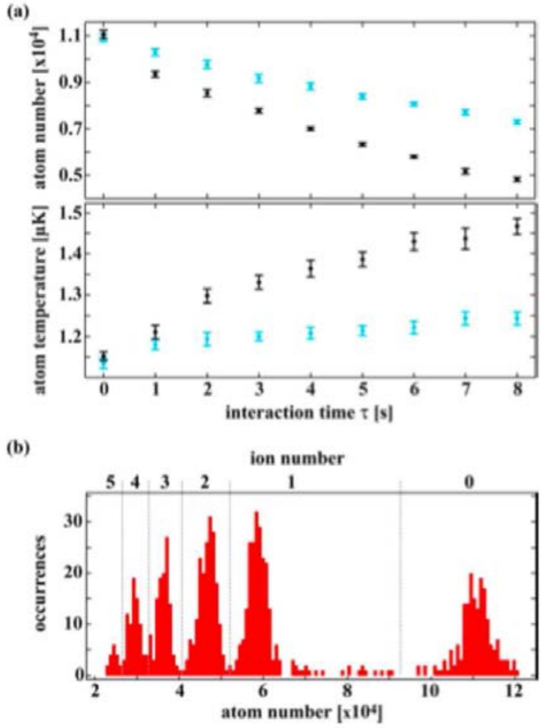

FIG. 1. Atomic signals after atom-ion interaction. (a) Evolution of atom numbers (upper panel) and atomic temperatures (lower panel) during interaction with a single ion. The measurement was performed both for $\varepsilon_r < 0.1$ V/m (blue data points) and for $\varepsilon_r = 4$ V/m (black data points). (b) Histogram of

Figure 2: Perte d'atome et échauffement atomique, selon Härter et al. [29].

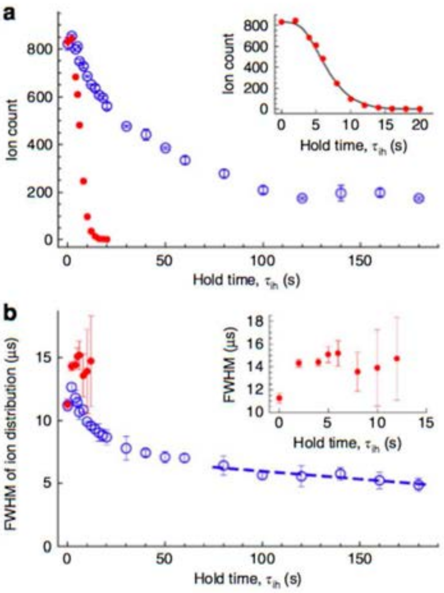

Figure 4 | Experimental demonstration of ion cooling. Evolution of trapped ion population and distribution is experimentally determined when the ions are held in the trap without MOT atoms (red filled circles) and with MOT atoms (blue empty circles). **(a)** Plots the number of Rb^+ ion counts as a function of τ_{ih}. Without a MOT, the ions exit the trap rapidly, whereas with cold atoms the ion loss is much slower and a stable number of ions (187±9) is trapped without detectable loss beyond $\tau_{ih} \geq 2$ min. The inset in **(a)** shows the detail of the ion loss (red circles) when the ions are held without the MOT atoms. This ions loss is fitted with a function (black solid line) obtained by the Monte-Carlo model described in the text. **(b)** Illustrates the variation of the FWHM of the ion ToF distribution against τ_{ih}. In the absence of the MOT atoms, the FWHM increases in time as the trap empties out, the detail of which is shown in the inset. In contrast, when ions are held with the MOT atoms, a systematic decrease in the ion ToF distribution is seen, consistent with ion cooling. For $\tau_{ih} \geq 2$ min, when the trapped ion number has stabilized, the ToF width is still decreasing indicating continued ion cooling, as illustrated by a least square fit to the last six data points. The statistical s.d.e. bars are shown.

Figure 3: Refroidissement d'un nuage d'ions, d'après Ravi et al. [31].

piège et peut même introduire des changements soudains dans la phase de l'ion au moment de collision.

Ils concluent qu'en raison de l'effet cumulé de ces facteurs, le refroidissement sympathique des ions a une limite naturelle et est maximisé dans les cas où la masse de l'atome est inférieure à celle de l'ion. Chen et al. [50] arrivent à la même conclusion en utilisant l'approche d'une équation de taux, où ils estiment la distribution d'énergie de l'ion selon les trois dimensions spatiales en raison de la collision.

Les expériences sur les systèmes atome-ion [21 - 36] signalent également largement le taux de pertes d'atomes du piège lorsque l'ion est introduit dans le nuage atomique ultra-froid. Quelques mesures sont présentées sur les Fig.1.1, Fig.1.2 et Fig.1.3.

Plan de la thèse

Cette thèse fournit une approche plus directe dans le traitement des micro-mouvements lors des collisions entre un atome et un ion en conservant la dépendance temporelle mais en la transformant dans l'espace des fréquences et en utilisant des méthodes standard de dynamique moléculaire quantique, comme la propagation de la dérivée logarithmique pour résoudre l'équation de dispersion de Schrödinger. Le comportement en dépendance par rapport au temps des fonctions d'onde des ions a été analytiquement et élégamment dérivé par Glauber [52] et ces fonctions sont utilisées comme des fonctions asymptotiques pour le système à micro-mouvements. Nous utilisons un potentiel atome-ion simplifié modélisé par un pseudo-potentiel delta dans une dimension (Cf. Ch.3 et Ch.4) ainsi que dans les trois dimensions (Cf. Ch.5). Bien qu'il ne décrive pas exactement les conditions réelles des expériences, ce potentiel sert à comprendre les effets de micro-mouvements dépendant du temps tout en gardant raisonnables les temps de calcul.

La thèse commence par une brève description des différentes méthodes numériques utilisées. Le Chapitre 3 décrit une modélisation simplifiée de collision en une dimension entre un atome confiné dans une dimension mais pouvant s'y mouvoir librement dans un guide d'ondes, et une autre particule dans un potentiel harmonique monodimensionnel. Nous étudions les propriétés de diffusion et les état liés du système. Dans le Chapitre 4, le système est alors étendu pour y inclure une oscillation du potentiel harmonique dépendant du temps, dans une dimension. La nature du domaine temporel du piège à ion est transformé dans l'espace fréquentiel, ce qui permet d'analyser le spectre d'énergie de Floquet de l'ion. La collision et les effets suivant l'échange inélastique d'énergie entre l'atome et l'ion sont étudiés dans des conditions de confinement fort ou faible de l'oscillateur.

Les résultats obtenus sont examinés dans le contexte des résultats expérimentaux disponibles et d'un travail théorique similaire.

La nature fondamentale des micro-mouvements entraîne des limitations numériques qui ne permettent pas de dépasser une certaine gamme de valeurs pour le paramètres q qui peut être artificiellement introduit pour étudier la physique dans des conditions de confinement fortement dynamique. Un changement de coordonnées a permis de résoudre le problème, quoique partiellement. Dans les expériences réelles le confinement de l'ion est presque exclusivement dynamique mais ce cas est numériquement très difficile à faire converger étant donné qu'un tel système subissant de forts micro-mouvements aurait une fonction d'onde de l'ion fortement délocalisée et il faudrait une grille très large dans la mesure où on garderait constante la grille de densité de points. De tels problèmes deviennent numériquement énormes et ne permettent pas de converger. La perte progressive de convergence avec*croisement des paramètres d'entrée est documentée pour ces méthodes numériques.

Nous avons essayé d'étendre l'étude d'une à trois dimensions grâce à une méthode robuste de discrétisation par éléments finis d'ordre élevé des états liés d'un ion en présence de micro-mouvements et interagissant avec un atome infiniment lourd au centre du piège. Un cylindre anisotrope de type *piège de Paul* est utilisé pour modéliser le piège à ion et l'interaction atome-ion est modélisée à nouveau par un pseudo-potentiel delta au lieu d'un potentiel de longue portée. Puisque le problème est résolu dans l'espace fréquentiel, la base du domaine de fréquences et la base d'harmoniques sphériques utilisée pour décrire ce problème tridimensionnel rend le taille de matrice de problème très large. L'utilisation de potentiel à longue portée aurait des limitations sévères en terme d'espace mémoire, de temps de calcul etc. Le but est d'étudier les croisements évités et réels des niveaux d'énergie de l'ion dans un tel piège en présence d'une interaction accordable en pseudo-potentiel delta au centre du piège. Les références existent qui documentent bien l'utilisation de pièges séparés d'atomes et d'ions pour effectuer des opérations de portes logiques lors des passages adiabatiques.

Ce travail de thèse se termine par une conclusion et une annexe qui clarifient la dynamique classique et la dynamique quantique d'un unique ion dans un piège de Paul à une dimension. Etant donné que le mouvement de l'ion est séparable en trois dimensions, le résultat de l'annexe peut être généralisé à trois dimensions pour comprendre le mouvement d'un ion dans un piège tridimensionnel.

Chapter 1

Introduction

The advent of optical molasses, laser cooling and eventual development of the magneto-optical trap (MOT) to trap and cool atoms encouraged much interest from many branches of physics since it presented the prospect of trapping an *almost* deterministic number of atoms or ions with electromagnetic fields to study quantum behaviour. Since then the field of cold atom physics has developed potential applications and tests of fundamental physics ranging from metrology to quantum communications, from simulating fundamental phenomena to help move forward the frontier of quantum computation and even quantum simulations of high energy phenomena. The field of cold atom physics has seen the study of various types of systems including atoms, molecules, ions, molecular ions, photons, mixtures of different atoms and recently mixtures of atoms and ions as well. The hybrid atom-ion system has sparked much interest since it had been fairly unexplored until recent times, with proposals and implementations coming up for using hybrid systems range over a wide variety of applications and fields of study.

1.1 Motivation

Most of the proposals on atom-ion hybrid systems exploit the long range polarization potential and the rich physics that underlies its use. There are proposals to build an atomic analogue of a scanning probe to sense the local properties of ultracold atoms [1, 2]. The strong atom-ion interaction carries with it the possibility of charge exchange interactions in a system [3, 4] and exploiting this, there is a proposal to study transitions from insulating to conducting phases of matter [5]. Use of ultracold systems to simulate the physics of other physical systems has always drawn attention and to this end there is a proposal to use atom-ion systems to simulate solid state physics by having an ultracold gas interact with a linear ion crystal [6]. Perhaps one of the very first ideas to use atom-ion hybrid systems came out of the demand in ion trap quantum computation community to find ways to reduce decoherence. The ion trapping field by its nature is time dependent and non-conservative which poses an issue to those wishing to use coherent state of ions to perform quantum logic operations. The ideas initially were to use an ultracold atom cloud as a refrigerator to *cool* the ions [7, 8]. The cold atom community at large is very keen on trying to understand heterogenous condensed systems and how impurities in ultracold systems can be used for fruitful applications. To this end, there have been experiments that have demonstrated introducing controlled impurities in ultracold matter via immersion of a neutral atom [9–11] in a Bose Einstein Condensate and also an ion [27, 28]. There have also been many theoretical findings and proposals on ionic impurities in degenerate gases [12–16]. The idea of having a strongly interacting impurity in a homogenous ultracold gas will naturally motivate the study of polarons in ultracold gases [17–20]. There have also been proposals to implement an atom-ion quantum gate using phase accumulated by the particle during adiabatic transfer across avoided crossings [38–40] in tunable bound systems [37].

1.2 Trapped Ions and Micromotion

Charged particle traps are time dependent dynamical, non-conserved systems that rely on time averaged localization of the ion leading to trapping. This inherent feature of the trap is prone to micromotion, a high frequency *jitter* of the ion trajectory on top of the global slow moving orbit in the trap. This motion is driven by a radio frequency field that gives dynamical trapping. Micromotion can only be reduced but never avoided. Though in most theoretical calculations and simulations the effect of micromotion is neglected, in practice its effect cannot. At the least experimenters ensure the ion is cooled and micromotion is reduced [103, 104] before continuing to use the ions for coherent applications. Atom-ion systems are particularly interesting due to the presence of a long range attractive potential between the atom and ion that goes as $-C_4/(2r^4)$ and the presence of micromotion, an intrinsic artifact of the dynamical confinement fields for the ion. Experiments involving an ion interacting with ultracold gases report vital details about the effects of micromotion, cross sections for collisions with such long range potentials, inelastic exchange of energy between the atoms and ion, charge exchange phenomena etc.

Though various aspects of atom-ion collision have been studied in the cold and ultracold regime [42-46], interest in theoretical work on addressing the effects of micromotion rose only recently. Although the experimental implementations report observation of effects due to micromotion, not much literature can be found on the full quantum treatment of micromotion in atom-ion systems except for Nguyen et. al. [48] and Krych et al. [47]. In [48], the true effect of micromotion is averaged out over the time period of the radio frequency, using the harmonic approximation formulated by Cook et al. [51]. This is done to reduce the ion motion to an effective harmonic motion, referred to as *secular* motion in this thesis. This provides computational ease and a basis of comparison to a static oscillator, thus in a sense isolating the effect of the micromotion.They report on the possibility of implementation of a quantum phase gate using adiabatic transitions. Krych et al. [47] on the other hand provide a full description of micromotion and model a system of ion interacting with a Bose condensate. The ion trap parameters a and q (See Appendix.A.1) that decide the static and dynamic confinement are used as input parameters. They report no ion cooling, except for the case when the trap operates at the edge of the stability region, where the effect of micromotion is pronounced. Some literature exists that details the effect of micromotion on atom-ion collision using classical and semi-classical approaches [49, 50]. Cetina et al. [49] perform a classical dynamical calculation to estimate the work done by the field on the ion. They include the real atom-ion potential in the problem and postulate that the interplay of the long range polarization potential and the ion trapping rf field cause the ion to be displaced from the trap centre and even introduce sudden change in ion phase at the instance of collision. They conclude that due to cumulative effect of these factors ion sympathetic cooling has a natural limit and is maximized for cases where the mass of the atom is lighter than

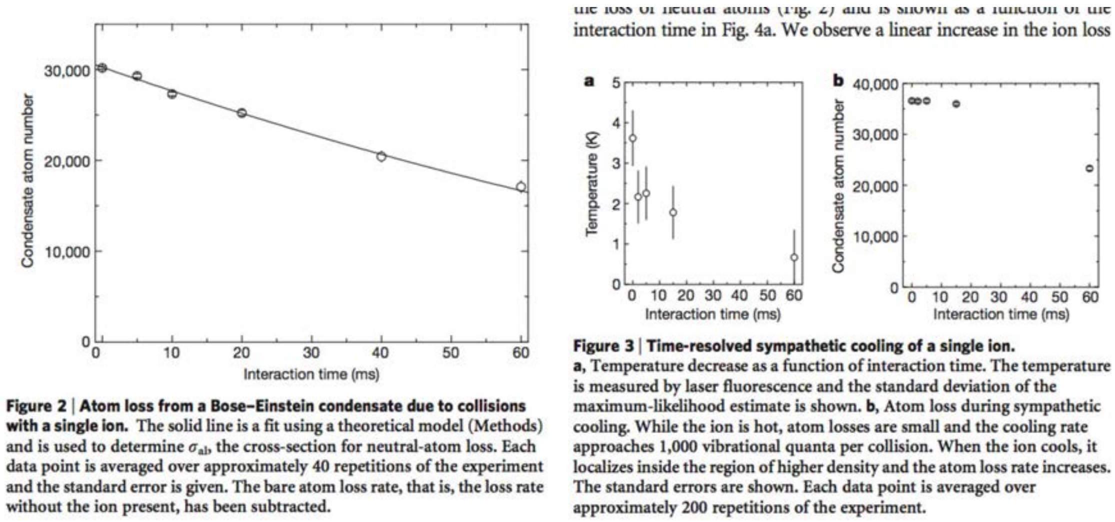

Figure 2 | Atom loss from a Bose–Einstein condensate due to collisions with a single ion. The solid line is a fit using a theoretical model (Methods) and is used to determine σ_{al}, the cross-section for neutral-atom loss. Each data point is averaged over approximately 40 repetitions of the experiment and the standard error is given. The bare atom loss rate, that is, the loss rate without the ion present, has been subtracted.

interaction time in Fig. 4a. We observe a linear increase in the ion loss

Figure 3 | Time-resolved sympathetic cooling of a single ion. **a,** Temperature decrease as a function of interaction time. The temperature is measured by laser fluorescence and the standard deviation of the maximum-likelihood estimate is shown. **b,** Atom loss during sympathetic cooling. While the ion is hot, atom losses are small and the cooling rate approaches 1,000 vibrational quanta per collision. When the ion cools, it localizes inside the region of higher density and the atom loss rate increases. The standard errors are shown. Each data point is averaged over approximately 200 repetitions of the experiment.

Figure 1.1: Atom loss from the condensate and ion sympathetic cooling, reported by Zipkes et al. [27].

the mass of the ion. Chen et al. [50] arrive at a similar conclusion using a rate equation approach, where they estimate the energy distribution of the ion along the three axes due to the collision.

Experiments on atom-ion systems [21 - 36] also report extensively on the rate of atom loss from the trap, when the ion is introduced into the ultracold atomic cloud. Some of the measurements are shown in Fig.1.1, Fig.1.2 and Fig.1.3.

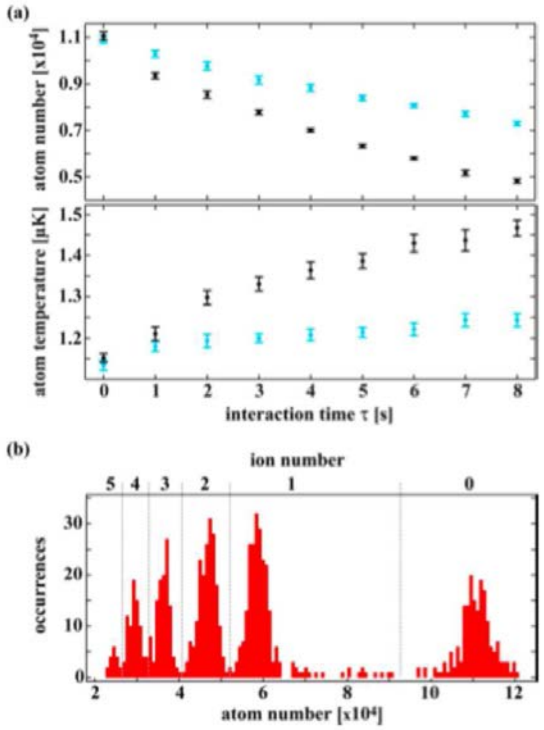

FIG. 1. Atomic signals after atom-ion interaction. (a) Evolution of atom numbers (upper panel) and atomic temperatures (lower panel) during interaction with a single ion. The measurement was performed both for $\varepsilon_r < 0.1$ V/m (blue data points) and for $\varepsilon_r = 4$ V/m (black data points). (b) Histogram of

Figure 1.2: Atom loss and atom heating, reported by Härter et al. [29].

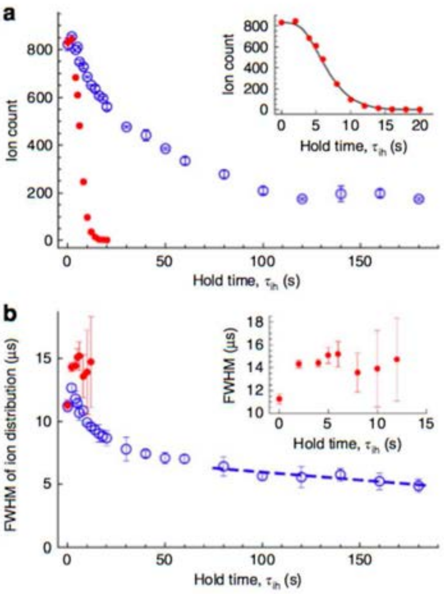

Figure 4 | Experimental demonstration of ion cooling. Evolution of trapped ion population and distribution is experimentally determined when the ions are held in the trap without MOT atoms (red filled circles) and with MOT atoms (blue empty circles). **(a)** Plots the number of Rb$^+$ ion counts as a function of τ_{ih}. Without a MOT, the ions exit the trap rapidly, whereas with cold atoms the ion loss is much slower and a stable number of ions (187±9) is trapped without detectable loss beyond $\tau_{ih} \geq 2$ min. The inset in **(a)** shows the detail of the ion loss (red circles) when the ions are held without the MOT atoms. This ions loss is fitted with a function (black solid line) obtained by the Monte-Carlo model described in the text. **(b)** Illustrates the variation of the FWHM of the ion ToF distribution against τ_{ih}. In the absence of the MOT atoms, the FWHM increases in time as the trap empties out, the detail of which is shown in the inset. In contrast, when ions are held with the MOT atoms, a systematic decrease in the ion ToF distribution is seen, consistent with ion cooling. For $\tau_{ih} \geq 2$ min, when the trapped ion number has stabilized, the ToF width is still decreasing indicating continued ion cooling, as illustrated by a least square fit to the last six data points. The statistical s.d.e. bars are shown.

Figure 1.3: Cooling of ion cloud, reported by Ravi et al. [31].

1.3 Plan of the thesis

The work in this thesis assumes a more direct approach in treating the micromotion in atom-ion collisions by retaining the time dependence but transforming it into frequency domain and using standard methods of quantum molecular dynamics like Log Derivative Propagation to solve the scattering Schrödinger equation. The time dependent behaviour of ion wavefunctions has been analytically and elegantly derived by Glauber [52] and are used as asymptotic wavefunctions for the system with micromotion. This work uses a simplified atom-ion potential modelled by a delta pseudopotential in one dimension (in Ch.3 and Ch.4) and in three dimensions (in Ch.5). Though it does not correctly describe the real conditions in experiments, it serves to understand effects of time dependent micromotion and keeping the computational size of the problem fairly manageable.

The thesis begins with a brief description of the various numerical methods used. Chapter 3 describes simplified model of collision in one dimension between an atom confined to move freely in one dimension, in a waveguide and another particle in a one dimensional harmonic oscillator potential. We study the scattering properties and bound state properties of the system. In Chapter 4 the system is then extended to include a time dependent oscillation of the harmonic oscillator potential in one dimension. The time domain nature of the ion trap is transformed to frequency domain, which helps analyze the ion's Floquet energy spectrum. The collision and the effects due to inelastic exchange of energy between the atom and the ion are studied under the conditions of tight and weak static confinement of the oscillator. The results obtained are discussed in the context of the available experimental results and similar theoretical work.

The basic nature of micromotion results in numerical limitations which do not give results over a wide range of micromotion parameter q that can be artificially introduced to study the physics under strongly dynamical confinement of the ion. A change of coordinates at one stage served to solve the problem, albeit partially. In real experiments the ion confinement is almost purely dynamical but numerically that case appears very difficult to converge since such a system at high micromotion would have a highly delocalized ion wavefunction and one would require a very large grid if keeping a constant grid density of points. Such problems become computationally huge and yield fairly bad convergence. The gradual loss of convergence with input parameters is documented for these numerical methods.

As an attempt at extending the study from one to three dimensions, a robust high order finite element discretization method is used to study the bound states of an ion in the presence of micromotion and interacting with an infinitely heavy atom at the trap centre. An anisotropic cylindrical Paul trap geometry is used to model the ion trap and the atom-ion interaction is again modelled by a delta pseudopotential instead of the use of long range potentials. Since the problem is solved in frequency domain, the frequency domain basis and the spherical harmonic basis used to describe the problem in 3D, makes it very large. Use of long range potentials would have severe limitations in terms of memory usage, computation time etc. The goal is to study the avoided and real crossings of the energy levels of the ion in such a trap configuration in the presence of a tunable delta pseudopotential interaction at the trap centre. Literature exists that well documents the use of separated traps of atoms and ions to perform logic gate operations using adiabatic crossings of the ion molecular levels. The thesis ends with a conclusion and an appendix that elucidates the classical and quantum dynamics of a single ion in a Paul trap in one dimension. Since the ion motion is separable in three dimensions, the result in the appendix can be generalized to three dimensions to understand the ion motion in 3D traps.

Chapter 2

Numerical Methods

The various numerical methods used in the thesis to solve the Schrödinger equation are discussed in this chapter. The problem explained in Ch.3 and Ch.4 is a two-body problem for collision in one dimension. We attempt to solve the two body Schrödinger equation for this problem using three different methods (a) The Schrödinger equation is recast into an integral equation which is solved numerically by pseudospectral method [63-66]. (b) The Schrödinger equation is written as a matrix equation in terms of the logarithmic derivative (or *log-derivative*) of the wavefunction and solved by a propagation algorithm [67-70]. (c) The Spectral Element Method which recasts the Schrödinger Equation as a sparse matrix using high order finite element discretization of the Hamiltonian. The resulting linear equation is then solved using a standard sparse linear solver, called PARDISO [77-81].

The problem explained in Ch.5 is an eigenvalue problem in three dimensions. The Schrödinger equation is written for a system consisting of an ion in a time dependent trap interacting with a heavy atom in the trap centre through a normalized delta pseudopotential. Since the atom mass is much greater than the ion mass, the problem is reduced to solving a one body Schrödinger equation for the ion. The Schrödinger equation in three dimensions is discretized using a high order (or *spectral*) finite element representation scheme. The resulting Hamiltonian is diagonalized using a sparse matrix eigenvalue solver called FEAST [75, 76].

A brief summary of pseudospectral discretization method is provided initially. These methods show super algebraic convergence with point density and rely on very efficient quadrature rules which give exact results for polynomial functions of degree $2N-1$ or less for N discretization points. The Integral Equation Method is then explained concisely but a detailed summary of this methods is given in [63], which is also based on previous results by [64-66]. Then we explain the Log Derivative method of solution of the close coupled Schrödinger Equation followed by the Spectral Element Method.

2.1 Pseudospectral Method

An introduction to the pseudospectral method is provided in [56 p.89 - 58] and is extensively used in various applications of quantum scattering calculations. An introduction to applications of the subject and applications is provided in [96-97]. Pseudospectral method is a specific variation of the method of weighted residuals. We begin by briefly introducing the method of weighted residuals. The method is based on the fact that a solution of a partial differential equation can be expressed as a series expansion over a basis of trial functions. A sufficiently large finite basis can be used to represent the solutions to very high accuracy. Consider a linear differential operator $\mathcal{L}$ with boundary conditions defined on a boundary Ω given by

$$\mathcal{L}u(x) = f(x) \qquad \text{with} \qquad u(\Omega) = u_0 \tag{2.1}$$

where $u(x)$ and $f(x)$ are functions of x. Let solutions to the differential equation (2.1) be a linear combination of N basis functions $\phi_i(x)$ given by

$$\bar{u}(x) = \sum_{i=1}^{N} c_i \phi_i(x) \tag{2.2}$$

The basis functions $\phi_i(x)$ are also called trial functions and c_i are the coefficients of expansion. The solution $\bar{u}(x)$ satisfies the differential equation (2.1) and is nearly exact but leaves a small residual given by

$$\mathcal{R} = \mathcal{L}\bar{u}(x) - f(x) \tag{2.3}$$

If the chosen trial functions are polynomials of high order and smooth over the whole integration interval, the method is termed a *Spectral Method*. Since a basis is chosen of high order polynomials the Spectral method is similar to taking a Fourier series expansion of functions and hence the name. Low order and smooth polynomials chosen as trial functions over the whole integration interval give a *Finite Difference Method*. They are overlapping polynomials since more than one of those functions are non-zero at each discretized point. Low order smooth polynomials can also be chosen only over selected intervals or elements. They can be taken to be zero outside the elements to give the *Finite Element Method*. For periodic problems, Fourier series (trigonometric functions) are chosen as trial functions and orthogonal polynomials (Chebyshev or Legendre) are chosen for non-periodic problems.

The aim of the method of weighted residuals is to minimize the residual $\mathcal{R}$ such that the solution $\bar{u}(x)$ tends to the exact solution of the differential equation. The residual is minimized in an approximate sense by taking its inner product with certain test or weight functions $\chi_i(x)$, given by

$$(\mathcal{L}\bar{u}(x) - f(x), \chi_i(x))_x = \int_\alpha^\beta (\mathcal{L}\bar{u}(x) - f(x))\chi_i(x)dx = 0$$
$$\sum_{j=1}^{N} c_j \int_\alpha^\beta (\mathcal{L}\phi_j(x))\chi_i(x)dx = \int_\alpha^\beta f(x)\chi_i(x)dx \tag{2.4}$$

which in matrix form can be written as $\mathbf{Lc} = \mathbf{f}$. The matrix linear equation can be solved to obtain the set of expansion coefficients c_i of the solution. The exact form of the test functions $\chi_i(x)$ determines the specific variety of weighted residual method being employed.

The *Galerkin Spectral Method* uses the trial functions per se as test functions. The *Collocation* or *Pseudospectral Method* uses delta functions $\chi_i(x) = \delta(x - x_i)$ as test functions at specific collocation points x_i with associated weights w_i which are determined by a certain quadrature rule. In DVR, cardinal functions are chosen as the set of trial functions, on a set of discrete grid points. A delta function and a cardinal function are qualitatively similar to the extent that matrix elements are computed using Gauss quadrature rule corresponding to the chosen DVR basis. This in essence means the Pseudospectral method is a special case of Galerkin Spectral method. The integration limits $[\alpha, \beta]$ in (2.4) determine the kind of quadrature rule being used. All problems described in this work use Gauss-type quadrature rule. An interval of $[\alpha, \beta] = [-1, +1]$ uses either a Legendre polynomial basis or a Chebyshev Polynomial basis and is accordingly called Gauss-Legendre quadrature or Gauss-Chebyshev quadrature respectively. Similarly an interval of $[\alpha, \beta] = [-\infty, +\infty]$ uses a Hermite polynomial basis and is called Gauss-Hermite quadrature. Though integrals of Hermite polynomials do not converge over any interval, this method uses a Gaussian term e^{-x^2} as weight function for the integral that results in functions that are similar to eigenfunctions of harmonic oscillator states that tend to zero as $x \to \infty$ and they converge numerically (See 59 or 62). Gauss-Legendre quadrature is used in the Integral Equation Method, where the points for an arbitrary interval of $[\alpha, \beta]$ can be rescaled to $[-1, +1]$.

The Pseudospectral Method with delta functions as test functions and an appropriately chosen Gauss quadrature rule gives a residual minimization criterion.

$$(\mathcal{R}, \chi_i(x))_x = \int_{-1}^{+1} (\mathcal{L}\bar{u}(x) - f(x))\chi_i(x)dx = 0$$
$$\sum_{j=1}^{N} c_j \int_{-1}^{+1} \mathcal{L}\phi_j(x)\delta(x - x_i)dx = \int_{-1}^{+1} f(x)\delta(x - x_i)dx \tag{2.5}$$

Over a discrete set of points, the integral reduces to

$$\sum_{j=1}^{N} c_j \mathcal{L}\phi_j(x_i) = f(x_i) \tag{2.6}$$

This criterion clearly gives the residue $\mathcal{R} = 0$ at the discretization or *collocation* points x_i which are chosen as per the appropriate Gauss quadrature rule. The trial functions $\phi_i(x)$ can be chosen to form an orthogonal basis with respect to a weight function. For an interval of $[\alpha, \beta] = [-1, +1]$, we choose a basis of Legendre polynomials of the order $(N-1)$. The normalization condition can be given by

$$\int_{-1}^{+1} \phi_i(x)\phi_j(x)dx = \delta_{ij} \quad \text{or as} \quad \sum_{k=1}^{N} \phi_i(x_k)\phi_j(x_k)w_k = \delta_{ij} \tag{2.7}$$

The solutions $\bar{u}(x)$ expanded over a basis of trial functions taken to be Legendre polynomials is given by

$$\bar{u}(x) = \sum_{i=1}^{N} c_i P_i(x) \quad \text{where} \quad c_i = \frac{1}{||P_i(x)||^2}(P_i(x), \bar{u}(x)). \tag{2.8}$$

The scalar product $(P_i(x), \bar{u}(x))$ can be integrated using Gauss-Legendre quadrature as

$$\int_{-1}^{+1} P_i(x)\bar{u}(x)dx = \sum_{j=1}^{N} P_i(x_j)\bar{u}(x_j)w_j \tag{2.9}$$

where x_j and w_j are the Gauss-Legendre points and weights respectively. The coefficients c_i are then given by

$$c_i = \frac{1}{||P_i||^2}\sum_{j=1}^{N} P_i(x_j)\bar{u}(x_j)w_j \quad \text{where} \quad ||P_i||^2 = \sum_{k=1}^{N} P_i(x_k)P_i(x_k)w_k \tag{2.10}$$

2.2 Integral Equation Method (IEM)

Drawing from pseudospectral method of discretization that gives super-algebraic convergence with number of grid points used, integral equations can be efficiently solved using appropriately chosen basis functions as demonstrated in [63–65]. Integral equations in scattering theory have a form given by

$$\psi(x) = \phi(x) + \int_{-\infty}^{\infty} G(x, y')V(y')\psi(y')dy' \tag{2.11}$$

The integral involving the kernel $G(x, y')V(y')$ on the right hand side can be written as

$$\hat{W}\psi(x) = \int_{-\infty}^{+\infty} G(x, y')V(y')\psi(y')dy' \ \text{ then } \ \psi(x) = (\hat{I} - \hat{W})^{-1}\phi(x) \tag{2.12}$$

Thus the solution to the integral equation reduces to solving a linear system once the integral is discretized. To better illustrate the Integral Equation Method we consider an example. Let the integral equation we wish to solve be

$$f(x) = g(x) + \int_{-\infty}^{+\infty} e^{ik|x-x'|} f(x')dx' \tag{2.13}$$

where $g(x)$ is an initial condition for the function $f(x)$. The idea is to use pseudospectral method to solve the integral in Eq.(2.13), as demonstrated in [63]. Alternately, the integral in the above equation can also be computed using the well known trapezoidal method and also by a modification to the Simpson's method, as suggested in [82]. We describe below the pseudospectral integration method and the modified Simpson's methods.

2.2.1 Pseudospectral Integration

The integration coordinate is partitioned into sectors of equal size and a local discretization is done using a Gauss-Legendre DVR basis within the sectors, as shown in Fig.2.1. The schematic is shown for an integration range of $[-\infty, +\infty]$. The N points chosen per sector are the zeroes of the $N-$th order Legendre polynomial.

The integral in Eq.(2.13) can be split into two as

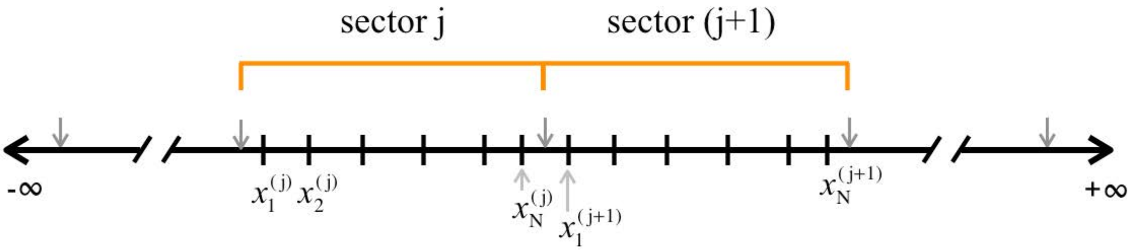

Figure 2.1: Schematic of integration coordinate with N local Legendre quadrature discretization points per sector. $x_i^{(j)}$ denotes the i^{th} point of the j^{th} sector.

$$f(x) = g(x) + \left[\int_{-\infty}^{x} e^{ik(x-x')} f(x')dx' + \int_{x}^{+\infty} e^{-ik(x-x')} f(x')dx' \right] \tag{2.14}$$

where the arguments of the exponential terms are always positive, in keeping with the fact that the original integrand is $e^{ik|x-x'|}f(x')$ in Eq.(2.13). We take a large finite integration range of $[-b, +b]$, the range is partitioned into N_b different sectors of equal length $L = 2b/N_b$. N_b can be taken as even to ensure symmetric partitioning about the origin. The end points of the sectors are given by $a_{-N_b/2} < a_{-N_b/2+1} < \ldots < a_{-1} < a_0 = 0 < a_1 < \ldots < a_{N_b/2-1} < a_{N_b/2}$, where $a_{\pm N_b/2} = \pm b$. Integration is performed over N discretization points in each sector and the result is added to obtain the total integral. Following the method in [63], the integration on a discrete set of points can be performed by a simple right-multiplication of the integrand with a *spectral integration matrix* that is built for the particular basis function used for discretization (Legendre polynomial for Gauss-Legendre basis, as in this case). The definition and procedure of building the spectral integration matrix for integration over a sector is described below.

Spectral Integration Matrices and Their Usage: To build spectral integration matrices for the Gauss-Legendre polynomial basis, we begin by noting that DVR basis functions (See 98 p.8 or 99) are given by

$$\phi_i(x) = \sum_{k=1}^{N} A_{ik} P_k(x) = \sum_{k=1}^{N} \sqrt{w_i} P_k(x_i) P_k(x) \tag{2.15}$$

where $P_k(x)$ are unit normalized Legendre polynomials with normalization constant $\sqrt{(2k+1)/2}$ and the matrix element $A_{ik} = \sqrt{w_i} P_k(x_i)$ forms the DVR-FBR transformation matrix $\mathbb{A}$ with the basis polynomials along the columns (See 96, 97, 98 p.8 and 99). The DVR functions evaluated at the grid points (quadrature points) gives

$$\phi_i(x_j) = \sum_{k=1}^{N} A_{ik} P_k(x_j) = \sum_{k=1}^{N} A_{ik} A_{jk} w_j^{-1/2} = \delta_{ij} w_j^{-1/2} \tag{2.16}$$

Orthonormality relations in arguments and in order over an arbitrary interval $[a, b]$ (where a and b maybe $\pm\infty$) for the DVR functions are given by

$$\sum_{k=1}^{N} \phi_k(x_i)\phi_k(x_j) = \delta_{ij} \quad \text{and} \quad \int_a^b \phi_i(x)\phi_j(x)dx = \delta_{ij} \tag{2.17}$$

As an example, we consider the integrand of Eq.(2.13) $F(x, x') = e^{ik|x-x'|} f(x')$. Expressing the integrand $F(x, x')$ in DVR basis over a set of discrete points in x' variable, we have

$$F(x, x') = \sum_{k=1}^{N} \alpha_k(x)\phi_k(x') \tag{2.18}$$

and the two integrands in Eq.(2.14) as

$$e^{ik(x-x')} f(x') = \sum_{k=1}^{N} c_k(x)\phi_k(x') \text{ and } e^{-ik(x-x')} f(x') = \sum_{k=1}^{N} d_k(x)\phi_k(x') \tag{2.19}$$

To integrate the function over the global interval $[-b, +b]$, we partition the integration coordinate into N_b sectors (with N points per sector) and sum the integrals over the sectors. The end points of the sectors are given by $a_{-N_b/2} < a_{-N_b/2+1} < \ldots < a_{-1} < a_0 = 0 < a_1 < \ldots < a_{N_b/2-1} < a_{N_b/2}$, where $a_{\pm N_b/2} = \pm b$. Similar to Eq.(2.14), the two integral terms are partitioned into integrals over each sector, over the ranges $]a_l, x^{(l)}]$ and $[x^{(l)}, a_{l+1}[$ respectively. $x^{(l)}$ is a variable in each sector labelled l such that $x^{(l)} \in [x_1^{(l)}, x_N^{(l)}]$ and $l = (-N_b/2, \ldots, N_b/2)$. This ensures the arguments of the exponential terms are always positive, in keeping with the fact that the original integrand is $e^{ik|x-x'|}f(x')$ in Eq.(2.13).

$$\begin{aligned}\int_{-b}^{+b}F(x,x')dx' &= \sum_{l=-N_b/2}^{N_b/2-1}\left(\int_{a_l}^{x}e^{ik(x-x')}f(x')dx' + \int_{x}^{a_{l+1}}e^{-ik(x-x')}f(x')dx'\right)\\ &= \sum_{l=-N_b/2}^{N_b/2-1}\left(\sum_k\int_{a_l}^{x}c_k(x)\phi_k(x')dx' + \sum_k\int_{x}^{a_{l+1}}d_k(x)\phi_k(x')dx'\right) \quad (2.20)\end{aligned}$$

Substituting Eq.(2.15), into Eq.(2.20)

$$\begin{aligned}\int_{-b}^{+b}F(x,x')dx' = \sum_{l=-N_b/2}^{N_b/2-1}\Bigg(\sum_k c_k(x)\int_{a_l}^{x}\sum_j\sqrt{w_j}P_j(x_k)P_j(x')dx' +\\ \sum_k d_k(x)\int_{x}^{a_{l+1}}\sum_j\sqrt{w_j}P_j(x_k)P_j(x')dx'\Bigg) = \sum_{l=-N_b/2}^{N_b/2-1}\Bigg(\sum_k\sum_j c_k(x)A_{jk}\int_{a_l}^{x}P_j(x')dx' +\\ \sum_k\sum_j d_k(x)A_{jk}\int_{x}^{a_{l+1}}P_j(x')dx'\Bigg) \quad (2.21)\end{aligned}$$

A_{jk} are matrix elements of $\mathbb{A}$. Thus the integration of a given function is reduced to an integral over the polynomial chosen as basis, unit-normalized Legendre polynomial in this case. From [60] and [61], using the recurrence relation for non-unit normalized polynomials $\bar{P}_n(x')$ such that $\int_{-1}^{+1}\bar{P}_m(x')\bar{P}_n(x')dx' = \frac{2}{(2n+1)}\delta_{mn}$, we get

$$\begin{aligned}\int_{x}^{+1}\bar{P}_n(x')dx' = \frac{\bar{P}_{n-1}(x)-\bar{P}_{n+1}(x)}{2n+1} = S_n^+(x) \text{ and}\\ \int_{-1}^{x}\bar{P}_n(x')dx' = \frac{\bar{P}_{n+1}(x)-\bar{P}_{n-1}(x)}{2n+1} = S_n^-(x) \quad (2.22)\end{aligned}$$

with $n = 1,2,3,\ldots$ and special conditions for $n = 0$ set by $\int_{x}^{+1}\bar{P}_0(x')dx' = 1 - \bar{P}_1(x)$ and $\int_{-1}^{x}\bar{P}_0(x')dx' = \bar{P}_1(x)+1$. Writing these in terms of unit-normalized polynomials $P_n(x')$, we have $\bar{P}_n(x') = \sqrt{\frac{2}{2n+1}}P_n(x')$. Thus rewriting Eq.(2.22) in terms of unit-normalized polynomials $P_n(x')$, we have

$$\begin{aligned}S_n^+(x) = \int_{x}^{+1}P_n(x')dx' = \frac{1}{\sqrt{2n+1}}\left(\sqrt{\frac{1}{2n-1}}P_{n-1}(x) - \sqrt{\frac{1}{2n+3}}P_{n+1}(x)\right)\\ S_n^-(x) = \int_{-1}^{x}P_n(x')dx' = \frac{1}{\sqrt{2n+1}}\left(\sqrt{\frac{1}{2n+3}}P_{n+1}(x) - \sqrt{\frac{1}{2n-1}}P_{n-1}(x)\right) \quad (2.23)\end{aligned}$$

It is seen the matrix representation of Eq.(2.23) has a tri-diagonal structure in the n index basis. Thus defining $\beta_n = 1/\sqrt{(2n+1)(2n-1)}$ if $n = 1, 2, 3, \ldots$ and with condition that $\beta_0 = +1$ we can write the spectral integration matrix as

$$\begin{bmatrix} 1 & \mp\beta_1 & 0 & 0 & \ldots & 0 \\ \pm\beta_1 & 0 & \mp\beta_2 & 0 & \ldots & \vdots \\ 0 & \pm\beta_2 & 0 & \mp\beta_3 & \ldots & \vdots \\ 0 & 0 & \pm\beta_3 & 0 & \ddots & 0 \\ \vdots & \vdots & \vdots & \ddots & \ddots & \mp\beta_{N-1} \\ 0 & \ldots & \ldots & 0 & \pm\beta_{N-1} & 0 \end{bmatrix} \begin{bmatrix} P_0(x) \\ P_1(x) \\ P_2(x) \\ P_3(x) \\ \vdots \\ P_{N-1}(x) \end{bmatrix} = \begin{bmatrix} S_0^{\pm}(x) \\ S_1^{\pm}(x) \\ S_2^{\pm}(x) \\ S_3^{\pm}(x) \\ \vdots \\ S_{N-1}^{\pm}(x) \end{bmatrix}$$

$$\Rightarrow \mathbb{M}^{\pm}\bar{\mathbf{P}}(x) = \bar{\mathbf{S}}^{\pm}(x) \quad (2.24)$$

where the vectors $\bar{\mathbf{P}}(x) = [P_0(x), P_1(x), \ldots, P_{N-1}(x)]^T$ and $\bar{\mathbf{S}}^{\pm}(x) = [S_0^{\pm}(x), S_1^{\pm}(x), \ldots, S_{N-1}^{\pm}(x)]^T$. The spectral integration matrices $\mathbb{M}^{\pm}$ are in the function basis (FBR). Given any two functions $f(x) = \sum_k \alpha_k P_k(x)$ and $F(x) = \sum_k \beta_k P_k(x)$, an integral $F(x) = \int_{x'}^{1} f(x')dx'$ can be computed using these matrices in FBR as $\bar{\beta} = \mathbb{M}^{+}\bar{\alpha}$. These can be converted to DVR and rescaled to the sector size as

$$\mathbb{G}^{\pm} = \mathbb{A}^T \mathbb{M}^{\pm} \mathbb{A}\ (L/2) \quad (2.25)$$

Thus, analogous integration in DVR can be given as $\bar{\mathbf{F}}(x) = \mathbb{A}^T\mathbb{M}^{+}\mathbb{A}\ \bar{\mathbf{f}} = \mathbb{G}^{+}\ \bar{\mathbf{f}}$. Defining the integrands over the grid $e^{ik(x-x')}$ and $e^{-ik(x-x')}$ as elements of two matrices $\mathbb{C}(k)$ and $\mathbb{D}(k)$, given by

$$C_{jj'}(k) = e^{-ik(x_j^{(l)} - x'^{(l)}_{j'})};\ D_{jj'}(k) = e^{ik(x_j^{(l)} - x'^{(l)}_{j'})} \text{ with } x_j^{(l)} \in [x_1^{(l)}, x_N^{(l)}], x'^{(l)}_{j'} \in [x'^{(l)}_1, x'^{(l)}_N] \quad (2.26)$$

It is important to note that the term $(x_j^{(l)} - x'^{(l)}_{j'}) \in [0, x'_N[$ and is independent of the sector since they are taken to be of equal length. So the integration can be done just once instead of being repeated for each sector. The two integrals in Eq.(2.20) done over each sectors can be written as matrix product involving the solution term $f(x)$ defined over each sector as

$$\int_{a_l}^{x} e^{ik(x-x')} f(x')dx' + \int_{x}^{a_{l+1}} e^{-ik(x-x')} f(x')dx' \rightarrow \mathbb{D}(k)\mathbb{G}^{-}\mathbf{f}_l + \mathbb{C}(k)\mathbb{G}^{+}\mathbf{f}_l \quad (2.27)$$

where the vector $\mathbf{f}_l = [f(x_1^{(l)}), f(x_2^{(l)}), \ldots, f(x_N^{(l)})]^T$ is defined over a sector with index l. The superscripts and subscripts for the grid points $x_j^{(l)}$ are as defined in Fig.2.1. Thus we re-write the integral equation in Eq.(2.14) in discretized form over a sector and its final solution in the sector, on the lines of Eq.(2.12)

$$\mathbf{f}_l = \mathbf{g}_l + [\mathbb{D}(k)\mathbb{G}^{-}\mathbf{f}_l + \mathbb{C}(k)\mathbb{G}^{+}\mathbf{f}_l] \Rightarrow \mathbf{f}_l = (\mathbb{I} - [\mathbb{D}(k)\mathbb{G}^{-} + \mathbb{C}(k)\mathbb{G}^{+}])^{-1}\,\mathbf{g}_l \quad (2.28)$$

where the vector $\mathbf{g}_l = [g(x_1^{(l)}), g(x_2^{(l)}), \ldots, g(x_N^{(l)})]^T$.

2.2.2 Modified Simpson's Method

Simpson's method is another way to discretize an integral equation. It can for instance be applied for an example problem given in Eq.(2.13). Integral equation of a similar form also arises in one dimensional collision problem of a particle in a harmonic oscillator and a free atom, as shall be explained in Sec.3.1.1. The integrand of Eq.(2.13) has a cusp discontinuity that arises from the $e^{ik|x-x'|}$ term in the integrand. The adaptation done to handle such discontinuity has been presented in [82] and is briefly reproduced here. Three point trapezoidal rule works well for integrands with discontinuous first derivative. Simpson's rule works well as long as the cusp is located on the end of a three-point Simpson's rule but shows poor convergence if the cusp is located at the midpoint. Simpson's method is modified for this problem by using a modified Simpson's rule when the cusp falls on the midpoint of the three point step. Let x_1, x_2 be the endpoints and x_3 as the midpoint. If the cusp discontinuity is at the center of a three point step, [82] suggests using the following second order modification to the Simpson's rule

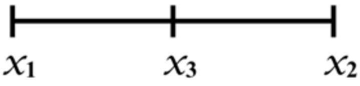

Figure 2.2: Schematic of a three-point grid for modified Simpson's integation.

$$\int_{x_1}^{x_2} e^{ik|x-x_3|}F(x)dx = \frac{1}{3}\Delta x\left[F(x_1)e^{ik\Delta x} + (4+ik\Delta x)F(x_3) + e^{ik\Delta x}F(x_2)\right] \quad (2.29)$$

where $\Delta x = x_2 - x_3$ or $\Delta x = x_3 - x_1$ is always positive. This expression reduces to the regular Simpson's rule if $k = 0$. After computing the integral with the modified Simpson's method, the final solution is obtained using Eq.(2.12).

2.3 Log Derivative Propagation

Log derivative propagation is a robust numerical technique used to obtain the solution of a Schrödinger equation [67-70]. It has the advantages of being easy to implement, easy of handling energetically closed channels and the step size of propagation can be changed easily. This method is numerically stable even if propagation is started from deep inside the forbidden region of the potential. We present a brief reproduction of this well-known method (Also see 70 and 68). The coupled channel Schrödinger equation can be written in a general form as

$$\left[\mathbb{I}\frac{d^2}{dx^2} + \mathbb{W}(x)\right]\mathbf{\Psi}(x) = 0 \quad (2.30)$$

where $\mathbb{I}$ is the identity matrix, the wavefunction $\mathbf{\Psi}(x)$ is a square matrix of linearly independent solutions and $\mathbb{W}(x) = 2\mu/\hbar^2(\mathbb{I}E - \mathbb{V}(x))$. E is the total energy, μ is the reduced mass and the potential matrix $\mathbb{V}(x)$.We define the log-derivative matrix as

$$\mathbb{Y}(x) = \mathbf{\Psi}(x)'\mathbf{\Psi}(x)^{-1} \tag{2.31}$$

Substituting Eq.(2.31) into Eq.(2.30), we get a first order differential equation for the log-derivative matrix

$$\mathbb{Y}'(x) + \mathbb{W}(x) + \mathbb{Y}^2(x) = 0 \tag{2.32}$$

The matrix equation Eq.(2.32) cannot be solved by standard numerical integration since the log derivative is singular at points where the wavefunction is zero. Instead the log derivative is *propagated* directly instead of the wavefunction and its derivative.

2.3.1 Propagation

The log derivative algorithm [67-70] is fundamentally a solution following method where the initial log derivative matrix is built with the boundary condition for the wavefunction i.e at $x = 0$ for zero-range potentials and $x > 0$ for realistic potentials. A brief description of Manolopoulos modification [70] of the original log-derivative algorithm by Johnson [67] is provided here. We note the log derivative matrix is indeterminate if $\Psi(x)$ is singular. To overcome this an imbedding-type propagator, $\mathcal{Y}$ is defined. A sector $[x_n, x_{n+1}]$, is divided into two half-sectors with a mid-point $x_m = (x_n + x_{n+1})/2$ and step size $h = (x_{n+1} - x_n)/2$. Thus, the imbedding type propagators over a half-sector $[x', x'']$ are given by

$$\begin{bmatrix} \Psi'(x') \\ \Psi'(x'') \end{bmatrix} = \begin{bmatrix} \mathcal{Y}_1(x', x'') & \mathcal{Y}_2(x', x'') \\ \mathcal{Y}_3(x', x'') & \mathcal{Y}_4(x', x'') \end{bmatrix} \begin{bmatrix} -\Psi(x') \\ \Psi(x'') \end{bmatrix} \tag{2.33}$$

where the interval $[x', x'']$ are the two half sectors $[x_n, x_m]$ and $[x_m, x_{n+1}]$. We obtain a recursion relation from the two linear equations above, given by

$$Y(x'') = \mathcal{Y}_4(x', x'') - \mathcal{Y}_3(x', x'') \times [Y(x') + \mathcal{Y}_1(x', x'')]^{-1}\mathcal{Y}_2(x', x'') \tag{2.34}$$

A constant reference potential is defined over each sector as $W_{ref}(x)_{ij} = \delta_{ij}k_j^2$ where are k_j are the reference wave vectors. We define a residual potential matrix $\mathbb{Q}(x)$ as

$$\mathbb{Q}(x_n) = \frac{h}{3}(\mathbb{W}(x_n) - \mathbb{W}_{ref}(x_n)); \;\; \mathbb{Q}(x_m) = \frac{4}{h}\left[\mathbb{I} - \frac{h^2}{6}(\mathbb{W}(x_m) - \mathbb{W}_{ref}(x_m))\right]^{-1} - \mathbb{I}\frac{4}{h}$$

$$\mathbb{Q}(x_{n+1}) = \frac{h}{3}(\mathbb{W}(x_{n+1}) - \mathbb{W}_{ref}(x_{n+1})) \tag{2.35}$$

The half-sector propagators $\mathcal{Y}_n$ over $[x', x'']$ for locally open channels with wave vectors $k_j^2 \geq 0$ are given by

$$\begin{aligned}&\mathcal{Y}_1(x',x'')_{ij} = \delta_{ij} k_j / \tan(k_j h) + Q_{ij}(x'); \;\; \mathcal{Y}_2(x',x'')_{ij} = \delta_{ij} k_j / \sin(k_j h)\\ &\mathcal{Y}_3(x',x'')_{ij} = \delta_{ij} k_j / \sin(k_j h); \;\; \mathcal{Y}_4(x',x'')_{ij} = \delta_{ij} k_j / \tan(k_j h) + Q_{ij}(x'')\end{aligned} \tag{2.36}$$

and for locally closed channels with $k_j^2 < 0$ as

$$\begin{aligned}&\mathcal{Y}_1(x',x'')_{ij} = \delta_{ij} k_j / \tanh(k_j h) + Q_{ij}(x'); \;\; \mathcal{Y}_2(x',x'')_{ij} = \delta_{ij} k_j / \sinh(k_j h)\\ &\mathcal{Y}_3(x',x'')_{ij} = \delta_{ij} k_j / \sinh(k_j h); \;\; \mathcal{Y}_4(x',x'')_{ij} = \delta_{ij} k_j / \tanh(k_j h) + Q_{ij}(x'')\end{aligned} \tag{2.37}$$

The half-sector propagators $\mathcal{Y}_2$ and $\mathcal{Y}_3$ are diagonal matrices and $\mathcal{Y}_1$ and $\mathcal{Y}_4$ are full matrices. Given a log derivative matrix at a point x_n, the relation in Eq.(2.34) gives the matrix at a point $n + 1$. Splitting up the propagation coordinate into a set of discrete points $(x_0, x_1, x_2, \ldots, x_N)$ we can iteratively propagate the matrix to x_N in N steps.

2.3.2 Asymptotic Matching

The log derivative matrix is propagated to a large enough value of x_N such that we are in the asymptotic region where the potential goes to zero. The asymptotic wavefunction for a particle is composed of a regular and irregular parts, given by

$$\mathbf{\Psi}_{x > x_N}(x) = \mathbb{F}(x) + \mathbb{G}(x)\mathbb{K} \tag{2.38}$$

We can obtain the Reactance matrix or K-Matrix from the asymptotic wavefunction. In the region $x > x_N$, we can write the log-derivative matrix as

$$\mathbf{\Psi} = \mathbb{F} + \mathbb{G}\,\mathbb{K}; \;\; \mathbf{\Psi}' = \mathbb{F}' + \mathbb{G}'\,\mathbb{K} \Rightarrow \mathbb{Y}(x) = (\mathbb{F}' + \mathbb{G}'\,\mathbb{K})(\mathbb{F} + \mathbb{G}\,\mathbb{K})^{-1}. \tag{2.39}$$

The prime denotes a derivative with respect to x and K-Matrix is

$$\mathbb{K} = (\mathbb{Y}(x)\mathbb{G} - \mathbb{G}')^{-1}\,(\mathbb{F}' - \mathbb{Y}(x)\mathbb{F}) \tag{2.40}$$

The K-Matrix contains elements connecting open and closed channels.

$$\mathbb{K} = \begin{bmatrix} \mathbb{K}_{oo} & \mathbb{K}_{oc} \\ \mathbb{K}_{co} & \mathbb{K}_{cc} \end{bmatrix} \tag{2.41}$$

The S-Matrix is related to the K-Matrix by a Cayley transform given by

$$\mathbb{S} = \frac{\mathbb{I} + i\mathbb{K}_{oo}}{\mathbb{I} - i\mathbb{K}_{oo}}. \tag{2.42}$$

The log derivative method described thus far is with respect to the relative coordinate for collision problem of two particles. Log derivative propagation for the collision problem can also be done in plane polar coordinates (See Sec.3.1.3 and Sec.4.4).

2.4 Spectral Element or High Order Finite Element Method

The general idea of Spectral Method was discussed in Sec.2.1. The method of weighted residuals with smooth trial functions chosen over a finite interval gives the Finite Element Method. Spectral Element Method as the name suggests is a combination of both Finite Element and Spectral Methods where smooth, high order trial functions are chosen for each interval or element. The local discretization basis is composed of high order polynomials using an appropriate quadrature rule. Legendre-Gauss-Lobatto quadrature is used to determine the points and weights. An example of the Legendre-Gauss-Lobatto cardinal basis for $N = 8$ is shown in Fig.2.3. Convergence can then be optimized by varying (a) the order of the element polynomial basis i.e number of points per sector or (b) the number of elements or (c) the size of elements.

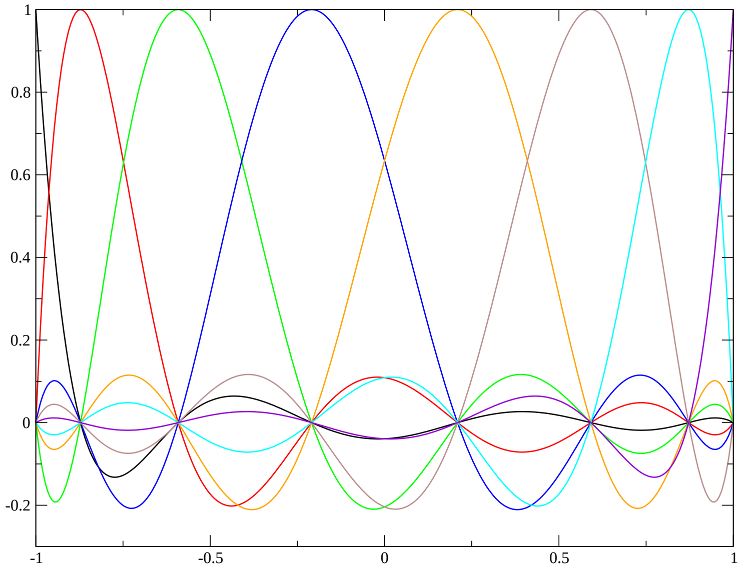

Figure 2.3: Legendre-Gauss-Lobatto Cardinal basis functions for N=8.

Elements, Basis Functions and their Properties

The integration range is divided into several elements(sectors) with one point common to adjoining elements(sectors) with the condition that the global solution is continuous at the points of intersection, as shown in Fig.2.4. Considering an example with N points per sector and M sectors, the index j indicates the element (sector), then the intersection or inter-element point is such that

$$x_N^{(j-1)} = x_1^{(j)} \qquad \text{with} \qquad j = (2, ...M). \tag{2.43}$$

In each element (sector) N Legendre-Gauss-Lobatto points and weights $(x_i^{(j)}, w_i^{(j)})$

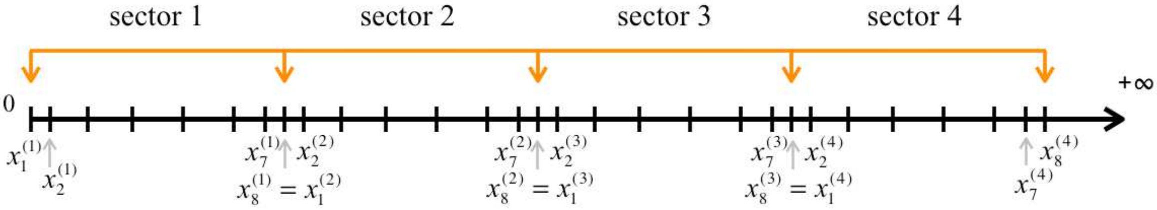

Figure 2.4: Schematic of the Spectral Element grid with $N = 8$ local quadrature discretization points per sector and $M = 4$ sectors. $x_i^{(j)}$ denotes the i^{th} point of the j^{th} sector.

where $i = 1, 2, ..., N$ are generated to implement a quadrature rule for the element, given by

$$\int_{x_1^{(j)}}^{x_N^{(j)}} f(x)dx = \sum_{i=1}^{N} w_i^{(j)} f(x_i^{(j)}) \tag{2.44}$$

The Legendre-Gauss-Lobatto cardinal functions are rescaled and taken to be over the interval $(x_1^{(j)}, x_N^{(j)})$ as

$$p_i^{(j)}(x) = C_i\left(\frac{2(x - x_1^{(j)})}{(x_N^{(j)} - x_1^{(j)})} - 1\right) \tag{2.45}$$

where the corresponding cardinal functions $C_i(x)$ are defined over the interval $(-1, +1)$ and can be found in [56]p.572. The argument $x_i^{(j)}$ denotes a grid point in the interval $(x_1^{(j)}, x_N^{(j)})$. These cardinal functions are defined at grid points in an element j such that $p_i^{(j)}(x_{i'}^{(j)}) = \delta_{ii'}$ and zero outside the element such that $p_i^{(j)}(x_{i'}^{(j')}) = \delta_{ii'}\delta_{jj'}$. The normalized basis functions are then given by

$$\phi_i^{(j)}(x) = p_i^{(j)}(x)/\sqrt{w_i^{(j)}}. \tag{2.46}$$

The quadrature weight $w_i^{(j)}$ at the inter-element grid point is taken as the sum of the weights of the two adjacent elements i.e $w_N^{(j-1)} + w_1^{(j)}$. The corresponding basis function at these inter-element grid point is given by

$$\phi_{i=1}^{(j)}(x) = \begin{cases} p_N^{(j-1)}(x)/\sqrt{w_N^{(j-1)} + w_1^{(j)}} & x \in [x_1^{(j-1)}, x_N^{(j-1)}] \\ p_1^{(j)}(x)/\sqrt{w_N^{(j-1)} + w_1^{(j)}} & x \in [x_1^{(j)}, x_N^{(j)}] \end{cases} \tag{2.47}$$

Hamiltonian Discretization

The Hamiltonian is then developed, with local representation in internal coordinates at each grid point. The resulting matrix representation of the linear differential operator has a sparse structure. For solving a scattering problem, similar to Eq.(2.30), consider an example of a Schrödinger equation for a 1D collision of two particles written in centre-of-mass and relative coordinates (X and x respectively).

$$\frac{\partial^2}{\partial x^2}\Psi(x,X) = \left[-\frac{\mu}{M}\frac{\partial^2}{\partial X^2} + \frac{2\mu}{\hbar^2}V(x,X) - k^2\right]\Psi(x,X) \tag{2.48}$$

where $k^2 = 2\mu E/\hbar^2$. The global finite element discretization is done in the propagation variable. x is chosen as the propagation coordinate and X as the internal coordinate. We present here the discretization of an example Hamiltonian over a element (sector) in the x coordinate with the range $[R_1, R_2]$. We expand the solutions $\Psi(x,X)$ over a set of DVR basis functions $\phi_i(x)$ as $\Psi(x,X) = \sum_i \phi_i(x)F_i(X)$

$$-\sum_i \frac{\partial^2\phi_i(x)}{\partial x^2}F_i(X) - \frac{\mu}{M}\sum_i \phi_i(x)\frac{\partial^2}{\partial X^2}F_i(X) + \frac{2\mu}{\hbar^2}V(x,X)\sum_i \phi_i(x)F_i(X) - k^2\sum_i \phi_i(x)F_i(X) = 0 \tag{2.49}$$

Multiplying from the left by $\phi_j(x)$ and integrating over the range (R_1, R_2) with respect to x, we get

$$-\sum_i \int_{R_1}^{R_2} \phi_j(x)\frac{\partial^2\phi_i(x)}{\partial x^2}F_i(X)dx - \frac{\mu}{M}\frac{\partial^2}{\partial X^2}\sum_i \int_{R_1}^{R_2} \phi_j(x)\phi_i(x)F_i(X)dx + \frac{2\mu}{\hbar^2}\sum_i F_i(X)\int_{R_1}^{R_2} \phi_j(x)V(x,X)\phi_i(x)dx - k^2\sum_i F_i(X)\int_{R_1}^{R_2} \phi_j(x)\phi_i(x)dx = 0 \tag{2.50}$$

The first term in Eq.(2.50) above can be integrated by parts as

$$\int_{R_1}^{R_2} \phi_j(x)\frac{\partial^2\phi_i(x)}{\partial x^2}dx = \left[\phi_j(x)\frac{\partial\phi_i(x)}{\partial x}\right]_{R_1}^{R_2} - \int_{R_1}^{R_2} \frac{\partial\phi_j(x)}{\partial x}\frac{\partial\phi_i(x)}{\partial x}dx = \left[\phi_j(x)\frac{\partial\phi_i(x)}{\partial x}\right]_{R_1}^{R_2} - \left\langle \frac{\partial\phi_j(x)}{\partial x}\middle| \frac{\partial\phi_i(x)}{\partial x}\right\rangle \tag{2.51}$$

The second term on the right hand side in Eq.(2.51) above can also be written using the projection operator $\sum_k |\phi_k(x)\rangle\langle\phi_k(x)|$, which acts as the identity in the finite dimensional space spanned by DVR functions. We have

$$\left\langle \frac{\partial\phi_j(x)}{\partial x}\middle| \frac{\partial\phi_i(x)}{\partial x}\right\rangle_x = \sum_k \left\langle \frac{\partial\phi_j(x)}{\partial x}\middle| \phi_k(x)\right\rangle_x \left\langle \phi_k(x)\middle| \frac{\partial\phi_i(x)}{\partial x}\right\rangle_x = (\mathbf{A}^T\mathbf{A})_{ji} \tag{2.52}$$

The term $(\mathbf{A}^T\mathbf{A})_{ji}$ is an element of the matrix $\mathbb{A}^T\mathbb{A}$. Substituting this into Eq.(2.50) we obtain the matrix elements of the equation in x coordinate basis

$$\sum_i (\mathbf{A}^T\mathbf{A})_{ji} F_i(X) - \frac{\mu}{M}\frac{\partial^2}{\partial X^2}\sum_i \delta_{ji} F_i(X) + \frac{2\mu}{\hbar^2}\sum_i \delta_{ji} V(x_i, X) F_i(X) - k^2 \sum_i \delta_{ji} F_i(X) = \left[\phi_j(x)\frac{\partial \Psi(x,X)}{\partial x}\right]_{R_1}^{R_2} \tag{2.53}$$

The term $\delta_{ji}V(x_i,X) = V^{DVR}_{ji}(X)$ is the diagonal representation of the potential energy on the DVR basis in x coordinate, with x_i as the grid points within the element. Let the indices i,j be associated with the basis in x coordinate and α,β with the basis in X coordinate. The solutions $\Psi(x,X)$ can further be expanded over a DVR basis in the X coordinate as $\Psi(x,X) = \sum_i \sum_\alpha \phi_i(x)\chi_\alpha(X)\Psi_{i\alpha}$. Thus we take $F_i(X) = \sum_\alpha \chi_\alpha(X)\Psi_{i\alpha}$, substitute into Eq.(2.53), multiply from the left by $\chi_\beta(X)$ and integrating over the range $(-L,+L)$ with respect to X, we have

$$\sum_\alpha\sum_i (\mathbf{A}^T\mathbf{A})_{ji}\delta_{\beta\alpha}\Psi_{i\alpha} - \frac{\mu}{M}\sum_\alpha\sum_i \delta_{ji}\int_{-L}^{+L}\chi_\beta(X)\frac{\partial^2\chi_\alpha(X)}{\partial X^2}\Psi_{i\alpha}dX - k^2\sum_\alpha\sum_i \delta_{ji}\delta_{\beta\alpha}\Psi_{i\alpha} + \frac{2\mu}{\hbar^2}\sum_\alpha\sum_i \delta_{ji}\delta_{\beta\alpha}V(x_j,X_\beta)\Psi_{i\alpha} = \sum_\alpha\sum_i\left[\phi_j(x)\frac{\partial\phi_i(x)}{\partial x}\right]_{R_1}^{R_2}\delta_{\beta\alpha}\Psi_{i\alpha} \tag{2.54}$$

We adopt Dirichlet boundary conditions for the X coordinate grid over $[-L,+L]$, such that $\phi(-L) = \phi(+L) = 0$. It is noted that eigensolutions of a particle in a infinite square well have an identical boundary condition and can be used to define DVR functions, as explained in [100] (Also known as Fourier grid basis). Performing integration by parts on the second term in Eq.(2.54) above and using a projection operator $\sum_{k'} |\chi_{k'}(X)\rangle\langle\chi_{k'}(X)|$, which acts as the identity in the finite dimensional space spanned by DVR functions, we have

$$\int_{-L}^{+L}\chi_\beta(X)\frac{\partial^2\chi_\alpha(X)}{\partial X^2}dX = \left[\chi_\beta(X)\frac{\partial\chi_\alpha(X)}{\partial X}\right]_{-L}^{+L} - \int_{-L}^{+L}\frac{\partial\chi_\beta(X)}{\partial X}\frac{\partial\chi_\alpha(X)}{\partial X}dX = 0 - \left\langle\frac{\partial\chi_\beta(X)}{\partial X}\middle|\frac{\partial\chi_\alpha(X)}{\partial X}\right\rangle = -\sum_{k'}\left\langle\frac{\partial\chi_\beta(X)}{\partial X}\middle|\chi_{k'}(X)\right\rangle\left\langle\chi_{k'}(X)\middle|\frac{\partial\chi_\alpha(X)}{\partial X}\right\rangle = -(\mathbf{B}^T\mathbf{B})_{\beta\alpha} \tag{2.55}$$

The term $(\mathbf{B}^T\mathbf{B})_{\beta\alpha}$ is a matrix element of $\mathbb{B}^T\mathbb{B}$.

$$\sum_\alpha\sum_i (\mathbf{A}^T\mathbf{A})_{ji}\delta_{\beta\alpha}\Psi_{i\alpha} + \frac{\mu}{M}\sum_\alpha\sum_i \delta_{ji}(\mathbf{B}^T\mathbf{B})_{\beta\alpha}\Psi_{i\alpha} + \frac{2\mu}{\hbar^2}\sum_\alpha\sum_i \delta_{ji}\delta_{\beta\alpha}V(x_j,X_\beta)\Psi_{i\alpha} - k^2\sum_\alpha\sum_i \delta_{ji}\delta_{\beta\alpha}\Psi_{i\alpha} = \sum_\alpha\sum_i\left(\phi_j(R_2)\frac{\partial\phi_i(R_2)}{\partial x} - \phi_j(R_1)\frac{\partial\phi_i(R_1)}{\partial x}\right)\delta_{\beta\alpha}\Psi_{i\alpha} \tag{2.56}$$

Using the property of the DVR functions $\phi_i(x_j) = \delta_{ij} 1/\sqrt{w_j}$, the right hand term reduces to

$$\left(\phi_j(R_2)\frac{\partial\phi_i(R_2)}{\partial x} - \phi_j(R_1)\frac{\partial\phi_i(R_1)}{\partial x}\right) = \left(\delta_{jN}\frac{1}{\sqrt{w_N}}\frac{\partial\phi_i(R_2)}{\partial x} - \delta_{j1}\frac{1}{\sqrt{w_1}}\frac{\partial\phi_i(R_1)}{\partial x}\right) \tag{2.57}$$

The potential term $V_{\beta j;\alpha i} = \delta_{ji}\delta_{\beta\alpha}V(x_j, X_\beta)$ is a matrix element with composite row(column) indices $\beta j(\alpha i)$. Eq.(2.56) above can thus be written as a matrix equation

$$\left[\mathbb{T} + \mathbb{W} - \mathbb{I}k^2\right]\bar{\mathbf{\Psi}} = \partial_x\bar{\mathbf{\Psi}}\big|_{x=0}^{x=R_2} \qquad \text{where } \partial_x\bar{\mathbf{\Psi}} = \frac{\partial}{\partial x}\bar{\mathbf{\Psi}} \tag{2.58}$$

$$\mathbb{T} \text{ has elements } T_{\beta j;\alpha i} = (\mathbf{A}^T\mathbf{A})_{ji}\delta_{\beta\alpha} \text{ and } W_{\beta j;\alpha i} = \frac{\mu}{M}\delta_{ji}(\mathbf{B}^T\mathbf{B})_{\beta\alpha} + \frac{2\mu}{\hbar^2}V_{\beta j;\alpha i}$$

where the column vector $\bar{\mathbf{\Psi}} = [\bar{\mathbf{\Psi}}_1, \bar{\mathbf{\Psi}}_2, \ldots, \bar{\mathbf{\Psi}}_N]^T$ or $\bar{\mathbf{\Psi}} = [(\Psi_{11}, \Psi_{21}, \ldots, \Psi_{n1}), (\Psi_{12}, \Psi_{22}, \ldots, \Psi_{n2}), \ldots, (\Psi_{1N}, \Psi_{2N}, \ldots, \Psi_{nN})]^T$, where $\alpha \in [1, n]$. We have N discretization points in x coordinate and n discretization points in the X coordinate.
The boundary term $\partial_x\bar{\mathbf{\Psi}}|_{x=0}^{x=R} = [(\Psi'_{11}, \Psi'_{21}, \ldots, \Psi'_{n1}), 0, \ldots, 0, (\Psi'_{1N}, \Psi'_{2N}, \ldots, \Psi'_{nN})]^T$, is taken over end points of elements in the x coordinate such that they cancel at the interelement nodes.
This matrix equation can be written for an example case of $N = 3$ points per sector and 2 sectors as follows. Thus $i, j \in [1, N]$ and $\alpha, \beta \in [1, n]$, where we have n discretization points in the X coordinate. The range $[0, R]$ is partitioned and can be written as

$$\begin{bmatrix} \mathbb{T}_{11} + \mathbb{W}_{11} - \mathbb{I}_N E & \mathbb{T}_{12} & \mathbb{T}_{13} \\ \mathbb{T}_{21} & \mathbb{T}_{22} + \mathbb{W}_{22} - \mathbb{I}_N E & \mathbb{T}_{23} \\ \mathbb{T}_{31} & \mathbb{T}_{32} & \mathbb{T}_{33} + \mathbb{W}_{33} - \mathbb{I}_N E \end{bmatrix}$$

$$\begin{bmatrix} \bar{\mathbf{\Psi}}_1 \\ \bar{\mathbf{\Psi}}_2 \\ \bar{\mathbf{\Psi}}_3 \end{bmatrix} = \begin{bmatrix} \bar{\mathbf{\Psi}}'_1 \\ 0 \\ -\bar{\mathbf{\Psi}}'_3 \end{bmatrix} \tag{2.59}$$

and

$$\begin{bmatrix} \mathbb{T}_{33} + \mathbb{W}_{33} - \mathbb{I}_N E & \mathbb{T}_{34} & \mathbb{T}_{35} \\ \mathbb{T}_{43} & \mathbb{T}_{44} + \mathbb{W}_{44} - \mathbb{I}_N E & \mathbb{T}_{45} \\ \mathbb{T}_{53} & \mathbb{T}_{54} & \mathbb{T}_{55} + \mathbb{W}_{55} - \mathbb{I}_N E \end{bmatrix}$$

$$\begin{bmatrix} \bar{\mathbf{\Psi}}_3 \\ \bar{\mathbf{\Psi}}_4 \\ \bar{\mathbf{\Psi}}_5 \end{bmatrix} = \begin{bmatrix} \bar{\mathbf{\Psi}}'_3 \\ 0 \\ -\bar{\mathbf{\Psi}}'_5 \end{bmatrix} \tag{2.60}$$

We note the elements of the diagonal matrices $\mathbb{T}_{ji} = T_{\beta j;\alpha i}$ and those of the full matrices $\mathbb{W}_{ji} = W_{\beta j;\alpha i}$ and the vectors $\bar{\boldsymbol{\Psi}}_i = [\Psi_{1i}, \Psi_{2i}, \ldots, \Psi_{ni}]^T$. The first and last points of each sector of the right hand side of Eq.(2.52) are taken to be of opposite sign so as to retain the boundary condition over the global range $[0, R]$ after the sectors are all linked. The matrix element value at intersection points, in this case point-3, is the sum of the values of this point from each sector.

$$
\begin{bmatrix}
\mathbb{T}_{11} + \mathbb{W}_{11} - \mathbb{I}_N E & \mathbb{T}_{12} & \mathbb{T}_{13} & \ldots \\
\mathbb{T}_{21} & \mathbb{T}_{22} + \mathbb{W}_{22} - \mathbb{I}_N E & \mathbb{T}_{23} & \ldots \\
\mathbb{T}_{31} & \mathbb{T}_{32} & 2[\mathbb{T}_{33} + \mathbb{W}_{22} - \mathbb{I}_N E] & \ldots \\
0 & 0 & \mathbb{T}_{43} & \ldots \\
0 & 0 & \mathbb{T}_{53} & \ldots
\end{bmatrix}
$$

$$
\begin{bmatrix}
\ldots & 0 & 0 \\
\ldots & 0 & 0 \\
\ldots & \mathbb{T}_{34} & \mathbb{T}_{35} \\
\ldots & \mathbb{T}_{44} + \mathbb{W}_{44} - \mathbb{I}_N E & \mathbb{T}_{45} \\
\ldots & \mathbb{T}_{54} & \mathbb{T}_{55} + \mathbb{W}_{55} - \mathbb{I}_N E
\end{bmatrix}
\begin{bmatrix}
\bar{\boldsymbol{\Psi}}_1 \\ \bar{\boldsymbol{\Psi}}_2 \\ \bar{\boldsymbol{\Psi}}_3 \\ \bar{\boldsymbol{\Psi}}_4 \\ \bar{\boldsymbol{\Psi}}_5
\end{bmatrix}
=
\begin{bmatrix}
\bar{\boldsymbol{\Psi}}'_1 \\ 0 \\ 0 \\ 0 \\ -\bar{\boldsymbol{\Psi}}'_5
\end{bmatrix}
\tag{2.61}
$$

The propagation variable has a global finite element structure which is sparse. This representation essentially reduces a log-derivative propagation algorithm to a linear system of equations solved in a one-shot computation. The above equations are written for a single solution denoted by the column vector $\bar{\boldsymbol{\Psi}}_i$, with $i = [1, \ldots, N]$. For multichannel calculations, we can denote the solutions by a matrix $\boldsymbol{\Psi} = \Psi_{\beta i;J}$, where we take $J = n \times N$ linearly independent solutions to ensure a square marix. The boundary condition on the right hand side in the above equations are thus determined by matrices $\boldsymbol{\Psi}_1 = \Psi_{\beta 1;\alpha 1}$ and $\boldsymbol{\Psi}_N = \Psi_{\beta N;\alpha N}$. For a scattering problem, we use the boundary condition $\boldsymbol{\Psi}'_1 = \boldsymbol{\Psi}'_1 \boldsymbol{\Psi}_1^{-1} \boldsymbol{\Psi}_1 = \mathbb{Y}\,\boldsymbol{\Psi}_1$ at the first point of propagation coordinate and an R-matrix at the last step of propagation given by $\boldsymbol{\Psi}'_5 = \mathbb{I} \Rightarrow \boldsymbol{\Psi}_5 = \mathbb{R}$. This sparse matrix can then be solved with linear solution packages optimized to exploit matrix sparsity like PARDISO [77-81].

The Eq.(2.61) can also be used to compute bound states. We drop the right hand side term in Eq.(2.61). The term $\mathbb{I}_N E$ in the diagonal blocks of the Hamiltonian now becomes the unknown in the right hand side. We also drop the first and last rows and columns of the matrix on the left hand side due to the boundary conditions for bound states imposed of the vectors $\bar{\boldsymbol{\Psi}}_1 = \bar{\boldsymbol{\Psi}}_5 = 0$. The Hamiltonian to be diagonalized reduces to the central 3×3 sub-matrix of the left hand side in Eq.(2.61). This sparse matrix can be diagonalized to solve for bound states by using sparsity based eigenvalue solvers like FEAST [75, 76].

The global sparse matrix structure is show in Fig.2.5, for an example case with $N = 4$ grid points per element and $M = 5$ elements. The overlap matrices are diagonal square matrices if the discretization basis size in the internal coordinates

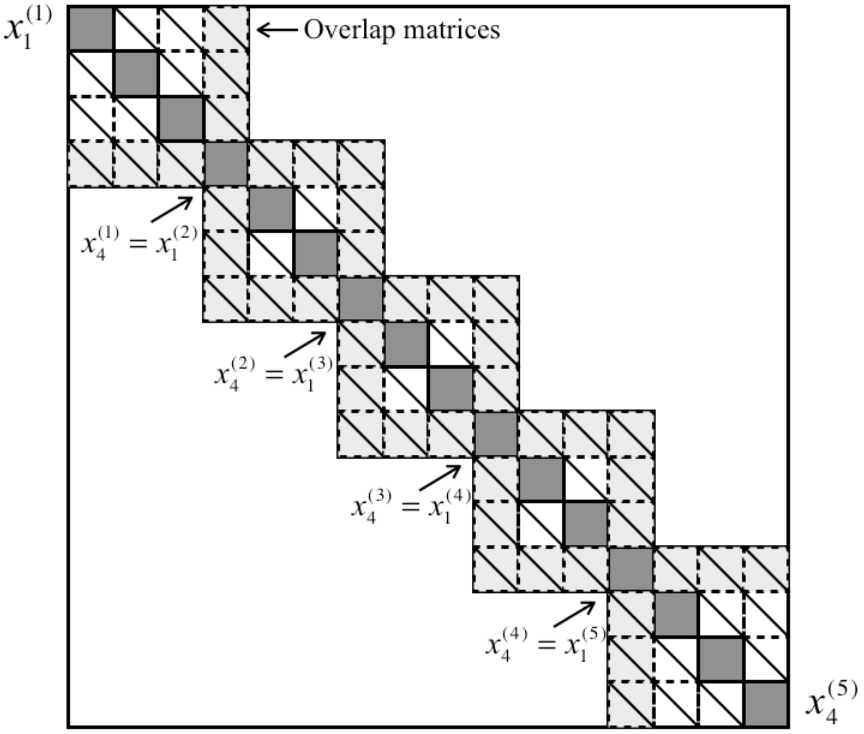

Figure 2.5: Schematic of the Spectral Element Representation of the Hamiltonian, in $M = 5$ elements, with $N = 4$ points per element. The diagonal blocks are full, as explained earlier. The sectors share a common grid point at intersection (labelled with arrows). Overlap matrix (in lighter shade) are diagonal square matrices but can be rectangular and full if sectors have different discretization basis size in the internal coordinates.

are held constant across the two adjacent sectors. If the internal coordinate basis size is different, these matrices are rectangular and full.

Chapter 3

Collisions in Mixed Dimensions

We begin the study of collisions in mixed dimensions with a simple model in one dimension to study collision of a free particle and a particle in a time independent harmonic oscillator potential. The interaction potential between the particles is simplified in this problem by using a zero-range Delta pseudopotential to aid in studying the effects of confinement geometry on scattering parameters. Such a system is modelled in experiments by a very shallow harmonic confinement potential along the longitudinal z-axis ($\omega_{\parallel}$) and tight confinement of the particles along two transverse axes ($\omega_{\perp}$), with $\omega_{\parallel} \ll \omega_{\perp}$. Due to the tight confinement along transverse directions the energy levels have a large spacing in these two axis. This creates an effective one dimensional motion or a waveguide. The shallow trapping potential along the longitudinal axis results in very closely spaced oscillator levels along this axis, thereby creating a quasi-continuum i.e free motion of the particle along the wave guide axis. Such a waveguide is spatially overlapped with another

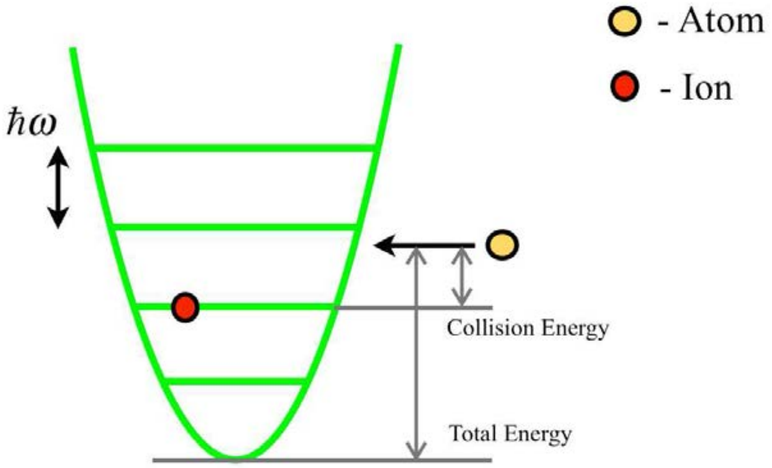

Figure 3.1: Atom-Ion collision in one dimension

particle in an isotropic harmonic trap, as shown in Fig.3.1. In the model we consider, it is assumed that the trapped particle is in a harmonic potential in one dimension such that $\omega = \omega_{\parallel}$ and $\omega << \omega_{\perp}$, implying collision along the waveguide axis would result in energy transitions of the trapped particle between oscillator energy levels of the order of $\hbar\omega$ do not cause transitions of the trapped particle within the transverse energy levels $\hbar\omega_{\perp}$. Thus it is good to approximate the problem to one dimension. We are interested in studying the transmission and reflection probability of the free particle after collision and the probability of transition of the trapped particle between the eigenstates of the trap. Such a model also serves as a prelude to an atom-ion collision problem, where the ion is in a time dependent one dimensional potential, presented in Chapter.4.

3.1 The Two Body Hamiltonian

To serve as a prelude to what lies ahead, we assume the particle trapped in the harmonic potential is an ion and free particle in the one dimensional waveguide is an atom. The two-body Hamiltonian for this collision problem is given by

$$\hat{H} = -\frac{\hbar^2}{2m_A}\frac{\partial^2}{\partial x_A^2} - \frac{\hbar^2}{2m_I}\frac{\partial^2}{\partial x_I^2} + \frac{1}{2}m_I\omega^2 x_I^2 + g\delta(x_A - x_I) \tag{3.1}$$

where m_A, x_A (m_I, x_I) are the atom (ion) mass and coordinate respectively. Using harmonic oscillator units, with lengths in units of $a_{ho} = \sqrt{\hbar/(m_I\omega)}$ and energy in units of $\hbar\omega$, the time independent Schrödinger equation can be rewritten as

$$\left[-\frac{1}{2m}\frac{\partial^2}{\partial \bar{x}_A^2} - \frac{1}{2}\frac{\partial^2}{\partial \bar{x}_I^2} + \frac{1}{2}\bar{x}_I^2 + \bar{g}\delta(\bar{x}_A - \bar{x}_I)\right]\Psi(\bar{x}_A, \bar{x}_I) = \bar{E}\Psi(\bar{x}_A, \bar{x}_I) \tag{3.2}$$

where $m = m_A/m_I$ is the mass ratio, $\bar{E} = E/(\hbar\omega)$, $\bar{x}_I = x_I/a_{ho}$, $\bar{x}_A = x_A/a_{ho}$ and $\bar{g} = g/(a_{ho}\hbar\omega)$. The pseudopotential coupling indicated by $\bar{g}$ here is related to physical parameters in 3D, given by the elegant result by Olshanii [86]

$$\bar{g} = 2\frac{a_{3D}}{a_{ho}}\left(1 - \zeta(1/2)\frac{a_{3D}}{a_{ho}}\right)^{-1} \tag{3.3}$$

where the Reimann zeta function ζ is given by $\zeta(1/2) = 1.4603$. The 3D scattering length a_{3D} relates to 3D pseudopontetial coupling g_{3D} by $a_{3D} = \frac{\mu}{2\pi\hbar^2}g_{3D}$. Since the potential in this case is time independent, the time dependence of the Schrödinger equation via the term $i\hbar\frac{\partial\Psi}{\partial t}$ appears as a phase term $e^{-i\bar{E}t}$ in the total solution. For notational simplicity variables $\bar{x}_I, \bar{x}_A, \bar{g}$ and $\bar{E}$ will be denoted by x_I, x_A, g and E respectively, and oscillator units are implied unless otherwise stated. This Schrödinger equation can be solved either by (a) Integral Equation Method (Sec.2.2) or (b) Log Derivative Propagation (Sec.2.3) in Cartesian coordinates or (c) in plane polar coordinates.

3.1.1 Solution by IEM

The Integral Equation approach to solving this Hamiltonian has been well elucidated in [82], [84]. The motivation for the study of such a system originally was to describe the collinear collision of an atom and a diatomic molecule simplified as a harmonic oscillator. The Schrödinger equation can be written as

$$\left[-\frac{1}{2m}\frac{\partial^2}{\partial x_A^2}-\frac{1}{2}\frac{\partial^2}{\partial x_I^2}+\frac{1}{2}x_I^2-E\right]\Psi(x_A,x_I)=-g\delta(x_A-x_I)\Psi(x_A,x_I) \tag{3.4}$$

We can define a Green's function for the differential operator by

$$\left[-\frac{1}{2m}\frac{\partial^2}{\partial x_A^2}-\frac{1}{2}\frac{\partial^2}{\partial x_I^2}+\frac{1}{2}x_I^2-E\right]G(x_A,x_I;x'_A,x'_I)=\delta(x_A-x'_A)\delta(x_I-x'_I) \tag{3.5}$$

The harmonic oscillator eigenfunctions in oscillator units are given by

$$\psi_{ho,n}(x_I)=\frac{1}{\sqrt{2^n n!\sqrt{\pi}}}H_n(x_I)e^{\frac{-x_I^2}{2}} \tag{3.6}$$

The Green's function in terms of $\psi_{ho,n}(x_I)$ is well known (See 117, p.803) and given by

$$G(x_A,x_I;x'_A,x'_I)=\sum_{j=0}^{\infty}\frac{m\psi_{ho,j}(x_I)\psi_{ho,j}(x'_I)e^{ik_j|x_A-x'_A|}}{2ik_j}. \tag{3.7}$$

where $k_j=\sqrt{2m(E-(j+1/2))}$ are the wave vectors in the calculation and j are the oscillator level indices. The wave vectors are real for energetically open channels and imaginary for closed channels. The integral equation now has the general form

$$\Psi_{n_I}(x_A,x_I)=\psi_{ho,n_I}(x_I)e^{-ik_{n_I}x_A}+\sum_{j=0}^{\infty}\int_{-\infty}^{\infty}\int_{-\infty}^{\infty}\frac{m\psi_{ho,j}(x_I)\psi_{ho,j}(x'_I)}{2ik_j}e^{ik_j|x_A-x'_A|} g\delta(x'_A-x'_I)\Psi_{n_I}(x'_A,x'_I)dx'_A dx'_I \tag{3.8}$$

where the subscripts n_I indicate the initial state. The infinite sum in the Green's function is truncated to a sufficiently high value. The convergence properties of the method and dependence on truncation of this term is discussed in Sec.3.1.1.1. Following the method used in [83], we define an *Amplitude Density Function* $F_{j,n_I}(x_A)$. The scattering problem can be partitioned into smaller problems and later added to obtain the total solution by recasting the integral equation in terms of Amplitude Density Functions. Thus we define $F_{j,n_I}(x_A)$ as

$$F_{j,n_I}(x_A)=\int_{-\infty}^{\infty}\psi_{ho,j}(x_I)g\delta(x_A-x_I)\Psi_{n_I}(x_A,x_I)dx_I=\psi_{ho,j}(x_A)g\Psi_{n_I}(x_A,x_A). \tag{3.9}$$

In the asymptotic region where x_A is large, the real potential $V(x_A - x_I) = -C_4/(2(x_A - x_I)^4)$ goes to zero. So the amplitude density functions is zero at points where the potential or the wavefunction goes to zero. Substituting Eq.(3.9) in the integral equation Eq.(3.8) we get

$$\Psi_{n_I}(x_A, x_I) = \psi_{ho,n_I}(x_I)e^{-ik_{n_I}x_A} + \sum_{j=0}^{\infty} \psi_{ho,j}(x_I)e^{ik_j x_A} \int_{-\infty}^{\infty} \frac{me^{-ik_j x'_A}F_{j,n_I}(x'_A)}{2ik_j} dx'_A \tag{3.10}$$

The second term on the right hand side is due to scattering and it is seen the asymptotic solution is defined by the integral term. This term can be easily calculated if the *amplitude densities* $F_{j,n_I}(x'_A)$ are known. Thus to recast the integral equation to solve for $F_{j,n_I}(x'_A)$, we multiply Eq.(3.10) by $\psi_{ho,j}(x_I)g\delta(x_A - x_I)$ and integrate over the interval $[-\infty, \infty]$, to get

$$F_{j',n_I}(x_A) = P_{j'n_I}(x_A)e^{-ik_{n_I}x_A} + \sum_{j=0}^{\infty} \frac{mP_{j'j}(x_A)}{2ik_j} \int_{-\infty}^{\infty} e^{ik_j|x_A - x'_A|}F_{j,n_I}(x'_A)dx'_A \tag{3.11}$$

where $P_{j'n_I}(x_A)$ is given by

$$P_{j'n_I}(x_A) = \int_{-\infty}^{\infty} \psi_{ho,j'}(x_I)g\delta(x_A - x_I)\psi_{ho,n_I}(x_I)dx_I = \psi_{ho,j'}(x_A)g\psi_{ho,n_I}(x_A) \tag{3.12}$$

The solution of this integral equation has been attempted by three discretization schemes (a) Pseudospectral Method (Sec.2.2.1) (b) modified Simpson's rule as explained in [82] (Sec.2.2.2) (c) Trapezoidal method.

Discretization

The integral in equation Eq.(3.11) can be replaced by a discrete sum. The ion is in an initial state n_I before collision. Discretization for solution by Integral Equation Method using pseudospectral integration (See Sec.2.2.1) gives an equation similar to Eq.(2.28). The integration coordinate x'_A is partitioned into sectors as explained in Fig.2.1 (and Sec.2.2.1) and a discretized integral equation is written for a solution vector which is defined over a sector l with N points. The spectral integration matrices $\mathbb{G}^+$ and $\mathbb{G}^-$ are given in Eq.(2.25). We then have

$$\bar{\mathbf{F}}^{(l)}_{j',n_I}(x_A) = \bar{\mathbf{Q}}^{(l)}_{j'n_I}(x_A) + \sum_{j=0}^{N_{ch}} \frac{m\bar{\mathbf{P}}^{(l)}_{j'j}(x_A)}{2ik_j} \left[\mathbb{D}(k_j)\mathbb{G}^- \,\bar{\mathbf{F}}^{(l)}_{j,n_I}(x_A) + \mathbb{C}(k_j)\mathbb{G}^+ \,\bar{\mathbf{F}}^{(l)}_{j,n_I}(x_A)\right] \tag{3.13}$$

where we define the vectors

$$\begin{aligned}
\bar{\mathbf{Q}}^{(l)}_{j'n_I}(x_A) &= [P_{j'n_I}(x^{(l)}_{A,1})e^{-ik_{n_I}x^{(l)}_{A,1}}, P_{j'n_I}(x^{(l)}_{A,2})e^{-ik_{n_I}x^{(l)}_{A,2}}, \ldots, P_{j'n_I}(x^{(l)}_{A,N})e^{-ik_{n_I}x^{(l)}_{A,N}}]^T \\
\bar{\mathbf{P}}^{(l)}_{j'n_I}(x_A) &= [P_{j'n_I}(x^{(l)}_{A,1}), P_{j'n_I}(x^{(l)}_{A,2}), \ldots, P_{j'n_I}(x^{(l)}_{A,N})]^T \\
\bar{\mathbf{F}}^{(l)}_{j',n_I}(x_A) &= [F_{j,n_I}(x^{(l)}_{A,1}), F_{j,n_I}(x^{(l)}_{A,2}), \ldots, F_{j,n_I}(x^{(l)}_{A,N})]^T
\end{aligned} \tag{3.14}$$

and similar to Eq.(2.26) the matrices $\mathbb{C}(k_j)$ and $\mathbb{D}(k_j)$ as

$$\mathbb{C}(k_j) \to C_{nl}(k_j) = e^{-ik_j(x_{A,n}-x_{A,l})} \quad \text{and} \quad \mathbb{D}(k_j) \to D_{nl}(k_j) = e^{ik_j(x_{A,n}-x_{A,l})} \tag{3.15}$$

To avoid multiple subscripts atom coordinate is changed to $x_A \to x^A$, for the following equation alone. The discretization for solution by Integral Equation Method using modified Simpson's integration (See Sec.2.2.2) and trapezoidal rule gives the integral equation as

$$F_{j',n_I}(x^A_n) = P_{j'I}(x^A_n)e^{-ik_{n_I}x^A_n} + \sum_{j=0}^{N_{ch}} \frac{mP_{j'j}(x^A_n)}{2ik_j} \sum_{l=1}^{N} w_l e^{ik_j|x^A_n - x^A_l|} F_{l,n_I}(x^A_l) \tag{3.16}$$

The discrete integral equation for $F_{j',n_I}(x_A)$ in Eq.(3.13) and Eq.(3.16) can then be decomposed into complex reflection and transmission amplitudes for an incoming channel I as

$$r_{jn_I} = \sum_{l=1}^{\infty} \frac{mw_l e^{-ik_j x^A_l}}{2ik_j} F_{j,n_I}(x^A_l) \quad \text{and} \quad \bar{t}_{jn_I} = \sum_{l=1}^{\infty} \frac{mw_l e^{ik_j x^A_l}}{2ik_j} F_{j,n_I}(x^A_l) \tag{3.17}$$

The transmission amplitudes given here is without the shadow term i.e $|\bar{t}_{ii}|^2 = 0$ when $g = 0$ for an incoming channel i. Thus the real transmission probability is $T_{ij} = |t_{ij}|^2 = |\bar{t}_{ij} + \delta_{ij}|^2$. The wave vectors are given by $k_n = \sqrt{2m(E - (n + 1/2)}$ with $n = \{(1-n_I), (2-n_I), \ldots, (n_{ch}-n_I)\}$. For a given total energy of the system, real values of k_n are the energetically open out-going channels.

3.1.1.1 Convergence Properties of IEM with Pseudospectral Integration

The calculations are done for Na atom as the free particle and Ca$^+$ ion as the trapped particle with a mass ratio $m = m_{Na}/m_{Ca^+} = 0.57$.

Influence of Number of Channels

The Green's function in Eq.3.7 is a slowly converging infinite series over the channels. This summation is truncated at a sufficiently large number of channels (N_{ch}) for the test case with total energy $E_{tot} = 1.7\ \hbar\omega$, 2 open channels and ion in the trap ground state initially ($n_I = 0$).

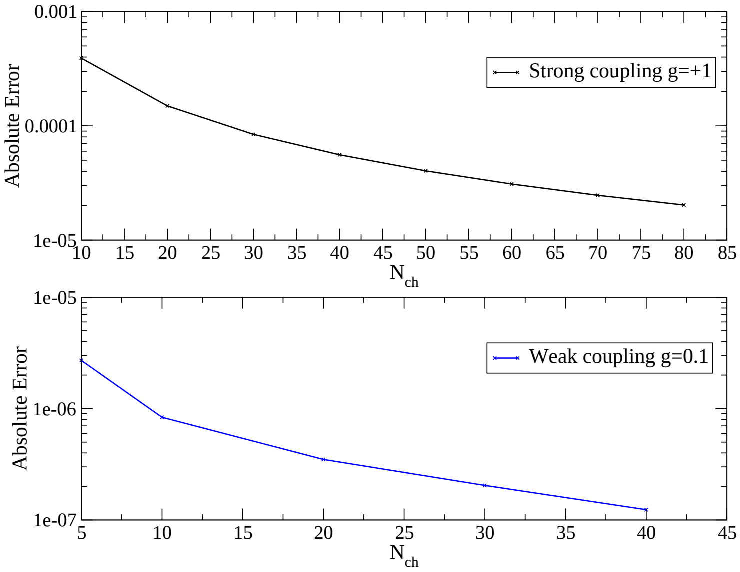

Figure 3.2: Strong coupling $g = +1$ requires large N_{ch} (top panel) but the method converges very well for weak couplings (bottom panel).

We take a grid with 15 points per sector and 10 sectors over a range of $[-10\ a_{ho}, +10\ a_{ho}]$. The calculation is done to estimate the number of channels N_{ch} required in the case of a weak ($g = 0.1$) and strong ($g = 1$) pseudopotential coupling respectively. We calculate absolute error on the total reflection probability i.e reflection probability summed over all open channels $R_0 = \sum_{j=0}^{N_{op}} |r_{0j}|^2$ with an incoming channel $n_I = 0$. The forward difference of the y-axis data (i.e the total reflection probability) at a point is taken as the absolute error.

A strong pseudopotential coupling ($g = 1$) couples to a large number of channels, even closed channels. We note from Fig.3.2 that we require $N_{ch} \approx 80$ to obtain an absolute error $\sim 2 \times 10^{-5}$. At weak couplings $g = 0.1$ the calculation converges with absolute error $\sim 1 \times 10^{-7}$ requiring only around $N_{ch} \approx 40$. With the above specified grid parameters, the calculation with $N_{ch} = 5$ takes ≈ 3 *secs* and with $N_{ch} = 50$ takes ≈ 9 *mins*. The calculation at strong couplings with around $N_{ch} = 90$ is the maximum possible when using the maximum allotted memory of $128GB$ on a machine and takes ≈ 45 *mins*. Running on MATLAB, this calculation is done without parallelism.

Influence of Number of Points and Closed Channels

The convergence depends on the number of closed channels in the calculation. More closed channels are needed in the calculation with increasing collision energy.

We consider an example case of ion in ground state ($n_I = 0$), weak coupling of

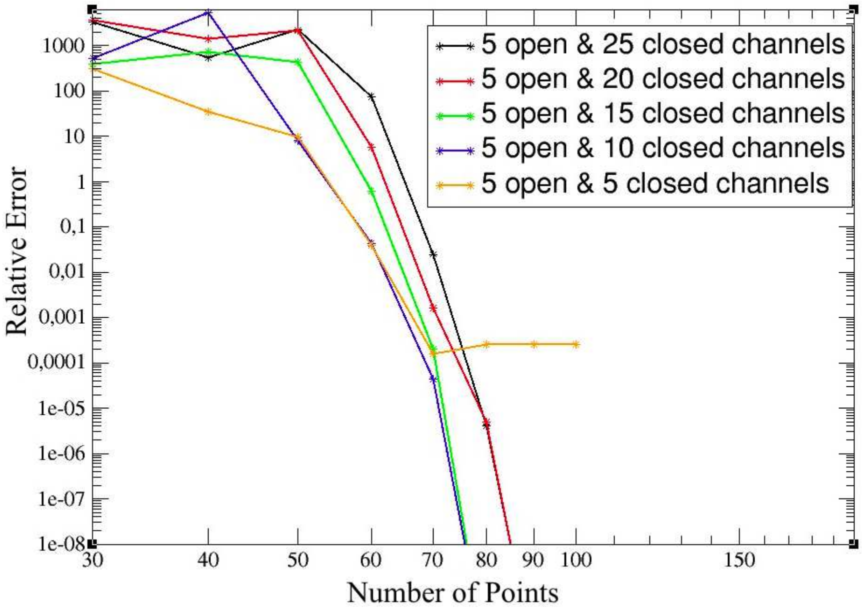

Figure 3.3: Convergence with number of closed channels in the calculation, using pseudospectral method.

$g = 0.1$ and energy $E_{tot} = 5.1\ \hbar\omega$ i.e 5 open channels. We calculate the relative error on the summed reflection probability as a function of the number of points. For relative error we use a reference calculation done with 10 sectors, 15 points per sector taken over $[-10\ a_{ho}, +10\ a_{ho}]$, $N_{ch} = 50$ and vary the number of closed channels in the calculation to see in Fig.3.3 that a minimum of at least 10 closed channels are required for a convergence better than 1×10^{-8} with sufficient number of points.

Comparison of Convergence Rates

To illustrate the super-algebraic convergence of pseudospectral method a comparison is made with modified Simpson's and trapezoidal methods, with respect to the total number of integration points as shown in Fig.3.4.

The absolute error on the summed reflection probability is calculated with respect to a reference calculation with 10 sectors, 15 points per sector over $[-10\ a_{ho}, +10\ a_{ho}]$, $N_{ch} = 50$, $E_{tot} = 2.1\ \hbar\omega$ and weak coupling $g = 0.1$. The trapezoidal and Simpson's methods are known to be $O(n^{-2})$ and $O(n^{-4})$ respectively, where n is the total number of points. The convergence rate of pseudospectral method is seen to be exponential (or super-algebraic) i.e $O(n^{-n})$ (See 56), as seen in Fig.3.4.

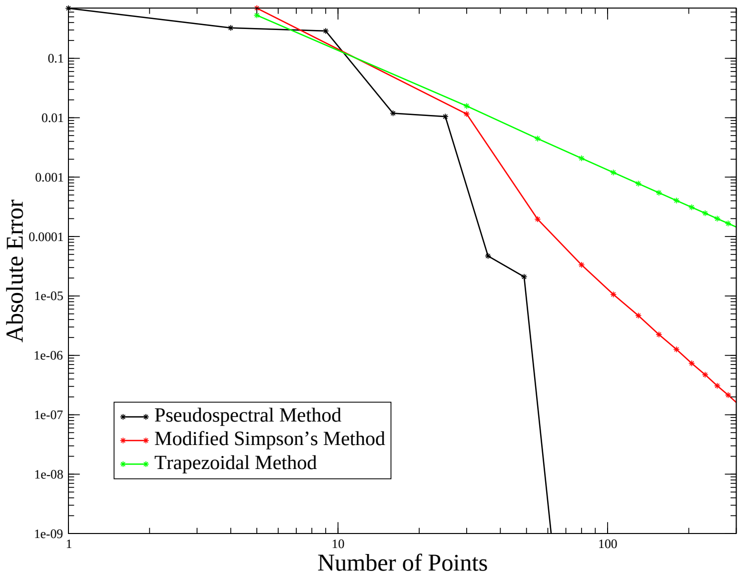

Figure 3.4: Comparison of convergence properties of pseudospectral, modified Simpson's and Trapezoidal methods.

3.1.2 Solution by Propagation in Cartesian Coordinates

We introduced solution method by IEM in the previous section and explained the convergence characteristics of the method with various grid and physical parameters. The slow convergence of the Green's function limits the range of parameters that can be used, requires a large memory and has a very large computation time. As an alternative to the integral equation method, we implement the log derivative method, which is considerably faster and more robust. A concise introduction to the method was given in Sec.2.3.

Rewriting the Schrödinger equation in Eq.(3.2) in centre-of-mass and relative coordinates, we have

$$\left[-\frac{1}{2M}\frac{\partial^2}{\partial X^2}-\frac{1}{2\mu}\frac{\partial^2}{\partial x^2}+\frac{1}{2}\left(X-\frac{m}{M}x\right)^2+g\delta(x)\right]\Psi(X,x)=E\,\Psi(X,x) \tag{3.18}$$

where $X=(mx_A+x_I)/(m+1)$ is the centre-of-mass, mass ratio is $m=m_A/m_I$, $M=m+1$ is the total mass, the reduced mass is $\mu=[1/m+1]^{-1}$ and relative coordinate is $x=x_A-x_I$. The atom and ion coordinates in terms of the centre-of-mass and relative coordinates are in turn given by

$$x_A=X+\frac{x}{M}\qquad\text{and}\qquad x_I=X-\frac{m}{M}x. \tag{3.19}$$

The centre-of-mass is taken as the internal coordinate and relative coordinate is

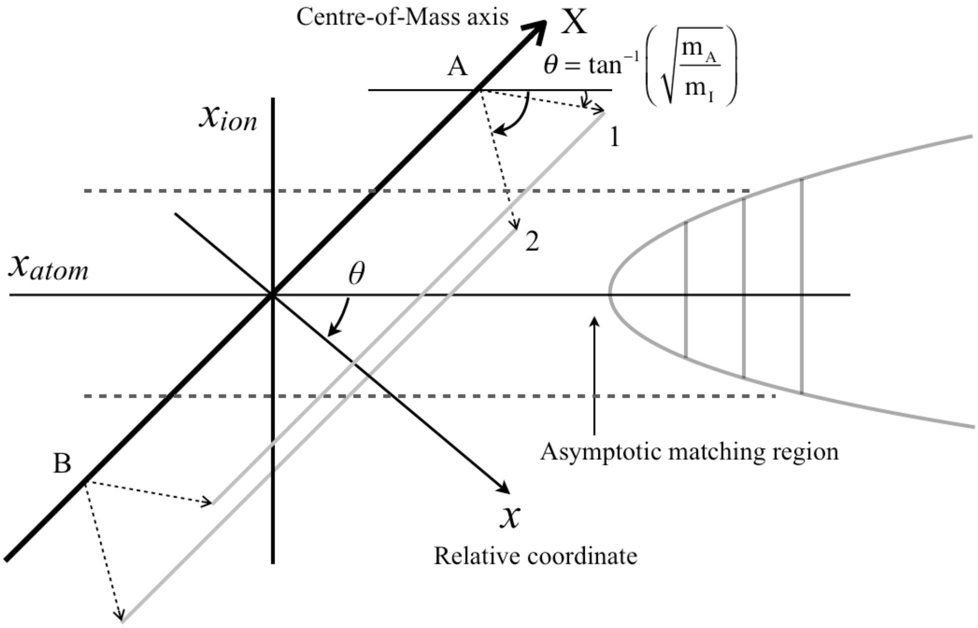

Figure 3.5: Schematic of Log-Derivative propagation in Cartesian coordinates. The relative coordinate x is also oriented at an angle θ with respect to the centre-of-mass axis X depending on the mass ratio m. $\theta = 45°$ if $m = 1$. Labels 1 and 2 denote the propagation direction for mass ratios $m << 1$ and $m >> 1$ respectively.

the propagation coordinate. Since the atom-ion potential is modelled by a delta pseudopotential $V_{AI} = g\delta(x)$, the potential is non-zero only if $x_I = x_A$. Thus any potential that is a function of the relative coordinate fixes the centre-of-mass axis at a 45° angle from the x-axis (labelled x_{atom} in Fig.3.5). The direction of propagation angle $\theta = \tan^{-1}(\sqrt{m_A/m_I})$ is proportional to the mass ratio, as shown in Fig.3.5. For smaller values of m, the propagated grid between points A and B along the X axis remains within the defined waveguide width or oscillator size (labelled 1 in the figure) and thus can completely define the asymptotic wavefunctions which gives good matching at the boundary. The method begins to fail for higher values of m (labelled 2 in the figure) where the grid AB moves out of the waveguide region and one would have to define an extremely large grid with sufficient point density. This increases the size of the propagated matrix. Let the solutions be given by $\Psi_j(X,x) = \sum_{i'} \phi_{i'}(X) F_{i'j}(x)$. Following the procedure in Sec.2.3, we substitute these solutions in Eq.(3.18), multiple by $\phi_i(X)$ and integrate with respect to X. We have

$$\frac{\partial^2}{\partial x^2} F_{ij}(x) = \sum_{i'} \langle \phi_i(X) \,|\, W(x,X) \,|\, \phi_{i'}(X) \rangle_X \, F_{i'j}(x) \Rightarrow \mathbb{W}(x)\mathbb{F}(x) \tag{3.20}$$

where the *effective* potential matrix $\mathbb{W}(x)$ has matrix elements

$$W_{ii'}(x) = -\left[-\frac{\mu}{M}\left\langle\phi_i(X)\middle|\frac{\partial^2}{\partial X^2}\middle|\phi_{i'}(X)\right\rangle_X + 2\mu\left\langle\phi_i(X)\middle|\left(X-\frac{m}{M}x\right)^2\middle|\phi_{i'}(X)\right\rangle_X + 2\mu g\delta_{ii'}\delta(x) - 2\mu E\delta_{ii'}\right] \tag{3.21}$$

The second term on the right side is diagonal since $\left\langle\phi_i(X)\middle|\left(X-\frac{m}{M}x\right)^2\middle|\phi_{i'}(X)\right\rangle_X = \delta_{ii'}\left(X_i-\frac{m}{M}x\right)^2$. The various grid and physical parameters for a converged calculation are specified in Sec.3.1.2.2. The log derivative matrix defined in terms of the relative coordinate is $\mathbb{Y}(x) = \mathbb{F}'(x)\mathbb{F}^{-1}(x)$ and is propagated along the x axis.

The second derivative kinetic energy term in the effective potential is represented by a matrix in DVR (See 96, 97). This term has a standard representation on a Fourier basis (See 100). The log derivative algorithm has been briefly explained in Sec.2.3.

3.1.2.1 Initial Condition

The analytical boundary condition at the origin for 1D scattering of a particle of mass m from a delta pseudopotential $g\delta(x)$ is well known.Following [100], a basis of sine functions is taken for this case. The pseudopotential is centered at the origin, this gives the initial log derivative $\mathbb{Y}^{IN} = \mathbb{F}'(x)\mathbb{F}^{-1}(x)|_{x=0}$. The solution $\Psi(X,x)$ is expanded on a basis of trignometric DVR functions $\phi_j(X)$ along the X axis as $\Psi_i(x,X) = \sum_j \phi_j(X)F_{ji}(x)$. $F_{ji}(x)$ are the propagated functions and their properties at the location of the delta pseudopotential (x=0) determine the correct initial condition. Substituting it into Eq.(3.18) and integrating in x over $[-\epsilon,+\epsilon]$, where $\epsilon\to 0$, we arrive at

$$-\frac{1}{2M}\int_{-\epsilon}^{+\epsilon} F_{ji}(x)\partial_X^2\phi_j(X)dx - \frac{1}{2\mu}\partial_x F_{ji}(x)\phi_j(X)|_{-\epsilon}^{+\epsilon} + g\int_{-\epsilon}^{+\epsilon} F_{ji}(x)\phi_j(X)\delta(x)dx + \frac{1}{2}\int_{-\epsilon}^{+\epsilon} F_{ji}(x)\phi_j(X)\left(X-\frac{m}{M}x\right)^2 dx = \int_{-\epsilon}^{+\epsilon} EF_{ji}(x)\phi_j(X)\,dx \tag{3.22}$$

where ∂_X and ∂_x denote the derivatives with respect to X and x respectively. All terms except the second and third terms on the left hand side tend to zero as $\epsilon\to 0$. Multiplying Eq.(3.22) by $\phi_j(X)$ and integrating with respect to X gives

$$\left(F'_{ji}(-\epsilon) - F'_{ji}(\epsilon)\right) + 2\mu g\int_{-\epsilon}^{+\epsilon} F_{ji}(x)\delta(x)dx = 0$$

$$\begin{gathered}\text{If } F'_{ji}(\epsilon) = -F'_{ji}(-\epsilon) \Rightarrow F_{ji}(0) = F'_{ji}(0)/(g\mu) \Rightarrow + \text{ total parity } Y^{IN}_{ji} = 2g\mu\delta_{ji}\\ \text{If } F'_{ji}(\epsilon) = F'_{ji}(-\epsilon) \Rightarrow F_{ji}(0) = 0 \Rightarrow - \text{ total parity } Y^{IN}_{ji} = \infty\delta_{ji}\end{gathered} \tag{3.23}$$

Writing the solution as a product of functions $\Psi(x,X) = F(x)f(X)$, $\Psi(-x,-X) = \pm\Psi(x,X)$ for the positive (or negative) total parity respectively.
$+$ total parity→ $\Psi(-x,-X) = F(-x)\ f(-X) = \pm F(x). \pm f(X)$
$-$ total parity→ $\Psi(-x,-X) = F(-x)\ f(-X) = \pm F(x). \mp f(X)$
The initial log derivative matrix is built on the X coordinate basis that is obtained by symmetrizing the Fourier DVR grid[1]. Details of symmetrization procedure is given in Appendix B. The potential matrix in Eq.(3.21) is accordingly symmetrized at each step of propagation. Thus for positive total parity we have

$$\mathbb{Y}^{IN} = \begin{pmatrix} 2g\mu & 0 & \dots & \dots & 0 \\ 0 & 2g\mu & \dots & 0 & \vdots \\ \vdots & \vdots & \ddots & \vdots & \vdots \\ \vdots & 0 & \dots & \infty & 0 \\ 0 & \dots & \dots & 0 & \infty \end{pmatrix} \tag{3.24}$$

The grid point $X = 0$ is always of positive parity, thus the corresponding element along the diagonal in the above matrix will be $2g\mu$. The negative total parity initial condition interchanges the values ∞ and $2g\mu$ along the diagonal.

3.1.2.2 Asymptotic Matching

The procedure of asymptotic matching has been explained in Sec.2.3.2. From Eq.(3.19) we see x_A and x_I are functions of x and X. Asymptotic functions are to be built at the final step of propagation $x = x_N$, on the X coordinate grid $X_j \in [-L,+L]$. The regular and irregular asymptotic functions $\mathscr{F}$ and $\mathscr{G}$ used to build the matrices $\mathbb{F}$ and $\mathbb{G}$ are

$$\begin{aligned} \mathscr{F}_{j,j'} &= \frac{1}{\sqrt{k_{j'}}} f^{\pm}(k_{j'}x_A)\psi_{ho,j'}(x_I) = \frac{1}{\sqrt{k_{j'}}} f^{\pm}\left(k_{j'}\left[X_j + \frac{x_N}{M}\right]\right)\psi_{ho,j'}\left(X_j - \frac{m}{M}x_N\right) \\ \mathscr{G}_{j,j'} &= \frac{1}{\sqrt{k_{j'}}} g^{\pm}(k_{j'}x_A)\psi_{ho,j'}(x_I) = \frac{1}{\sqrt{k_{j'}}} g^{\pm}\left(k_{j'}\left[X_j + \frac{x_N}{M}\right]\right)\psi_{ho,j'}\left(X_j - \frac{m}{M}x_N\right) \end{aligned} \tag{3.25}$$

where wave vectors $k_{j'} = \sqrt{2m(E-(j'+1/2))}$ are real for energetically open channels and imaginary for closed channels, $\psi_{ho,j'}(x_I)$ are asymptotic harmonic oscillator ion wavefunctions given in Eq.(3.6), $f^{\pm}(k_{j'}x_A)$ and $g^{\pm}(k_{j'}x_A)$ are the regular and irregular free asymptotic solutions for the atom. Since $f^{\pm}(k_{j'}x_A)$, $g^{\pm}(k_{j'}x_A)$ and $\psi_{ho,j'}(x_I)$ are functions of both x and X and are expanded on a DVR function basis along the X coordinate by integration which gives value of the integrand at

---

[1] Symmetrization follows a consistent convention in all routines.

the DVR grid points. The functions $f^{\pm}(k_{j'}x_A)$, $g^{\pm}(k_{j'}x_A)$ for the open channels are taken as

$$\begin{aligned} f^{+}(k_{j'}x_A) &= k_{j'}^{-1/2}\cos(k_{j'}x_A) \qquad g^{+}(k_{j'}x_A) = k_{j'}^{-1/2}\sin(k_{j'}|x_A|) \\ f^{-}(k_{j'}x_A) &= k_{j'}^{-1/2}\sin(k_{j'}x_A) \qquad g^{-}(k_{j'}x_A) = -k_{j'}^{-1/2}\mathrm{sign}(x_A)\cos(k_{j'}x_A) \end{aligned} \tag{3.26}$$

and for the closed channels as

$$\begin{aligned} f^{+}(k_{j'}x_A) &= k_{j'}^{-1/2}\cosh(k_{j'}x_A) \quad g^{+}(k_{j'}x_A) = -k_{j'}^{-1/2}\exp(-k_{j'}|x_A|) \\ f^{-}(k_{j'}x_A) &= k_{j'}^{-1/2}\sinh(k_{j'}x_A) \quad g^{-}(k_{j'}x_A) = -k_{j'}^{-1/2}\mathrm{sign}(x_A)\exp(-k_{j'}|x_A|) \end{aligned} \tag{3.27}$$

These functions are linearly independent since their Wronskian for each parity is non zero, giving $W(f^{\pm}, g^{\pm}) = 1$. The parity of these functions are chosen depending on the parity of the oscillator functions $\psi_{ho,j'}(x_I)$ for a given total parity of the total solution.

Given N_{ch} channels are propagated, in the asymptotic region N_{asy} channels with $(N_{asy} < N_{ch})$ are taken to build the functions $\mathscr{F}_{j,n}(x_A, x_I)$ and $\mathscr{G}_{j,n}(x_A, x_I)$. N_{asy} is chosen so as to include all energetically open channels and sufficient number of closed channels to account for exponentially decaying yet non-negligible amplitude in the closed channels. It is seen from Fig.3.5 that there is a 45° angle between the asymptotic region and the propagated log derivative along the X-axis grid. Strongly closed channels need to be eliminated during matching asymptotic solutions and this truncation can be done by a basis transformation. This transformation matrix $\mathbb{T}_N$ is built with the eigenfunctions of the lowest N_{asy} eigenvalues of the matrix of the effective potential $\mathbb{W}(x)$ given in Eq.(3.21), computed at the final propagation point x_N. The second derivative term (first term on the right hand side) is a full matrix. The final log-derivative $\mathbb{Y}_f$ for N_{asy} number of channels in the asymptote is then given by

$$\bar{\mathbb{Y}}_f = \mathbb{T}_N^T \mathbb{Y}_f \mathbb{T}_N \tag{3.28}$$

The K-matrix for a given parity is then given by Eq.(2.40) and the S-matrix is obtained from open-open blocks of the K-matrix, using Eq.(2.42). The total S-Matrix is then given in terms of the positive and negative parity S-matrices $\mathbb{S}^{+}$ and $\mathbb{S}^{-}$ of dimension $(N_{op} \times N_{op})$ where N_{op} the number of open channels

$$\mathbb{S}_{total} = \frac{1}{2}\begin{bmatrix} \mathbb{S}^{+} + \mathbb{S}^{-} & \mathbb{S}^{+} - \mathbb{S}^{-} \\ \mathbb{S}^{+} - \mathbb{S}^{-} & \mathbb{S}^{+} + \mathbb{S}^{-} \end{bmatrix} \tag{3.29}$$

Grid and Physical Parameters From Fig.3.5, if the grid $X \in [-L, +L]$ with N_X number of points, then $x_I \in [-\left(L - x\frac{m}{M}\right), +\left(L - x\frac{m}{M}\right)]$, thus in the asymptotic

region precision with respect to the number of grid points is lost if (a) we propagate to large distances x_N for a given mass ratio and/or (b) mass ration m is high. These two parameters determine if the asymptotic matching is done efficiently. Since we use a zero-range potential, we need to propagate to a distance $x_N \propto \sqrt{g}$ (a few oscillator lengths) so as to converge the weakly closed channels in the x coordinate. The propagation step size needed is $\sim 1 \times 10^{-4}$ with $N_{asy} \approx 20$ closed channels. Some of the grid and physical inputs for a converged calculation are specified here.
For mass ratio $m = 0.1$ - $L = [-10, +10], N_X = 120, x_N = 5$.
For mass ratio $m = 0.57$ - $L = [-10, +10], N_X = 130, x_N = 5$.
For mass ratio $m = 2$ - $L = [-20, +20], N_X = 250, x_N = 5$.

It is thus seen that we require a very large grid and number of points to converge the calculation with high mass ratios ($m > 2$). It is seen from Fig.3.5 that at high mass ratios the propagated grid along X-axis shifts out of the oscillator region. The pseudopotential coupling and total energy constrain the minimum propagated distance. To overcome this constraint we propagate in plane polar coordinates, avoiding the need for a basis transformation at the final step of propagation.

3.1.3 Solution by Propagation in Plane Polar Coordinates

The Log Derivative propagation in Cartesian coordinates has intrinsic limitations while solving for a two body problem since it requires having very large grids for higher mass ratios $m_A/m_I >> 1$, as explained in Sec.3.1.2.2. This increases the number of channels N_{ch} to be propagated and since the propagation algorithm involves matrix inversion and multiplication, the computation time increases as $O(N_{ch}^3)$. This drawback can be overcome if we propagate in plane polar instead of Cartesian coordinates. Rewriting the two body Hamiltonian in Eq.(3.2) in oscillator units

$$\left[-\frac{1}{2m}\frac{\partial^2}{\partial x_A^2} - \frac{1}{2}\frac{\partial^2}{\partial x_I^2} + \frac{1}{2}x_I^2 + g\delta(x_A - x_I)\right]\Psi(x_A, x_I) = E\Psi(x_A, x_I) \tag{3.30}$$

and using mass-ratio scaled coordinates taking $\tilde{x}_A = \sqrt{m}x_A$, we have

$$\left[-\frac{1}{2}\frac{\partial^2}{\partial \tilde{x}_A^2} - \frac{1}{2}\frac{\partial^2}{\partial x_I^2} + \frac{1}{2}x_I^2 + g\delta(\tilde{x}_A - x_I)\right]\Psi(\tilde{x}_A, x_I) = E\Psi(\tilde{x}_A, x_I) \tag{3.31}$$

In plane polar coordinates, with $\rho = \sqrt{\tilde{x}_A^2 + x_I^2}$, the Hamiltonian is rewritten as

$$\left[-\frac{1}{2\rho^2}\frac{\partial^2}{\partial\theta^2} - \frac{1}{2}\frac{\partial^2}{\partial\rho^2} - \frac{1}{2\rho}\frac{\partial}{\partial\rho} + \frac{1}{2}[\bar{\rho}\ \cos(\alpha) - \rho\ \cos(\theta-\alpha)]^2 + \frac{g\sin(\alpha)}{\rho}\delta(\theta)\right]\Psi(\rho,\theta) = E\Psi(\rho,\theta) \tag{3.32}$$

where $\bar{\rho} = \overline{OO'}$ and $\alpha = \tan^{-1}(\sqrt{m})$, as shown in Fig.3.6. The origin is redefined to O' and ρ-axis is at an angle α before propagation. The grid end points ρ_1 and ρ_2 are chosen sufficiently far apart so to encompass the waveguide region during propagation and $\rho > 0$. Thus at any angle θ along the propagation coordinate $\hat{\theta}$, the atom and ion coordinates can be given by $x_A = [\bar{\rho}\sin(\alpha) + \rho\sin(\theta-\alpha)]$ and $x_I = [\bar{\rho}\cos(\alpha) - \rho\cos(\theta-\alpha)]$.

The Log Derivative built along the ρ axis is propagated along the angular coordinate $\hat{\theta}$. So taking ρ as the internal coordinate, we apply the angular log derivative propagation to

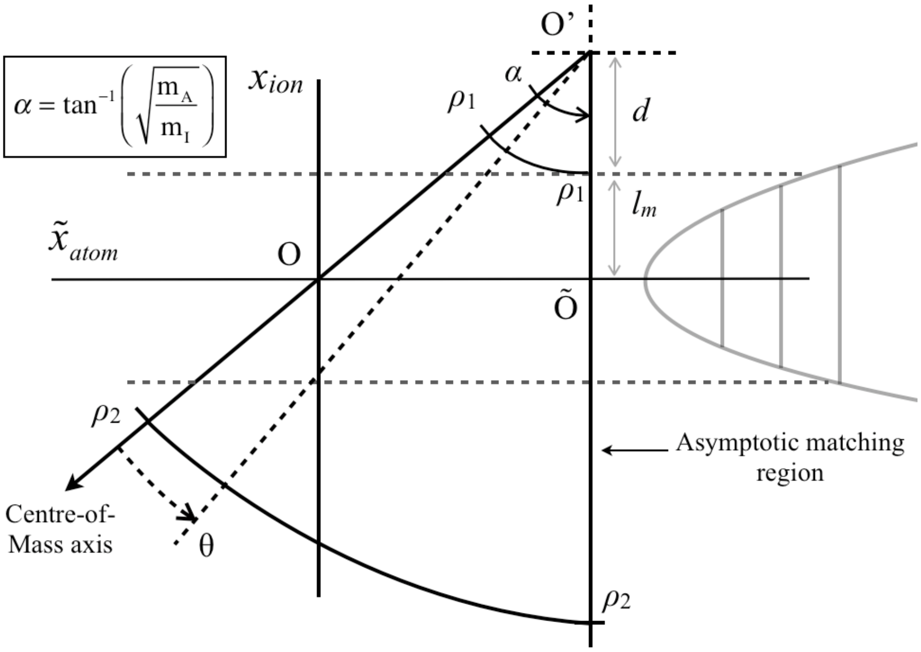

Figure 3.6: Log-Derivative Propagation in plane polar coordinates.

$$\frac{\partial^2}{\partial\theta^2}\Psi(\rho,\theta) = -2\rho^2\left[\frac{1}{2}\frac{\partial^2}{\partial\rho^2} + \frac{1}{2\rho}\frac{\partial}{\partial\rho} - \frac{1}{2}[\bar{\rho}\ \cos(\alpha) - \rho\ \cos(\theta-\alpha)]^2 - \frac{g\sin(\alpha)}{\rho}\delta(\theta) + E\right]\Psi(\rho,\theta) \tag{3.33}$$

Let the solutions be given by $\Psi_j(\rho,\theta) = \sum_{i'} \phi_{i'}(\rho) F_{i'j}(\theta)$. Following the procedure in Sec.2.3, we substitute these solutions in Eq.(3.33), multiple by $\phi_i(\rho)$ and integrate with respect to $\frac{d\rho}{\rho}$. This modification to the DVR basis is explained in Sec.3.1.3.1. We have

$$\frac{\partial^2}{\partial\theta^2} F_{ij}(\theta) = \sum_{i'} \langle \phi_i(\rho) \,|\, W(\rho,\theta) \,|\, \phi_{i'}(\rho) \rangle_\rho \, F_{i'j}(\theta) \rightarrow \mathbb{W}(\theta)\mathbb{F}(\theta) \tag{3.34}$$

where the *effective* potential matrix $\mathbb{W}(\theta)$ has matrix elements

$$\begin{aligned} W_{ii'}(\theta) = -\left\langle \phi_i(\rho) \left| \left(\rho^2 \frac{\partial^2}{\partial \rho^2} + \rho \frac{\partial}{\partial \rho} \right) \right| \phi_{i'}(\rho) \right\rangle_\rho + 2g \sin(\alpha) \langle \phi_i(\rho) \,|\, \rho \,|\, \phi_{i'}(\rho) \rangle_\rho \, \delta(\theta) + \\ \left\langle \phi_i(\rho) \,\middle|\, \left(\rho^2 [\bar{\rho} \, \cos(\alpha) - \rho \, \cos(\theta - \alpha)]^2 \right) \middle|\, \phi_{i'}(\rho) \right\rangle_\rho - 2 \left\langle \phi_i(\rho) \,\middle|\, \rho^2 \,\middle|\, \phi_{i'}(\rho) \right\rangle_\rho E \end{aligned} \tag{3.35}$$

All terms in the above equation except the first are diagonal in the ρ basis. The log derivative matrix defined in terms of the relative coordinate is $\mathbb{Y}(\theta) = \mathbb{F}'(\theta)\mathbb{F}^{-1}(\theta)$ is propagated along the θ axis. Log derivative algorithm has been briefly explained in Sec.2.3. The derivative term in the right hand side in Eq.(3.35)

$$\hat{T}_\rho = \rho^2 \frac{\partial^2}{\partial \rho^2} + \rho \frac{\partial}{\partial \rho} \tag{3.36}$$

is unlike the second order derivative term encountered in most problems. It is important to have a symmetric representation of this term.

3.1.3.1 Modified DVR Basis

The kinetic energy term $\hat{T}_\rho = \rho^2 \frac{\partial^2}{\partial \rho^2} + \rho \frac{\partial}{\partial \rho}$ in the effective potential is represented on a Legendre-Gauss-Lobatto grid [56]p.572. Modified DVR basis functions $\phi_j(\rho)$ are needed for a symmetric representation of this term. A modified basis with coordinate dependent weights is defined as

$$\phi_j(\rho) = c_j(\rho) \sqrt{\frac{\rho_j}{w_j}} \quad \text{with} \quad c_j(\rho) = C_j \left(\frac{2(\rho - \rho_1)}{\rho_2 - \rho_1} - 1 \right) \tag{3.37}$$

The functions $c_j(\rho)$ are the rescaled Legendre-Gauss-Lobatto cardinal functions defined over the interval (ρ_1, ρ_2) and $C_j(\rho)$ are the same cardinal functions defined over $(-1, +1)$, as given in [56]p.572. The orthonormality in order is given by

$$\langle \phi_i(\rho) \,|\, \phi_j(\rho) \rangle = \int_{\rho_1}^{\rho_2} \phi_i(\rho) \phi_j(\rho) \frac{1}{\rho} d\rho = \delta_{ij} \tag{3.38}$$

In this modified basis, we check if the matrix representation of $\hat{T}_\rho$ is symmetrix. Taking matrix elements of this operator

$$\begin{aligned}\langle\psi_i(\rho)|\hat{T}_\rho|\psi_j(\rho)\rangle &= \int_{\rho_1}^{\rho_2}\psi_i(\rho)\left[\rho^2\frac{\partial^2\psi_j(\rho)}{\partial\rho^2} - \rho\frac{\partial\psi_j(\rho)}{\partial\rho}\right]\frac{1}{\rho}d\rho \\ &= \int_{\rho_1}^{\rho_2}\left[\psi_i(\rho)\rho\psi_j''(\rho) - \psi_i(\rho)\psi_j'(\rho)\right]d\rho\end{aligned}$$

Integrating the first term on the far right hand side, we have

$$\begin{aligned}\langle\psi_i(\rho)|\hat{T}_\rho|\psi_j(\rho)\rangle = -\psi_i(\rho)\rho\psi_j'(\rho)|_{\rho_1}^{\rho_2} + \int_{\rho_1}^{\rho_2}\big[\psi_i'(\rho)\rho\psi_j'(\rho) + \cancel{\psi_i'(\rho)\psi_j(\rho)} - \\ \cancel{\psi_i'(\rho)\psi_j(\rho)}\big]\,d\rho\end{aligned}$$

The first term on the right hand side tends to zero since we adopt Dirichlet boundary condition as $\rho \in]\rho_1, \rho_2[\Rightarrow \psi(\rho_1) = \psi(\rho_2) = 0$ and the second term is symmetric upon integration with respect to $d\rho/\rho$ in the new representation

$$\langle\psi_i(\rho)|\hat{T}_\rho|\psi_j(\rho)\rangle = \int_{\rho_1}^{\rho_2}\psi_i'(\rho)\rho\psi_j'(\rho)d\rho = \int_{\rho_1}^{\rho_2}\psi_i'(\rho)\rho^2\psi_j'(\rho)\frac{1}{\rho}d\rho.$$

The DVR weights have a $1/\sqrt{\rho}$ dependence. The eigensolutions and eigenvalues for a differential operator of the kind $\hat{T}_\rho$ are similar to eigensolutions of a particle in an infinite square well.

$$\psi_n(\rho) = \sin\left[\frac{n\pi\ln(\rho/\rho_1)}{\ln(\rho_2/\rho_1)}\right] \quad \text{with} \quad \lambda_n = \frac{n^2\pi^2}{\ln^2(\rho_2/\rho_1)}. \tag{3.39}$$

The eigenvalues and eigenfunctions of the $\hat{T}_\rho$ operator are derived in Appendix.C.

3.1.3.2 Initial Condition and Asymptotic Matching

The derivative term $\hat{T}_\rho$ is built along the $\hat{\rho}$ axis, symmetrically about the origin O, over a set of grid points given by $X_i = (\bar{\rho} - \rho_i)$, where $\rho_i \in]\rho_1, \rho_2[$. Since DVR weights have a $1/\sqrt{\rho_i}$ dependence, it is noted that symmetrization like that done in Sec.3.1.2.1 about the origin O of the ρ grid is a non-orthogonal transformation since the grid weights are dependent on the coordinate as given in Eq.(3.37). The potential matrix cannot be symmetrized at each step of propagation and thus the initial log derivative is transformed to Finite Basis Representation (FBR) [93-95]. The Legendre-Gauss-Lobatto DVR basis is changed to a new basis of sine (and cosine) functions or *box functions* (i.e solutions to a particle in a box) assuming the box of half-width L with endpoints at ρ_1 and ρ_2 (See [100] and Sec.3.1.2.1).

The transformation matrix elements corresponding to positive and negative parity basis functions are

$$T_{ij} = \frac{1}{\sqrt{L}}\cos\left(\frac{j\pi X_i}{2L}\right)\sqrt{w_i/\rho_i} \text{ and } T_{ij} = \frac{1}{\sqrt{L}}\sin\left(\frac{j\pi X_i}{2L}\right)\sqrt{w_i/\rho_i} \tag{3.40}$$

where $X_i = (\bar{\rho} - \rho_i)$ and $\rho_i \,\epsilon\,]\rho_1, \rho_2[$. w_i are the Legendre-Gauss-Lobatto weights at the grid points and $\sqrt{w_i/\rho_i}$ refers to the modified DVR weights at the grid points as shown in Eq.(3.37). Thus we build a matrix $\mathbb{T}_B$ with the functions in Eq.(3.40) along the columns of the matrix. Following the method in Sec.3.1.2.1, an expansion of the solution $\Psi(\rho,\theta)$ on a basis of DVR functions $\Psi_i(\rho,\theta) = \sum_j \phi_j(\rho)F_{ji}(\theta)$. Substituting this into Eq.(3.32) and integrating over $[-\epsilon, +\epsilon]$ with respect to θ with $\epsilon \to 0$, we have

$$\begin{aligned} -\partial_\theta F_{ji}(\epsilon)\phi_j(\rho)|_{-\epsilon}^{+\epsilon} - \rho^2 \int_{-\epsilon}^{+\epsilon} F_{ji}(\theta)\partial_\rho^2\phi_j(\rho)d\theta + \rho \int_{-\epsilon}^{+\epsilon} F_{ji}(\theta)\partial_\rho\phi_j(\rho)d\theta + \\ \int_{-\epsilon}^{+\epsilon} 2\rho^2 V_{HO}(\rho,\theta)\, F_{ji}(\theta)\phi_j(\rho)d\theta + 2\rho g\sin(\alpha)\int_{-\epsilon}^{+\epsilon} F_{ji}(\theta)\phi_j(\rho)\delta(\theta)d\theta = \\ 2\rho^2 E\int_{-\epsilon}^{+\epsilon} F_{ji}(\theta)\phi_j(\rho)d\theta \end{aligned} \tag{3.41}$$

where ∂_ρ and ∂_θ denote the derivatives with respect to ρ and θ respectively. The harmonic oscillator potential is $V_{HO}(\rho,\theta) = [\bar{\rho}\ \cos(\alpha) - \rho\ \cos(\theta - \alpha)]^2$. All terms in this equation except the first and fifth terms on the left side are zero. Multiplying Eq.(3.41) from the left by $\phi_{j'}(\rho)$ and integrating with respect to ρ leaves

$$(-F'_{ji}(\epsilon) + F'_{ji}(-\epsilon)) + 2g\sin(\alpha)F_{ji}(0)\,\langle\phi_{j'}(\rho)\,|\,\rho\,|\,\phi_j(\rho)\rangle = 0 \tag{3.42}$$

Taking $M_{jj'} = \langle\phi_{j'}(\rho)\,|\,\rho\,|\,\phi_j(\rho)\rangle = \rho_j\delta_{jj'}$ as a matrix element of matrix $\mathbb{M}$, we see it is diagonal in DVR. From Eq.(3.42) above, we define log derivative channels $Y_{ji}^{IN}(\theta) = F'_{ji}(0)F_{ji}^{-1}(0)$

$$\begin{aligned} &\text{If } F'_{ji}(\epsilon) = -F'_{ji}(-\epsilon) \Rightarrow F_{ji}(0) = \chi'_{ji}(0)M_{ji}^{-1}/(g\sin(\alpha)) \Rightarrow +\text{ total parity channels} \\ &\qquad\qquad\qquad\qquad\qquad\qquad\qquad\qquad\qquad\qquad\qquad Y_{ji}^{IN} = gM_j\sin(\alpha) \\ &\text{If } F'_{ji}(\epsilon) = F'_{ji}(-\epsilon) \Rightarrow F_{ji}(0) = 0 \Rightarrow -\text{ total parity channels } Y_{ji}^{IN} = \infty \end{aligned} \tag{3.43}$$

It is noted that the initial log derivative is transformed to FBR by $\mathbb{T}_B\mathbb{Y}_{IN}\mathbb{T}_B^{-1}\mathbb{M}^{-1}$, where $\mathbb{T}_B$ is the matrix of basis functions, with elements given in Eq.(3.40). Matrix $\mathbb{T}_B$ is a full matrix and since log derivative term has infinities along the diagonal, the initial condition will have matrix elements close to infinity and remain insensitive to the value of pseudopotential coupling g. We instead choose to begin propagation with an R-Matrix condition which is $\mathbb{R}^{IN} = (\mathbb{Y}^{IN})^{-1}$. Thus we have the initial conditions for each parity as

$$\begin{aligned} Y^{IN}_{ji} = g\sin(\alpha)M_{ji};\; R^{IN}_{ji} = \frac{1}{g\sin(\alpha)}M^{-1}_{ji} \quad &\text{- Positive total parity} \\ Y^{IN}_{ji} = \infty;\; R^{IN}_{ji} = 0 \qquad &\text{- Negative total parity} \end{aligned} \tag{3.44}$$

The initial condition matrix for positive total parity is given by

$$\mathbb{R}^{IN} = \mathbb{T}\begin{pmatrix} 1/(g\sin(\alpha)) & 0 & 0 & 0 & \dots \\ 0 & 0 & 0 & 0 & \dots \\ 0 & 0 & 1/(g\sin(\alpha)) & 0 & \dots \\ 0 & 0 & 0 & 0 & \dots \\ \vdots & \vdots & \vdots & \vdots & \ddots \end{pmatrix}\mathbb{T}^{-1}\,\mathbb{M}^{-1}_{\rho} \tag{3.45}$$

The terms 0 and $1/(g\sin(\alpha))$ are interchanged to obtain an initial condition with negative total parity. Since R-Matrix initial condition chosen here is singular, the initial few steps $(1 \sim 3)$ of propagation are modified to propagate the R-matrix initial condition after which it is found to be non-singular for stable inversion. After the initial few steps of modified R-matrix propagation the regular Log Derivative recursion relation in Eq.(2.34) is used. The recursion relation in Eq.(2.34) over an interval $[x', x'']$ is modified as

$$Y(x'') = \mathcal{Y}_4(x', x'') - \mathcal{Y}_3(x', x'') \times [\mathrm{I} + R(x')\mathcal{Y}_1(x', x'')]^{-1}(R(x') \times \mathcal{Y}_2(x', x'')) \tag{3.46}$$

where $R(x')$ is the R-matrix at the propagation coordinate x'. Taking the interval to be two half-sectors x_n, x_m and $[x_m, x_{n+1}]$, where the x_m is the midpoint of $[x_n, x_{n+1}]$, the resulting Log Derivative after propagation in the first half-sector is inverted and the resulting R-Matrix is propagated again to obtain the Log Derivative. This relation gives a non-singular Log Derivative $Y(x_{n+1})$ at step x_{n+1}. This can be further inverted to give $R(x_{n+1}) = Y(x_{n+1})^{-1}$ and this process is repeated for the initial few steps only (approximately $1 \sim 3$ steps), until the Log Derivative inversion is stable. These few steps involve extra matrix multiplications and inversions and thus is it computationally efficient to continue the rest of the propagation with the usual Log Derivative recursion relation as explained in Sec.2.3.1.

The procedure for asymptotic matching is similar to that in Sec.3.1.2.2, with asymptotic wavefunctions transformed to the appropriate coordinates.

Grid and Physical Parameters

From Fig.3.6, we specify the length of segments l_m and d as inputs to define the

ρ-axis grid over interval $]\rho_1, \rho_2[$ with N_ρ points. We require d of at least one oscillator length to include the weakly closed channels the calculation. Propagation in the θ coordinate is over $\theta \in [0, \alpha]$, where the limit $\alpha = \tan^{-1}(\sqrt{m_A/m_I})$ is fixed by the mass ratio of the system. The propagation step size needed is $\sim 1 \times 10^{-4}$, $d = 1a_{ho}$ and all propagated channels are included in the asymptotic matching since the method is devised to specifically forego the intermediate basis selection procedure, explained in Sec.3.1.2.2. Some of the grid and physical inputs for a converged calculation are specified here.
For mass ratios $m = [0.1, 0.57]$ - $l_m = 10, N_\rho = 150$.
For mass ratio $m = 1.0$ - $l_m = 10, N_\rho = 200$.
For mass ratio $m = 2.0$ - $l_m = 10, N_\rho = 210$.
For mass ratio $m = 5.0$ - $l_m = 10, N_\rho = 340$.

3.2 Results and Discussion

Asymptotic matching at the end of propagation gives the K-Matrix directly, as per Eq.(2.40) and using Eq.(2.42) the S-matrix is obtained from the open-open block of the K-Matrix (in Eq.(2.41)). The transmission and reflection probabilities and their relation to parity dependent S-matrix elements are given in the beginning of Sec.3.2. The reflection and transmission coefficients are $R_{If} = |r_{If}|^2$ and $T_{If} = |t_{If}|^2$ respectively. r and t are the complex transition amplitudes, I, f are the initial and final state of the trapped particle in the harmonic oscillator. The complex reflection and transmission amplitudes are elements of the total S-Matrix. From Eq.(3.29), the complex transmission and reflection amplitudes are given in terms of the elements of the parity dependent S-matrices by $r_{If} = S^+_{If} - S^-_{If}$ and $t_{If} = S^+_{If} + S^-_{If}$ respectively.
The scattering wavefunction in 1D for this problem has the asymptotic form

$$\Psi_n(x_A, x_I) = \psi_n(x_A, x_I) + \sum_{k_i^2>0} f_{ni}(k_n \to \text{sign}(x)k_i)\psi_i(x_A, x_I) \tag{3.47}$$

where the relative coordinate is defined as $x = x_A - x_I$. The reflection and transmission coefficients can then be given in terms of scattering amplitudes as

$$R_{nn'} = |f_{nn'}(k_n \to \text{sign}(x)k_{n'})|^2 \text{ and } T_{nn'} = |\delta_{nn'} + f_{nn'}(k_n \to \text{sign}(x)k_{n'})|^2 \tag{3.48}$$

with the sign convention as shown in Fig.3.7. Following the analysis of [85], we define the scattering amplitudes in terms of even and odd parity components as

$$f_{nn'}(k_n \to \text{sign}(x)k_{n'}) = f^+_{nn'} + \text{sign}(x)f^-_{nn'} \text{ where } f^\pm_{nn'} = i\mathbb{K}^\pm(\mathbb{I} - i\mathbb{K}^\pm)^{-1} \tag{3.49}$$

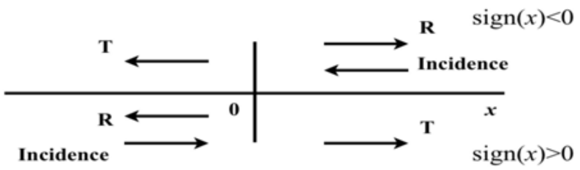

Figure 3.7: Sign convention adopted for incoming and outgoing particles.

where $\mathbb{K}^{\pm}$ is the K-Matrix of the concerned total parity. The summed reflection probability is defined for an incoming channel $n_I = 0$ as $R_0 = \sum_{j=0}^{N_{\rm op}} |r_{0j}|^2$, where $N_{\rm op}$ is the number of open channels for the given collision energy.

From Eq. (3.49) and Eq. (3.48), one can also define the even and odd parity scattering amplitudes in terms of the complex reflection and transmission amplitudes for the low energy elastic open channel as

$$f_{00}^{+} = (r_{00} + \tilde{t}_{00})/2 \quad \text{and} \quad f_{00}^{-} = (\tilde{t}_{00} - r_{00})/2 \tag{3.50}$$

where $\tilde{t}_{00} = t_{00} - \delta_{nn'}$ is the complex transmission amplitude without the *shadow* and r_{00} and t_{00} are the complex reflection and transmission amplitudes. Scattering by a delta pseudopotential and a harmonic oscillator can be characterized by an effective coupling constant. This coupling constant g_{eff} is equivalent to modelling a new delta pseudopotential, with the coupling term that encapsulates the combined effect of the 1D delta and harmonic oscillator potentials. g_{eff} for each parity can be given by

$$g_{eff}^{+} = \frac{iRe(f_{ii}^{+})}{2(2 + Re(f_{ii}^{+}))} k_i/\mu \quad \text{and} \quad g_{eff}^{-} = \frac{iRe(f_{ii}^{-})}{2(2 + Re(f_{ii}^{-}))k_i/\mu} \tag{3.51}$$

where $\mu = (m_I/m_A + 1)^{-1}$. To obtain the above expressions (See 92), we take a general asymptotic form of solution for scattering on the redefined delta pseudopotential $g_{eff}\delta(x)$ as $\psi_{\infty}^{\pm}(x) = e^{-ikx} + f^{\pm}e^{ik|x|}$ and substitute it in the Schrödinger equation $[-(2m)^{-1}d^2/dx^2 + g_{eff}^{\pm}\delta(x)]\psi(x) = E\psi(x)$, to give these expressions. The effective coupling g_{eff}^{+} characterizes the combined effect of the harmonic confinement and pseudopotential coupling as a 1D zero-range interaction given by $g_{eff}\delta(x)$. In oscillator units, the effective coupling is related to the scattering length a_{1D} by $g_{eff} = -1/(ma_{1D})$ where the scattering length is $a_{1D} = -\lim_{k\to 0}\frac{\phi(k)}{k}$ with $\phi(k)$ as the phase shift of the asymptotic form of solution. The interplay of the harmonic oscillator and the delta pseudopotential is expected to give rise to new bound states for this system.

Born Approximation

As an initial test to check if the different methods are in agreement, we compare the results from the three methods with Born approximation.

For this 1D scattering problem the reflection coefficient using Born approximation is given by

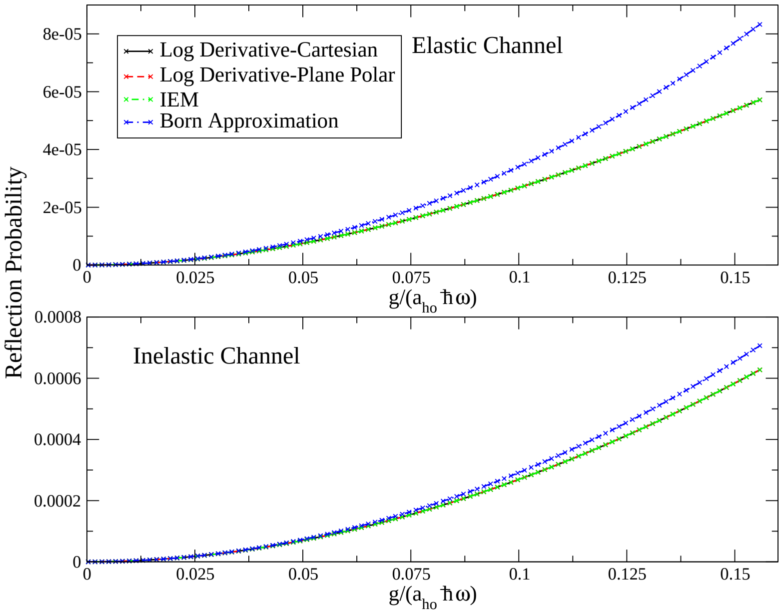

Figure 3.8: Born Approximation for elastic and inelastic collision. Comparison of the three methods - IEM, Log Derivative Propagation in Cartesian and plane polar coordinates.

$$R_{If} = \frac{m}{i\sqrt{k_I k_f}} \left| \int_{\infty}^{\infty} \int_{\infty}^{\infty} \psi_I(x_A, x_I) g\delta(x) \psi_f(x_A, x_I) dx_A dx_I \right|^2 \tag{3.52}$$

where $\psi_I(x_A, x_I)$ and $\psi_f(x_A, x_I)$ are the asymptotic incoming and outgoing wavefunctions. They are the product of the wavefunction of the two particles. Reflection coefficient is calculated for elastic and inelastic collision. As an example, we take an energy of $E/(\hbar\omega) = 1.6$ for a system of Na atom and Ca$^+$ ion, with mass ratio $m = 0.57$. The ion is in an initial state $n_I = 1$ of the trap.

The reflection coefficient for the elastic channel is $R_{11} = |r_{11}|^2$ and $R_{10} = |r_{10}|^2$. As one might expect, it is seen that the reflection coefficients calculated with the three methods for elastic and inelastic channels agree very well with the Born approximation at low pseudopotential couplings. The Born Approximation is not a valid approximation for the scattering amplitude at larger values of the coupling g.

Resonance and Threshold Features

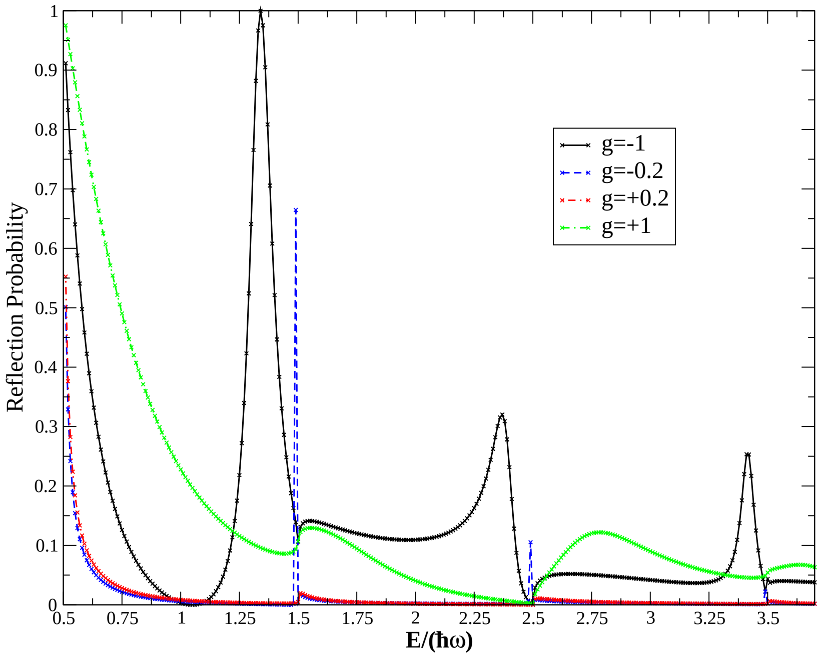

Figure 3.9: Resonance peaks and threshold features in the summed reflection probability for various values of coupling g.

In Fig.3.9, the summed probability over all open channels with the ion initial state as the oscillator ground state and N_{op} is the number of open channels. For an incoming channel of $n_I = 0$, resonance peaks are observed for negative pseudopotential couplings i.e for positive 1D scattering lengths. In 1D systems, the scattering length a_{1D} is related to the pseudopotential coupling g by $g = -2\hbar^2/(\mu a_{1D})$, for a system of reduced mass μ. The scattering quantities in Fig.3.9 are seen to obey Wigner laws near zero collision energy i.e when total energy $E \to (n + \frac{1}{2})$. To further illustrate the threshold phenomenon at new channel openings we plot the reflection probability in each open channel, with $g = -1$. From Fig.3.10, as the collision energy crosses the threshold for a new channel i.e an excited harmonic oscillator state, we notice a new transition probability evolves from zero at the threshold energy. The resonance peaks occurring at energies $E > 1.5\hbar\omega$ can now be decomposed into contributions arising due to transitions to different open channels like R_{01}, R_{02} and R_{03} in this case.

The asymptotic property of the even and odd total parity elastic scattering amplitudes f^+_{nn} and f^-_{nn} for the nth channel with infinitesimal collision energy go as [90]

$$f^+_{nn} \sim -1 + \mathrm{O}(k_n) \qquad \text{and} \qquad f^-_{nn} \to 0 \tag{3.53}$$

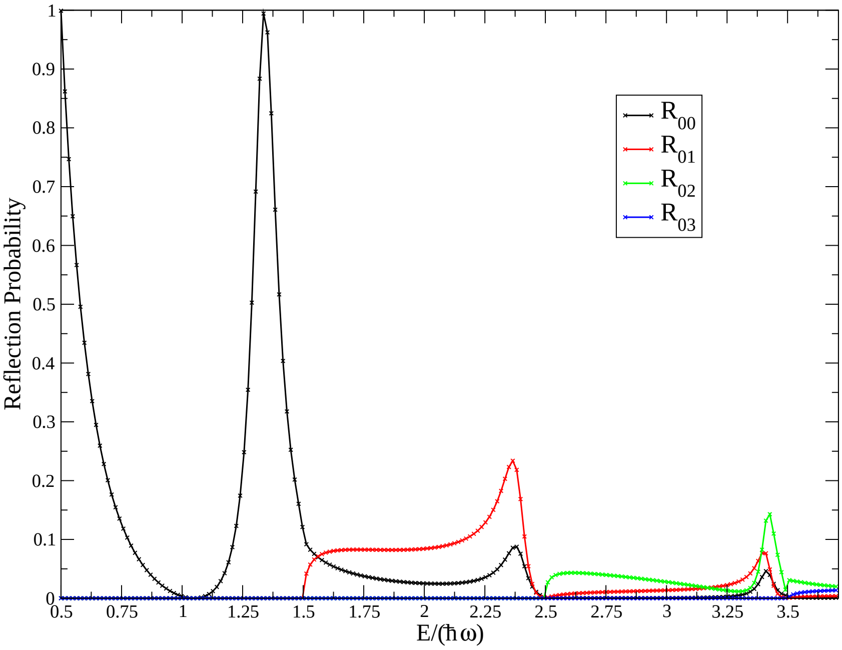

Figure 3.10: Resonance peaks and threshold channel openings for state-to-state reflection probability at coupling $g = -1$.

It is easy to see from the above that the particle will be reflected with probability ≈ 1 at thresholds where collision energy goes to zero and odd scattering amplitude goes to zero. As total energy increases, new channels open i.e with larger energy the ion has a probability to end up in one of the open excited state of the oscillator. From [90], the even and odd total parity scattering amplitudes to newly opened inelastic channels n' are given by $f^{\pm}_{nn'} \sim k_{n'}$.

It is interesting to note that since the scattering amplitudes $f^{\pm}_{ij}$ are dependent on total parity, the behaviour of the elastic channel threshold laws change depending on the parity of the harmonic oscillator state in the elastic channel. For example, since $n_I = 0$ state of the oscillator has positive parity, the threshold laws in the elastic channel hold as explained in Eq.(3.55) for $E_{coll} \approx 0$ but for a low collision energy and $n_I = 1$ as the incoming channel, the threshold laws in the elastic channel for positive and negative total parities are reversed, that is

$$f^{+}_{nn} \to 0 \qquad \text{and} \qquad f^{-}_{nn} \sim -1 + \mathrm{O}(k_n) \tag{3.54}$$

To continue the study on these lines, we decompose the resonance-like peaks into contributions from the even and odd total parity scattering amplitudes $f^{+}_{nn'}$ and $f^{-}_{nn'}$. These can be constructed using the resulting K-Matrix from the log derivative propagation and using Eq.(3.49). In order to study the first resonance peak in Fig.3.10, arising from the elastic channel, we plot f^{+}_{00} and f^{-}_{00}, calculate the

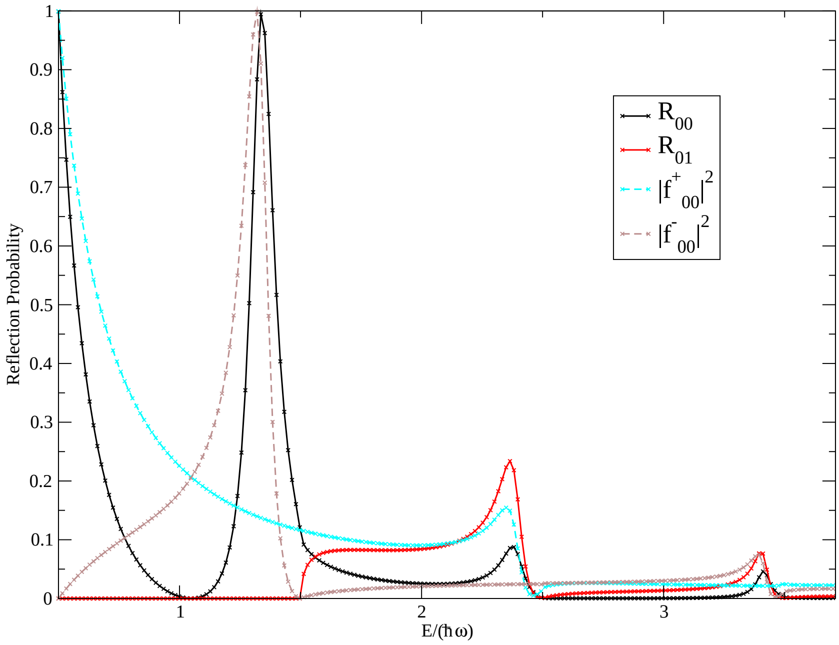

Figure 3.11: Reflection in the elastic channel R_{00} and contribution of f^+_{00} and f^-_{00} to the resonances-like peaks.

reflection coefficients $R_{00} = |f^+_{00} - f^-_{00}|^2$. A pattern of alternating parity dependence of the different resonance peaks is observed. The first peak in the elastic channel is seen to have contribution from the negative parity f^-_{00}. The delta potential affects only the positive parity (s-wave) during scattering, yet in this case a contribution from the negative parity f^-_{00} is observed. This is due to the fact that the total parity of the problem can be decomposed into parities along the two coordinates X and x. Though the grid along the X-axis is symmetrized, propagation is done with different initial conditions for different parities along the x-axis. This coupling between the centre-of-mass and relative coordinates results in a negative parity contribution to resonance peaks at low energies. Analyzing the time delay involved with such peaks will confirm if they arise out of resonant interaction.

Olshanii [86] predicts that with delta potentials the odd parity scattering amplitude $f^-_{nn} \to 0$, indicating only an even parity contribution for resonances observed at positive scattering lengths. It is also reported for short range neutral atom scattering [88]. The elastic channel resonance at low energy is seen to have a contribution from negative parity f^-_{00}. Granger et al. [89], show that this case is analgous to a p-wave contribution. They report on the collision of two spin-polarized fermions in quasi-1D, under 3D free-space p-wave scattering which can be mapped to a system of two 1D bosons in collision and resulting in a contribution of only the odd parity scattering amplitude to resonance at low energies.

Time Delay of S-Matrix

Resonances have a dependency on energy that goes as a Lorentzian function, with the characteristic peak. In the ultracold regime however the Lorentzian is modified due to background scattering. To help conclusively confirm such peaks as resonances, it is instructive to calculate the time delay matrix $Q^{\pm}$, from the S-Matrix [91]. The time delays for resonances show up as broad positive peaks in delay time, as function of energy. The time delay matrix is a derivative of the S-matrix with energy, for each parity. It is given by

$$Q^{\pm} = -i\hbar (S^{\pm})^{\dagger} \frac{dS^{\pm}}{dE}. \tag{3.55}$$

The time delay matrix is obtained using only the open channel S-matrix. The eigenvalues of the time delay matrix are the delay times, which essentially indicate phase is accumulated by the outgoing particle due to scattering. The delay time can be positive or negative. A positive delay time indicates a positive phase accumulated by the particle i.e it is *slowed* down by the scatterer due to attractive potential. This generally indicates a bound state or molecular resonance-like feature. Conversely, a negative delay time indicates the is particle accelerated and thus accumulates negative phase. It indicates repulsive potential in the scattering.

The diagonal elements correspond to elastic channels i.e in this model system the ion remains in the same oscillator state. The off-diagonal elements of the S-matrix indicate inelastic processes and the total delay time for a given incoming channel can be obtained as explained in [91]. The delay-time matrix can be built with from parity-specific S-matrices from the relation $\Delta t = Re\left[-i\hbar (S^{\pm})^{-1} dS^{\pm}/dE\right]$. The matrix elements Δt_{ij} are time delays of a particle in the incoming channel i and outgoing channel j. Thus the total time delay in the presence of inelastic transition probabilities is obtained as a sum of the time delays over all open channels weighted by the probability of the j^{th} outgoing channel, for an incoming channel i, given by $\langle \Delta t_i \rangle = \sum_j |S_{ij}|^2 \Delta t_{ij} = Re\left[-i\hbar \sum_j S^{\dagger}_{ij} dS_{ij}/dE\right]$.

The eigenvalues of the life time matrix $Q^{\pm}$ are thus the time delays (eigenlifetimes) in the elastic channels. We plot the maximum eigenvalue for a given incoming channel, for each parity separately against energy and we find resonances show a broad positive bell-shaped profile in time delay. The S-matrix is unitary such that $S.S^{\dagger} \approx \mathbb{I}$, thus $S.S^{\dagger}$ has very low values for the off diagonal elements (usually less than 1×10^{-10} for very well-converged calculations). Thus we take only the real parts of the time delay (eigenlifetime) matrix $Q^{\pm}$.

We plot the eigenvalue at points before the $n = 1$ threshold and two largest

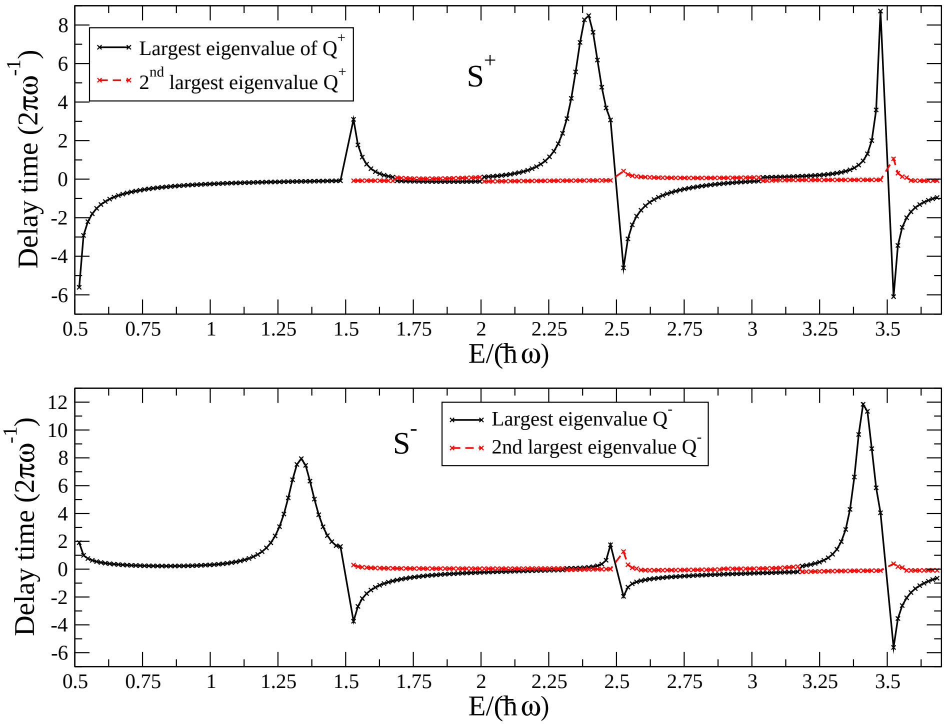

Figure 3.12: Delay time (eigenlifetime) indicating the peaks are of resonant nature. Two largest eigenvalues of +parity time delay matrix Q^+ (top panel) and -parity time delay matrix Q^- (bottom panel).

eigenvalues before the $n = 2$ threshold. The resonances showed contribution from one of the parities and these peaks are at fixed distance from thresholds in Sec.3.2. Similarly they show clear parity dependence even in this case. The first peak in the elastic region at low energies before the $n = 1$ threshold is seen to have a negative parity delay time. Sharp discontinuities in delay times are observed at thresholds that occur at $E = (n + 1/2)$ with $n = 1, 2, 3, \ldots$

Dependence on Mass Ratio

The numerical approaches used can accommodate the use of a wide range of mass ratios, as seen in Fig.3.13. The numerical methods used are stable and guarantee a relative error of $\leq 10^{-5}$ with larger mass ratios. As a test parameter, the relative error is taken on the off-diagonal elements of the K-matrix at an arbitrary energy and two open channels. K-matrix elements are ensure to be converged and stable with respect to grid and other input parameters when calculating the relative error. The diagonal elements are also seen to guarantee a relative error of $\leq 10^{-5}$ with larger mass ratios.

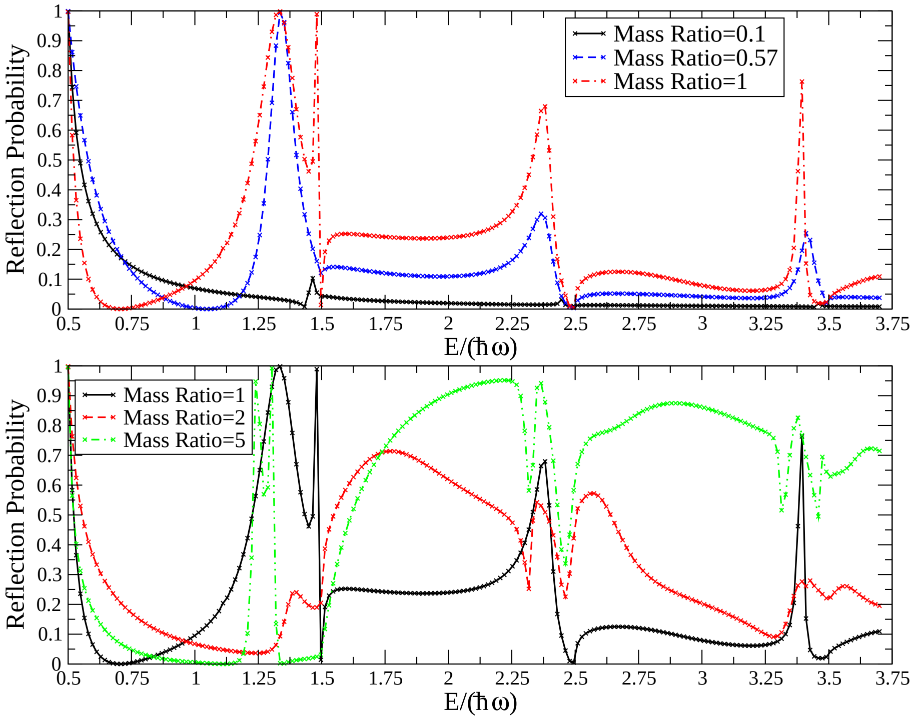

Figure 3.13: Resonances and Threshold phenomena for $m \leq 1$ (top panel)and $m \geq 1$ (bottom panel), ion initial state $n = 0$ and coupling $g = -1$.

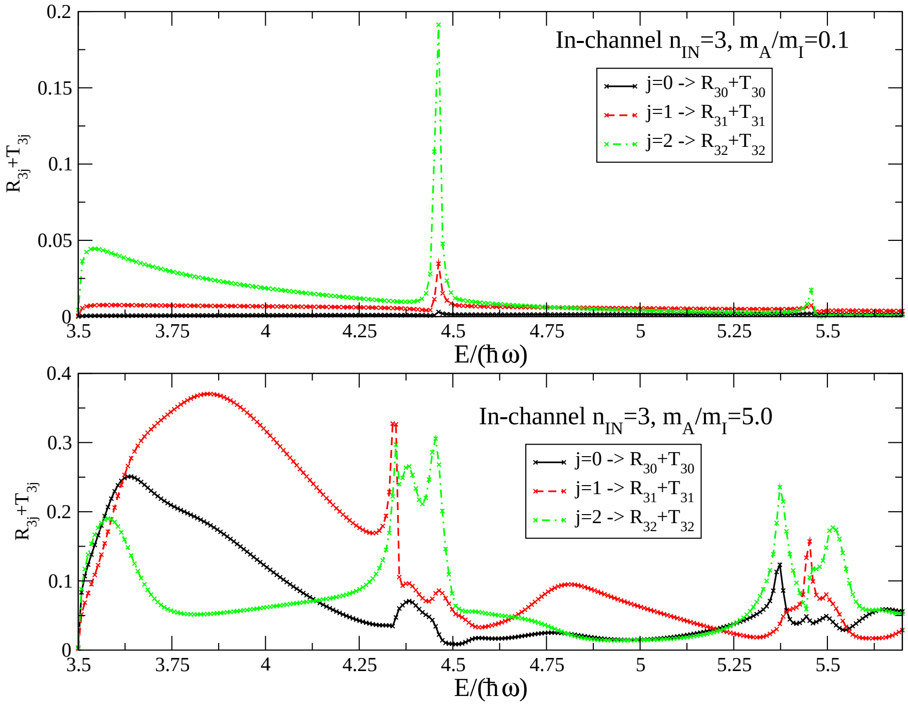

Figure 3.14: Total relaxation transitions of ion from initial state $n = 3$. mass ratio $m_A/m_I = 0.1$ (upper panel), $m_A/m_I = 5$ (lower panel).

The plots are made for $g = -1$ and ion in an initial state $n_I = 0$. The reflection coefficient taken in Fig.3.13 is $R_0 = \sum_{j=0}^{N_{\text{op}}} |r_{0j}|^2$, with N_{op} number of open channels.

To better illustrate the effect of mass ratio on the probability of decay of the ion to lower states in the oscillator, we show the probability of the ion relaxation to lower trap levels if the ion starts in an excited state. It is instructive to plot the sum of the state-to-state reflection and transmissions coefficients for each lower open channel, with the ion in an initial state $n_I > 0$. The plots in Fig.3.14 are made for two steep mass ratios of $m = 0.1$ and $m = 5$ and with ion in an initial state $n_I = 3$.

For large mass ratios ($m_A >> m_I$), ion has comparatively greater probability of relaxation to lower trap levels. Lighter ion tends to cool more efficiently in this model with a delta pseudopotential. At low collision energies, far from thresholds and resonances ($3.5\hbar\omega < E < 4.5\hbar\omega$), the ion tends to decay to states with same parity as the incoming channel. $n = 3$ and $n = 1$ are negative parity ion states.

Zero Energy Resonances as Signatures of Bound States

Since we would like to look for zero-energy resonances, the calculation is done at a low total energy $E \to 0$, thus the complex amplitudes f^+ and f^- are scalar (not a matrix). We plot $g^{\pm}_{eff}$ calculated as a function of pseudopotential coupling g at low total energies $E \approx 0$. The effective couplings g^+_{eff} and g^-_{eff} as a function of pseudopotential coupling g at low energies show signatures of bound states arising at negative couplings g, in Fig.3.16. They form a two particle complex at negative energies, arising due to the combined effect of pseudopotential coupling g and harmonic oscillator potential. These signatures show up as zero crossings of the symmetric effective couplings g^+_{eff} and divergences of the anti-symmetric effective couplings g^-_{eff}, in Fig.3.15. It is seen in the plot that these signatures coincide with values of the x-axis intercept (coupling g) of bound states, indicating a signature of underlying molecular levels at negative energies. These resonances that show up at $E \approx 0$ coincide with the location of the bound states and evolve further into resonances that are dependent on physical parameters (trapping geometry and potential). It is also noted that the positive (negative) parity zero-energy signatures correspond to positive (negative) parity bound states. The bound states calculated are largely influenced by the parity characteristics of harmonic oscillator levels since a negative delta potential alone has only one bound state. Upon closer examination, more than one bound states are found for a given value of g, in Fig.3.16. So the multiple bound states are in essence a contribution of the harmonic oscillator to the effective coupling. These bound states are seen to follow the parity of harmonic oscillator states since on comparison with zero energy resonances, it is see that the resonance structures in the g^+_{eff} follow the parity ordering of harmonic oscillator levels.

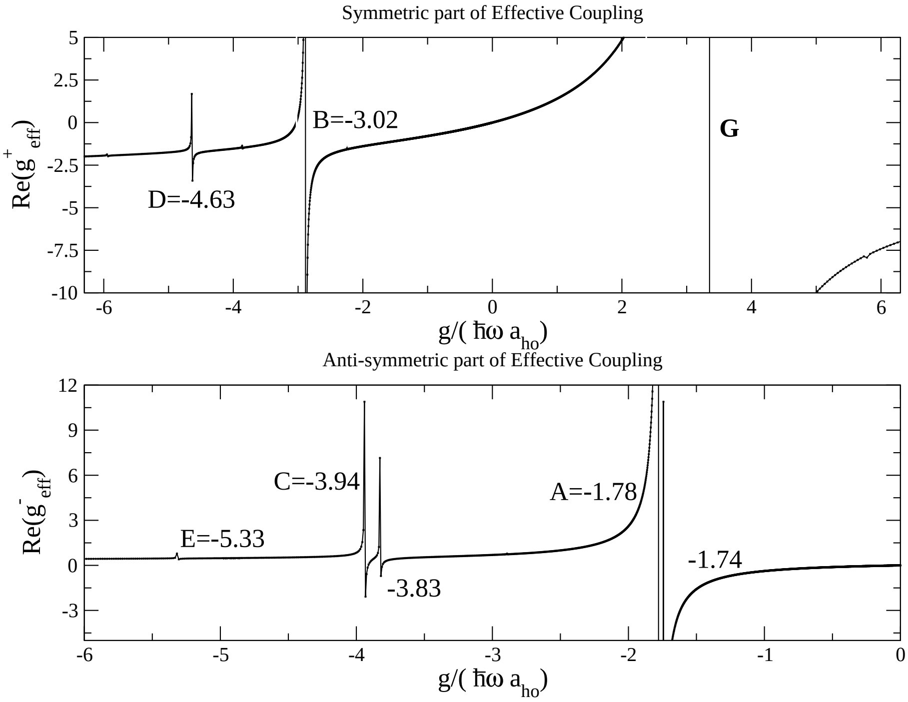

Figure 3.15: Zero-Energy Resonances observed in g_{eff}, plotted separately for symmetric (top panel) and anti-symmetric (bottom panel) cases.

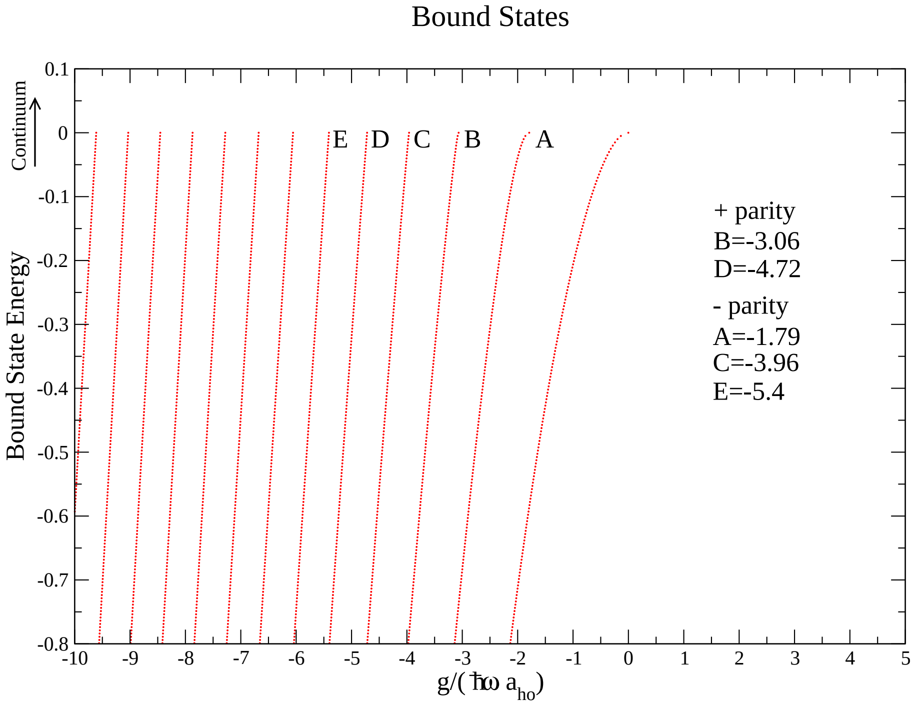

Figure 3.16: Bound States of the two particle complex

The divergence of g^{+}_{eff} labelled G at positive coupling constant is the position where $a_{1D} = 0$ and thus shows up as a divergence in g_{eff}.The bound states are generated using the integral equation method and the zero-energy resonances with the log derivative method.

3.3 Conclusions

Thus we have presented three different methods to solve the Schrödinger equation for a collision problem of an ion in a harmonic potential and a free atom in 1D. The numerical characteristics of log derivative method is well documented in literature since it has been in use over many years. The limitation of Integral Equation Method (IEM) due to the infinite summation term of Green's function term in the kernel, is explained in Sec.3.1.1.1 and efforts were ensured to get converged results with respect to the number of states taken in the summation term when using this method. We also made a comparison of IEM with finite or lower order grid methods to highlight the super-algebraic convergence of the method.

Foreseeing possible limitations (in Sec.3.1.3) in solving the Schrödinger equation over a range of mass rations with linear log derivative method, a solution in an alternate coordinate system is presented. The use of linear log derivative method is limited to a small range of mass ratios $m = m_A/m_I$ and use of this geometry for larger mass ratios will require very large grid and matrix sizes. Instead, propagation in plane polar coordinate is proposed, with proof provided that the matrix representation of the Hamiltonian is symmetric. It is thus seen in the results section that angular propagation is indeed robust over a fairly wide range of mass ratios.

To conclude it is noted that study of 1D collision of a free particle and a trapped particle reveals rich underlying physics of confinement induced resonance-like structures even with a simplified delta pseudopotential. The study of such confinement induced effects will help in tailoring cold atom experiments in low dimensions and to exploit the intrinsic scattering characteristics arising out of the geometry. The existence of zero-energy resonances further serves to illustrate fundamental principles of bound and scattering states and the interplay of the two at the zero-energy interface. The collision problem is shown to exhibit relaxation probability of the trapped particle (ion) to lower states and the influence of mass ratio on this relaxation probability is discussed.

Chapter 4

One Dimensional Atom-Ion Collision with Micromotion

The study of collision of a free atom and a particle (ion) in a time independent harmonic trap was described in Ch.3. Fundamental electrostatics states that no charged particle can be held in a stable equilibrium by a stationary, time independent configuration of charges and(or) fields. This is other wise known as *Earnshaw's Theorem* [101]. This condition also arises due to the fact that any general potential Φ used to confine ions have to fulfill the Laplace equation $\nabla^2\Phi = 0$. Owing to this fact an ion can only be dynamically contained in a given volume of space using time dependent fields. Due to the time dependent nature of such a trap, the dynamics of an ion is not harmonic but is composed of multiple frequencies. Though the time averaged motion of an ion is nearly harmonic, it shows high frequency oscillations on a smaller time scale superimposed on the harmonic motion on longer time scales called *secular* motion. This short time scale, high frequency motion of the ion is called the *micromotion*. The classical and quantum dynamical equations of an ion in such a model time dependent potential is explained in Appendix A. We study the one dimensional of an ion in such a time dependent rf-trap and a free atom. The system can be modelled in experiments in a manner similar to that explained in Ch.3. The harmonic trapping potential is seen to have a high frequency time dependency apart from the static quadratic term, as shown in Fig.4.7. The long range atom-ion potential that goes as $\sim 1/r^4$ is modelled by a zero range delta pseudopotential in this model.

The quantum mechanical description of a single trapped ion in such a trapping potential was elegantly derived by Glauber [52] and is presented in Appendix.A.2. Following Glauber's description of a single ion, the chapter is started with an explanation of the general idea of ion traps and energy spectrum of an ion in a time dependent Paul trap. We then describe the one dimensional collision model used and the Fourier-Floquet Decomposition used to convert the time dependent problem from time domain to frequency domain, followed by the solution schemes attempted in Cartesian and plane polar coordinates respectively. A comparison of a realistic long range atom-ion polarization potential and the delta pseudopotential is provided. The chapter concludes with a discussion of results to study the effect of micromotion on scattering in confined geometry. The effect of micromotion in cooling (and/or hearing) of the ion is discussed. The limitations of the methods used are also explained.

4.1 Ion Traps and the Floquet Spectrum

The time dependent electric potential for the ion is taken to be a static harmonic potential superimposed on a time varying harmonic potential going as $\cos(\omega_{rf}t)$.

$$V_{el}(x,y,z,t) = U\frac{1}{2}(\alpha' x^2 + \beta' y^2 + \gamma' z^2) + \tilde{U}\cos(\omega_{rf}t)\,\frac{1}{2}(\alpha'' x^2 + \beta'' y^2 + \gamma'' z^2) \tag{4.1}$$

where $\alpha', \alpha'', \beta', \beta'', \gamma'$ and γ'' are dimensionless quantities. This potential has to fulfill Laplace equation $\nabla^2\Phi = 0$, which gives the conditions

$$\alpha' + \beta' + \gamma' = 0 \quad \text{and} \quad \alpha'' + \beta'' + \gamma'' = 0 \tag{4.2}$$

These conditions decide the configuration of the trapping field to be used in three dimensions. A choice of

$$\alpha' = \beta' = \gamma' = 0 \quad \text{and} \quad \alpha'' + \beta'' = -\gamma'' \tag{4.3}$$

gives a purely time dependent three dimensional confinement with an aspect ratio 1:2 in the $\hat{x}(\hat{y}) : \hat{z}$ axes. A choice of

$$\alpha' + \beta' = -\gamma' \ ; \ \ \gamma' > 0 \quad \text{and} \quad \alpha'' = -\beta'' \ ; \ \ \gamma'' = 0 \tag{4.4}$$

gives dynamical confinement in the $\hat{x}$ and $\hat{y}$ axes and static confinement in the $\hat{z}$ axis, caused by a static electric field. This configuration is called a Paul trap. This results in ion trapping at the saddle point of the potential, as shown in Fig.4.1. For studying the case of collision in one dimension, we take the electric potential to be of the form

$$V_{el}(x,t) = \frac{1}{2}\left[U\alpha' + \tilde{U}\cos(\omega_{rf}t)\alpha''\right]x^2 \tag{4.5}$$

The solution of ion dynamics in a potential of type in Eq.(4.5) is provided in Appendix A.1. The quantum potential for an ion in a 3D Paul trap in Cartesian coordinates is separable. The potential along the $\hat{x}$-axis is given by

$$V_{HO}(x,t) = \frac{1}{2}m_i\frac{\omega_{rf}^2}{4}\left[a_x + 2q_x\cos(\omega_{rf}t)\right]x^2 \tag{4.6}$$

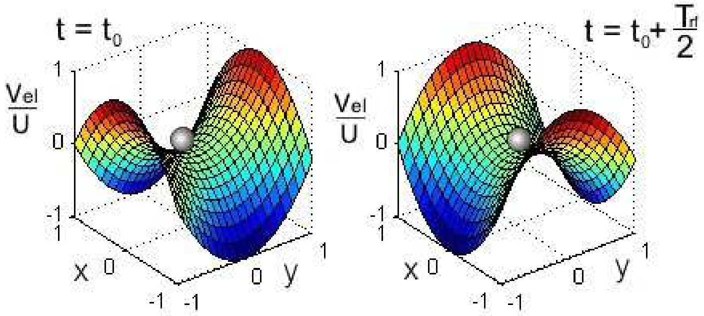

Figure 4.1: Time dependent electric potential of a Paul trap. Ion is dynamically trapped in the saddle point

where a_x and q_x are dimensionless parameters that dictate the static and time dependent components of the harmonic potential. As has been explained in Appendix.A.1 and [102], a_x and q_x are given by $a_x = 4U\alpha'/(m_I\omega_{rf}^2)$ and $q_x = 2\tilde{U}\alpha''/(m_I\omega_{rf}^2)$. They are related to experimentally valid parameters namely the static and rf voltages U and $\tilde{U}$, frequency ω_{rf}, ion mass m_I. The resulting Schrödinger equation belongs to a general class of differential equations with time periodic coefficients called Mathieu Equation. The general solutions for these differential equations follow from the Floquet Theorem (See 117, 119, 120). The ion wavefunctions are taken to be Floquet solutions of a general form

$$\Psi(x,t) = e^{-i\frac{E}{\hbar}t}\phi(x,t) \tag{4.7}$$

where E are the ion quasi-energies and the function $\phi(x,t)$ is time periodic with a period $T = 2\pi/\omega_{rf}$. The Floquet type ion solutions satisfy the time dependent Schrödinger equation, with a general time dependent Hamiltonian term $H(t)$. The Hamiltonian for the one dimensional collision of an ion in a 1D Paul trap and a free atom is discussed in Sec.4.2. Substituting Eq.(4.7) into the time dependent Schrödinger equation,

$$i\hbar\frac{\partial}{\partial t}\Psi(x,t) = H(t)\Psi(x,t) \Rightarrow \left[H(t) - i\hbar\frac{\partial}{\partial t}\right]\phi(x,t) = E\phi(x,t) \tag{4.8}$$

We note in Eq.(4.7) that for any integer n', we have

$$\Psi(x,t) = e^{-i\frac{E}{\hbar}t}\phi(x,t) = e^{-i(\frac{E}{\hbar}-n'\omega_{rf}+n'\omega_{rf})t}\phi(x,t) = e^{-\frac{i}{\hbar}(E+n'\hbar\omega_{rf})t}\left[\phi(x,t)e^{-in'\omega_{rf}t}\right] \tag{4.9}$$

Thus the two states $\phi(x,t)$ and $\phi(x,t)e^{-in'\omega_{rf}t}$ are identical except that their eigenvalues are E and $E + n'\hbar\omega_{rf}$ respectively. Thus ion spectrum has a modulo $\hbar\omega_{rf}$ structure, very similar to that of Brillouin zones for electrons in solids. The details of classical and quantum equations of motion of the ion are given in

Appendix.A. It is shown in Appendix.A.2 that the ion quasi-energies are given by $E = (n + 1/2)\hbar\omega_{sec}$, where the modified frequency is referred to as a *secular* frequency $\omega_{sec} = \beta\omega_{rf}/2$. β is the characteristic exponent of the classical solution of the Mathieu type differential equation (See Eq.(A.7) in Appendix.A.1). The ion spectrum shows the characteristics of a harmonic oscillator of *effective* frequency ω_{sec} but it ranges over $[-\infty, +\infty]$. It can be seen that the ion frequency is composed of self-similar *copies* of oscillator states, each separated by integer multiples of $\hbar\omega_{rf}$. For convenience we label a set of distinct oscillator states with the spectrum $(n + \frac{1}{2})\hbar\omega_{sec}$ as *manifolds*. The total ion spectrum is then given by $(n + \frac{1}{2})\frac{\beta}{2}\hbar\omega_{rf} + n'\hbar\omega_{rf}$, where n' is the manifold index that gives the multiple self-similar copies of a manifold of states (See Fig.4.2).

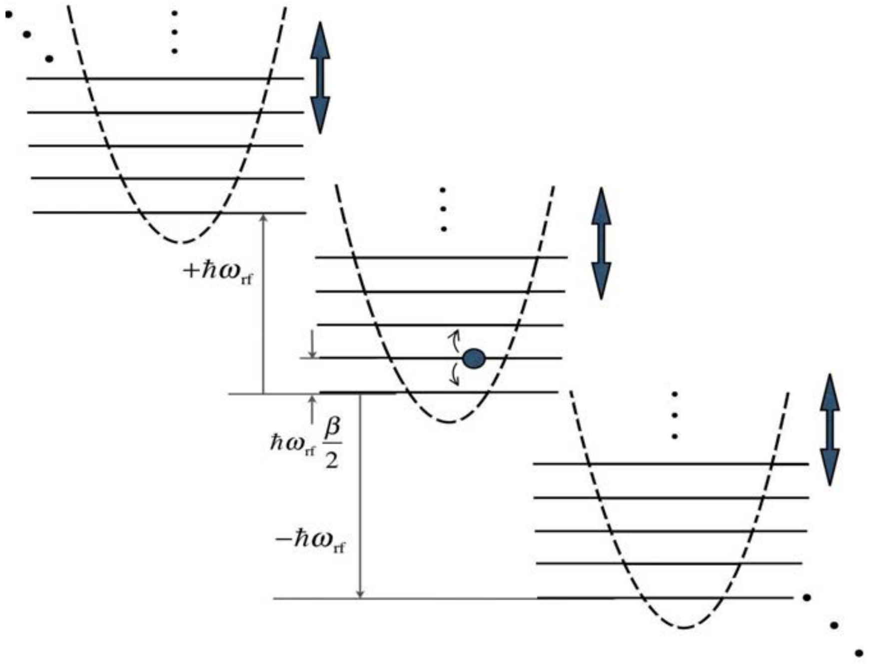

Figure 4.2: Ion spectrum in a time-dependent Paul trap potential. The spectrum shown is for the case when $\beta << 1$, resulting in energy scales $\hbar\omega_{sec} << \hbar\omega_{rf}$.

The time dependent term in the potential in Eq.(4.6) is responsible for dynamical trapping which also manifests as micromotion. The analytical wavefunction for an ion in such a potential was originally derived by Glauber [52](See also 53, 54, 102 p.39). The Mathieu characteristic exponent β must be real to have confined ion trap states. The values of a and q that give real values of β is shown in Fig.A.1. Fig.4.3 illustrates the classical trajectory of the ion as a function of time in one dimension for different values of Mathieu parameters a and q.

Micromotion parameter q can be taken as a perturbation of the time indepen-

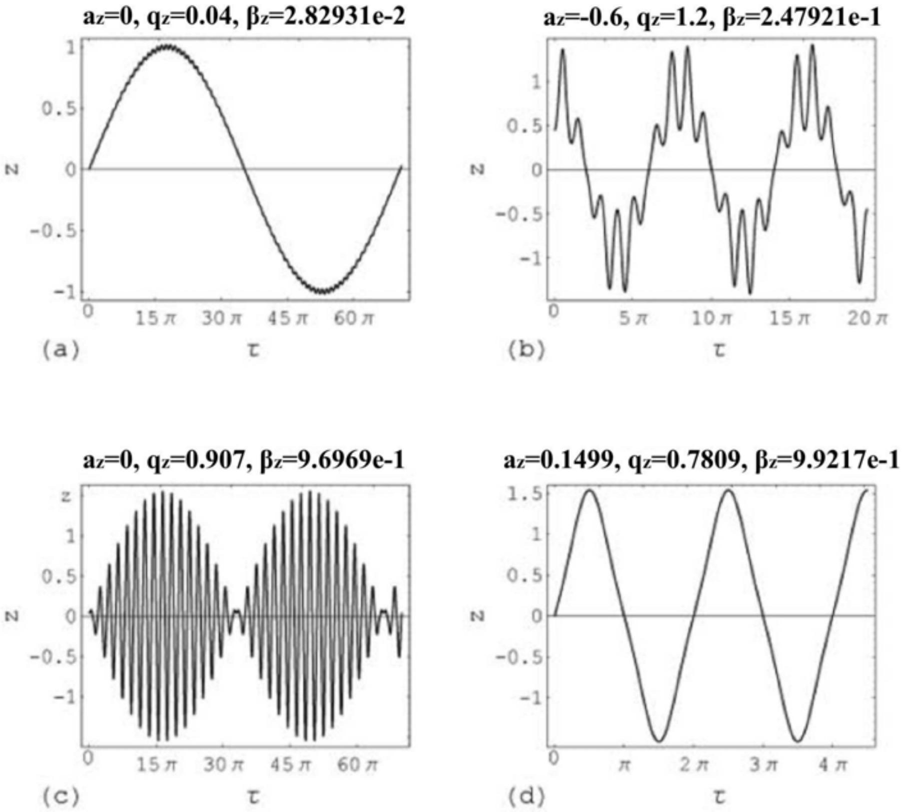

Figure 4.3: Ion motion in 1D shown for different a and q. $\tau = \omega_{rf}t/2$. Image taken from [102] p.22.

dent harmonic potential in the limit that $|a| << 1$ and $q^2 << 1$ (called the *lowest order approximation*) and in such cases the micromotion can be viewed as *breathing* oscillations of the ion wavefunction. As shown in Fig.A.1, when $a = 0$ only q contributes to confinement and in practical ion traps to obtain 3D trapping of ion, the condition in Eq.(4.4) restrains the trap operation to values of $a \to 0$ in the $\hat{x}$ and $\hat{y}$ axes, which gives values of $q_x, q_y \in [0, \pm 0.9]$. This gives values for $\beta < 1$ and since secular harmonic oscillator has energy scales of $\beta\omega_{rf}/2$, it results in a very small level spacing in a manifold of oscillator states i.e increases the density of states within the manifolds.

An interval of energy $[0, \hbar\omega_{rf}]$ is seen to be composed of states that show an oscillator spectrum $(n + \frac{1}{2})\hbar\omega_{sec}$ and $n' = 0$ i.e with the band character of the first Brillouin zone (manifold). But there are also energy levels in this interval corresponding to states of very highly excited character, belonging to harmonic oscillators that have been shifted in energy by $-n'\hbar\omega_{rf}$ where $n' > 0$ i.e highly excited states of the $-(n')^{th}$ manifold. As shall be explained later, the present calculation can be numerically converged only in the presence of at least a weak static confinement $a \geq 0.5$.

4.1.1 Ion Wavefunction - Micromotion Effect

Analytical expression for the time dependent wavefunction, as derived by Glauber [52] has been presented briefly in Appendix.A.2. The ion wavefunction for a oscillator state $j \in [0, \infty]$ from Eq.(A.19) is given by

$$\Phi_j(x_I, t) = \frac{1}{\sqrt{2^j j!}} \left(\frac{m_I \nu}{\pi \hbar}\right)^{1/4} \frac{\exp(-ij \arg[\varphi(t)])}{[\varphi(t)]^{1/2}} \\ H_j\left(\left[\frac{m_I \nu}{\hbar |\varphi(t)|^2}\right]^{1/2} x_I\right) \exp\left(-\frac{m_I \mu}{2\hbar}\left[1 - \frac{i\dot{\varphi}(t)}{\mu \varphi(t)}\right] x_I^2\right) \tag{4.10}$$

where $\mu = \beta/2$, $\varphi(t) = \sum_{n=-\infty}^{+\infty} C_{2n} e^{in\omega_{rf} t}$ and $\nu = \omega_{rf} \sum_{n=-\infty}^{\infty} C_{2n}(n + \beta/2)$ as explained in Appendix A.2. From the periodic nature of $\varphi(t)$ it follows that the ion wavefunction can be expressed as a Fourier series, composed of various harmonics. These Fourier series expanded functions are used in asymptotic matching (See Sec.4.3.1). The general form of the ion quantum wavefunction is similar to the solution of the ion's classical equation of motion in Eq.(A.13)

$$\Psi_j(x_I, t) = e^{-i\frac{E}{\hbar}t} \Phi_j(x_I, t) = e^{-i\frac{E}{\hbar}t} \sum_{n'=-\infty}^{+\infty} \tilde{\Phi}_j(x_I, n') e^{in'\omega_{rf} t} \tag{4.11}$$

where n' is the Fourier basis index, $\Phi_j(x_I, t)$ are the ion wavefunctions as derived by Glauber and $\tilde{\Phi}_j(x_I, n')$ are its Fourier series expansion. The ion secular oscillator quasi energies are $E = (j + \frac{1}{2})\beta\omega_{rf}/2$. The Fourier-Floquet expanded wavefunction $\tilde{\Phi}_j(x_I, n')$ is then given by

$$\tilde{\Phi}_j(x_I, n') = \int_0^{2\pi/\omega_{rf}} \Phi_j(x_I, t) e^{-in'\omega_{rf} t} dt \tag{4.12}$$

Classical solution of the Mathieu equation in Appendix.A.2 shows that the Fourier-Floquet spectrum of ion dynamics broadens with increasing micromotion parameter q. The usage of *low* micromotion is valid only when Fourier-Floquet spectrum of the ion is narrow i.e fewer Fourier terms in Eq.(A.4) are required to converge the series. At points closer to stability edge (boundary) of the stability plot in Fig.A.1 in the $a - q$ plane, the classical motion of the ion becomes more complicated (Fig.4.3, panel (c)). The phase space structure of the ion dynamics also becomes more complex, as seen in Fig.A.2. It means the ion classical trajectory gradually becomes anharmonic and is eventually expelled from the trap as one traverses across the stability edge in the $a-q$ plane.

This fact is not directly evident from the ion wavefunction. So the ground and first excited states of the ion wavefunction as a function of time are shown in Fig.4.4 to show that *low* micromotion is related distance of the operating point of the trap from the stability edge in any direction in the $a-q$ plane.

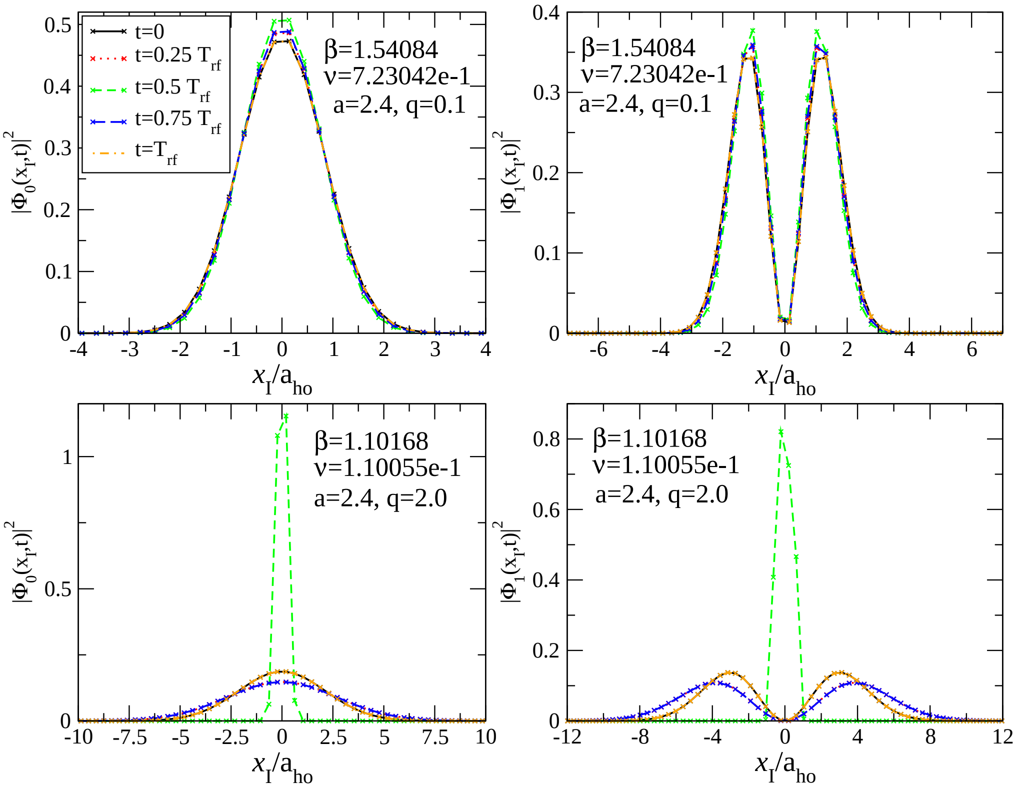

Figure 4.4: $|\Phi_0(x_I,t)|^2$ (left column) and $|\Phi_1(x_I,t)|^2$ (right column) from Eq.(4.10) at $a = 2.4, q = 0.1$ (top panels) and closer to stability edge at $a = 2.4, q = 2.0$ (bottom panels). 5 equally spaced snapshots of the wavefunction are taken in time over a period T_{rf} of the rf-field. At the edge of stability wavefunction cannot be represented on a grid at all times, thus loses normalization at $t = 0.5T_{rf}$ (in bottom left panel).

It is seen in Fig.4.4 that the ion shows low amplitude *breathing* modes at $q = 0.1$ (top panels). At $q = 2.0$ the ion wavefunction changes drastically at different points in a time period T_{rf} since its classical motion is more anharmonic at the stability edge and spreads out over a larger range. For a trap parameter of $a = 2.4$, ion has stable trapped modes over $q = [0, 2.065]$ and if $a = 0$, q ranges over $q = [0, 0.908]$. In experiments, 3D Paul traps operate at around $a \approx 0$, there is no static confinement and trapping is purely dynamical. In such cases, the ion is too delocalized to obtain converged numerical results for a scattering problem.

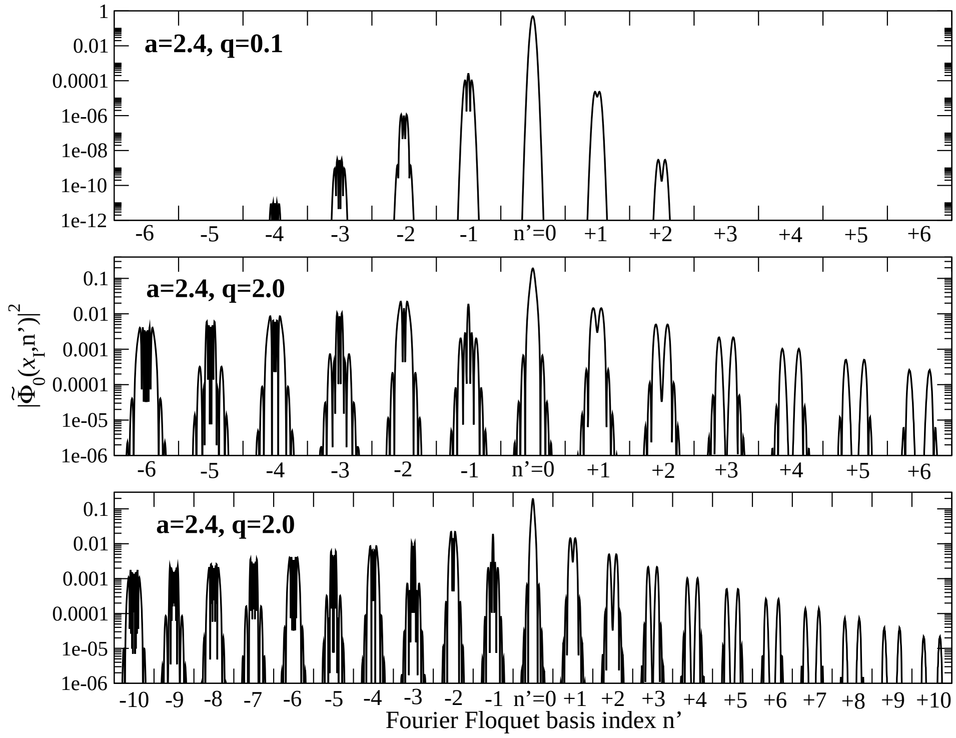

Figure 4.5: Fourier series expanded ground state ion wavefunction in Eq.(4.12) $|\tilde{\Phi}_0(x_I, n')|^2$ at $a = 2.4, q = 0.1$ (top panel) and closer to stability edge at $a = 2.4, q = 2.0$ (middle and bottom panel). Despite increasing the number terms, the Fourier series converges very slowly at the stability edge (bottom panel). Each Fourier-Floquet component has the full wavefunction grid plotted between the tick marks along x-axis. See Fig.4.6 for plots of individual Fourier-Floquet components.

The Fourier series spectrum of the ion quantum wavefunction is also narrow for *low* micromotion and the spectrum broadens for *large* micromotion in Fig.4.5. In Fig.4.5 ion probability in the high frequency components ($n' = \pm 6$ in top panel) is ≈ 0 at $q = 0.1$ but the same ($n' = \pm 6$ or ± 10 in middle and bottom panels) is large $\approx 1 \times 10^{-3}$ at $q = 2.0$. We will present results for two sets of trap parameters namely (a) tight static confinement with $a = 2.4, q \in [0, 0.908]$ and (b) for shallow static confinement with $a = 0.5, q \in [0, 0.473]$. The Fourier components of the ground state wavefunction relevant in the numerical calculations are shown in Fig.4.6.

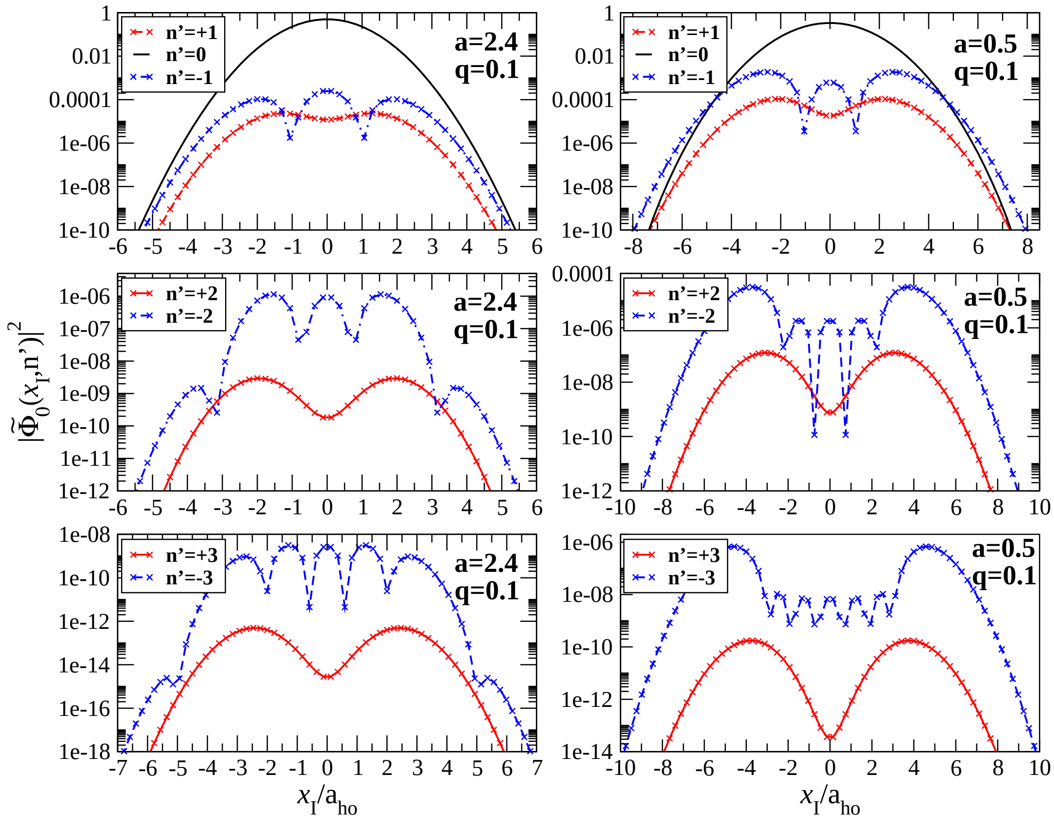

Figure 4.6: Relevant Fourier series components of the ion ground state wave-function $\tilde{\Phi}_0(x_I, n')$ for trap parameters of $a = 2.4, q = 0.1$ (left column) and $a = 0.5, q = 0.1$ (right column).

4.2 Atom-Ion Collision and Fourier-Floquet Decomposition

Atom-ion collision in 1D in such a time dependent potential is presented in this section. A schematic of such a collision in a time dependent harmonic trap for the ion is shown in Fig.4.7. The time dependent nature of the ion trapping potential and the resulting energy spectrum have been explained in Sec.4.1. It was shown that the oscillator energy level spacing $\hbar\omega_{sec}$ remains constant in time despite the potential varying with frequency ω_{rf}. As in Ch.3, the atom-ion potential is taken to be a delta pseudopotential. The pseudopotential is a good approximation to the realistic atom-ion potential if the length scale of the long range interaction is much smaller than the trap dimensions, which is characterized by the oscillator length a_{ho} corresponding to the secular trap frequency given by $a_{ho} = \sqrt{\hbar/(m_I\omega_{sec})}$. In reality the physics of the problem changes drastically when using a long range

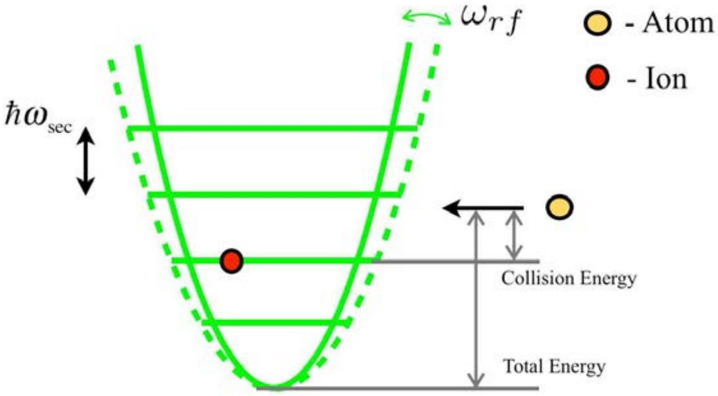

Figure 4.7: Atom-Ion collision with micromotion

polarization potential $C_4 r^{-4}$ in a tight trap [38].

4.2.1 Delta Pseudopotential Vs Long Range Potential

We compare the realistic atom-ion potential to the delta pseudopotential to put the study of this model system into perspective. The properties of the atom-ion polarization potential are well described in [38]. At large atom-ion separations, given by r the polarization potential is given by $V_{AI}(r) = -\alpha e^2/(2r^4) = -C_4/(2r^4)$. α is the polarizability of the atom, taken to be at the ground state for most calculations in literature. We adopt the same here.

This attractive potential between the induced dipole in the atom and the ion is characterized by a length scale within which the potential is larger than the centrifugal term $\hbar^2\hat{L}^2/(2mr^2)$ in the general Schrödinger equation for radial solutions in three dimensions. The characteristics of inter-particle separation in comparison with the centrifugal term are used to define the long range nature of the potential and the potential is considered to be zero if the separation is $r >> R^*$. This characteristic length for atom-ion polarization potential is given by $R^* = \sqrt{\alpha\mu e^2/\hbar^2}$, where the reduced mass of the system is $\mu = (1/m_A + 1/m_I)^{-1}$. Delta pseudopotential is a good approximation to the realistic long range potential only if the length scale characterizing the long range potential is much smaller than the ion trap size (oscillator length).

The calculations in this work are done for a model system composed of a Ca$^+$ ion and Na atom. From [106], the ground state polarizability of Na in atomic units is $\alpha_{Na} = 162.6a_0$ [106], with Böhr radius $a_0 = 5.2917 \times 10^{-11}m$. The reduced mass of the Na-Ca$^+$ system is $\mu = 2.6603 \times 10^4 m_e$ and a mass ratio $m = m_A/m_I = 0.57$ (which is used to make most of the plots explained in the results section). This gives a characteristic length of $R^* = 2075.983a_0$.

The properties of an ion trap are explained in Sec.4.1, thus we infer that the oscillator length pertaining to secular motion is the length scale to define the trap dimension. It is given by $a_{ho} = (m_I \beta \omega_{rf}/2)^{1/2}$. From the geometry of the ion trap potential in Eq.(4.4), 3D Paul traps have an aspect ration of 1:2 in the $\hat{x}(\hat{y} : \hat{z})$ axes. This gives a different values of $\beta_\perp$ and $\beta_\parallel$ for the two different Mathieu equations for the $\hat{x}(\hat{y})$ and $\hat{z}$ axes respectively. As an example, we take the trap parameters for Ca$^+$ as mentioned in [107]. This experiment reports measuring secular frequencies of the ion as $\omega_\parallel = 700kHz$ and $\omega_{perp} = 2MHz$. This gives secular oscillator lengths as $a_{ho,\parallel} = 896a_0$ and $a_{ho,\perp} = 530.5a_0$ in the longitudinal and transverse axes. Since R^* for a realistic $\sim r^{-4}$ atom-ion potential is much larger than the effective trap dimension, the potential cannot be approximated by a delta pseudopotential to give experimentally valid (quantitative) results. Thus the calculations done in this work are for a model system with micromotion.

4.2.2 1D Collision with Micromotion

We study the one dimensional collision problem of an ion in a potential time dependent potential and a free atom. The time dependent potential is taken to be of type in Eq.(4.6). In a manner similar to Eq.(3.2) but with static harmonic oscillator term is replaced by the potential in Eq.(4.6), we can write the time dependent Schrödinger equation as

$$\left[-\frac{\hbar^2}{2m_A}\frac{\partial^2}{\partial x_A^2} - \frac{\hbar^2}{2m_I}\frac{\partial^2}{\partial x_I^2} + \frac{1}{2}\frac{m_I}{4}\omega_{rf}^2[a + 2q\cos(\omega_{rf}t)]x_I^2 + g\delta(x)\right]\Psi(x_A, x_I, t)$$
$$= i\hbar\frac{\partial}{\partial t}\Psi(x_A, x_I, t) \quad (4.13)$$

where m_A, m_I are the atom and ion masses respectively, x_A, x_I are the atom and ion coordinate respectively. Rewriting the above in oscillator units, with energy in units of $\hbar\omega_{rf}$, lengths in oscillator length $a_{ho} = \sqrt{\hbar/(m_I\omega_{rf})}$, we have

$$\left[-\frac{1}{2m}\frac{\partial^2}{\partial \bar{x}_A^2} - \frac{1}{2}\frac{\partial^2}{\partial \bar{x}_I^2} + \frac{1}{8}[a + 2q\cos(\omega_{rf}t)]\bar{x}_I^2 + \bar{g}\delta(x)\right]\Psi(\bar{x}_A, \bar{x}_I, t) =$$
$$\frac{i}{\omega_{rf}}\frac{\partial\Psi(\bar{x}_A, \bar{x}_I, t)}{\partial t} \quad (4.14)$$

where $\bar{x}_I = x_I/a_{ho}$, $\bar{x}_A = x_A/a_{ho}$, $\bar{g} = g/\hbar\omega_{rf}$ and mass ratio is $m = m_A/m_I$. We replace $\bar{x}_I$, $\bar{x}_A$ and $\bar{g}$ by x_I, x_A and g for simplicity in notation. The time-dependent Schrödinger equation for this system in centre-of-mass and relative coordinates can be written as

$$\left[-\frac{1}{2M}\frac{\partial^2}{\partial X^2}-\frac{1}{2\mu}\frac{\partial^2}{\partial x^2}+\frac{1}{8}[a+2q\cos(\omega_{rf}t)]\left(X-\frac{m}{M}x\right)^2+g\delta(x)\right]\Psi(X,x,t) = \frac{i}{\omega_{rf}}\frac{\partial\Psi(X,x,t)}{\partial t} \tag{4.15}$$

where $X = (mx_A + x_I)/(m+1)$ is the centre-of-mass, the relative coordinate is $x = x_A - x_I$, $M = m+1$ is the total mass, the reduced mass is $\mu = [1/m+1]^{-1}$. The atom and ion coordinates in terms of the centre-of-mass and relatives coordinates are in turn given by $x_A = X + \frac{x}{M}$ and $x_I = X - \frac{m}{M}x$. We assume Floquet type solutions, given in Eq.(4.7), with a time periodic function $\Phi_n(X,x)$ and having the form as shown below

$$\Psi(X,x,t) = e^{-iEt/\hbar}\sum_{n=-\infty}^{+\infty} e^{in(\omega_{rf}t)}\tilde{\Phi}(X,x,n) \tag{4.16}$$

where n is the Fourier-Floquet basis index. The time dependent wavefunction is expanded in terms of Fourier components with the time independent solutions $\tilde{\Phi}(X,x,n)$ as the coefficients of expansion. The cosine term in Eq.(4.15) is expressed as $\cos(\omega_{rf}t) = (e^{i\omega_{rf}t}+e^{-i\omega_{rf}t})/2$. This leads to coupling terms $\delta_{n,n'+1}$ and $\delta_{n,n'-1}$ lead to exchange of $\hbar\omega_{rf}$ between the ion and the rf-field. Substituting it in Eq.(4.14), multiplying by $e^{-in'(\omega_{rf}t)}/\sqrt{T}$ and integrating over $[0,T]$ with respect to t, we have

$$\left[-\frac{1}{2M}\frac{\partial^2}{\partial X^2}-\frac{1}{2\mu}\frac{\partial^2}{\partial x^2}+\frac{1}{8}a\left(X-\frac{m}{M}x\right)^2+\bar{g}\delta(x)+n'\right]\tilde{\Phi}(X,x,n')+ \\ \frac{1}{8}q\left(X-\frac{m}{M}x\right)^2\tilde{\Phi}(X,x,n'+1)+\frac{1}{8}q\left(X-\frac{m}{M}x\right)^2\tilde{\Phi}(X,x,n'-1) = \bar{E}\tilde{\Phi}(X,x,n') \tag{4.17}$$

where $\bar{E} = E/(\hbar\omega_{rf})$. We denote $\bar{E}$ by E for notational simplicity. The first term on the left hand side is a diagonal term in the matrix representation of the Hamiltonian in the Fourier-Floquet basis (n' index) and the second term forms the $+1$ and -1 diagonals of the matrix. The infinite sum in Eq.(4.16) is truncated to a sufficiently large N_f in practice i.e $n = [-N_f, +N_f]$. Thus the time dependent Schrödinger equation in time domain is converted to a time independent Schrödinger equation in frequency domain. This equation is solved by Log Derivative Propagation (see Sec.2.3) in two system of coordinates namely (a) Cartesian Coordinates (b) Plane polar coordinates. Two different numerical approaches were attempted (a) Log Derivative Propagation algorithm (as explained in Sec. 2.3) (b) Spectral Element Method, where we do a one-shot calculation to get the R-matrix in the asymptotic region (see Sec.2.4).

4.3 Solution by Propagation in Cartesian Coordinates

It is seen from Eq.(4.17) that we have to propagate multiple blocks of the Hamiltonian, corresponding to each Fourier-Floquet component, indicated by the index n or n'. This increases the size of the propagated matrix drastically. The row and column indices are separated by a semi-colon henceforth, in this chapter. Let the solutions be given by $\tilde{\Phi}_i(X,x) = \sum_{i'} \phi_{i'}(X) F_{i';i}(x)$. $\phi_{i'}(X)$ are the DVR basis functions related to the grid point in X coordinate.
Following the method in Sec.3.1.2, we substitute these solutions in Eq.(4.17), multiply by $\phi_j(X)$ and integrate with respect to X, we get the second order equation solved by log derivative method. Eq.(4.17) initially discretized over the Fourier index n' is further discretized over the coordinate basis and thus develops composite indices where if row(column) indices are denoted by the grid point index $i'(j)$ and the corresponding Fourier index $n'(n)$. This equation for global row and column indices $i'n'$ and jn is written as

$$\frac{\partial^2 F_{i'n';jn}(x)}{\partial x^2} = \sum_{n'}\sum_{i'} \langle \phi_i(X) \,|\, W_{n;n'}(X,x) \,|\, \phi_{i'}(X)\rangle_X \, F_{i'n';jn}(x) \Rightarrow \mathbb{W}(x)\mathbb{F}(x) \tag{4.18}$$

where j is the solution index, $i(i')$ are grid point indices and $n(n')$ are Fourier-Floquet basis indices respectively. The term $W_{n;n'}(x,X)$ is in itself a matrix representation of the effective potential term in the Fourier-Floquet basis. The effective potential $\mathbb{W}(x)$ has matrix elements over a DVR basis $\phi_i(X)$, given by

$$\begin{aligned} W_{in;i'n'}(x) = {} & -\frac{\mu}{M}\delta_{nn'} \left\langle \phi_i(X) \left| \frac{\partial^2}{\partial X^2} \right| \phi_{i'}(X) \right\rangle_X + \delta_{ii'}\delta_{nn'} 2Mg\delta(x) \\ & + \frac{1}{8}(a\delta_{nn'} + q[\delta_{n,n'+1} + \delta_{n,n'-1}]) \left\langle \phi_i(X) \left| \left(X - \frac{m}{M}x\right)^2 \right| \phi_{i'}(X) \right\rangle_X + \\ & \delta_{ii'}\delta_{nn'}n' - \delta_{ii'}\delta_{nn'}2ME \end{aligned} \tag{4.19}$$

where the subscript indices are composite with $in(i'n')$ denoting the row(column) index. The structure of the $\mathbb{W}(x)$ is as shown in Fig.4.8.
The third term on the right side is diagonal since $\left\langle \phi_i(X) \left| \left(X - \frac{m}{M}x\right)^2 \right| \phi_{i'}(X) \right\rangle_X = \delta_{ii'} \left(X - \frac{m}{M}x\right)^2$. The log derivative matrix is given by $\mathbb{Y}(x) = \mathbb{F}'(x)\mathbb{F}^{-1}(x)$.

The kinetic energy term in the effective potential has a standard representation on a Fourier basis and is a full matrix, as detailed in [100]. The atom-ion potential (modelled by a delta pseudopotential) is always diagonal in this representation. The effective potential with $q = 0$ is the same effective potential for a problem without micromotion, in Eq.(3.21). If $q = 0$ and $n' \neq 0$, the potential

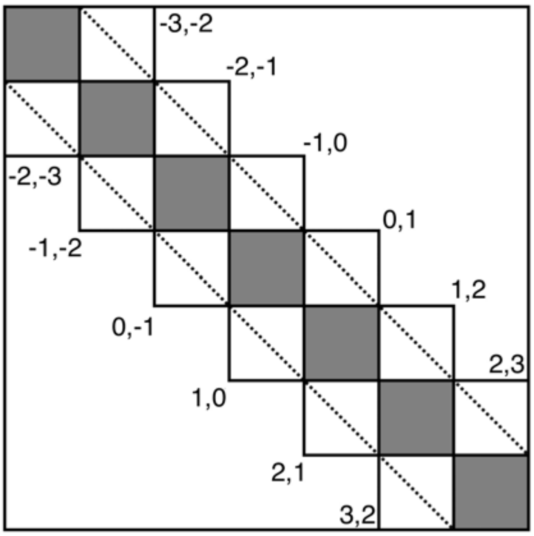

Figure 4.8: Structure of the effective potential $\mathbb{W}(x)$ over a Fourier-Floquet basis $n(n') = [-3, +3]$. Indices of the off diagonal coupling blocks are indicated. All blocks are matrices of order $(N_{ch} \times N_{ch})$.

essentially has a block diagonal structure with n' as index of the diagonal blocks. When $q \neq 0$ and $n' \neq 0$, besides the global block diagonal structure of the effective potential, the true potential has a tridiagonal structure in n' basis. This corresponds to the $q[\delta_{n,n'+1} + \delta_{n,n'-1}]$ term in the harmonic oscillator potential. The -1^{th} and $+1^{th}$ diagonal elements of the potential correspond to couplings between the different Fourier-Floquet blocks of the effective potential.
These couplings, combined with the pseudopotential coupling g enable certain transitions in energy of the order of $\hbar\omega_{rf} >> \hbar\omega_{rf}\beta/2$, in atom-ion experiments that operate the ion trap at points in the $a-q$ plane, with $\beta < 1$. The numerical methods for our 1D model are able to converge results only in the presence of at least a weak static confinement (as shall be explained in Sec.4.5), where the value of $\beta \in [0.5, 1.6]$.

4.3.1 Initial Condition and Asymptotic Matching

The initial condition for propagation in this case is exactly similar to the case in Sec.3.1.2.1 for each of the diagonal Floquet blocks. It is given by Eq.(3.43) and the initial condition log derivative matrix for each block is identical to the matrix in Eq.(3.24). The global initial log derivative matrix is diagonal and is built on the X coordinate basis that is obtained by symmetrizing the Fourier DVR grid. Details of symmetrization procedure is given in Appendix B. The potential matrix in Eq.(4.19) is accordingly symmetrized at each step of propagation. If N_{floq} number of Floquet components are to be propagated, each with N_{ch} number of grid points in X coordinate, the total log derivative matrix is of the order $N_{tot} = N_{floq} \times N_{ch}$. N_f is the number of Fourier-Foquet sidebands and $(2N_f + 1)$ is the truncated Fourier-Floquet basis size, as explained in Sec.4.1.1. We thus have the condition that $N_{floq} = (4N_f + 1)$. For our calculation with linear log derivative propagation, with trap parameters of $a = 2.0, q = 0.1$, we need 120 grid points and $N_{floq} = 13$ Fourier-Floquet components. This gives a matrix size of (1560×1560).

Similar to the case in Sec.3.1.2.2, asymptotic functions in Eq.(3.25) are built with wavefunctions of the atom $\psi_{atom}(k_n x_A)$ and the ion $\psi_{ion}(x_I, n') = \tilde{\Phi}(x_I, n')$ developed on the DVR grid points in the X coordinate at the final step of propagation in the x coordinate. The atom wavefunction $\psi_{atom}(k_n x_A)$ is developed as the regular and irregular free asymptotic solutions $f^{\pm}(k_{j'} x_A)$ and $g^{\pm}(k_{j'} x_A)$ for the positive and negative parities, as in Eq.(3.26) for open channels and Eq.(3.27) for the closed channels (See Sec.3.1.2.2). The asymptotic wavefunction for the ion is taken to be the Fourier-Floquet series expanded wavefunction of an ion in an rf-Paul trap, as given in Eq.(A.18). A brief reproduction of the derivation of this wavefunction and explanation is provided in Appendix.A.2. It has also been derived in detail in [52], [53] and [102]. The ion wavefunction in ω_{rf} oscillator units is given in Eq.(4.10). This time domain equation is converted to frequency domain using Fourier-Floquet expansion in Eq.(4.11) and Eq.(4.12).

As with the case of atom-ion collision without micromotion, as explained in Sec.3.1.2.2, at final step of propagation the centre-of-mass axis is at a 45° angle with respect to the asymptote. Thus a basis transformation is necessary to re-represent the log derivative on a grid of points that is parallel to the asymptotic region. The energy spectrum of Floquet type problems have no lower bounds. Thus problems arise when selecting the lowest N_{asy} eigenfunctions of the effective potential matrix in Eq.(4.19) which has a Floquet structure. This matrix is built on a basis of a truncated infinite series whose spectrum (as seen in Fig.4.2) theoretically ranges over $[-\infty, \infty]$. Eigenvalues close to zero will be the best converged ones. Thus selecting the lowest N_{asy} eigenfunctions proves ineffective. This drawback in turn appears as asymmetry of the open-open block of the Reactance matrix $\mathbb{K}_{oo}$ and in turn as non-unitarity of the open block of the S-Matrix $\mathbb{S}_{oo}$. Since asymptotic functions are built with exact expressions for the asymptotic ion wavefunctions, attempts were made to select the best possible states by selecting only those eigenfunctions that have maximum projection onto the N_{asy} states of the Fourier transformed ion wavefunction. This method is effective over a small range of q values. Thus this inherent drawback is suspected to limit the convergence of this method at large micromotion i.e maximum value of $q \approx 0.35$ at which we can propagate and match solutions in the asymptote successfully, as shall be seen in Sec.4.6.

4.3.2 Propagation by Spectral Element Method

The Spectral Element Method (explained in Sec.2.4) has also been applied to this problem with appropriate log-derivative boundary conditions. The propagation axis, in this case the relative coordinate, is split into elements and each elements is discretized with a local high order Legendre-Gauss-Lobatto basis (See Fig.2.4). The main advantage of this method is that the solution is obtained in one shot by solving the resulting linear system in sparse representation. The K-matrix calculated by this method agrees to better than 10 decimal places with that calculated by Log Derivative propagation. Despite the computational advantage of this method, the inherent drawback of the geometry and the need for a basis transformation just before performing asymptotic matching limits the accuracy of this method.

4.4 Solution by Propagation in Plane Polar Coordinates

Solution of the problem by propagation in Cartesian coordinates is possible only for $q \leq 0.35$ and the reasons for this were explained As explained in Sec.4.3.1, Sec.4.1.1 and Sec.4.6, the drawback is due to the inherent geometry of the problem which tends to limit the range of micromotion q in which numerical convergence is possible. To overcome the need for performing the basis transformation and selecting eigenfunctions from an unbounded spectrum, we attempt to shift the system to plane polar coordinates. We then propagate the log derivative along the $\hat{\theta}$ axis effectively trying to *swing* the initial centre-of-mass axis by an angle α which is determined by the mass ratio, to arrive at a grid that is parallel to the asymptotic region and eventually removing the need for a basis transformation after the final step of propagation. The propagation geometry is shown in Fig.4.9.

Starting with Eq.(4.14), it can be rewritten in mass-ratio scaled coordinates with $\tilde{x}_A = \sqrt{m}\bar{x}_A$ to give the equation in terms of $\tilde{x}_A$ and $\bar{x}_I$

$$\left[-\frac{1}{2}\frac{\partial^2}{\partial\tilde{x}_A^2} - \frac{1}{2}\frac{\partial^2}{\partial\bar{x}_I^2} + \frac{1}{8}[a + 2q\mathrm{Cos}(\omega_{rf}t)]\bar{x}_I^2 + \bar{g}\delta(x)\right]\Psi(\tilde{x}_A, \bar{x}_I, t) = \frac{i}{\omega_{rf}}\frac{\partial\Psi(\tilde{x}_A, \bar{x}_I, t)}{\partial t} \quad (4.20)$$

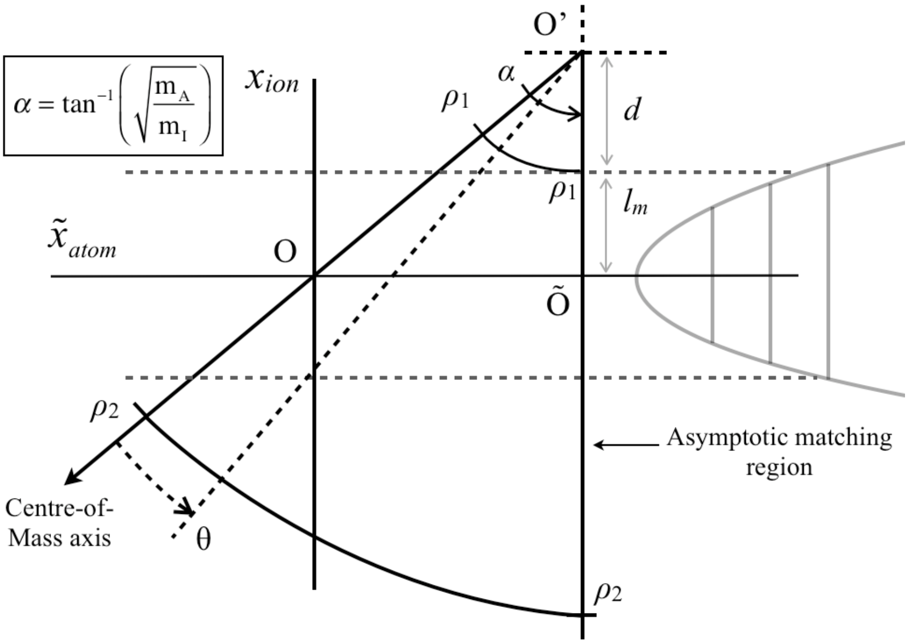

Figure 4.9: Log-Derivative Propagation in plane polar coordinates.

We denote $\tilde{x}_A, \bar{x}_I$ and $\bar{g}$ by x_A, x_I and g respectively for notational simplicity, the equation can be rewritten in plane polar coordinates with $\rho = \sqrt{x_A^2 + x_I^2}$ as

$$\Big[-\frac{1}{2\rho^2}\frac{\partial^2}{\partial\theta^2} - \frac{1}{2}\frac{\partial^2}{\partial\rho^2} - \frac{1}{2\rho}\frac{\partial}{\partial\rho} + \frac{1}{8}[a + 2q\,\cos(\omega_{rf}t)][\bar{\rho}\,\cos(\alpha) - \rho\,\cos(\theta - \alpha)]^2 + \frac{g\sin(\alpha)}{\rho}\delta(\theta)\Big]\Psi(\rho,\theta,t) = \frac{i}{\omega_{rf}}\frac{\partial\Psi(\rho,\theta,t)}{\partial t} \tag{4.21}$$

where $\alpha = \tan^{-1}(\sqrt{m})$ and $\bar{\rho} = \overline{OO'}$ is the shift of the origin to O'. The coordinates x_A and x_I are then given by

$$x_A = (\bar{\rho}\,\sin(\alpha) + \rho\,\sin(\theta - \alpha)) \text{ and } x_I = (\bar{\rho}\,\cos(\alpha) - \rho\,\cos(\theta - \alpha)) \tag{4.22}$$

Following the same procedure as in Sec.4.2.2 and with Fourier-Floquet general solution of the form

$$\Psi(\rho,\theta,t) = e^{-iEt/\hbar}\sum_{n=-\infty}^{+\infty} e^{in\omega_{rf}t}\tilde{\Phi}(\rho,\theta,n) \tag{4.23}$$

The time dependent Schrödinger equation Eq.(4.21) is converted to a time independent Schrödinger equation in frequency domain

$$\left[-\frac{1}{2\rho^2}\frac{\partial^2}{\partial\theta^2}-\frac{1}{2}\frac{\partial^2}{\partial\rho^2}-\frac{1}{2\rho}\frac{\partial}{\partial\rho}+\frac{1}{8}a[\bar{\rho}\,\cos(\alpha)-\rho\,\cos(\theta-\alpha)]^2+\frac{g\sin(\alpha)}{\rho}\delta(\theta)+n'\right]\dots$$
$$\dots\tilde{\Phi}(\rho,\theta,n')+\frac{1}{8}q[\bar{\rho}\,\cos(\alpha)-\rho\,\cos(\theta-\alpha)]^2\,\tilde{\Phi}(\rho,\theta,n'+1)+$$
$$\frac{1}{8}q[\bar{\rho}\,\cos(\alpha)-\rho\,\cos(\theta-\alpha)]^2\,\tilde{\Phi}(\rho,\theta,n'-1)=\bar{E}\tilde{\Phi}(\rho,\theta,n') \quad (4.24)$$

where $\bar{E}=E/(\hbar\omega_{rf})$. We denote $\bar{E}$ by E for notational simplicity. As explained earlier in Sec.4.3, we propagate multiple blocks of the Hamiltonian in Eq.(4.24), corresponding to each Fourier-Floquet component indicated by the index $n(n')$. The first term within square brackets on the left hand side in Eq.(4.24) is a diagonal term in the matrix representation of the Hamiltonian in the Fourier-Floquet basis (n' index) and the second term forms the +1 and −1 diagonals of the matrix.

We recall again that a convention of row and column indices being separated by a semi-colon is adopted in this chapter. We take solutions with composite index in and the form $\tilde{\Phi}_i(\rho,\theta)=\sum_{i'}\phi_{i'}(\rho)F_{i';i}(\theta)$. Since $\phi_{i'}(\rho)$ are DVR basis functions related to the grid point in ρ coordinate. Substituting these into Eq.(4.24), left multiplying by $\phi_i(\rho)$ and integrating over ρ, we have the second order equation to be solved by log derivative method. Eq.(4.24) initially discretized over the Fourier index n' is further discretized over the coordinate basis and thus develops composite indices where if row(column) indices are denoted by the grid point index $i'(j)$ and the corresponding Fourier index $n'(n)$. This equation in terms of global row and column indices $i'n'$ and jn' is given by

$$\frac{\partial^2 F_{i'n';jn}(\theta)}{\partial\theta^2}=\sum_{n'}\sum_{i'}\langle\phi_i(\rho)\,|\,W_{n;n'}(\rho,\theta)\,|\,\phi_{i'}(\rho)\rangle_\rho\,F_{i'n';jn}(\theta)\Rightarrow\mathbb{W}(\theta)\mathbb{F}(\theta) \quad (4.25)$$

where j is the solution index, $i(i')$ are the grid point indices and $n(n')$ Fourier-Floquet basis indices respectively. The term $W_{n;n'}(\rho,\theta)$ is in itself a matrix representation of the effective potential term in the Fourier-Floquet basis. The effective potential $\mathbb{W}(\theta)$ has elements over a DVR basis $\phi_i(\rho)$ given by

$$W_{in;i'n'}(\theta)=-\delta_{nn'}\left\langle\phi_i(\rho)\left|\left(\rho^2\frac{\partial^2}{\partial\rho^2}+\rho\frac{\partial}{\partial\rho}\right)\right|\phi_{i'}(\rho)\right\rangle_\rho+\delta_{nn'}2n'\left\langle\phi_i(\rho)\,|\,\rho^2\,|\,\phi_{i'}(\rho)\right\rangle_\rho$$
$$\delta_{nn'}2g\sin(\alpha)\left\langle\phi_i(\rho)\,|\,\rho\,|\,\phi_{i'}(\rho)\right\rangle_\rho\delta(\theta)-2\delta_{nn'}E\left\langle\phi_i(\rho)\,\middle|\,\rho^2\,\middle|\,\phi_{i'}(\rho)\right\rangle_\rho$$
$$\frac{1}{4}[a\delta_{nn'}+2q(\delta_{n,n'+1}+\delta_{n,n'-1})]\left\langle\phi_i(\rho)\,\middle|\,\rho^2(\bar{\rho}\cos(\alpha)-\rho\cos(\theta-\alpha))^2\,\middle|\,\phi_{i'}(\rho)\right\rangle_\rho \quad (4.26)$$

where the subscript indices are composite with $in(i'n')$ denoting the row(column) index. Simplifying the above equation, we can re-write it as

$$W_{in;i'n'}(\theta) = -\delta_{nn'}\left\langle \phi_i(\rho)\left|\left(\rho^2\frac{\partial^2}{\partial\rho^2}+\rho\frac{\partial}{\partial\rho}\right)\right|\phi_{i'}(\rho)\right\rangle_\rho + \delta_{nn'}\delta_{ii'}2\rho^2 n' - 2\delta_{nn'}\delta_{ii'}\rho^2 E + \delta_{nn'}\delta_{ii'}2g\sin(\alpha)\rho\delta(\theta)+\frac{1}{4}\delta_{ii'}[a\delta_{nn'}+2q(\delta_{n,n'+1}+\delta_{n,n'-1})]\rho^2(\bar{\rho}\cos(\alpha)-\rho\cos(\theta-\alpha))^2 \tag{4.27}$$

4.4.1 Initial Condition and Asymptotic Matching

The initial conditions for propagation in plane polar coordinates is as explained earlier in Sec.3.1.3.2. Similar to the solution by propagation in Cartesian coordinates, the initial log derivative matrix is diagonal. If N_{floq} number of Floquet components are to be propagated, each with N_{ch} number of grid points in each block, the total log derivative matrix is of the order $N_{tot} = N_{floq} \times N_{ch}$. We impose the condition $N_{floq} = (4N_f + 1)$, where N_f is the number of truncated Fourier-Foquet sidebands and $(2N_f + 1)$ is the truncated Fourier-Floquet basis size similar to Sec.4.3.1. This condition ensures the asymptotic functions built for angular propagation can be square matrices. The asymptotic functions are built as matrices using the coordinate transforms $x_A = [\bar{\rho}\ \sin(\alpha)+\rho\ \sin(\theta_{max}-\alpha)]$ and $x_I = [\bar{\rho}\ \cos(\alpha)-\rho\ \cos(\theta_{max}-\alpha)]$, where $\theta_{max} = \alpha$ and asymptotic functions for matching are built in a similar manner to that in Sec.4.3.1 on propagation in Cartesian coordinates.

Grid and Physical Parameters From Fig.4.9, we specify the length of segments l_m and d as inputs to define the ρ-axis grid over interval $]\rho_1,\rho_2[$ with N_ρ points. We require d of at least one oscillator length to include the weakly closed channels in the calculation. Propagation in the θ coordinate is over $\theta \in [0,\alpha]$, where the limit $\alpha = \tan^{-1}(\sqrt{m_A/m_I})$ is fixed by the mass ratio of the system. The propagation step size needed is $\sim 1\times10^{-4}$, $d = 1a_{ho}$ and all the N_{tot} propagated channels are included in the asymptotic matching since the method is devised to specifically forego the intermediate basis selection procedure, explained in Sec.3.1.2.2. Some of the grid and physical inputs for a converged calculation are specified here. The inputs in brackets are the range of values used for increasing micromotion q.
With tight static confinement $a = 2.4, q = [0,0.5]$.
For $m = 0.1$ - $l_m = [10\ a_{ho}, 12\ a_{ho}], N_\rho = [160,180], N_{floq} = 13, N_{tot} = [2054,2314]$.
For $m = 0.57$ - $l_m = [10\ a_{ho}, 12\ a_{ho}], N_\rho = [160,180], N_{floq} = 13, N_{tot} = [2054,2314]$.
For $m = 1.0$ - $l_m = [10\ a_{ho}, 12\ a_{ho}], N_\rho = [160,180], N_{floq} = 13, N_{tot} = [2054,2314]$.
With shallow static confinement $a = 0.5, q = [0,0.1]$.

For $m = 0.1$ - $l_m = 18\ a_{ho}, N_\rho = [160, 190], N_{floq} = 13, N_{tot} = [2054, 2444]$.
For $m = 0.57$ - $l_m = 18\ a_{ho}, N_\rho = [160, 190], N_{floq} = 13, N_{tot} = [2054, 2444]$.

Computation time is around the same value for all the above parameter ranges. On processors with Intel-AVX feature - 25 ~ 30 *mins* with 8 threads (optimal). On processors without Intel-AVX feature - 70 ~ 75 *mins* with 8 threads.

4.5 Ion Cooling and Atom Heating

Many experimental papers [27-32] and theory papers [45-50] explain the role played by micromotion in affecting the rate of cooling of the ion (possibility of sympathetic cooling), the rate of heating of the atom and the manifestation of this effect. Experiments involving a single ion immersed in a BEC report observing ion cooling with increasing interaction time between condensate atoms and ion [27]. Ravi et al. [31] also report on observing cooling of an ensemble of ions interacting with a cold atom cloud in a magneto-optical trap. At the same time all these experiments observe a constant loss of atoms from the condensate (cold cloud) and reason that it could be due to ion micromotion. The experiments demonstrate this by observing an increased atom loss rate after introducing a constant electric offset to the ion trap potential, which essentially pushes the ion off the trap minimum and increases the micromotion. The numerical study based on Langevin and semiclassical scattering [46] reveals the atom heating rates that agree with experimental results. By studying collision in 1D of a simpler model with a delta pseudopotential, it is possible to get a qualitative feel for effect of the micromotion in atom-ion scattering.

Due to the atom-ion interaction (modelled by a delta potential), there is always a non-zero probability of transition from the ion incoming channel to all possible outgoing channels. As illustrated in Fig.4.2, for a given collision energy there exist $N_0 < N_{-1} < N_{-2} < \ldots < N_{-\infty}$ secular oscillator levels in the open channels in the manifolds shifted in energy by $0 < -1\hbar\omega_{rf} < -2\hbar\omega_{rf} < \ldots < -\infty$ with respect to a 0^{th} manifold. Thus transitions between the N_0 open channels in the 0^{th} manifold are indicated by the diagonal $(N_0 \times N_0)$ block in the open-open S-matrix. Similarly diagonal blocks of dimension $(N_{-n} \times N_{-n})$ indicate the intra-manifold transitions within the $-n^{th}$ manifold. It is then seen that the off-diagonal block of dimension $(N_0 \times N_{-1})$ indicates the inter-manifold transitions between the 0^{th} to -1^{th} manifold and all off-diagonal blocks of dimension $(N_0 \times N_{-n})$ indicate inter-manifold transitions between 0^{th} and $-n^{th}$ manifold. A given ion state can be interpreted as a linear combination of infinite number of copies each separated by $\hbar\omega_{rf}$ and the ion energy is determined by state index i within a manifold of secular states. Ion transitions to state i in other manifolds leaves the ion quasi-energy unchanged but ion transitions to all secular states in all manifolds

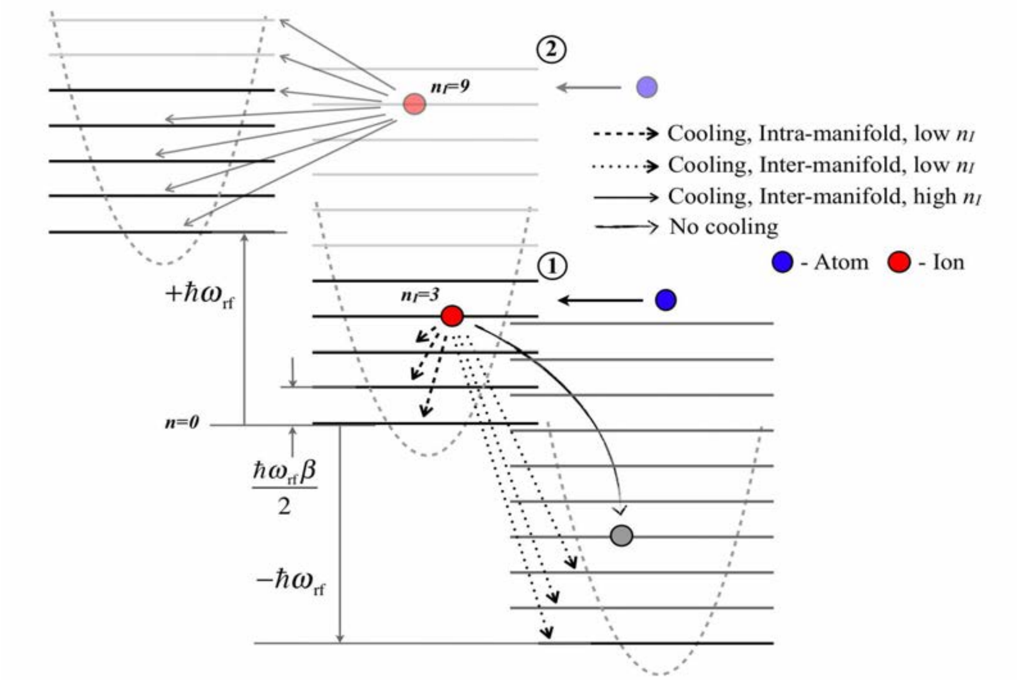

Figure 4.10: Transitions between manifolds that *cool* the ion.

with index $j < i$ amount to ion cooling and are show in Fig.4.10, labelled as ①. Only one low lying manifold is depicted here for simplicity. Such transitions to manifolds shifted *up* by $+n\hbar\omega_{rf}$, with $n > 0$ are all energetically closed in the example shown. It is possible if the ion incoming channel i is very high, there exist a few outgoing open channels in the manifolds shifted in energy by $+n\hbar\omega_{rf}$, labelled ② in Fig.4.10. Transitions to these states $j < i$ in the $+1^{th}$ manifold also leads to ion cooling and are indicated by thin solid lines. Transitions to any other states than the ones indicated by arrows in Fig.4.10 lead to ion heating and the ion transition indicated by the curved line leaves the ion energy unchanged.

Ion cooling transitions impart the energy lost to atoms, accelerating them. Thus atom-ion interaction also lead to atom heating in the time scales of the collision $\tau \ll T_{rf}$. It should however be noted that ion heating transitions are also non-zero during collisions. In experiments, Paul traps in 3D have a very low value of $a \approx 0$ and $q_x \in [0, 0.454]$, with $\beta_x \in [0, 0.335]$ in the x-axis and $q_z \in [-0.908, 0]$ with $\beta_z \in [0, 0.993]$ in the z-axis. Thus the density of states within each manifold of secular oscillator levels is high if $\beta << 1$.

The cooling (or heating) probabilities are sum of the modulus squared of the complex transition amplitudes i.e $R_{ij} + T_{ij} = |r_{ij}|^2 + |t_{ij}|^2$. A notation with two pairs of subscripts separated by semi-colon are used, where the first pair of subscripts indicate the incoming secular oscillator level index and the manifold index respectively. The second pair indicates the same for outgoing channels. The 0^{th} manifold is said to have N_0 open channels with ion in an initial state i_0. One can define ion cooling probability for an incoming channel index $(i_0, 0)$ with $0 < i_0 \le N_0$ as

$$\alpha_{i_0 0}^{IC} = \sum_{k=-\infty}^{\infty} \sum_{j=0}^{min(N_k-1, i_0-1)} (R_{i_0 0;jk} + T_{i_0 0;jk}) \tag{4.28}$$

The term in the summation with $k = 0$ corresponds to transitions within the initial 0^{th} manifold and the rest correspond to inter-manifold transitions (or the transitions labelled ① in Fig.4.10).Conversely, if the ion makes a transition to states $j > N_0$ in all manifolds, it corresponds to ion heating since the ion ends up in a secular oscillator level of highly excited state character. If N_k indicates the number of open channels in the k^{th} manifold, the ion heating probability is

$$\alpha_{i_0 0}^{IH} = \sum_{k=-\infty}^{0} \sum_{j=min(N_k+1, i_0+1)}^{N_k} (R_{i_0 0;jk} + T_{i_0 0;jk}) + \sum_{k=1}^{\infty} \sum_{j=max(N_k, i_0+1)}^{N_k} (R_{i_0 0;jk} + T_{i_0 0;jk}) \tag{4.29}$$

Similarly, the sum of ion transitions to open channels in all manifolds $k \le 0$ result in ion imparting energy and heating the atom. Transitions leading to ion cooling are a subset of these transitions. Besides the ion decay to lower states within the 0^{th} manifold, the sum of the inter-manifold ion transitions to open channels in all manifolds helps understand the contribution of micromotion to atom heating. This mechanism is seen to be the reason for a constant loss of condensate atoms in experiments with single ions (27, 28, 29) and multiple ions interacting with an ultracold cloud of atoms [31]. Using the same subscript notation as for ion heating, the atom heating rate for any incoming channel $(i_0, 0)$ such that $0 \le i_0 \le N_0$ can be given by

$$\alpha_{i_0 0}^{AH} = \sum_{k=-\infty}^{\infty} \sum_{j=0}^{min(N_k, i_0)} (R_{i_0 0;jk} + T_{i_0 0;jk}) \tag{4.30}$$

At large collision energies if $N_k > 0$ for $k > 0$, then the ion cooling transitions to states in the $+1^{th}$ manifold leads to atom heating and ion heating transitions to the $+1^{th}$ manifold lead to atom cooling. At the end of the time period T_{rf}, the exchange of rf-photons between the ion and the field changes the ion energy. Thus energy is on average conserved and it is not possible to continuously cool the ion below an inherent limit because the ion is not a closed system. Ion cooling shown in our results is valid only for time scales of the order of $\tau \ll T_{\omega_{rf}} = 2\pi/\omega_{rf}$. Theoretical and numerical studies on sympathetic cooling of ion in [49, 50] reveal similar limits on ion cooling. The ion cooling and atom heating probabilities are probabilities per collision event and multiplied by the atom velocity give the rate.

4.6 Results: Ion Cooling and Atom Heating Probabilities

The transition probabilities in Eq.(4.28) and Eq.(4.30) are calculated for different trap parameters and mass ratios and plotted against increasing q, total energy E_{tot} and pseudopotential coupling g. Since secular frequency $\beta\omega_{rf}/2$ depends on a and q, when varying q we are essentially changing the trap frequency and thus shifting the locations of channel thresholds (energy is in units of $\hbar\omega_{rf}$ all through this chapter). So it is important to have a constant collision energy at all data points and we maintain it at a fixed value with respect to a channel threshold energy. It is seen in Eq.(4.28) and Eq.(4.30) that the ion cooling and atom heating probabilities are composed of two types of transitions, transitions within the initial manifold (intra-manifold) and transitions to all open channels in other low lying manifolds (inter-manifold). These are not explicitly measured in experiments but the underlying physics holds true. Though the whole set of Floquet states are a result of micromotion parameters q and a, it is observed that intra-manifold transitions have a far higher probabilities than inter-manifold transition probabilities. So we consider intra-manifold transition probabilities to highlight the effect of micromotion.

4.6.1 Using Propagation in Cartesian Coordinates

Both the log derivative propagation and the Spectral Element Method are used. K-matrix elements from the two methods agree to better than 10-digits. The ion cooling and atom heating probabilities calculated for the Na-Ca$^+$ system with mass ratio 0.57 and two different ion initial states $n_I = 0$ and $n_I = 1$. Plots shown here are for a constant collision energy of 0.2 $\beta/2$ (i.e at a constant distance with respect to 2^{nd} energy threshold occurring at $E = 1.5\beta/2$). It has two open channels for the ion, total energy of $E_{tot} = 1.7\beta/2$ and tightly confined ion trap with $a = 2.0$.

Contributions of the inter-manifold and intra-manifold transitions to the cooling and heating probabilities are also shown. The ion cooling probabilities are seen to increase with micromotion, with a larger contribution to cooling probability arising out of inter-manifold transitions. Atom heating due to inter-manifold transitions in Fig.4.12 rises and nearly saturates with increasing q.

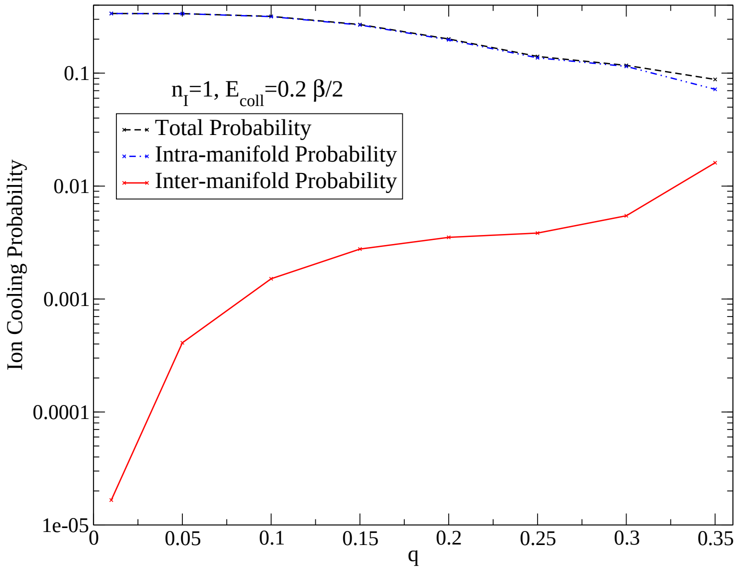

Figure 4.11: Ion Cooling Probability from all contributions for $a = 2.0, m = 0.57$ and total energy $E_{tot} = 1.7\beta/2$ (collision energy $E_{coll} = 0.2\beta/2$).

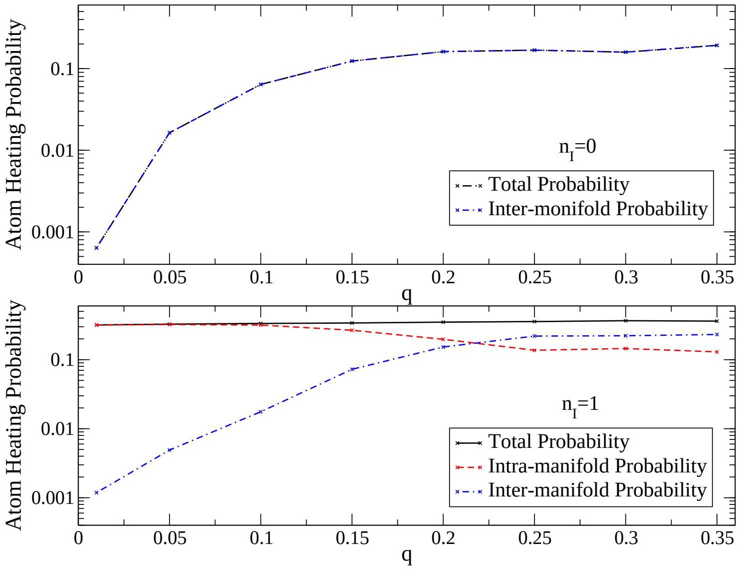

Figure 4.12: Atom Heating Probability from all contributions for $a = 2.0, m = 0.57$ and total energy $E_{tot} = 1.7\beta/2$ (collision energy $E_{coll} = 0.2\beta/2$). Ion in initial state $n_I = 1$. Atom heating probability at each collision event is non-negligible.

4.6.1.1 Limitations

As a standard method to quantify error, we calculate the relative error of the off-diagonal elements in open-open block of the K-Matrix for an arbitrary value of energy with two open channels. It is ensured the K-Matrix is converged with respect to all other physical and grid parameters at each of these data points. With increasing q, only the Fourier-Floquet basis size is increased, keeping all other parameters constant. We ensure a constant collision energy at each data point. As shown in Fig.4.13, for the case of tight confinement with $a = 2.0$, the relative error is very high at $q = 0.35$. For a test case of weak confinement with $a = 0.5$, it is noted that the method fails rapidly at extremely low value of $q = 0.02$.

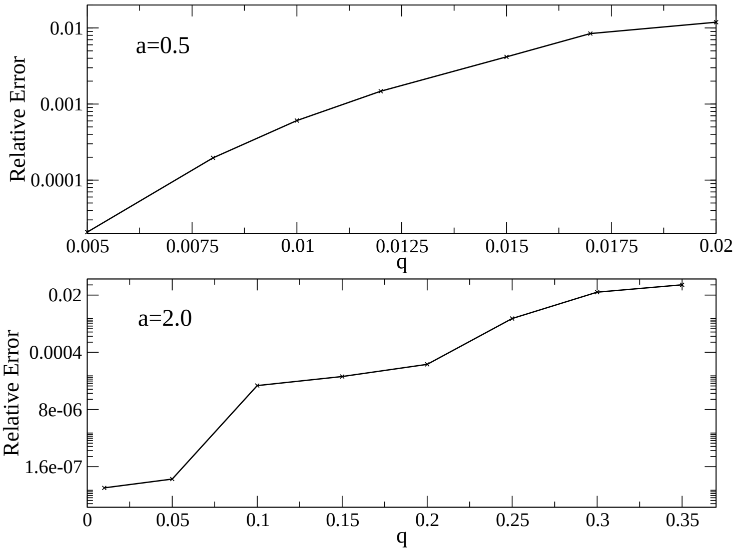

Figure 4.13: Relative error of K-Matrix off-diagonal elements as a test of convergence.

Taking a relative error of 1×10^{-4} as the maximum permissible, the case with tight confinement of $a = 2.0$, has maximum value of $q = 0.2$ using propagation in Cartesian coordinates. This corresponds to low micromotion, since we are still operating deep within the stability plot. The basis transformation identical to that in Eq.(3.28) is required for the problem with micromotion when using both Log Derivative Propagation and Spectral Element Method. The inherent drawback of this process of selecting a transformation matrix was explained in Sec.4.3.1. Selection of N_{asy} well-converged states from the eigenstates of the potential matrix in Eq.(4.19) is increasingly inefficient with increasing micromotion q. Since a finite number of Fourier components are propagated, only few eigenstates of the potential matrix centered around zero will be well converged. These are insufficient to form a complete basis, to account for all the closed channels required for efficient asymptotic matching. Increasing the number Fourier components makes the log derivative matrix very large, reaching the numerical limits of the algorithm with respect to number of propagated channels. If instead we increase N_{asy}, we select more badly converged eigenfunctions to build the basis transformation matrix. Thus these reasons is suspected to be the cause of the limit in maximum micromotion $q \leq 0.2$ that can be used to get converged results with this method. To bypass the drawback of this basis transformation, a change to plane polar coordinates is proposed and the log derivative matrix is propagated in angle θ.

4.6.2 Using Propagation in Plane Polar Coordinates

4.6.2.1 Ion in Tight Static Confinement

The ion cooling, ion heating and atom heating probabilities are calculated as a function of micromotion parameter q, coupling strength g and total energy E_{tot} for a static confinement parameter $a = 2.4$. With numerical methods implemented, plots are shown for a maximum micromotion parameter of $q = 0.5$. Since the trap secular frequency changes with a and q, we note that the secular frequency varies only slightly over $\omega_{sec} = [0.7746\hbar\omega_{rf}, 0.7604\hbar\omega_{rf}]$ with $q = [0, 0.5]$ in these plots.

Influence of Mass Ratio

It is noted here that ion cooling probabilities depend on the mass ratios $m_A/m_I = 0.1, 0.57$ and 1.0 in Fig.4.14 and Fig.4.15.

Larger mass ratios (i.e heavier atom, lighter ion) show comparatively greater probability of ion cooling. A maximum mass ration of $m_A/m_I = 1.0$ can be used ensuring a maximum relative error of 1×10^{-4}. As expected, an ion in an initial excited state in the trap $n = 2$ is seen to exhibit greater cooling probability ~ 0.01. As has been explained in Sec.4.5, these probabilities are per collision and their long time scale cumulative effects are limited by the periodic exchange of rf-photons between the ion and field. This is also attested by the fact that the ion heating probabilities are almost an order of magnitude larger for all mass ratios.

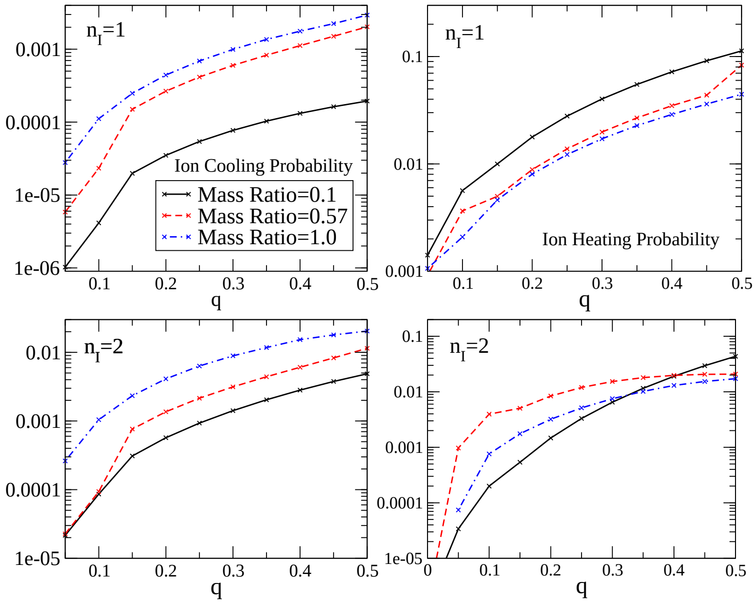

Figure 4.14: Ion Cooling (left) and Heating (right) probabilities due to inter-manifold transitions, for mass ratios $m = m_A/m_I = (0.1, 0.57, 1.0)$ and total energy $E_{tot} = 2.7\beta/2$.

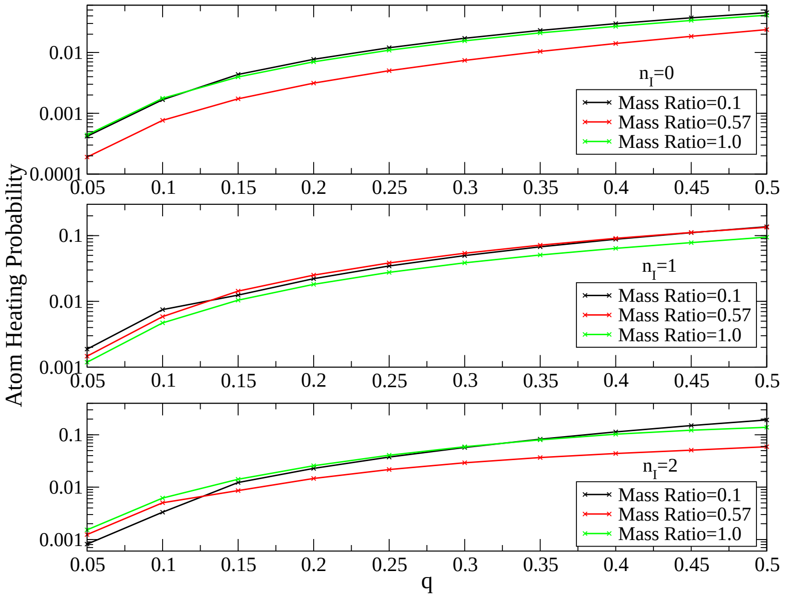

Figure 4.15: Atom Heating probabilities due to inter-manifold transitions with mass ratios $m = m_A/m_I = (0.1, 0.57, 1.0)$ and total energy $E = 2.7\beta/2$.

Similar effect is observed in experiments as reported in [27] and [31], where ion cooling is oberved with increased interaction time with the atoms (See Fig.1.1, 1.2, 1.3). At maximum micromotion, the ion cooling probabilities of $\sim 1\times10^{-3}$ and $\sim 1\times10^{-2}$ are shown in Fig.4.14, for an example case of ion starting in initial states of $n = 1$ and $n = 2$ respectively.

Atom heating probabilities in Fig.4.15 are also seen to increase with micromotion q. This is a factor contributing to a constant loss of atoms from the trap, as reported in atom-ion experiments [27-33]. Since ion transitions to states with highly excited state character are present in the total atom probability, an appreciably large energy is imparted to the atoms, accelerating them.

Influence of Coupling g_{1D}

The inter-manifold transitions are driven by atom-ion interaction under the presence of micromotion. Larger pseudopotential couplings should give larger probabilities of inter-manifold transitions. Total ion cooling and atom heating probabilities are shown in Fig.4.16 and Fig.4.18 for different values of incoming channel $n_I = 1$ (left column) and $n_I = 2$ (right column). As in the earlier case, the intra-manifold cooling transitions are of considerably larger probability than inter-manifold transitions. This general trend holds true for both ion cooling and atom heating.

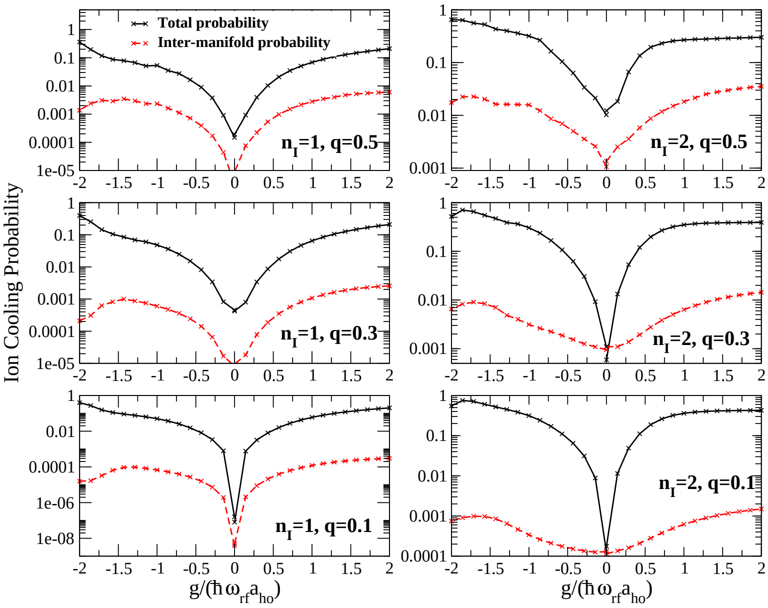

Figure 4.16: Ion cooling as a function of pseudopotential coupling g, at constant collision energy $E_{coll} = 0.2\beta/2$ and $m_A/m_I = 0.57$. Probabilities due to inter-manifold transitions are indicated separately.

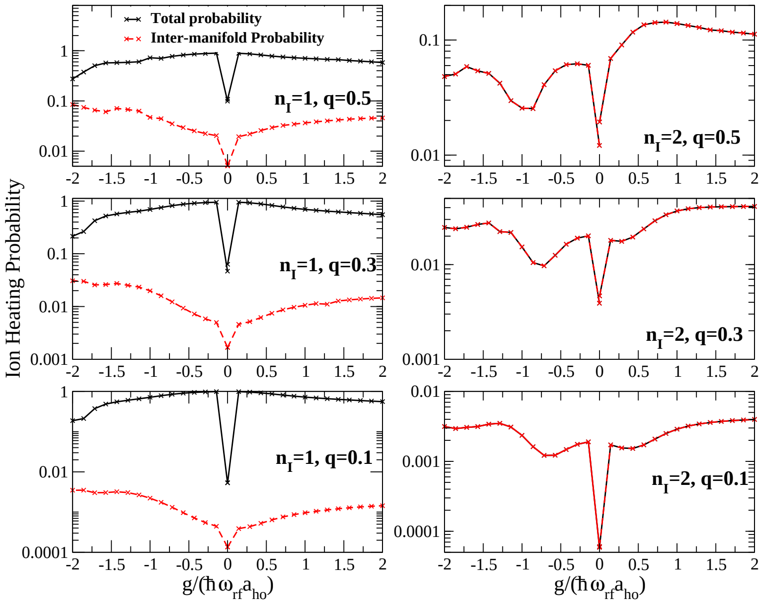

Figure 4.17: Ion heating as a function of pseudopotential coupling g, at constant collision energy $E_{coll} = 0.2\beta/2$ and $m_A/m_I = 0.57$. Probabilities due to inter-manifold transitions are indicated separately.

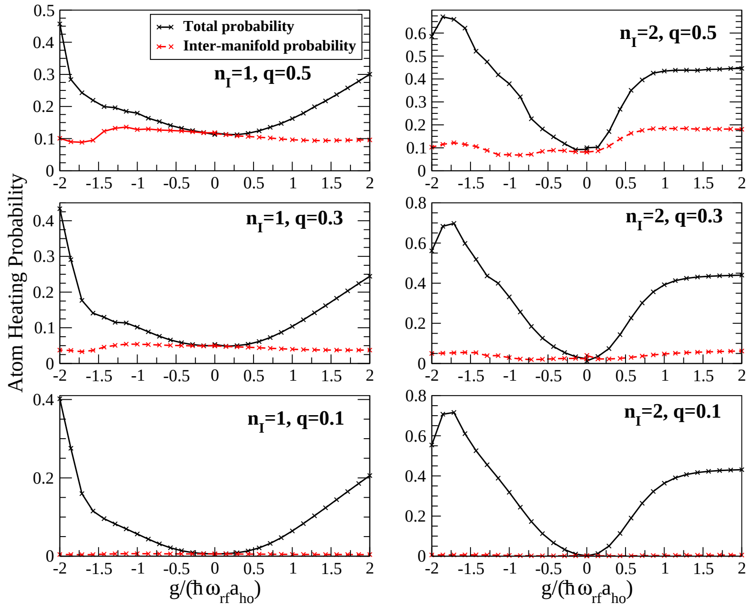

Figure 4.18: Atom heating as a function of pseudopotential coupling g, at constant collision energy $E_{coll} = 0.2\beta/2$ and $m_A/m_I = 0.57$. Probabilities due to inter-manifold transitions are indicated separately. Atom heating is seen to saturate for $n_I = 2$ (right column) with coupling.

Ion cooling probability increases with coupling g at larger values of q from Fig.4.16. At maximum $q = 0.5$, ion initial state $n_I = 2$ is seen to have slightly higher cooling probability ~ 0.03 than the case with ion in $n_I = 1$ initially (~ 0.008). In all of the above cases, ion heating probability (in Fig.4.17) due to inter-manifold transitions is see to be at least an order of magnitude of larger than ion cooling. Thus ion cooling is a very inefficient process for the mass ratios at which our calculations give numerical convergence. Where as atom heating probabilities in Fig.4.18 show clear saturation at larger coupling strengths $g \sim 2.0$. In this case too, inter-manifold transitions are more probable at larger micromotion parameters $q = 0.5$.

Influence of Collision Energy

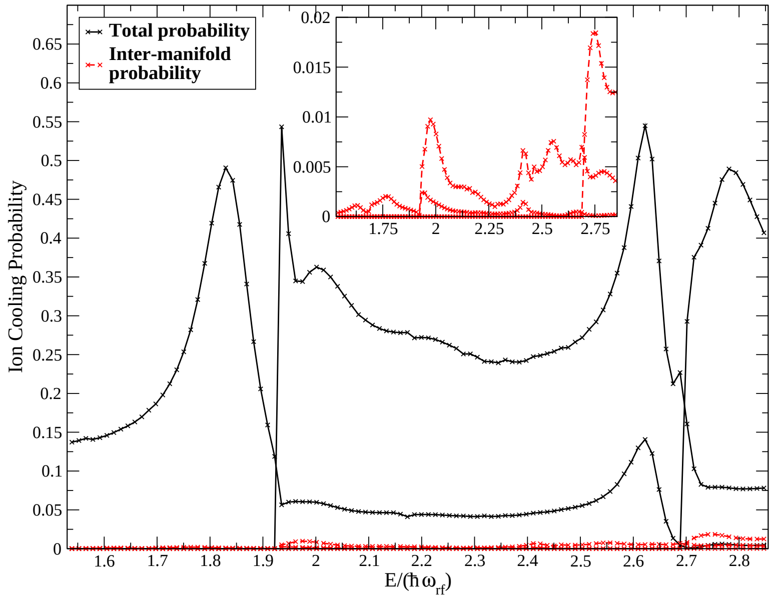

Figure 4.19: Ion cooling as a function of collision energy, for $a = 2.4, q = 0.3$ and $m_A/m_I = 0.57$. Inter-manifold (inset) and total cooling probabilities follow the resonance peaks and discontinuities at thresholds.

All plots so far were made at constant collision energy and the change in ion cooling probability with increasing collision energy is studied here. The cooling probability shows channel openings at n^{th} energy threshold, where total energy is $E_{tot} = n\hbar\beta\omega_{rf}/2$. By comparing Fig.4.19 and Fig.4.26, we note that the cooling probabilities follow the resonance features exactly, with the peaks located at the same energies where resonances are observed.

4.6.2.2 Ion in Shallow Static Confinement

3D ion traps in experiments operate at $a \approx 0$, so to model a realistic trap we calculate ion cooling probabilities for the least possible value of $a = 0.5$ i.e shallow static confinement that converges numerically. Similar to the case of tight confinement, the secular frequency varies only slightly over $\omega_{sec} = [0.3535\hbar\omega_{rf}, 0.3571\hbar\omega_{rf}]$ with $q \in [0, 0.1]$.

Influence of Mass Ratio

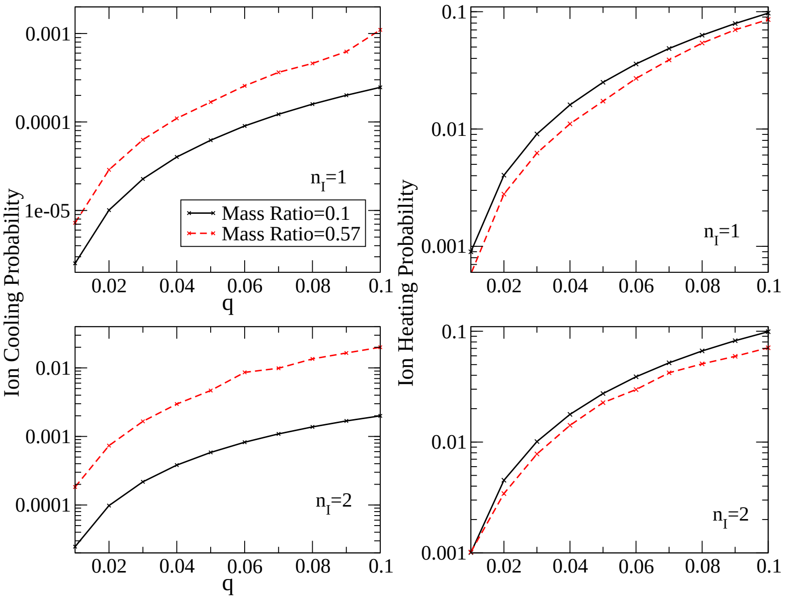

Figure 4.20: Ion cooling (right) and heating (left) probabilities for shallow confinement with $m_A/m_I = 0.1, 0.57, a = 0.5$ and total energy $E_{tot} = 2.7\beta/2$.

The maximum mass ratio that gives acceptable relative error ($\leq 1 \times 10^{-4}$) is $m_A/m_I \sim 0.6$. With ion in initial state $n_I = 2$, ion cooling probability is ~ 0.01 at $q = 0.1, m = 0.57$ in Fig.4.20 (bottom panel) i.e the same order of magnitude as the case with tight confinement $a = 2.4$ at $q = 0.5, m \geq 0.57$ in Fig.4.14 (bottom panel). Ion heating probabilities due to inter-manifold transitions are again at least an order of magnitude of larger than ion cooling probabilities. Similarly atom heating probabilities in Fig.4.21 are also of the same order of magnitude at $a = 0.5, q = 0.1$ for shallow trap and $a = 2.4, q = 0.5$ for the tight confinement case. Note that $q = 0.1$ is the maximum value that gives acceptable convergence and relative error. The log derivative matrix dimension is $\approx 2000 \sim 2500$, nearing the numerical limit of the log derivative propagation algorithm.

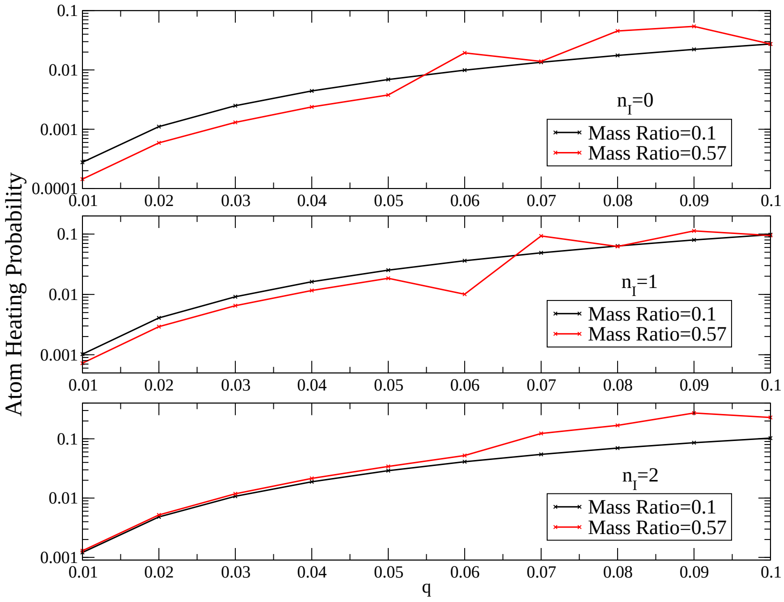

Figure 4.21: Atom heating probabilities for shallow confinement with $m_A/m_I = 0.1, 0.57$, $a = 0.5$, $E_{tot} = 2.7\beta/2$.

Influence of Coupling g_{1D}

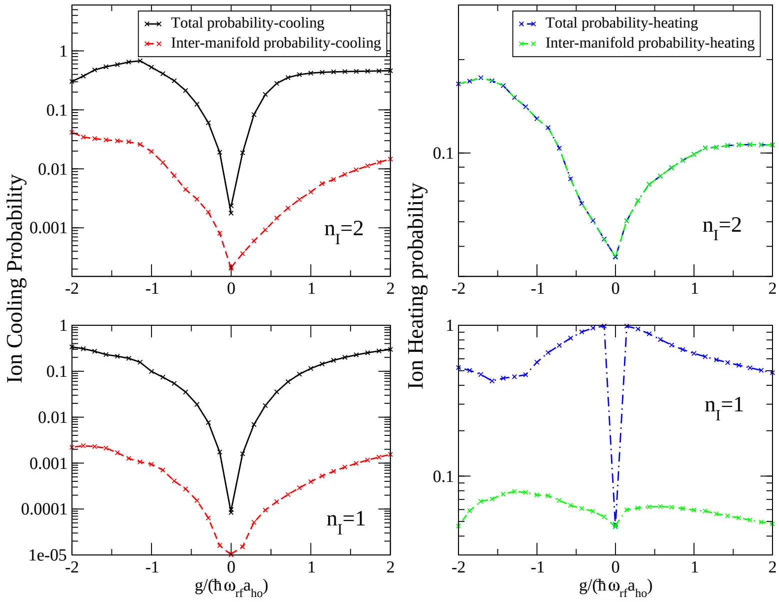

Figure 4.22: Ion cooling (right) and heating (left) probabilities as a function of pseudopotential coupling g, at constant collision energy $E_{coll} = 0.2\beta/2$ and $m_A/m_I = 0.57$.

Similar to the case in Fig.4.16 and Fig.4.18, the ion cooling probabilities shows low contribution from inter-manifold transitions. But ion heating transitions are again an order of magnitude larger in comparison. Larger ion cooling probability is observed with coupling g for ion in an excited initial state. The atom heating rates saturate with increasing pseudopotential coupling.

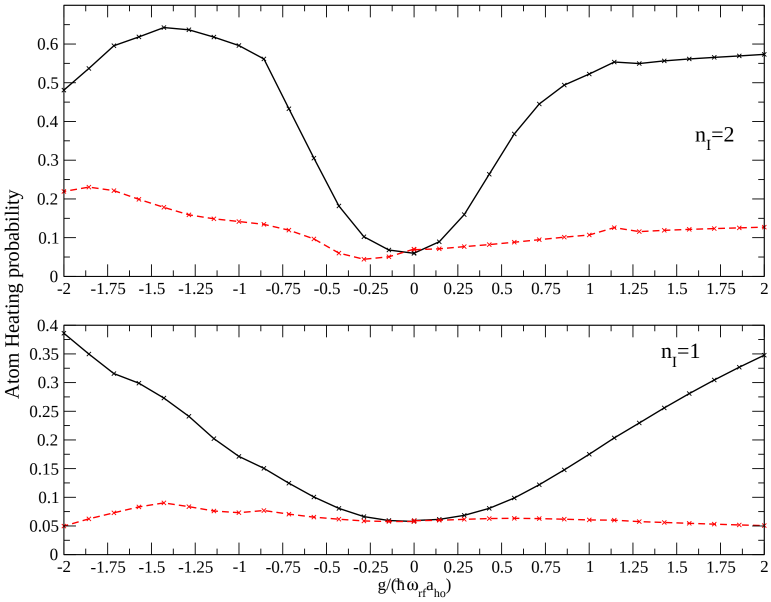

Figure 4.23: Atom heating probability as a function of pseudopotential coupling g, at constant collision energy $E_{coll} = 0.2\beta/2$ and $m_A/m_I = 0.57$.

4.6.2.3 Limitations

The Log Derivative Angular Propagation has its drawbacks, in that the maximum micromotion under which the method gives acceptable convergence is a small range of $q \in [0, 0.5]$. As a test parameter, the relative error is calculated on the off-diagonal K-Matrix elements of a test problem with collision energy resulting in two open channels of the ion. Like in the earlier instances, it is ensured that K-matrix elements are converged with respect to all physical and grid parameters while calculating the relative error. It is seen that this method is limited by the micromotion q and mass ratios at which it can give converged results with maximum relative error of 1×10^{-4}. It is easily seen from Fig.4.9, that for larger mass ratios we require a very large grid since at the final step of propagation a considerable portion of the grid is lost i.e rendered insignificant for asymptotic matching due to the ion bound state.

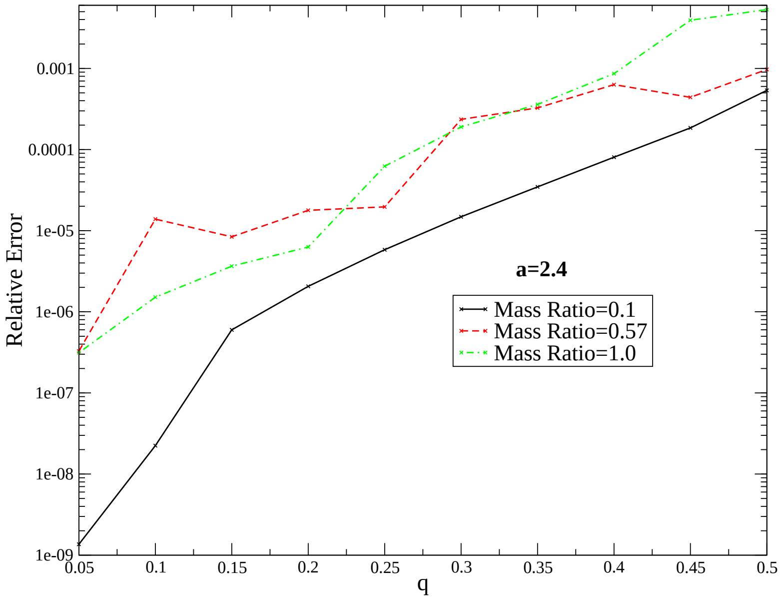

Figure 4.24: Relative error for tight confinement case $a = 2.4$, for $m_A/m_I = 0.1, 0.57, 1.0$.

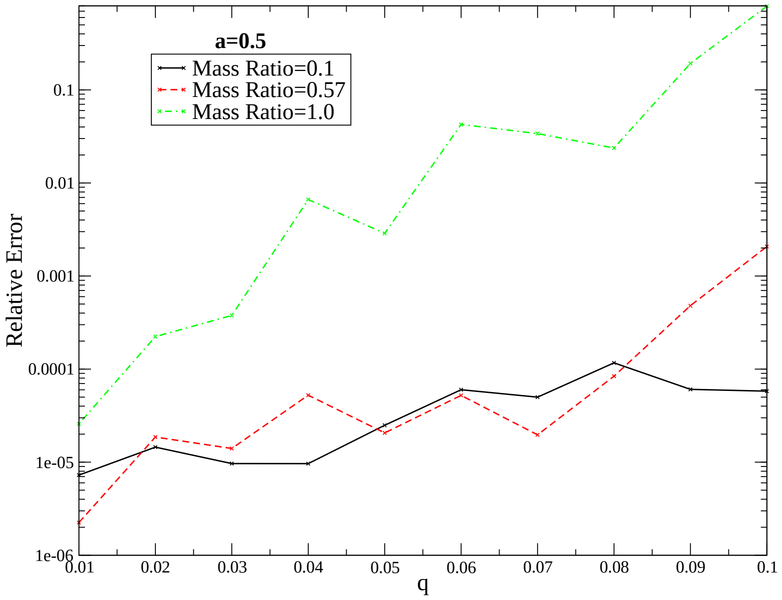

Figure 4.25: Relative error for shallow confinement case $a = 0.5$, for $m_A/m_I = 0.1, 0.57, 1.0$.

As shown in Fig.4.24, this method of angular propagation is susceptible to large errors for the case of shallow confinement. Since the confinement is weaker, the ion quasi-stationary states are slightly more delocalized due to stronger dynamical confinement. This requires a larger grid with sufficiently large density of points to converge the results. This increases total number channels propagated is 2000 ~ 2400, which is nearing the numerical limit of the propagation algorithm. Larger mass ratios require that we propagate over greater angle $\alpha = \tan^{-1}(\sqrt{m_A/m_I})$, thus propagating a larger number of steps. The algorithm begins to accumulate large error with increasing number of steps thus limits the range of mass ratios that can be used with this method. The requirements vis-a-vis grid and physical input parameters were presented in Sec.4.4.1.

4.6.3 Discussion

The trap can essentially be considered static over this range, though the calculation requires 13 Fourier components. The effect of micromotion can be treated as a perturbation on the secular motion of the ion, along the lines of treatment in [51]. The overall effect of micromotion on ion cooling in both the cases with tight and shallow confinement is seen to be rather weak, given the order of magnitude of the ion cooling probabilities per collision is around ≤ 0.01 for an ion starting in a initial state $n = 2$ (over the range of q accessible with the numerical methods we implement). The difference of an order of magnitude in the ion cooling probability at maximum q between the cases with $n_I = 1$ and $n_I = 2$ indicates that intra-manifold transitions dominate over inter-manifold transitions for excited ion. The cooling probability multiplied by the velocity gives the cooling rates which can possibly be used to estimate the total ion cooling rate in the presence of an ultra cold atom cloud, along the lines of analysis in [50]. In comparison, ion heating from excited levels is seen to be a more dominant process. Ion heating due to inter-manifold transitions too is seen to be at least an order of magnitude larger than the cooling probability. Ion cooling shows marginally better probability with larger mass ratios. The numerical methods used have poor convergence at larger mass ratios due to the angle between the centre-of-mass axis and the asymptotic region, in Fig.3.5. It must however be noted that this model is a simplified one with the delta pseudopotential in place of the long range polarization potential. Moreover, the ion dynamics is heavily perturbed at each cycle of the rf-field due to exchange of energy quanta between the ion and the field. Although ion cooling could be observed to a certain degree, the cumulative effect of efficient, continued cooling in the presence of micromotion on longer time scales cannot be expected unless the atom-ion system is strictly a closed system. Thus one can safely argue that the ion cooling rate would have a natural saturation, determined by the trap parameters a and q. This is a possible explanation for the observed saturation/limit of ion cooling observed over interaction time between a single ion and an ultra atom cloud, as observed in [27, 31] (Also see Fig.1.1, 1.3). Saturation of ion cooling probabilities with varying physical parameters like q and pseudopotential coupling g is evident from the plots shown in Sec.4.6.2.1 and 4.6.2.2, where the ion cooling probabilities show a gradual saturation with increasing parameter values. Estimates of cooling from pseudopotential model and based only on the effect of micromotion per collision can overlook the effect of interaction of the polarization potential and the rf-field. Classical calculations based on dipole forces given in [49] elegantly illustrate the subtle interplay of dipole forces and trapping fields. A full quantum calculation using the master equation approach in [47], where they treat the ultra cold atom cloud as a thermal bath illustrates a similar effect, that the cooling in the presence of micromotion is negligible unless the trap is operated at the edge of the stability region. At the edge of the stability region, the ion dynamics is largely dictated by the q parameter.

On the other hand, atom heating probabilities are seen to be non-negligible. It increases with micromotion and the exchange in energy accelerates the atom. In experiments, this is seen to be the mechanism that drives an atom loss from an ultracold cloud interacting with an ion. See 27-30, 32 and Fig.1.1, 1.2.

4.7 Effect of Ion Micromotion on Resonances

The effect of micromotion on scattering theory in one dimension is studied. In a manner similar to the one dimensional collision problem in Sec.3.2, we study threshold and resonance features and the effect of micromotion on the same. Along the lines of Sec.3.2 and [85], the resonance-like peaks are analyzed by building the time delay matrix.

4.7.1 Collision with Ion in a Tightly Confined Trap

Thresholds and Resonances

The variation of reflection probability is studied as a function of varying total energy. Plots are made for summed reflection probability for transitions within the 0^{th} manifold, given by $R_0 = \sum_{j=0}^{N_{\rm op}} |r_{00;j0}|^2$, reflection probability in all open channels summed, with ion in initial state $n_I = 0$. Threshold features and resonance-like peaks are observed in the summed reflection probability. The n^{th} energy threshold now exists at $(n+1/2)\omega_{sec} = (n+1/2)\beta\omega_{rf}/2$. The plots are made for $q = 0.1$ and $q = 0.3$. To isolate the effects of micromotion on these features, we define a reference secular oscillator. The calculation is repeated for the same system with no micromotion ($q = 0$) and oscillator frequency set to $a = \beta^2$, thus the reference secular oscillator frequency will be $\beta\omega_{rf}/2$ (shown in red in the plots).

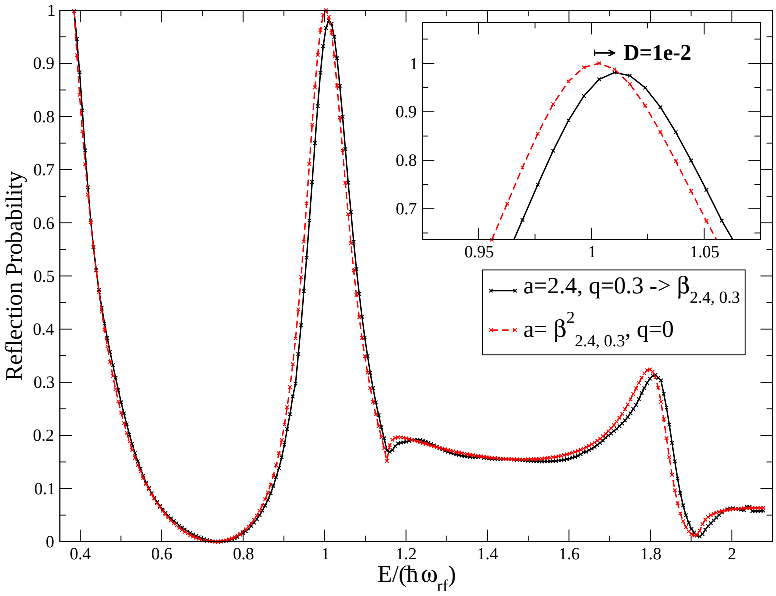

Figure 4.26: Thresholds and resonance-like peaks at $g = -1, q = 0.3$ and $m_A/m_I = 0.57$.

It is noted that at $q = 0.3$, there is very little change in resonance and threshold features with respect to the reference secular oscillator as seen in Fig.4.26. The threshold and resonance peaks are only slightly shifted with respect to the reference secular oscillator. The shift of $D \approx 1 \times 10^{-2}\hbar\omega_{rf}$ is seen in the location of resonance peaks, occurring at a larger energy when $q = 0.3$, shown inset in Fig.4.26. This shift in the resonance peaks is proportional to q since comparing the $q = 0.3$ and the reference secular oscillator, we find the location of thresholds at channel openings remain unchanged as expected.

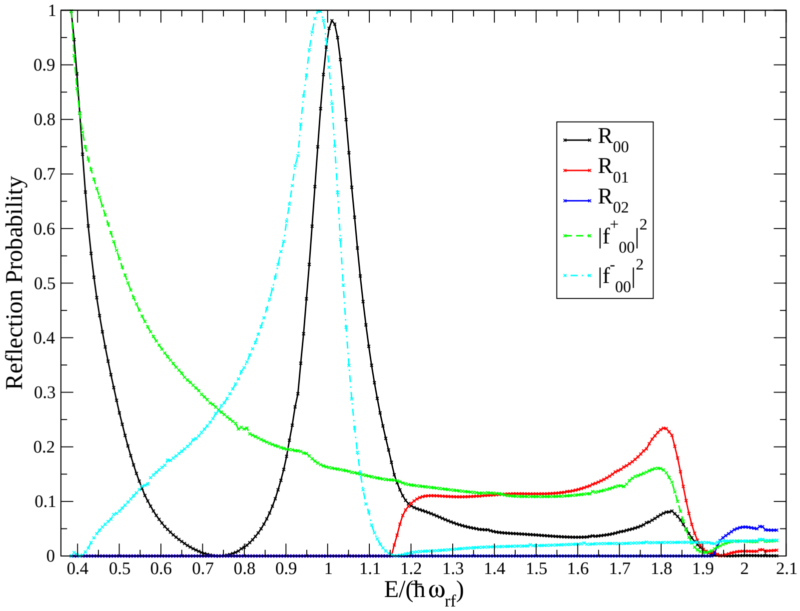

Figure 4.27: Reflection in the elastic channel R_{00} and contribution of f_{00}^{+} and f_{00}^{-} to the peaks at $g = -1, q = 0.3, m_A/m_I = 0.57$.

Parity Decomposition of Resonance Features The resonance peak in the elastic channel at low energies is again analyzed in terms of the contributions of f_{00}^{+} and f_{00}^{-} in a manner similar to that explained in Sec.3.2. For a tight confined ion and $q = 0.3$, the low energy resonance feature shows contribution only from the odd parity scattering amplitude f_{00}^{-}. As explained in Sec.3.2, the negative total parity scattering amplitude also contains contributions from the positive relative parity.

Time Delay of the S-Matrix

We analyze the resonance peaks in reflection probability by calculating the delay times, similar to that done in Sec.3.2. The time delay matrix is the derivative of

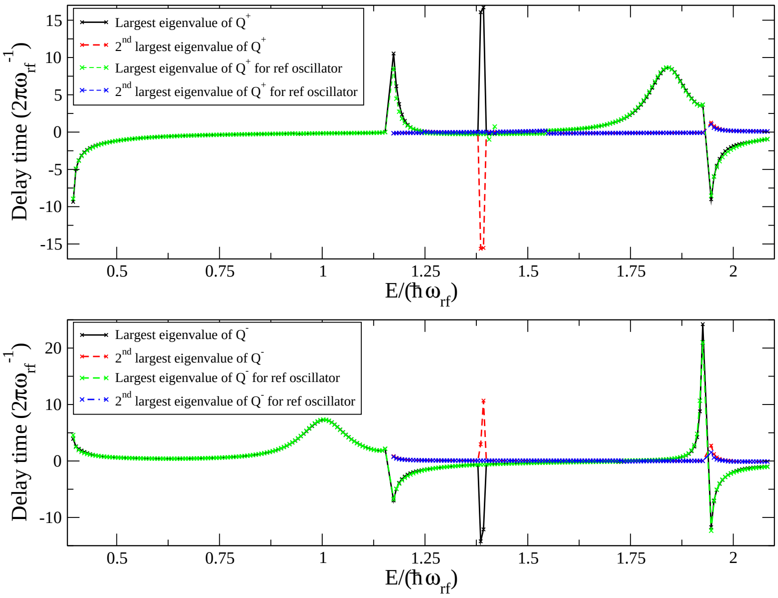

Figure 4.28: Delay time plot. Two largest eigenvalues of + and -parity time delay matrix Q^{+} and Q^{-} are shown for $g = -1, a = 2.4, q = 0.1, m_A/m_I = 0.57$.

the parity dependent S-matrix with respect to energy. Real eigenvalues of this matrix are the actual delay times and indicate the time delay accumulated by the scattering particle during collision. Time delay matrix [91]is given by

$$Q^{\pm} = -i\hbar(S^{\pm})^{\dagger}\frac{dS^{\pm}}{dE}. \tag{4.31}$$

The largest two eigenvalues for the time delay matrix of each parity are plotted against energy. For comparison, the time delay matrix eigenvalues of the reference secular oscillator, defined in Sec.4.7.1 are also plotted. The S-matrix is unitary such that $S.S^{\dagger} \approx \mathbb{I}$, thus $S.S^{\dagger}$ has very low values for the off diagonal elements (usually less than 1×10^{-10} for very well-converged calculations). Thus we take only the real component of the eigentimedelay of the matrix $Q^{\pm}$. Resonance peaks that showed up in reflection coefficients show a positive time delay accumulated by the scattered particle, with a broad profile (in Fig.4.29 and Fig.4.30). The time delays show discontinuities at channel thresholds. The time delay plot for $a = 2.4, q = 0.3$ given in Fig.4.29 and Fig.4.30 show a distinctive peak at energy $E \sim 1.39\hbar\omega_{rf}$ due to micromotion.

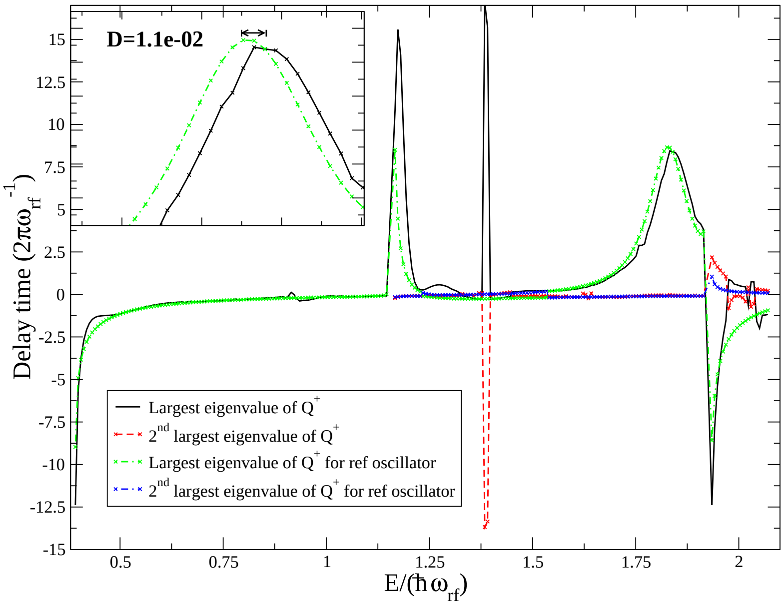

Figure 4.29: Delay time plot. Two largest eigenvalues of +parity time delay matrix Q^+ are shown for $g = -1, q = 0.3, m_A/m_I = 0.57$.

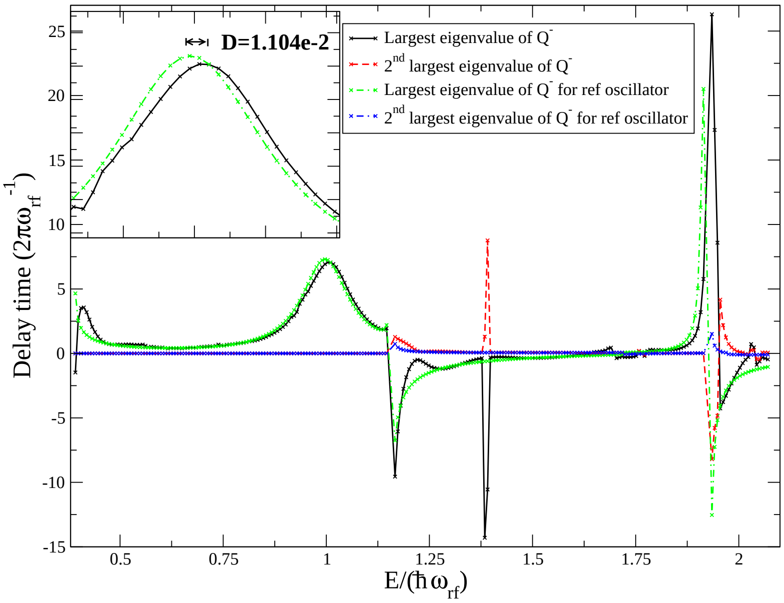

Figure 4.30: Delay time plot. Two largest eigenvalues of -parity time delay matrix Q^- are shown $g = -1, q = 0.3, m_A/m_I = 0.57$.

The positive parity time delay matrix Q^+ is close to the reference oscillator time delay, except for the slight shift in energy that was observed in Fig.4.26. This shift is clearly an effect of micromotion since the threshold discontinuities coincide for the two plots. In this case too, the shift towards larger energy is measured to be $D \sim 1.1 \times 10^{-2}$.

The negative parity time delay Q^{-} for $q = 0.3$ seems to show similar features as the positive parity counter-part. The shift in the resonance peaks with respect to reference oscillator is measured to be the same $D \sim 1.1 \times 10^{-2}$. The time delay at low energies deviates from the behaviour of the reference oscillator. Time delays of both parities, at $q = 0.3$ show the distinctive peak at $E \sim 1.38\hbar\omega_{rf}$.

4.7.2 Collision in Shallow Ion Trap

Lastly, scattering results are obtained for a low static confinement of $a = 0.5$. The density of states within the secular oscillator is high for shallow static confinement and the effect of micromotion is found to be more pronounced even at fairly low values of q, in comparison to the case of tight static confinement $a > 1$. This again confirms the argument that the micromotion is dictated not by the value of q alone but also by the static confinement contribution a and the operating point of the trap with respect to the stability edge, in Fig.A.1.

Resonances and Thresholds

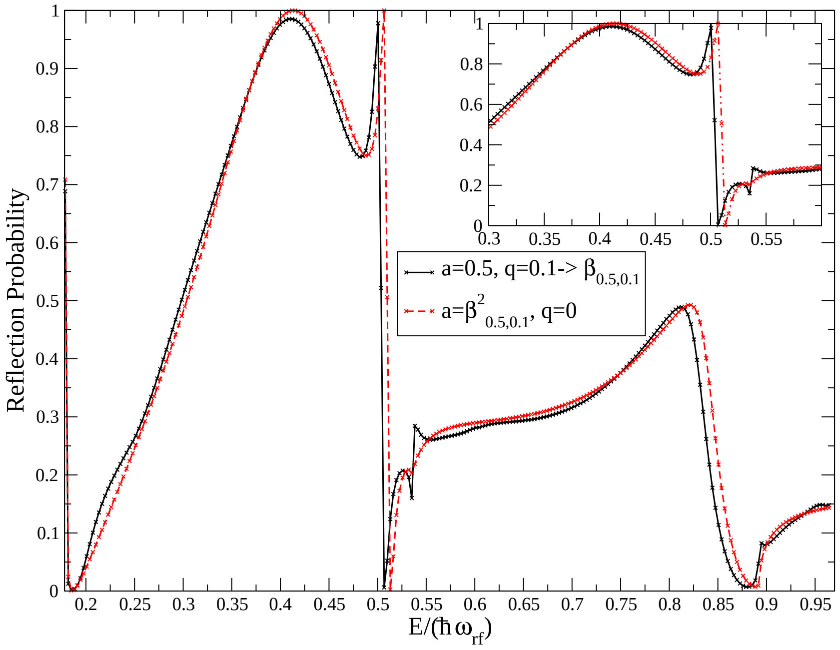

Figure 4.31: Resonances and threshold for shallow confinement with micromotion

Resonance and threshold features are observed in the summed reflection prob-

ability for transitions within the 0^{th} manifold $R_0 = \sum_{j=0}^{N_{\rm op}} |r_{00;j0}|^2$. The nth energy threshold exist at $(n+1/2)\omega_{sec} = (n+1/)\beta\omega_{rf}/2$ and in the manner similar to that explained in Sec.4.7.1, the thresholds and resonance-like features are compared with that obtained due to a secular oscillator of frequency $\beta/2$ and no micromotion.
Even at a low micromotion of $q = 0.1$ a noticeable change in the features is seen in Fig.4.31. The resonance-like peaks are shifted to slightly lower values of energy with respect to those observed in the secular oscillator. The shift in the resonance peaks is possibly proportional to q. This prevents us from further investigating the increase of the shift in resonance peaks with increasing micromotion parameter q.

The resonance in the elastic channel at low energies is again analyzed in Fig.4.32 in terms of the contributions of f^+_{00} and f^-_{00} in a manner similar to Sec.3.2. It is noted that the low energy confinement induced resonance shows contribution only from the even parity scattering amplitude f^+_{00}, as demonstrated for neutral atom scattering by [88].

Time delay analysis along the lines of Sec.3.2 reveals a large negative parity

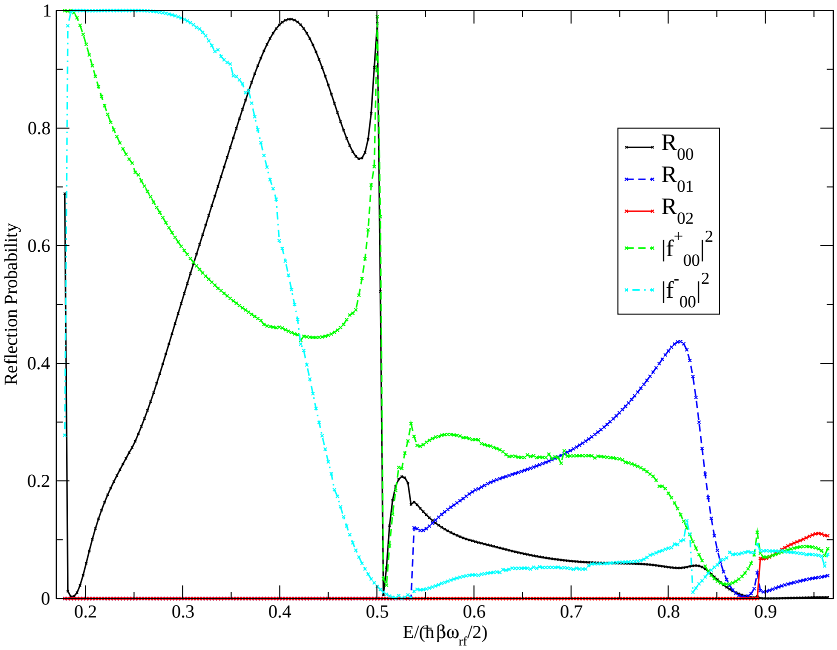

Figure 4.32: Reflection in the elastic channel R_{00} and contribution of f^+_{00} and f^-_{00} to the peaks at $g = -1, a = 0.5, q = 0.1, m_A/m_I = 0.57$.

scattering amplitude f^-_{00} elastic channel contribution to the resonance at around $E \approx 0.814\hbar\omega_{rf}$ in Fig.4.31, by noting the broad long lived time delay for the resonance at this location in Fig.4.33, bottom panel. The sharp discontinuity at

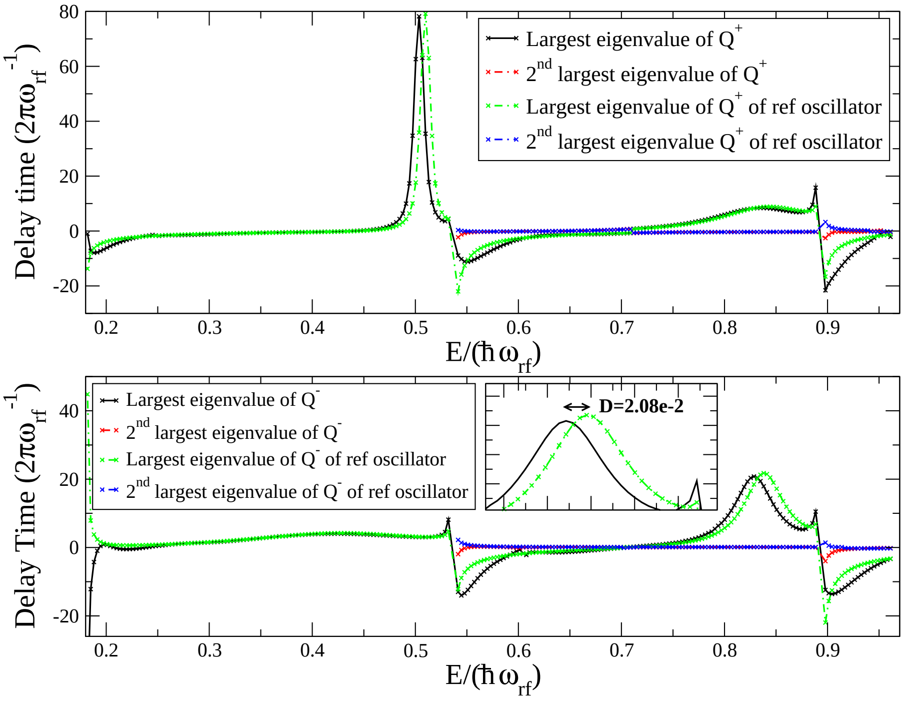

Figure 4.33: Delay time plot. Two largest eigenvalues of -parity time delay matrix Q^- are shown $g = -1, a = 0.5, q = 0.1, m_A/m_I = 0.57$.

$E \approx 0.536\hbar\omega_{rf}$, just after the $n = 1$ channel threshold in the plot, is absent in the reference oscillator curve in Fig.4.31. Time delay at this point shows a long lived, inverted bell-shape but with negative time delay (Fig.4.33, bottom panel).

4.8 Conclusions

We have presented methods to solve the 1D collision problem with micromotion with a fair bit of success. Linear propagation, its spectral element analogue and angular propagation schemes are described and implemented to solve this problem, with varying degrees of success. The associated error plots describing the limits of operation of the methods are elucidated. It is noted that the angular propagation method is comparatively more robust over a range of ion trap parameters a and q.

The nature of the time dependent ion traps, the resulting Floquet energy spectrum of the ion and its properties, the wavefunction of the ion both in time and frequency domain are described. The reason for converged results over a limited range of trap parameters is explained, with respect to how increased micromotion complicates the dynamics of the ion. The atom-ion collision problem is described, along with a justification as to why the delta pseudopotential instead of the long range atom-ion potential is a simplification and neglects the dipole forces that come into play along with the presence of micromotion. Ion cooling are found to be rather low. We have presented an argument to state as to why in our trap parameters, isolating the inter-manifold transitions highlights the effect of trap micromotion. The comparatively low ion cooling probabilities seem to agree qualitatively with experimental results, shown in Fig.1.1 and Fig.1.3. Though the classical calculations in [49], [50] point to keeping a low mass ration $m = m_A/m_I$, our results show that ion cooling probability seems to increase with mass ratio. It is argued that the disagreement could be due to the fact that our model system uses a delta pseudopotential, unlike in [49]. In agreement with [47], we find that the ion cooling is negligible for trap parameters that lie well within and away from the stability edge of the Mathieu stability region and calculations with trap parameters near the edge of the stability region is not possible by the numerical methods we use, as evidenced by the growing relative error on our calculations for fixed a and increasing q. Atom heating probability is found to be rather non-negligible in our methods, in qualitative agreement with the experimentally measured trend of atom loss from the trap. To conclude, we also find confinement induced resonances, whose resonant origin is confirmed by the positive time delays for each parities, as shown in Sec.4.7.1.

Chapter 5

Three Dimensional Atom-Ion Effective Interaction

The study of micromotion effects is extended to 3D in spherical coordinates. The problem would be extremely large with six degrees of freedom for a two body collision problem in 3D. Instead, we choose to study a simplified model where we assume a heavy atom and lighter ion in a time dependent Paul trap that is centered on the atom. As with the earlier chapters, a delta pseudopotential is used instead of the long range atom-ion polarization potential $(-C_4/r^4)$. Such a model system is effectively an ion in a Paul trap with a delta spike at the trap centre. Resonances can occur between the eigenstates of the trap and molecular bound states due to the atom-ion potential. If the system parameters like position of the atom within the Paul trap or the scattering length can be varied, such trap-induced shape resonances could be of interest since the real atom-ion potential is long range and interplay of trap eigenstates and molecular bound states can be expected to be more vigorous for such a system. Since we use a regularized 3D delta pseudopotential instead of the real long-range potential, amplitude and sign of the s-wave scattering length related to the delta pseudopotential coupling by $(a_{3D} = m_I g_{3D}/(2\pi\hbar^2))$. The s-wave scattering length can then be varied using magnetic fields to reveal trap induced shape resonances of the system. We aim to find the eigenvalues of this bound state problem at different s-wave scattering lengths. Avoided avoided crossings between the Floquet states are found and by estimating the non-adiabatic transition probabilities and switching speed of the scattering length, we explore the possibility of using these avoided crossings for quantum control applications such as adiabatic state transfer of the ion to different trap states [6,39,40]. The possible limitations in the implementation of an atom-ion phase gate [37] arising due to micromotion is discussed..

The effective atom-ion interaction in this model is revealed in the interaction of ion states in a Paul trap with a delta potential in the trap centre. From

Sec.4.1 it is seen that the constraint on the trapping potentials in 3D would give either a 2D time dependent confinement, with electrostatic confinement in the third dimension or a time dependent anisotropic 3D confinement of the ion. We choose the latter, a cylindrical Paul trap for this system. From Eq.(4.3), it is seen that the field has an anisotropy ratio of 1 : 2, which gives the micromotion parameters for the trapping potential in the three dimensions as $a_x = a_y = -2a_z$ and $q_x = q_y = -2q_z$.

5.1 Micromotion Hamiltonian

The time dependent potential for a cylindrical Paul trap (See [102]) is given by

$$V(x,y,z,t) = \frac{1}{2}\frac{m_I\omega_{rf}^2}{4}\left[a + 2q\cos(\omega_{rf}t)\right](2z^2 - x^2 - y^2). \tag{5.1}$$

Re-writing the term $(2z^2 - x^2 - y^2) = 2z^2 - r^2$, this potential has an anisotropic term along the $\hat{z}$ axis, resulting in the cylindrical symmetry. The Hamiltonian in radial coordinate is given by

$$\hat{H} = -\frac{\hbar^2}{2m_I}\frac{d^2}{dr^2} + \frac{\hbar^2}{2m_I}\frac{\hat{L}^2}{r^2} + \frac{1}{2}\frac{m_I\omega_{rf}^2}{4}[a + 2q\cos(\omega_{rf}t)](3z^2 - r^2) + g_{3D}\delta(r)\frac{\partial}{\partial r}r \tag{5.2}$$

where $g_{3D} = 2\pi\hbar^2 a_{3D}/\mu$. We will henceforth use atomic units (setting $\hbar = 1$). The time dependent Schrödinger equation is given by

$$\left[-\frac{1}{2m_I}\frac{d^2}{dr^2} + \frac{1}{2m_I}\frac{\hat{L}^2}{r^2} + \frac{1}{2}\frac{m_I\omega_{rf}^2}{4}[a + 2q\cos(\omega_{rf}t)](3z^2 - r^2) + g_{3D}\delta(r)\frac{\partial}{\partial r}r\right]\Psi(r,\theta,\phi,t) = i\frac{\partial}{\partial t}\Psi(r,\theta,\phi,t) \tag{5.3}$$

Performing the Fourier-Floquet decomposition, similar to what was done in Sec.4.2, we assume Floquet type solutions given by

$$\Psi(r,\theta,\phi,t) = e^{-iEt}\sum_{n=-\infty}^{+\infty} e^{in\omega_{rf}t}\Phi(r,\theta,\phi,n) \tag{5.4}$$

and substituting these solutions into Eq.(5.3), multiply it by $e^{i2n'\omega_{rf}t/2}/\sqrt{T_{rf}}$ and integrating over a time period of the rf-field, to get the Schrödinger equation in frequency domain as

$$\left[-\frac{d^2}{dr^2}+\frac{\hat{L}^2}{r^2}+\frac{m_I^2\omega_{rf}^2}{4}a(3z^2-r^2)+2m_I g_{3D}\delta(r)\frac{\partial}{\partial r}r+2m_I n'\omega_{rf}\right]\Phi(r,\theta,\phi,n')+ \\ \frac{m_I^2\omega_{rf}^2}{4}q(3z^2-r^2)\Phi(r,\theta,\phi,n'+1)+\frac{m_I^2\omega_{rf}^2}{4}q(3z^2-r^2)\Phi(r,\theta,\phi,n'-1)= \\ 2m_I\bar{E}\Phi(r,\theta,\phi,n') \quad (5.5)$$

where $\bar{E}=E/\omega_{rf}$. Let E denote $\bar{E}$ hence forth. The first term within square brackets on the left hand side is a diagonal term in the matrix representation of the Hamiltonian in the Fourier-Floquet basis (n' index) and the second term forms the $+1$ and -1 diagonals of the matrix. This is the eigenvalue equation we solve to calculate the ion states in the presence of a delta potential in the trap centre. The anisotropy term can also be written as $(3z^2-r^2)=r^2(3\cos^2(\theta)-1)$. It is proportional to a spherical harmonic given by

$$Y_2^0(\theta,\phi)=\frac{1}{4}\sqrt{\frac{5}{\pi}}(3\cos^2(\theta)-1) \quad (5.6)$$

It must be noted that since the potential has the spherical harmonic Y_2^0 term, it implies the solutions have cylindrical symmetry and m quantum number is conserved. Thus we fix $m=0$ for the problem and method will only detect ion states with $L_z=0$. For simplicity we drop the argument ϕ in the solution and rewrite $\Psi(r,\theta,\phi,t)\to\Psi(r,\theta,t)$ and $\Phi(r,\theta,\phi,n')\to\Phi(r,\theta,n')$. Further the dependence of $\Phi(r,\theta,n')$ on the Fourier-Floquet basis index n' is expressed by building multiple diagonal blocks of the Hamiltonian in Eq.(5.5), with different values of n'. The summation term in Eq.(5.5) is truncated over a basis $n'=(-N_f,+N_f)$ with N_f chosen sufficiently large to correctly calculate the eigenstates. We expand the solutions in spherical harmonics as

$$\Phi(r,\theta,n')=\sum_{l=0}^{l_{max}}R_l(r,n')Y_l^0(\theta) \quad (5.7)$$

Thus Eq.(5.5) can be represented on the spherical harmonic basis. Substituting Eq.(5.8) into Eq.(5.5), multiplying from the left by $Y_{l'}^0(\theta,0)$ and integrating over θ, we get

$$\left[-\frac{d^2}{dr^2}+2m_I g_{3D}\delta(r)\frac{\partial}{\partial r}r+2m_I n'\omega_{rf}\right]R_{l'}(r,n')+\sum_l\left\langle Y_{l'}^0\left|\frac{\hat{L}^2}{r^2}\right|Y_l^0\right\rangle R_l(r,n') \\ +\sum_l m_I^2\omega_{rf}^2\sqrt{\frac{\pi}{5}}\left\langle Y_{l'}^0\middle|Y_2^0\middle|Y_l^0\right\rangle r^2\left[aR_l(r,n')+qR_l(r,n'-1)+qR_l(r,n'+1)\right]= \\ 2m_I ER_{l'}(r,n') \quad (5.8)$$

The first term on the left hand side in the above is diagonal in both l and n' basis, the second term has a diagonal structure in both l and n' basis and third term has a tri-diagonal structure (with $0^{th}, +1$ and -1 diagonals since an even parity l basis is chosen) in the l basis and is diagonal in n' basis. Let the total Hamiltonian be written as $\hat{H} = \hat{K} + \hat{V}$, where the matrix elements of the operators $\hat{K}$ and $\hat{V}$ are given by

$$K_{l'n'ln}(r) = -\delta_{l'l}\delta_{nn'}\frac{\partial^2}{\partial r^2} \tag{5.9}$$

$$\begin{aligned} V_{l'n'ln}(r) = \Bigg[\delta_{nn'}\left\langle Y_{l'}^0 \middle| \frac{\hat{L}^2}{r^2} \middle| Y_l^0 \right\rangle + 2m_I g_{3D}\delta(r)\delta_{l'l}\delta_{nn'}\frac{\partial}{\partial r}r + 2m_I\delta_{l'l}\delta_{nn'}n'\omega_{rf} + \\ \frac{m_I^2\omega_{rf}^2}{4}[a\delta_{nn'} + q(\delta_{n,n'-1} + \delta_{n,n'+1})]4\sqrt{\frac{\pi}{5}}\left\langle Y_{l'}^0 \middle| Y_2^0 \middle| Y_l^0 \right\rangle r^2\Bigg] \end{aligned} \tag{5.10}$$

where the operator elements $V_{l'n'ln}(r)$ form the diabatic term and it is tri-diagonal in the ll' and nn' indices of the spherical harmonic and Floquet basis respectively. The problem now has 3 degrees of freedom namely r, θ (or the spherical harmonic index l) and t (or its conjugate n', since the Hamiltonian is in frequency domain). Like the 1D problem, the potential has a tridiagonal structure in the n' basis. Since the potential has the form Y_2^0, matrix element on spherical harmonics basis with $m = 0$ is given in [115], p.618 by

$$\begin{aligned} \int Y_{l'}^{m'}(\theta,\phi)Y_2^0(\theta,0)Y_l^m(\theta,\phi)d\Omega = \\ (-1)^m\sqrt{\frac{5(2l+1)}{4\pi(2l'+1)}}\langle l'2,00|l,0\rangle\langle l'2,m'0|l,-m\rangle \end{aligned} \tag{5.11}$$

where $m = 0$ and $m' = 0$. The potential is tridiagonal in the spherical index l as well. The radial coordinate is split into sectors and high order local polynomial basis is chosen to implement the Spectral Element Method solution to solve this problem (Sec.2.4). The Hamiltonian is expressed in the form of a sparse matrix, as described in Eq.(2.48). This sparse eigenvalue problem is then solved with FEAST [75, 76], which is a sparsity optimized diagonalization package that converts the eigenvalue problem to a set of linear equations which is solved with PARDISO [77-81], called from within FEAST itself. The package starts with a randomly generated trial eigenfunctions which are optimized over a pre-determined number of iterations. The search interval for the energy E specified is $(0, \hbar\omega_{rf})$, since this corresponds to the first Brillouin zone of the Floquet spectrum which has an $\hbar\omega_{rf}$ modulo structure. In atomic units, $\hbar\omega_{rf} = 6.047 \times 10^{-9} a.u.$ Calculations are done for a Be^+ ion in a Paul trap, with $\omega_{rf} = 2\pi \times 250 MHz$.

5.1.1 Delta Pseudopotential Vs Long Range Potential

Since the Hamiltonian is only for the separable relative motion in a system with low ion mass and high atom mass, the system consisting of the low mass Be$^+$ ion is chosen. The results could be applied to the systems like Cs-Be$^+$ with mass ratio $m = m_A/m_I = 14.75$, Rb-Be$^+$ with mass ratio $m = m_A/m_I = 9.6$ or Yb-Be$^+$ with mass ratio $m = m_A/m_I = 19.2$. The use of delta pseudopotential simplifies the long range character of the real potential and is equivalent to an ion in very loose traps. Like in Sec.4.2.1, the characteristic length of the realistic potential for these species is $R^* = 2469.62a_0$ for Cs-Be$^+$, $R^* = 2176.55a_0$ for Rb-Be$^+$ and $R^* = 1499.66a_0$ for Yb-Be$^+$. Though direct qualitative comparisons to experiments cannot be made with the results obtained with the delta pseudopotential, it would help in understanding the physics of adiabatic transitions under the influence of micromotion and how it affects the proposed implementation of phase gates and adiabatic state transfer in atom-ion systems. The Be$^+$ ion trap rf-frequency is $238MHz$ reported in experiments like [109]. We take it to be $250MHz$ and run our calculations for trap parameters $a_x = a_z = 0$ and $q_x = 0.1(q_z = -0.2)$, giving secular oscillator lengths of $a_{ho,x} \approx 533.04a_0$ and $a_{ho,z} \approx 375.80a_0$ in the $\hat{x}(\hat{y})$ and $\hat{z}$ axes. In this case too we notice $R^* >> a_{ho}$ for the Yb-Be$^+$ system. Calculation are made for for micromotion parameters of $a = 0$ and $q = 0.1$ since in 3D the stability plot for the ion is the overlapping region of the stability regions of different axes, as shown in Fig.5.1.

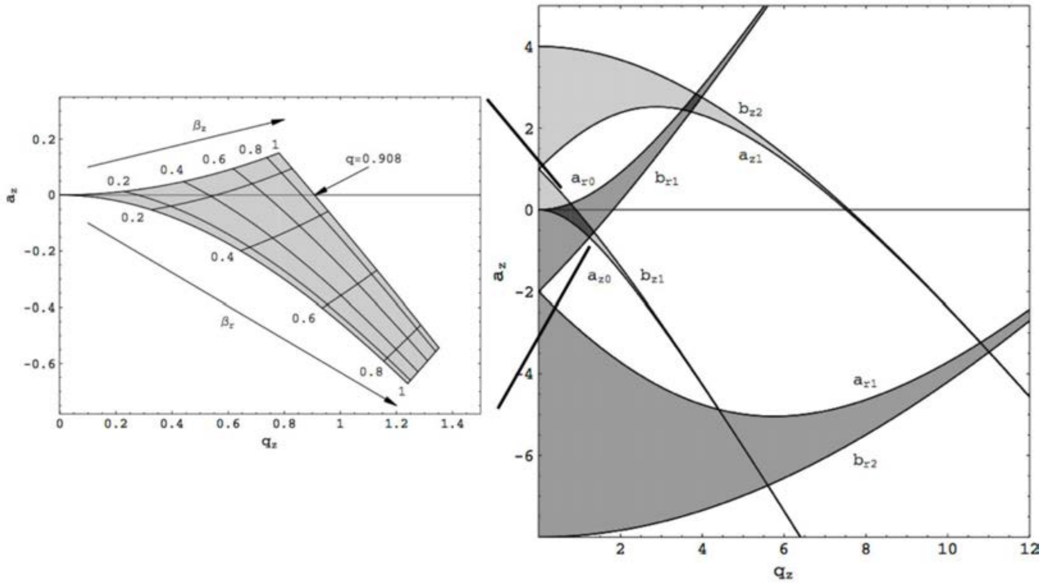

Figure 5.1: Stability region for a 3D Paul trap. Image from Major et al. [102]

5.2 Floquet Spectrum

Since the atom-ion potential is simplified by the use of a regularized delta pseudopotential, the computed spectrum for non-zero g_{3D} will be of even parity only, since the delta potential couples only to s-wave. Only states with $L_z = 0$ are computed.

Since Floquet spectrum is calculated over a large, finite basis, a large number of states detected in the given search interval are badly converged. For the system parameters we use, FEAST calculates about 900 ~ 1000 states and about 40 states are found to be well converged. We explain in this section the eigenstate properties we calculate to define a FEAST state as well converged. As explained earlier in Sec.4.1, these levels will include excited states from manifolds shifted from the reference manifold by $n'\hbar\omega_{rf}$, where $n' < 0$. To eliminate these badly converged states and select only the good, well converged states, tests are performed on the final eigenvalues and eigenfunctions calculated by FEAST.

5.2.1 Reference Static Oscillator

We have explained in Ch.4 the notion of a secular oscillator in the presence of micromotion. The effective trapping frequency of the ion in the three separable coordinates depends on the Mathieu characteristic exponent β of the separable classical potential for the particular coordinate, which for a 3D Paul trap are $\beta_x = \beta_y$ and β_z respectively. The ion quasi energies calculated using FEAST are expected to show the secular nature of the oscillators in the three axes. Thus as a reference, we can calculate the exact spectrum for a time independent anisotropic 3D oscillator with aspect ratio 1 : 2 which goes as

$$E_{exact} = \frac{\hbar\omega_{rf}}{2}[(n_\rho + 1)\beta_x + (n_z + \frac{1}{2})\beta_z] + n'\hbar\omega_{rf} \tag{5.12}$$

where $n_\rho = n_x + n_y$, the secular oscillator frequency is $\beta_x\omega_{rf}/2$ and $\beta_z\omega_{rf}/2$ in the $\hat{x}(\hat{y})$ and $\hat{z}$ directions. The constraint on even parity solutions requires that $n_x + n_y + n_z = j$, where j is any positive even number and the constraint of $L_z = 0$ implies n_ρ is conserved and must be even to give a total positive parity even if $n_z = 0$. This further constraints n_z to be even. The Floquet spectrum in the fundamental manifold is calculated with $n' = 0$ in Eq.(5.12). Since the Floquet spectrum has an $\hbar\omega_{rf}$-modulo structure, multiple copies of the fundamental manifold exist, with each copy shifted by $n'\hbar\omega_{rf}$ where n' is an integer. This means in any interval of $(0, \hbar\omega_{rf})$, all states are unique and are also composed of the excited states from all low lying manifolds, which can be calculated by varying n' in the interval $n' = (0, -N_f)$ in Eq.(5.12). This provides a way to check if the FEAST spectrum calculated at $a_{3D} = 0$ is correct.

Further the change in the bound state spectrum by varying s-wave scattering length is plotted for a reference static oscillator. Comparison of such a change with the change in the spectrum for the original problem with micromotion serves to isolate the effect of micromotion in creating avoided crossings among the multitude of the ion states detected. The reference oscillator is a time independent anisotropic 3D oscillator with a regularized delta perturbation at the origin. In keeping with the secular frequency for each coordinate calculated for the ion trap with micromotion, the reference oscillator frequencies in the three spatial coordinates are chosen as $\beta_i^2\omega_{rf}$ where $i = x, y, z$ and $\beta_x = \beta_y$. The time independent Schrödinger equation in atomic units is given by

$$\left[\frac{1}{2m_I}\frac{\partial^2}{\partial r^2} + \frac{1}{2m_I}\frac{\hat{L}^2}{r^2} + \frac{1}{2}\frac{m_I\omega_{rf}^2}{4}\left(\beta_x^2 x^2 + \beta_x^2 y^2 + \beta_z^2 z^2\right) + g_{3D}\delta(r)\frac{\partial}{\partial r}r\right] \Phi(r,\theta,\phi) = E_{ref}\Phi(r,\theta,\phi) \quad (5.13)$$

Let the solutions be $\Phi(r) = \sum_l R_l(r)Y_l^0(\theta,0)$, since we choose to fix $L_z = 0$, giving $m = 0$ like the original problem with micromotion. From the lowest order approximation (See 53 or Appendix.A.2) that $\beta = \sqrt{a + q^2/2}$. This gives a reference oscillator with secular oscillator frequency for each coordinate i.e $\beta_i\omega_{rf}/2$, with $i = x, y, z$. With $z = r\cos(\theta)$, the potential term can be reduced as

$$\frac{1}{2}\frac{m_I\omega_{rf}^2}{4}\left(\beta_x^2 x^2 + \beta_x^2 y^2 + \beta_z^2 z^2\right) = \frac{1}{2}\frac{m_I\omega_{rf}^2}{4}\left(\beta_x^2 r^2 + \left(\beta_z^2 - \beta_x^2\right) r^2\cos^2(\theta)\right) \quad (5.14)$$

where we take $\cos^2(\theta) = \left(\frac{4}{3}\sqrt{\frac{\pi}{5}}Y_2^0 + \frac{1}{3}\right)$ from Eq.(5.6). The potential thus reduces to a sum of a diagonal term and a tri-diagonal term in the spherical harmonic basis. Re-writing the Schrödinger equation in Eq.(5.13) on the spherical harmonic basis on the lines of Eq.(5.8) we have

$$\left[\frac{d^2}{dr^2} + 2m_I g_{3D}\delta(r)\frac{d}{dr}r + \frac{m_I^2\omega_{rf}^2}{4}r^2\left(\beta_x^2 + \frac{1}{3}\left(\beta_z^2 - \beta_x^2\right)\right) + \frac{l(l+1)}{r^2}\right]R_{l'}(r) + \sum_l m_I^2\omega_{rf}^2\frac{1}{3}\sqrt{\frac{\pi}{5}}\left\langle Y_{l'}^0 \middle| Y_2^0 \middle| Y_l^0\right\rangle r^2\left(\beta_z^2 - \beta_x^2\right)R_l(r) = 2m_I E_{ref}R_{l'}(r) \quad (5.15)$$

The first and second terms on the left hand side are diagonal and the third term is tri-diagonal with 0^{th}, +1 and −1 diagonals in the positive parity spherical harmonic l' basis. This reference oscillator is also solved with FEAST.

The energy levels shift up or down with respect to $+a_{3D}$ or $-a_{3D}$. As $a_{3D} \to \pm\infty$, the energy levels reach the same asymptote, giving the spectrum of the unperturbed anisotropic oscillator spectrum. In the absence of trapping potentials, the delta pseudopotential in 3D gives rise to a single bound state (molecular level)

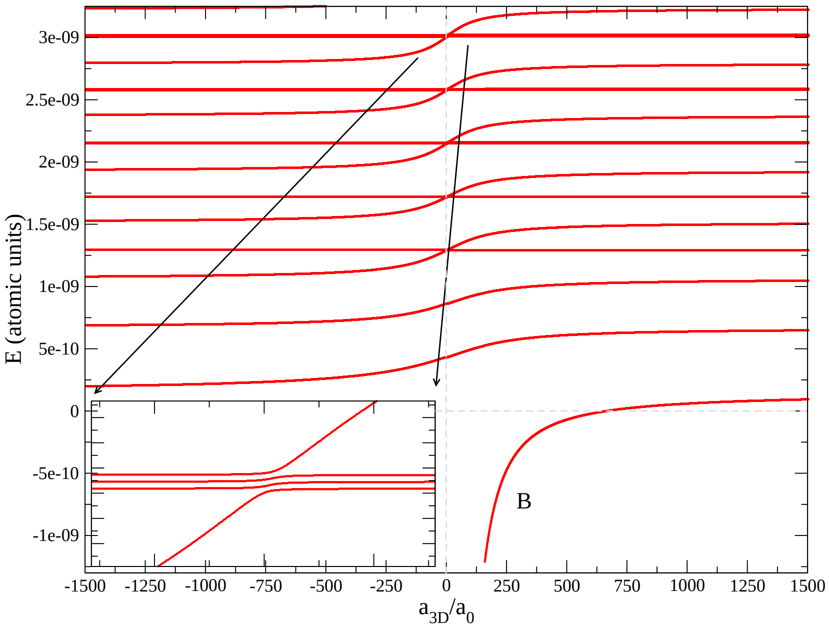

Figure 5.2: Evolution of the reference anisotropic oscillator states are shown as a function of a_{3D}. Though the levels show a periodic pattern, at $E >> 0$ many states are found that are very closely spaced (inset). A single molecular level (labelled B) arising due to the regularized delta potential is seen at positive a_{3D}, identical to [108].

at positive a_{3D}, with binding energy going as $1/a_{3D}^2$. But in the presence of a trapping potential, the bound state energy is shifted up (See 108). We note that the energy level rises sharply for the bound molecular level and is useful for application in phase gates, as shall be explained in Sec.5.4.

5.3 Diabatic-by-Sector Method

Initial trials of the problem indicated that due to the 1 : 2 anisotropy and the purely dynamical trapping potential, the basis size required in the l and n' degrees of freedom are too large and requires very large memory, with $l_{max} = 80$ and $n'_{max} = 80$. See Fig.5.3 for convergence with the l and n' primitive basis. Since the basis of isotropic spherical harmonics (since $L_z = 0$) are chose to represent anisotropic states, fairly high order spherical harmonics are required to well describe states that are highly anisotropic and localized far from the trap centre (long range) i.e excited trap states. This increase in the primitive basis drastically increases the matrix size.

Though the Hamiltonian is sparse, the full matrix size exceeded dimensions of

≈ 4million. Just a fraction of the total elements are non-zero and only those values are stored in the memory but the solvers by design are memory intensive and require memory in excess of the maximum available per machine of $128GB$ for matrix of such dimensions. To overcome this drawback and to choose a smaller, better defined basis within each sector, Diabatic-by-Sector (See [110-114]) method is attempted.

In a general sparse Hamiltonian representation, each grid point in a sector is a sparse matrix in the various internal degrees of freedom of this problem i.e Floquet basis index n' and spherical harmonic basis index l. The diabatic-by-sector method is used to reduce the matrix dimensions at each grid point. From Eq.(5.10), the diabatic term is taken at the midpoint r_m^i of the i^{th} sector, giving a matrix $\mathbb{V}(r_m^i)$. This primitive basis matrix in the i^{th} sector is of dimensions $(N_{el}^i \times N_{el}^i)$, where $N_{el}^i = l_{max}^i(2(n')^i + 1)$ and l_{max}^i, $(n')^i$ are the sizes of spherical and Floquet basis for the i^{th} sector. This matrix is diagonalized to given eigenfunctions

$$\mathbb{V}(r_m^i)\mathbf{U}_\alpha(r_m^i) = \epsilon_\alpha \mathbf{U}_\alpha(r_m^i) \tag{5.16}$$

where α is the solution index. Here again, it is known that the eigenvalue spectrum ϵ_α is unbounded since $\mathbb{V}(r_m^i)$ is a Floquet Hamiltonian. Similar to the eigenstate analysis done for FEAST eigenstates, basis dependent modulii defined for each of the states $\mathbf{U}_\alpha(r_m^i)$ are calculated. The eigenfunctions $\mathbf{U}_\alpha(r_m^i)$ are composed of internal coordinate indices n and l given by $U_{nl,\alpha}(r_m^i)$, thus the partial modulii are defined as

$$||\mathbf{U}_\alpha(r_m^i)||_{l_{max}}^2 = \sum_{n'=-N_f}^{+N_f} ||U_{n'l_{max},\alpha}(r_m^i)||^2 \text{ and}$$

$$||\mathbf{U}_\alpha(r_m^i)||_{n'_{max}}^2 = \sum_{l=0}^{l_{max}} \left(||U_{-N_f l,\alpha}(r_m^i)||^2 + ||U_{+N_f l,\alpha}(r_m^i)||^2\right) \tag{5.17}$$

These properties are computed to check and select states $\mathbf{U}_\alpha(r_m^i)$ that are well defined in the primitive basis of l and n' internal coordinates. Only states $\mathbf{U}_\alpha(r_m^i)$ with the two partial modulii in Eq.(5.17) lesser than 10^{-5} are chosen as an adiabatic basis function. The primitive basis in spherical harmonics index is limited to a maximum size of $l = (0, 20)$ at short range and $l = (0, 80)$ at long range and in Floquet basis it is a minimum of $n' = (-20, +20)$ at short range and $n' = (-80, +80)$ at large range, with linearly scaled variation from one sector to the next. We select a user defined number of basis functions N_{ad} for each sector i such that $N_{ad} <= (l^i(2(n')^{(i)} + 1))$. This results in a rectangular transformation matrix for each sector i denoted by $\mathbb{U}_D(r_m^i)$ composed of the chosen basis functions along each column. This matrix is used to transform the sparse matrix in primitive basis to a full matrix as $\tilde{\mathbb{V}}(r) = \mathbb{U}_D(r_m^i)^T \mathbb{V}(r) \mathbb{U}_D(r_m^i)$. The resulting matrix $\tilde{\mathbb{V}}(r)$ is smaller in total size but gives a full matrix at each grid point. For the given problem with Be^{+} ion, the oscillator lengths in the $\hat{x}(\hat{y})$ and $\hat{z}$ directions are $a_{ho,x} = 533\ a_0$ and $a_{ho,z} = 375.8\ a_0$ respectively. Thus a grid over the interval $r = (0, 6000a_0)$ is taken, with sectors of length $dr = 750\ a_0$. For a converged calculation, diabatic basis of $N_{ad} = 350$ basis functions are required. This is verified by the accuracy of the ground state and initial few states of the ion trap calculated by FEAST by comparison with the exact spectrum calculated with Eq.(5.12). This method is seen to give good convergence in calculating the low lying states of the fundamental manifold of the ion spectrum. Fig.5.3 shows the accuracy of calculating the ground state eigenvalue. As a test parameter, the relative error of the states in the 0^{th} (fundamental) manifold calculated by FEAST are compared with respect to the exactly calculated value, for trap parameters of $a = 0, q = 0.1$.

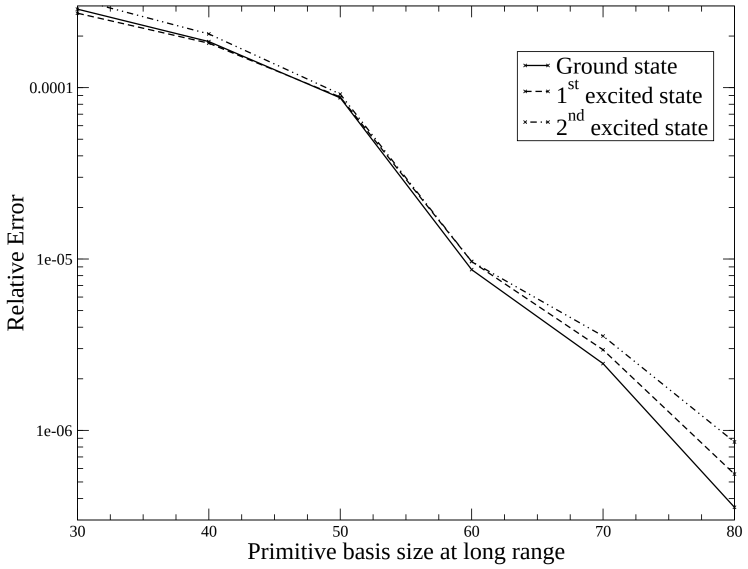

Figure 5.3: Relative error of the calculated ground state energy E_0 and the first two excited states as a function of the primitive basis size. The basis in both l and n' equal in size.

Much of the computation time is spent in diagonalizing the diabatic matrix $\mathbb{V}(r_m^i)$ in each sector, with the final sector taking the maximum time. For the given input values of the grid and primitive bases, the code takes around 11 hours, of which it needs 9 hours to diagonalize all the sector matrices. The sector basis transformation matrices are written to disk to avoid diagonalization at each point, if we only intend to vary the scattering length a_{3D}. The first sector is always taken in its primitive, undiagonalized basis to accommodate the changing initial condition with the delta pseudopotential at $r = 0$. Effectively the method only requires 1.5 ~ 2 hours to compute the ion states with FEAST and calculates

135 states as per the convergence criteria we define. In comparison, a calculation in fully primitive basis (Hamiltonian is build and only FEAST is used) required nearly 14 ~ 15 hours for the calculation with grid dimensions of $r = (0, 6000a_0)$, primitive basis varying from short range to long range as $l_{max} = (20, 60)$ and $n'_{max} = \pm N_f = (\pm 20, \pm 60)$. This method calculated around 40 states as per the defined convergence criteria.

5.4 Adiabatic Passage and Phase Gate

We briefly describe some notions of Landau Zener physics with respect to bound states. The basic idea of operation of an atom-ion phase gate is provided.

Adiabatic Passage
When a parameter for a system with many bound states is varied, certain states show evidence of coupling. These occur when two states cross as a function of the input parameter. Let the two states be labelled $|\psi_1(t_1)\rangle$ and $|\psi_2(t_1)\rangle$ at time t_1 and t_2 with energies E_1 and E_2 respectively. In the initial state we have $E_1|_{t_1} \neq E_2|_{t_1}$ and by varying this parameter with time, the states evolve reducing the energy gap $\Delta E = |E_1 - E_2| \to 0$, until they are equal at $E_1|_{t_2} = E_2|_{t_2}$. The eigenstate of this system now is a linear combination of $|\psi_1\rangle$ and $|\psi_2\rangle$. Such states form an avoided crossing and depend critically on the rate of change of the system parameter. For example, in the Fig.5.4 if the system parameter is varied very rapidly state $|\psi_1(t_1)\rangle$ skips any possibility of interaction with the coupled

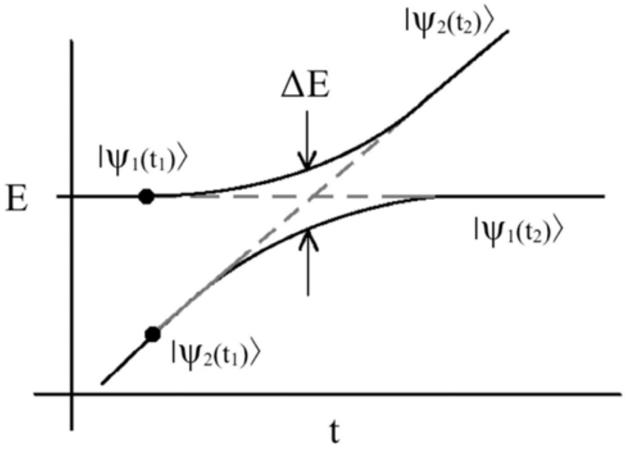

Figure 5.4: Avoided crossing of two coupled states that evolve adiabatically.

state $|\psi_2(t_1)\rangle$ and just evolves into state $|\psi_1(t_2)\rangle$. This is also called a non-adiabatic (diabatic) passage. But if the parameter is varied slowly, an adiabatic passage is possible such that $|\psi_1(t_1)\rangle$ ($|\psi_2(t_1)\rangle$) very smoothly evolves into $|\psi_2(t_2)\rangle$ ($|\psi_1(t_2)\rangle$). Thus it is possible with slow switching to effectively *change* a particle from one of the states to the other. The requirement for such transitions arise in the implementation of atom-ion phase gates [37] and coherent processes like transferring a particle between states [38, 39]. The energy gap ΔE at the closest separation between the states and the rate of change of the system parameter are the crucial parameters that decides successful adiabatic transfer. The probability of a non-adiabatic passage is generally given by

$$P_{na} = \exp\left(-2\pi \frac{|\Delta E|^2}{\hbar |\partial E_2(t) - \partial E_1(t)|/\partial t}\right) \tag{5.18}$$

In a system of an ion in a Paul trap with Floquet spectrum, there could be many avoided crossings that evolve when a tuning parameter is varied. For the model problem under consideration, the scattering length a_{3D} (i.e pseudopotential coupling g_{3D}) can be tuned with magnetic fields, on the lines of the method to address Feshbach resonances to attain $\partial a_{3D}/\partial t$. The probability of non-adiabatic passage (in atomic units) can then be given by

$$P_{na} = \exp\left(-2\pi \frac{|\Delta E|^2}{\partial a_{3D}/\partial t \, |\partial E_2(t) - \partial E_1(t)|/\partial a_{3D}}\right) \tag{5.19}$$

The aim would be to reduce the probability P_{na}. We show the behaviour of P_{na} with switching time for a couple of avoided crossings found between the states of the fundamental band of the Floquet spectrum.

Atom-Ion Phase Gate

The idea of a phase gate is fairly simple, in that it exploits the control over coupling between energy levels with external magnetic fields, by essentially changing the scattering length [37-39]. The atom and ion are trapped in individual potentials and their separation can be varied. The problem we deal with is one with trap separation set to zero and held constant. Multiple avoided crossings are observed in the ion Floquet spectrum with varying scattering length. The qubit states are encoded in the internal hyperfine structure of the particles (atom and ion), denoted by $|ij\rangle = |i\rangle_I |j\rangle_A$ with $i, j = 0, 1$. A conditional phase gate is realized, by the following

$$\begin{aligned}
|00\rangle &\rightarrow^{U_B} e^{i\phi_{00}} |00\rangle \rightarrow^{U_S} |00\rangle \\
|01\rangle &\rightarrow e^{i\phi_{01}} |01\rangle \rightarrow |01\rangle \\
|10\rangle &\rightarrow e^{i\phi_{10}} |10\rangle \rightarrow |10\rangle \\
|11\rangle &\rightarrow e^{i\phi_{11}} |11\rangle \rightarrow e^{i\phi} |11\rangle
\end{aligned} \tag{5.20}$$

The first transformation U_B is the application of the external field, that forms the actual gate operation and the second transformation U_S can reverse the phase $e^{i\phi_{ij}}$ accumulated due to the transformation U_B, in all except the $|11\rangle$ channel [41]. This channel gains a phase given by $\phi = \phi_{00} + \phi_{11} - \phi_{10} - \phi_{01}$. A phase of $\phi = \pi$ is termed a phase gate since it replicates a controlled-NOT logical operation.
Since the particles have internal structure, only specific qubit states will feel the Feshbach resonance (molecular level labelled B in Fig.5.2) due to the field and these resonances are exploited to accumulate phase in the $|11\rangle$ channel. The other two-qubit states will only gather much smaller phase due to linear Zeeman shift of the hyperfine levels. With changing magnetic field, avoided crossings can appear between the different trap states and these are traversed adiabatically. The Feshbach resonance that appears is used to create molecular states between the qubit states and the field is then reversed to go back to two single qubit states. These two qubit states then will have accumulated a phase and tuning the magnetic field far enough and back again to gather a phase of $\phi = \pi$ will create the controlled-NOT gate. Since we pass avoided crossings adiabatically to access the molecular state, the rate of change of magnetic field controls the probability of non-adiabatic passage. To avoid non-adiabatic transfer to excited trap states one would have to vary the magnetic field slowly enough, thus limiting the speed of operation of such phase gates.

Coherent Transfer to Excited Trap States
The proposed protocol for adiabatic transfer of particles to excited trap states in [39] involves controlling the scattering length magnetically and the separation of the individual single particle traps to shift the location of avoided crossings. The proposed protocol for such a coherent transfer again utilizes the molecular level (labelled B in Fig.5.2). The two particle state is driven into a molecular state magnetically, then the trap separation is varied to shift molecular state to a region of avoided crossings. The particles are then brought back into the two particle state by magnetic field sweep but now due to the avoided crossings with excited levels, they can be transferred to a two particle state in any of the excited states. Bringing the trap separation to zero will bring the system back to the unperturbed state with the two particles transferred coherently to excited trap states.

5.5 Results

The FEAST calculated spectrum is plotted for varying values of the delta pseudopotential coupling, expressed in terms of the 3D scattering length a_{3D}. This problem generates only the positive parity states of ion which have $L_z = 0$. As explained earlier, we choose a FEAST eigenvalue search interval of $[0, \hbar\omega_{rf}] \approx [0, 6.047 \times 10^{-9} a.u]$.

Molecular State of the System

To highlight the effect of micromotion, we also show the calculated spectrum and the reference static oscillator in red in Fig.5.5.

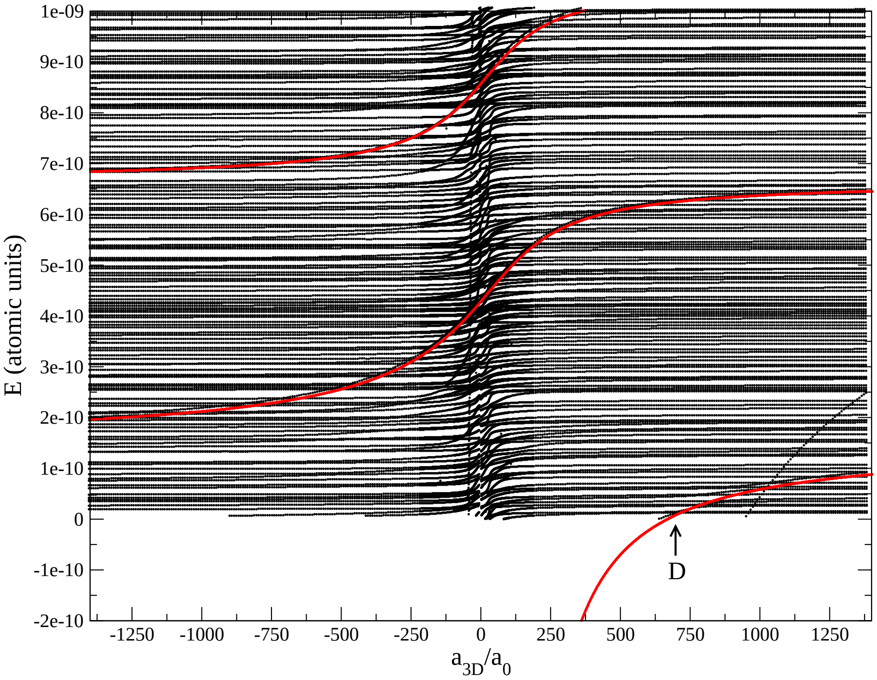

Figure 5.5: Evolution of all bound states of the ion Floquet spectrum with changing scattering length a_{3D}/a_0. Evolution of reference oscillator states are indicated in red. At $a_{3D}/a_0 \approx 700$, the molecular state of delta potential in a time dependent trap (labelled D) evolves into a bound state.

The dense, quasi-continuous Floquet spectrum shows many avoided crossings at low scattering lengths in the range $[-1400\ a_0, +1400\ a_0]$. The Floquet spectrum shows the molecular state due to the 3D regularized delta potential, labelled D in Fig.5.5.

For a closer look, Fig.5.6 shows the molecular level of the reference static oscillator (in red) superimposed on the FEAST calculation. Floquet spectrum for this problem has a modulo-$\hbar\omega_{rf}$ structure. Thus by adding (or subtracting) $\hbar\omega_{rf}$ we can build the spectrum for different *manifolds*. Floquet spectrum in the -1^{th} manifold (shown in blue in Fig.5.6) is built and we notice the excited states in this manifold indicate the existence of the molecular level and its perturbation

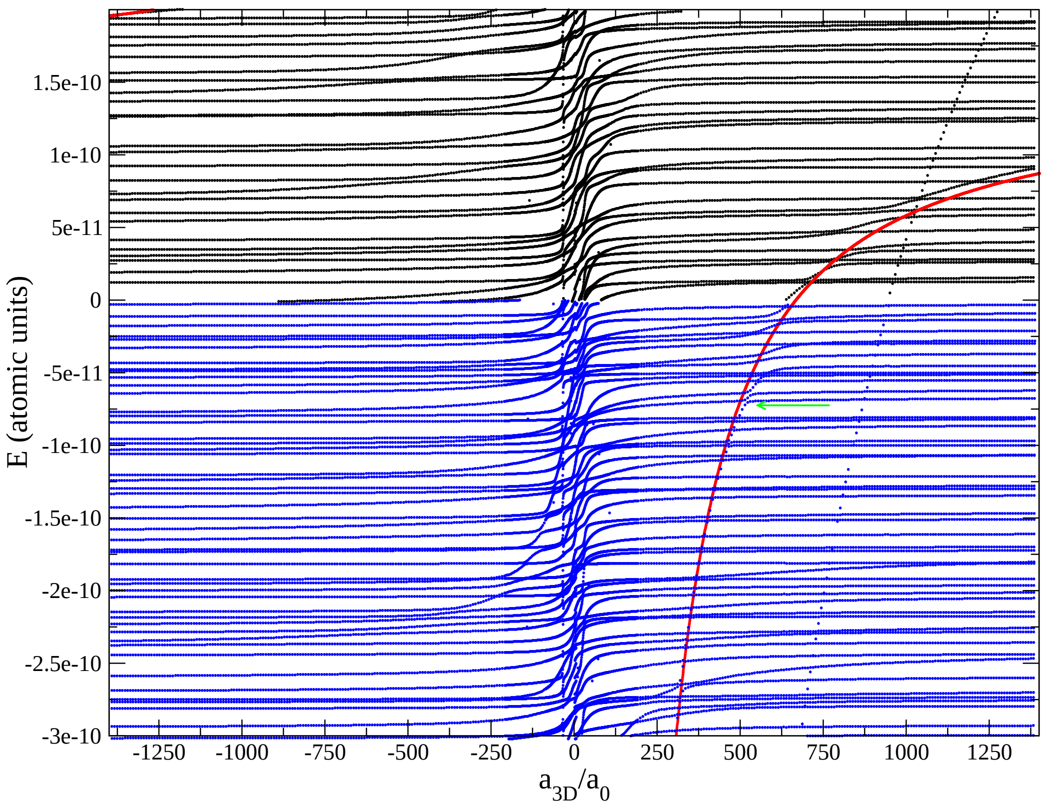

Figure 5.6: Evolution of the converged bound states of the ion with changing scattering length a_{3D}/a_0. Shows strong perturbation due to micromotion at $a_{3D} > a_{ho,x}$, where $a_{ho,x}$ = 533 a_0 (indicated by green arrow)

due to micromotion. Superimposing the molecular level of the reference static oscillator, we note that the micromotion perturbed spectrum coincides exactly with the reference calculation for scattering lengths upto $a_{3D} \approx 500$ a_0. The oscillator lengths for the time dependent trap in $x(y)$ and z are 533 a_0 and 375 a_0 respectively, as given in Sec.5.1.1. Thus we note that at larger scattering lengths, the effect of micromotion becomes more apparent because the binding energy of the molecular level goes as $\sim 1/a_{3D}^2$. We note from Fig.5.6) that at $a_{3D} > 500$ a_0 stronger avoided crossings and micromotion perturb the molecular state and for positive energies the molecular state deviates strongly from the reference oscillator molecular state. Thus molecular states cannot be created using qubit states prepared in ground state, with a good fidelity. Moreover the presence of many avoided crossings introduces an inherent limit to the speed of operation of an atom-ion gate, since a high switching speed can cause diabatic transition of the ion to wrong level.

Adiabatic State Transfer

The spectrum of the reference static oscillator in Fig.5.2 shows that at large scattering lengths $a_{3D} \to \pm\infty$, the asymptotic states are the same for $+\infty$ and $-\infty$. To show the same, we vary a_{3D} over $[-\infty, +\infty]$ and map it to a normalized scattering length ξ over the finite interval of $[-1, +1]$ such that $\xi = (2/\pi)\tan^{-1}(a_{3D}/a_{ho,x})$. a_{3D} ranges over $[-5\times10^4\ a_o, +5\times10^4\ a_0]$, in Fig.5.7. The asymptotic energy levels are found to be equal (shown by the red-dotted lines).

Thus similar to the asymptotic levels for the reference static oscillator (in Fig.5.2), we find levels that are asymptotically equal for the ion Floquet spectrum as well. Similar to Fig.5.2 (inset), we note that the oscillator states of the same manifold exhibit avoided crossings at very low scattering lengths. With a_{3D} increasing to very large values, the effect of micromotion is still seen, though comparatively less pronounced. At very large scattering lengths it shows closely avoided crossings with Floquet states. Thus implementation of a coherent transfer protocol is difficult since the micromotion badly distorts the molecular level. More such avoided crossings exist between the Floquet states from different manifolds as well. This further limits the possible controlled shifting of molecular level to the location of avoided crossings for eventual coherent transfer to excited

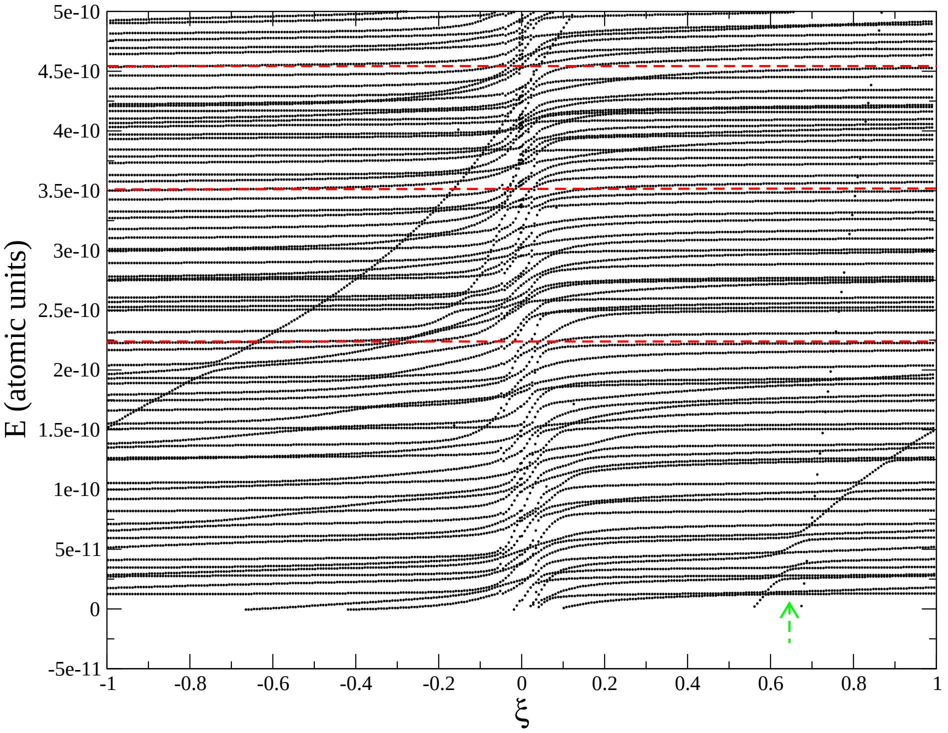

Figure 5.7: Evolution of states with changing normalized scattering length ξ.

trap states.

5.6 Conclusions

The study of micromotion effects for a model system in 3D was attempted initially in the primitive, non-diagonalized basis. Sparse representation of this basis was found to have enormous memory requirement $> 128 GB$ and computation time $\sim 18 hours$. Not all of the adiabatic basis functions in each sector might be required for accurate representation of the Hamiltonian and thus the diabatic-by-sector method was implemented [110-114]. This method was seen to be a better approach since diagonalization of the Hamiltonian in internal coordinates within each sector could be done just once and the selected sector basis functions, saved on file, could be used for calculation with changing scattering length a_{3D}. This drastically reduced the computation time required to build the Hamiltonian, though the full solution still required 1.5 ~ 2 hours. The implementation of this method helped understand what constitutes defining a well-converged state from a quasi-continuum in spectrally unbound systems with internal degrees of freedom. The method fails to converge for micromotion $q_x > 0.1$ where the method fails to resolve the ion ground state energy.

The aim of studying this model system was to understand the effect micromotion has on the secular oscillator levels and the resulting trap induced resonances and avoided crossings. Inherent limitations in the application of a phase gate is seen, since it relies heavily on using the molecular level of the system. Micromotion is seen to heavily perturb the molecular level at low binding energies $\epsilon \sim 1/a_{3D}^2$. Moreover, the molecular level is seen to have many avoided crossings with Floquet states from different manifolds. Thus presence of micromotion could drastically limit the operation time of atom-ion phase gates.

The asymptotic nature of the Floquet spectrum at very high scattering lengths is similar to the reference oscillator spectrum. But experiments involving state transfer of the ion to excited trap states would again fail even at large scattering lengths due to multiple closely avoided crossings.

Chapter 6

Conclusions and Perspectives

In this thesis we have demonstrated a few methods that can be used to solve the Schrödinger equation in one dimension for a scattering problem involving a free particle and a particle in a time independent trap. We utilize three different methods, namely (i) Integral Equation Method [63], (ii) Log-Derivative Propagation [67] and (iii) Spectral Element Method [73]. A modification of the Log-Derivative method is made for use in plane polar coordinates. Though all these methods show physical validity by agreement with the Born approximation, the Integral Equation Method is particularly sensitive number of channels in the calculations due to a slowly converging Greens function (series) in the kernel. The Log-Derivative method is seen to be a robust method and its variant in plane polar coordinates solves the problems in asymptotic matching arising due to the geometry of the problem. The Spectral Element Method is an elegant adaptation of the idea of Log-Derivative method, developed by [73], that instead of propagation a matrix recursively in the solution coordinate, relies on a one shot solution exploiting sparse representation of the Hamiltonian to directly give the R-matrix at the final step. The Hamiltonian is discretized using a combination of pseudospectral basis and finite elements in all spatial coordinates and Schrödinger equation is re-cast into a linear equation in the solution coordinate. Sparsity based linear system solvers are used to solve the linear system. The high order pseudospectral method is used to discretize the grid within each finite element. The same discretization method can also be used to model eigenvalue problems and calculate the eigenfunctions and values to a very high accuracy. A commercially available, robust and thoroughly parallelized sparsity-based linear system solver, PARDISO and its counter part to solve eigenvalue problems, called FEAST are utilized for the problem based on the kind of solution needed.

The scattering problem of a free atom and a trapped ion in one dimension is attempted by using the Integral Equation and Log-Derivative methods. The atom-ion potential is modelled by a delta pseudopotential all throughout the thesis. An inherent limitation in the range of mass ratios (m_A/m_I) that can be used with these method is observed in Cartesian coordinates and is resolved by shifting the calculation to plane polar coordinates where the propagation is done along the $\hat{\theta}$-axis instead the relative coordinate x. This method is seen to work very well with a wide variety of mass ratios. The physics of such a scattering problem in one dimension is seen to reveal rich variety of physics due to the mixed dimensionality. By varying the collision energy of the system, threshold features and resonance-like peaks are seen in the reflection probabilities indicating interesting scattering theory in the system, for an attractive delta potential coupling. The resonance peaks are analyzed by calculating their time delays and are seen to show negative time delays, indicating a resonant scattering event that accelerates the incoming particle. The contribution of the positive and negative total parity scattering amplitudes to these resonance peaks are analyzed, revealing a negative parity contribution to the peaks at low energies. This result is counterintuitive since a delta interaction in free space is known to affect only positive parity solutions but only positive relative parity. This is also due to a cumulative effect of the 1D geometry and the delta potential. Using the Integral Equation method, bound states are detected for the system at negative energies and using the Log-Derivative method signatures of bound states are detected at low total energies, yet again indicating that the different numerical methods employed give the correct physics when tested independently of each other. The ability to use a wide range of mass ratios is also shown.

Extending the 1D collision problem to include time dependent traps, the ion in a 1D Paul trap has a time dependent part in the harmonic oscillator potential term, oscillating at radio frequency. The ion solutions as per Floquet theory and the classical and quantum dynamics of the ion and its wavefunction are well documented in literature and briefly described in the thesis in the Appendix.A. We model the system with an ion in a 1D Paul trap and a free atom. A delta pseudopotential is used here too. The time dependent Schrödinger equation is Fourier-Floquet transformed (effectively Fourier transformed) to translate the problem from time domain to frequency domain. The unbounded nature of the Floquet spectrum and ion wavefunctions are described and relation is drawn between how the width of the ion dynamics is Fourier-Floquet space is related to the numerical limitations faced. The method was initially attempted with Log-Derivative method in Cartesian coordinates and seen to have a serious limitation due to the fact that the propagation is always done at an angle from the asymptotic solution region, which is partially solved by a basis transformation. The basis transformation method used works well only for systems with a bound spectra and in the case of unbounded spectrum the basis is selected by looking for the basis states which have the best projection on the asymptotic solutions to the system. This is seen to have shortcomings since it limits the range of the parameter q in the Mathieu equation, that we can use. The growth of error with increasing micromotion is shown.

To avoid this basis transformation, Propagation in plane polar coordinates is seen to work much better than in Cartesian coordinates but this method too has limited accuracy and convergence with increasing micromotion q. We calculate the probability of ion cooling, ion heating and atom heating per collision. We have explained in detail what kind of transitions constitute an ion cooling and what contributes to atom heating. We argue qualitatively that since these probabilities are per collision event, the cumulative cooling effect over longer time scales would not be drastic since the ion interacting with the rf-field changes its dynamics at each cycle and the average ion energy is conserved. We notice that the growth of cooling and heating probabilities with micromotion q are qualitatively related to observation of ion cooling (and atom loss rate) in experiments. Ion cooling is seen to increase but saturates with (atom-ion) interaction time indicating that micromotion puts a fundamental limit to cooling. We also have studied the scattering threshold features and shifting of resonance peaks in the system with micromotion. We have also tried to isolate the effect micromotion has in modifying the scattering results and argue that it is possible to isolate the contribution only under the low micromotion limit, which is related to the operating point of the Paul trap in the $a - q$ plane of the Mathieu stability plot the ion trap. We analyze the peaks for contribution from parity dependent scattering amplitudes and also study the time delay matrix for these features. We obtain these results for two cases of the ion trap operation. A tightly confined trap with micromotion and a shallow trap with micromotion. Ion traps operation without any static confinement in real Paul traps and we provide reasons why the methods fail in cases without static confinement.

Finally we attempt to extend the study of micromotion effects to 3D with a model system of an ion in a Paul trap with a regularized delta pseudopotential at the trap centre. Experimentally the scenario is similar to having a very heavy atom centered in a Paul trap with a light ion. We use the experimentally valid trap parameters with zero static, purely dynamical confinement. Since this system uses a regularized delta potential in 3D, we solve only for the positive parity solutions of the system. In the future, the problem could be extended to include both parities by varying the location of the delta spike in the trap along the axis of symmetry, which would couple partial waves of different parities. The Hamiltonian for this system is also Fourier-Floquet transformed from time to frequency domain. This increases the size of the problem by a factor of the number of frequency bands we take in the calculation. Using the Spectral Element, the Hamiltonian is discretized with a pseudospectral basis and represented in a sparse matrix. Initial attempts at solution revealed that the problem was too huge in its memory requirement, even on the node with the maximum memory of 128GB.

To reduce the problem in size, we adopt the Adiabatic-by-Sector method which essentially selects the few best basis functions required to represent the Hamiltonian. This is done by diagonalizing the Hamiltonian for the internal coordinates at the centre of each finite element sector and choosing a user-defined number of basis functions for use with the sector. In this case too, since the Hamiltonian is of the Floquet kind, it has an unbounded spectrum. So we device tests to check the eigenstates for convergence in terms of the different internal coordinate bases used. This method is seen to work for the problem with micromotion $q = 0.1$ but fails for larger values of q.
Since we wish to study the energy levels of an ion in a trap with a delta at the trap centre, we cast the problem as an eigenvalue problem that is solved with FEAST, a sparsity based eigenvalue solver that internally re-casts the problem into a linear system with an initial trial solution and optimized over a few iterations. We tune the delta potential coupling term g_{3D} which is proportional to the scattering length a_{3D} and calculate how the ion energy levels evolve. Many avoided crossings are observed between the energy levels of the same Fourier-Floquet band and also between the bands. The molecular state evolves smoothly between different *manifolds* but due to presence of micromotion shows multiple avoided crossings. It shows particularly strong avoided crossings with the Floquet spectrum in the range $a_{3D} \in \{500, 1000\}$. The presence of avoided crossings hinders the proposed atom-ion phase gate implementation since the phase gate utilizes the steep slope of the molecular level to rapidly gain phase in the qubit states but avoided crossings limits the speed of magnetic field sweep into the molecular state and slows the gate operation time. Using the molecular states for coherent transfer to excited trap states is again not an efficient process since the molecular level and also the ion spectrum shows multiple avoided crossings. The avoided crossings are not at deterministic positions for controlled shifting of the molecular levels to their location. This the prospects of coherent transfer of ion to excited trap states is also limited due to micromotion.

Thus micromotion is seen to play a major role in ultracold-ion experiments. It is seen to continuously accelerate (heat) atoms in ion-ultracold atom experiments. Owing to micromotion, ion sympathetic cooling seen to have very limited probability after each two-body collision but scattering observables are show that micromotion can perhaps be treated perturbatively. The problem in 3D shows that micromotion could cause serious limitations to coherent processes.

Appendix A

Classical and Quantum Dynamics of a Trapped Ion

A.1 Mathieu Equation and Classical Dynamics

The classical dynamics of an ion of mass m_I in a time dependent potential of the form given in Eq.(4.5). Since the three dimensional potential in Cartesian coordinates is separable, the dynamics is described in one dimension only. Assuming the ion is singly charged, the classical equation of motion along the x-axis can be written as

$$\frac{d^2x}{dt^2} = -\frac{|e|}{m_I}\left[U\alpha' + \tilde{U}\cos(\omega_{rf}t)\alpha''\right]x \tag{A.1}$$

Taking $\tau = \omega_{rf}t/2$, we get

$$\frac{d^2x}{d\tau^2} = -\frac{4|e|}{m_I\omega_{rf}^2}\left[U\alpha' + \tilde{U}\cos(2\tau)\alpha''\right]x \tag{A.2}$$

This equation can be converted to the standard form of a Mathieu type differential equation (See [117], [119], [120]) by taking $a = 4|e|U\alpha'/(m_I\omega_{rf}^2)$ and $q = 2|e|\tilde{U}\alpha''/(m_I\omega_{rf}^2)$.

$$\frac{d^2x}{d\tau^2} + \left[a + 2q\cos(2\tau)\right]x = 0 \tag{A.3}$$

This equation has a general solution of the Floquet form $x(\tau) = e^{i\beta\tau}\phi(\tau)$. β is called the characteristic exponent of the Floquet solution and the solutions are real and periodic only if β is real. The term $\phi(\tau)$ is time periodic and in this case we take $\phi(\tau)$ as a Fourier series and rewrite the solution as

$$x(\tau) = Ae^{i\beta\tau}\sum_{n=-\infty}^{+\infty} C_{2n}e^{i2n\tau} + Be^{-i\beta\tau}\sum_{m=-\infty}^{+\infty} C_{2m}e^{-i2m\tau} \tag{A.4}$$

The summation term in the above solution has a periodicity of $T_{rf} = 2\pi/\omega_{rf}$. Taking only one phase for this example, let B=0. Substituting the above solution into Eq.(A.3), we expand $\cos(2\tau) = (e^{i2\tau}+e^{-i2\tau})/2$. Multiplying Eq.(A.3) by $e^{i2n'\tau}$ and integrating over a period $T_{rf} = 2\pi/\omega_{rf}$, we have a recursion relation in terms of the coefficients $C_{2n'}$ as

$$[a-(\beta+2n')^2]C_{2n'} - q(C_{2n'+2}+C_{2n'-2}) = 0 \tag{A.5}$$

We truncate the infinite sum in Eq.(A.4) by taking a finite set of values $n' = [-N_f, +N_f$. This forms the Fourier-Floquet basis for our calculations. The above recursion relation can be written as a matrix equation called the Hill Matrix

$$\begin{pmatrix} \ddots & \vdots & \vdots & \vdots & \vdots & \vdots & ⋰ \\ \cdots & 1 & \frac{q}{a-(\beta-4)^2} & 0 & 0 & 0 & \cdots \\ \cdots & \frac{q}{a-(\beta-2)^2} & 1 & \frac{q}{a-(\beta-2)^2} & 0 & 0 & \cdots \\ \cdots & 0 & \frac{q}{a-\beta^2} & 1 & \frac{q}{a-\beta^2} & 0 & \cdots \\ \cdots & 0 & 0 & \frac{q}{a-(\beta+2)^2} & 1 & \frac{q}{a-(\beta+2)^2} & \cdots \\ \cdots & 0 & 0 & 0 & \frac{q}{a-(\beta+4)^2} & 1 & \cdots \\ ⋰ & \vdots & \vdots & \vdots & \vdots & \vdots & \ddots \end{pmatrix} \begin{bmatrix} \vdots \\ C_{-4} \\ C_{-2} \\ C_0 \\ C_2 \\ C_4 \\ \vdots \end{bmatrix} = 0 \tag{A.6}$$

The determinant of this matrix for an initial trial value of β, called the Hill's determinant $\Delta(\beta)$. The above determinant converges fast for as little as few tens of terms i.e $n' = (\sim -50, \sim +50)$. The determinant, calculated numerically, is used to find β for a given value of a and q. From the expressions derived in [118], β is given by

$$\beta = \frac{2}{\pi}\sin^{-1}\left(\sqrt{\Delta(0)\sin^2\left(\frac{\pi}{2}\sqrt{a}\right)}\right) \qquad \text{for} \qquad a \neq (2j)^2$$
$$\beta = \frac{1}{\pi}\cos^{-1}(2\Delta(1) - 1) \qquad \text{for} \qquad a = (2j)^2 \tag{A.7}$$

where j is a non-zero positive integer. From the general solution in Eq.(A.4) it is clear that the ion is subject to driven harmonic motion only if β is real. If β is imaginary, the ion will have an unstable *orbit* in the trapping field before being expelled out of the trap. β is real only for certain combination of values of a and q. Plotting the points in $a - q$ space where β is real gives us the stability plot for the ion, shown in Fig.A.1. As the name suggests, the ion shows stable driven harmonic motion composed of an infinite series of Fourier-Floquet components at certain values of a and q. The plot clearly shows that the ion can have stable trapped motional states even with no static confinement $a = 0$ or even negative values of a. The ion also has no trapped states at values of $a = n^2$, where n is an integer.

The ion dynamics is well described if the Fourier-Floquet basis n' is chosen to be sufficiently large value N_f such that $n' \in [-N_f, +N_f]$. A complete basis i.e a converged Fourier-Floquet series will ideally have the coefficients $C_{\pm 2N_f} \to 0$ for very large values of $N_f \to \infty$. In a truncated basis, we choose N_f sufficiently large to ensure $C_{\pm 2N_f} \approx 0$. It is seen that at points in the plot that lie close to the boundaries of the stability region, the ion dynamics is composed of many Fourier-Floquet components indicating complex ion motion composed of many high frequency components. At such points, the Fourier-Floquet series is difficult to converge and the truncation of the infinite sum term in the general solution in Eq.(A.4) must be done for larger values of N_f. As an illustration of this fact, a phase space plot of the ion motion in one dimension is shown for different values of micromotion q and a fixed value of $a = 0.1$ in Fig.A.2. To calculate the set of coefficients $C_{2n'}$ where $n' \in [-N_f, +N_f]$, we rewrite the recursion relation in Eq.(A.5) as

$$1 - \frac{q}{[a - (\beta + 2n')^2]}\left(\frac{C_{2n'+2}}{C_{2n'}} - \frac{C_{2n'-2}}{C_{2n'}}\right) = 0 \tag{A.8}$$

Taking $D_{2n'} = [a - (\beta + 2n')^2]/q$, we have

$$1 - \frac{1}{D_{2n'}}\left(\frac{C_{2n'+2}}{C_{2n'}} - \frac{C_{2n'-2}}{C_{2n'}}\right) = 0 \tag{A.9}$$

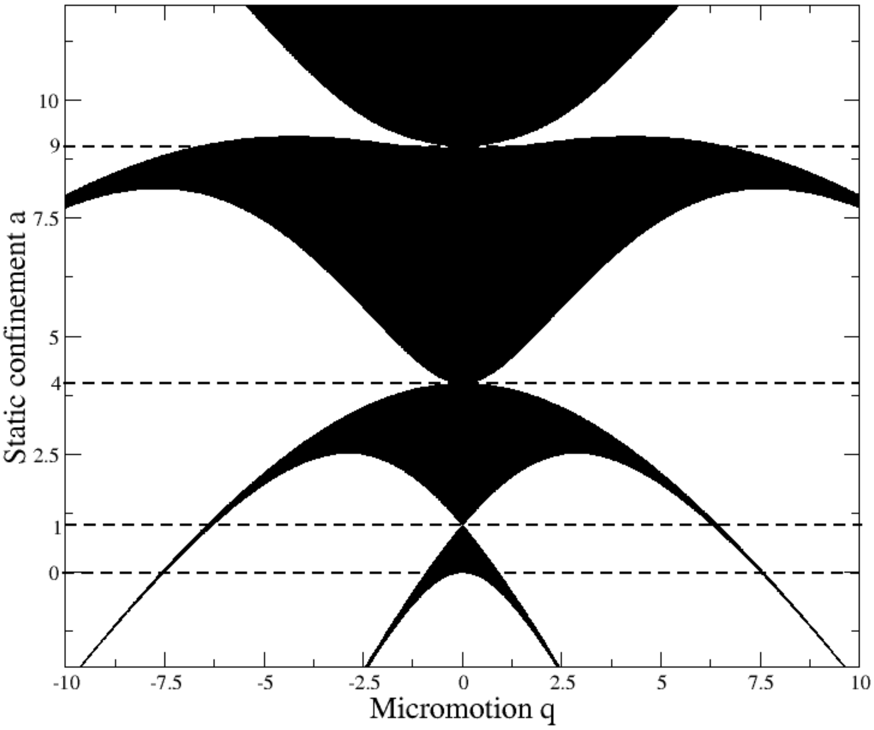

Figure A.1: Mathieu Equation Stability plot

From the above equation, we can derive partial fractions for positive and negative n' values of the coefficients $C_{2n'}$, given by

$$\frac{C_{2n'}}{C_{2n'+2}} = \cfrac{1}{D_{2n'} - \cfrac{1}{D_{2n'-2} - \cfrac{1}{D_{2n'-4} - \dots}}} \quad \text{for positive } n' \text{ and}$$

$$\frac{C_{2n'}}{C_{2n'-2}} = \cfrac{1}{D_{2n'} - \cfrac{1}{D_{2n'+2} - \cfrac{1}{D_{2n'+4} - \dots}}} \quad \text{for negative } n'. \tag{A.10}$$

The recursive calculation of all values of $C_{2n'}$ is done by assuming $C_0 = 1$ and normalizing over the sum the final set of $(2N_f + 1)$ values of $C_{2n'}$. Due to rapid convergence of partial fractions, we take only 10 terms in each partial fraction calculation. For given values of a and q, we assume the Fourier-Floquet basis size

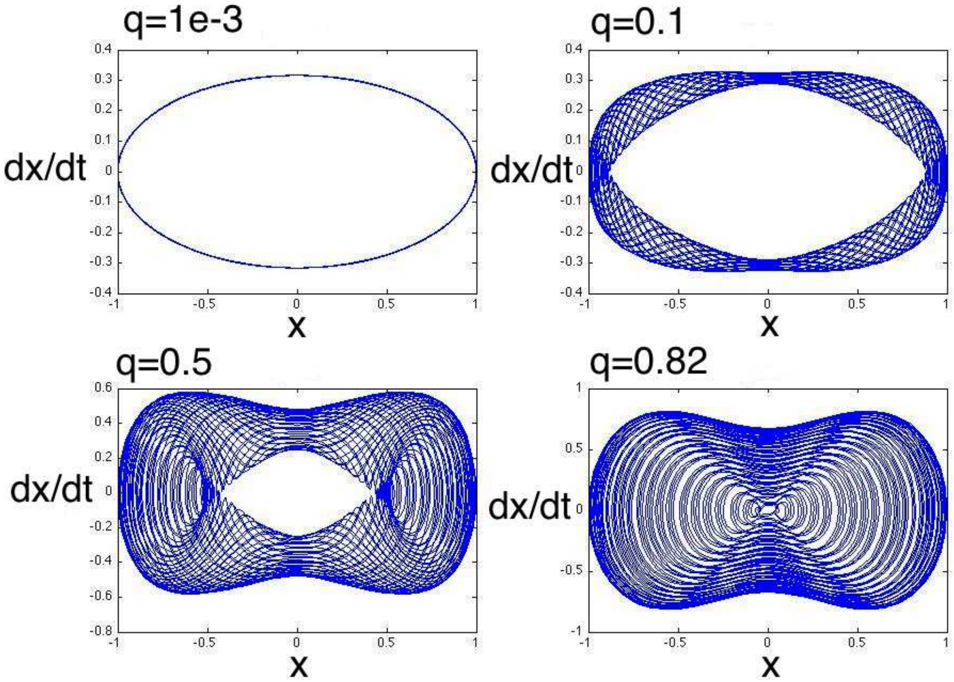

Figure A.2: Phase space dynamics for an ion in a 1D Paul trap. The plots are made for $a = 0.1$.

i.e N_f is large enough to describe the classical dynamics of the ion completely if the values of $|C_{2N_f}|$ and $|C_{-2N_f}|$ are sufficiently small i.e $< \sim 10^{-6}$.

A.2 Ion Quantum Dynamics

The quantum potential for the ion trap is separable in Cartesian coordinates. The elegant quantum description of ion in a time dependent trap in one dimension was given by Glauber [52] (Also see 53, 102). This derivation of the ion wavefunction is briefly reproduced here. The time dependent harmonic potential for the ion is given in Eq.(4.6). Writing the Hamiltonian for a single ion in such a potential

$$\hat{H} = -\frac{\hbar^2}{2m_I}\frac{\partial^2}{\partial x_I^2} + \frac{1}{2}m_I\frac{\omega_{rf}^2}{4}\left[a + 2q\cos(\omega_{rf}t)\right]x_I^2 \tag{A.11}$$

The Hamiltonian can also be written in terms of operators as

$$\hat{H} = \frac{\hat{p}^2}{2m_I} + \frac{m_I}{2}W(t)\hat{x}_I^2 \text{ taking } W(t) = \frac{\omega_{rf}^2}{4}\left[a + 2q\cos(\omega_{rf}t)\right] \tag{A.12}$$

where the operators are written in Heisenberg picture as $\dot{\hat{x}}_I = \frac{\hat{p}}{m_I}$ and $\dot{\hat{p}} = -m_I W(t)\hat{x}_I$. These expressions can be used to give a differential equation $\ddot{\hat{x}}_I + W(t)\hat{x}_I = 0$, which is similar in form to the classical Mathieu equation in Eq.(A.2). Thus $\hat{x}_I(t)$ and $u(t)$ are solutions to the same differential equation. Eq.(A.11) has solutions $u(t) = e^{i\beta\omega_{rf}t/2}\varphi(t)$ of the Floquet type and it is subject to special boundary conditions $u(0) = 1, \dot{u}(0) = i\nu$. The periodic function $\varphi(t)$ is taken as a Fourier series given by

$$u(t) = e^{i\beta\omega_{rf}t/2}\varphi(t) = e^{i\beta\omega_{rf}t/2}\sum_{n=-\infty}^{+\infty} C_{2n}e^{in\omega_{rf}t} \tag{A.13}$$

where $\varphi(t)$ is a periodic function with period $T_{rf} = 2\pi/\omega_{rf}$. The boundary conditions give

$$u(0) = \sum_{n=-\infty}^{+\infty} C_{2n} = 1 \text{ and } \dot{u}(0) = i\beta\omega_{rf}/2\sum_{n=-\infty}^{+\infty} C_{2n} + i\omega_{rf}\sum_{n=-\infty}^{+\infty} nC_{2n} = i\nu$$
$$\text{with } \nu = \omega_{rf}\sum_{n=-\infty}^{+\infty} C_{2n}\left(\frac{\beta}{2} + n\right). \tag{A.14}$$

From the Wronskian of the solution $u(t)$ it is seen $u(t)$ and $u^*(t)$ are linearly independent.

$$u^*(t)\dot{u}(t) - u(t)\dot{u}^*(t) = u^*(0)\dot{u}(0) - u(0)\dot{u}^*(0) = i\nu \tag{A.15}$$

The Hamiltonian in Eq.(A.11) is similar to Eq.(A.3). We see $u(t)$ and $\hat{x}_I(t)$ satisfy the same differential equation. Taking the complex linear combination of the two solutions, we define the operator

$$\hat{C}(t) = \sqrt{\frac{m_I}{2\hbar\nu}}\, i(u\dot{\hat{x}}_I - \dot{u}\hat{x}_I) \text{ with } \hat{C}(0) = \frac{1}{\sqrt{2m_I\hbar\nu}}(m\nu\hat{x}_I(0) - i\dot{\hat{x}}_I). \tag{A.16}$$

Eq.(A.15) has the form of an annihilation operator for a static harmonic oscillator of *reference* frequency ν. Thus $\hat{C}(t) = \hat{a}$ and $[\hat{C}, \hat{C}^\dagger] = [\hat{a}, \hat{a}^\dagger] = 1$. Similar to the case of a static harmonic oscillator, considering a set of basis states $|n,t\rangle$ with $n = 0, 1, 2, \ldots, \infty$. For the ground state $|n = 0\rangle$, we have $\hat{a}\,|n = 0\rangle = \hat{C}\,|n = 0\rangle = 0$. Taking $m_I\dot{\hat{x}}_I(t) = p$, we have $\hat{C}(t)\,|n = 0\rangle = [u(t)\hat{p} - m_I\dot{u}(t)\hat{x}_I]\,|n = 0, t\rangle = 0$ and rewriting the operators as coordinates $\left[u(t)\frac{\hbar}{i}\frac{\partial}{\partial x_I} - m_I\dot{u}(t)x_I\right]\langle x_I\,|\,n = 0, t\rangle = 0$. The time dependence of $|n = 0, t\rangle$ appears due to the following. Since $\hat{C}(t)$ is in Heisenberg picture, its equivalent in Schrödinger picture is $\hat{C}(t) = \hat{U}^\dagger(t)\hat{C}_S\hat{U}(t)$, where $\hat{U}(t) = \exp[-i/\hbar\hat{H}]$. $\hat{U}(t)\,|n = 0\rangle$ is then the time evolution of the ground state, which can be given by $|n = 0, t\rangle$. Thus $\hat{U}(t)\hat{U}^\dagger(t)\hat{C}_S\hat{U}(t)\,|n = 0\rangle = \hat{C}_S\,|n = 0, t\rangle$, which is equivalent to

$$\langle x_I\,|\,n = 0, t\rangle = \left(\frac{m_I\nu}{\pi\hbar}\right)^{1/4}\frac{1}{[u(t)]^{1/2}}\exp\left(\frac{im_I}{2\hbar}\frac{\dot{u}(t)}{u(t)}x_I^2\right). \tag{A.17}$$

The basis states $|n,t\rangle$ can be generated with the time independent creation operator in Schrödinger picture as $|n,t\rangle = \frac{[\hat{C}_S^\dagger(t)]^n}{\sqrt{n!}}\,|n = 0, t\rangle$. The solution $u(t)$ can then be written in the form of Eq.(A.13) gives

$$\langle x_I\,|\,n, t\rangle = \exp\left[-i\left(n + \frac{1}{2}\right)\mu\omega_{rf}t\right]\Phi_n(t) \tag{A.18}$$

where $\mu = \frac{\beta}{2}$ and the wavefunctions $\Phi_n(t)$ are given by

$$\Phi_n(x_I,t) = \frac{1}{\sqrt{2^n n!}}\left(\frac{m_I\nu}{\pi\hbar}\right)^{1/4}\frac{\exp(-in\arg[\varphi(t)])}{[\varphi(t)]^{1/2}} \\ H_n\left(\left[\frac{m_I\nu}{\hbar|\varphi(t)|^2}\right]^{1/2} x_I\right)\exp\left(-\frac{m_I\mu}{2\hbar}\left[1-\frac{i\dot{\varphi}(t)}{\mu\varphi(t)}\right]x_I^2\right) \quad \text{(A.19)}$$

It is noted here that the effect of micromotion appears here as a time dependent term within the arguments of the Hermite polynomial and the Gaussian exponential terms. Physically this manifests as a *breathing* oscillation of the harmonic oscillator states. The amplitude of this breathing is determined by q and the frequency by ω_{rf}. The evolution of eigenstates have a phase, from Eq.(A.18), which indicates that the ion spectrum for such a time dependent harmonic oscillator goes as integer multiples of $\hbar\mu = \hbar\beta/2 = \hbar\omega_{sec}$, which is called the *secular* frequency. It characterizes the effective harmonic motion of the ion in the trap for a given value of a and q. It is noted that the wavefunction $\Phi_n(x_I,t)$ are time dependent states, so they are not stationary but can be called quasistationary states with the pseudo-energy spectrum going as $(n+1/2)\hbar\omega_{sec}$.

Finally, in the limit of $|a| << 1$ and $q^2 << 1$, the classical Mathieu equation will have the coefficients $C_{2n'} = 0$ for all $n' \neq 0$ which means only the term C_0 in Eq.(A.14) is non-zero and gives $\nu = \beta\omega_{rf}/2$. This is referred to as the *lowest order approximation* in [53]. This also simplifies the expression for β as $\beta = \sqrt{a + q^2/2}$. Though, in our calculations we use the precise value of β computed using the Hill's determinant method described in Appendix.A.1.

Appendix B

Symmetrization Matrix $\mathbb{X}$

Any function $f(x)$ can be decomposed into symmetric $S(x)$ and asymmetric components $A(x)$ (See 56 p.163) as

$$f(x) = S(x)+A(x) \text{ where } S(x) = \frac{f(x)+f(-x)}{\sqrt{2}} \quad \text{and} \quad A(x) = \frac{f(x)-f(-x)}{\sqrt{2}} \tag{B.1}$$

In grid representation, if the discretization of x variable over $2N+1$ points is symmetric about the origin i.e $x_i \in [-L,+L], i = \{0,1,\ldots,N\}$, we have $\pm x_N = \pm L$ and $x_0 = 0$. The grid width $2L$ and the function $f(x)$ can thus be decomposed into symmetric and asymmetric components as

$$S(x_i) = \frac{f(x_i)+f(-x_i)}{\sqrt{2}} \quad \text{and} \quad A(x_i) = \frac{f(x_i)-f(-x_i)}{\sqrt{2}} \tag{B.2}$$

where $i \in [1, N]$. This will give a matrix representation of the decomposition in Eq.(B.2) is

$$\mathbb{X}\,\bar{\mathbf{f}}(x) \Longleftrightarrow \begin{pmatrix} \frac{1}{\sqrt{2}} & 0 & 0 & \cdots & 0 & 0 & \frac{1}{\sqrt{2}} \\ 0 & \frac{1}{\sqrt{2}} & 0 & \cdots & 0 & \frac{1}{\sqrt{2}} & 0 \\ 0 & 0 & \ddots & \cdots & \iddots & 0 & 0 \\ \vdots & \vdots & \vdots & 1 & \vdots & \vdots & \vdots \\ 0 & 0 & \iddots & \cdots & \ddots & 0 & 0 \\ 0 & -\frac{1}{\sqrt{2}} & 0 & \cdots & 0 & \frac{1}{\sqrt{2}} & 0 \\ -\frac{1}{\sqrt{2}} & 0 & 0 & \cdots & 0 & 0 & \frac{1}{\sqrt{2}} \end{pmatrix} \begin{bmatrix} f(-x_N) \\ \vdots \\ f(-x_1) \\ f(x_0) \\ f(x_1) \\ \vdots \\ f(x_N) \end{bmatrix} = \begin{bmatrix} S(x_N) \\ \vdots \\ S(x_1) \\ f(x_0) \\ A(x_1) \\ \vdots \\ A(x_N) \end{bmatrix} \tag{B.3}$$

Multiplication by this matrix essentially places the symmetric components in the top half of the vector $\bar{\mathbf{f}}(x)$ and asymmetric components in the bottom half. The matrix $\mathbb{X}$, which we call the symmetrization matrix is orthogonal i.e $\mathbb{X}\mathbb{X}^T = \mathbb{I}$ and has the determinant $|\mathbb{X}| = 1$. The origin $x = 0$ is left unchanged and the function $f(x)$ is taken to be of positive parity at $x = 0$. The above matrix is for an odd number of points. A symmetric grid in x may also not include the origin, in which case the symmetrization matrix $\mathbb{X}$ for an even number of points is written as in Eq.(B.4).

$$\mathbb{X} = \begin{pmatrix} \frac{1}{\sqrt{2}} & 0 & \cdots & \cdots & 0 & \frac{1}{\sqrt{2}} \\ 0 & \ddots & \vdots & \vdots & \iddots & 0 \\ \vdots & \cdots & \frac{1}{\sqrt{2}} & \frac{1}{\sqrt{2}} & \cdots & \vdots \\ \vdots & \cdots & -\frac{1}{\sqrt{2}} & \frac{1}{\sqrt{2}} & \cdots & \vdots \\ 0 & \iddots & \vdots & \vdots & \ddots & 0 \\ -\frac{1}{\sqrt{2}} & 0 & \cdots & \cdots & 0 & \frac{1}{\sqrt{2}} \end{pmatrix} \tag{B.4}$$

Thus the matrix representation (DVR) of an operator over a symmetric grid can be symmetrized by two matrix multiplications. For example, if $\mathbb{V}^{DVR}$ is the diagonal representation of a potential, we can symmetrize it by $\mathbb{V}^{DVR}_S = \mathbb{X}\mathbb{V}^{DVR}\mathbb{X}^T$.

Appendix C

Eigenfunctions of $\hat{T}_\rho$

We obtain the eigenfunctions of the derivative operator in Eq.(3.36) for a problem similar to a particle in a box. We write the Schrödinger equation for such a problem as

$$-\left(\rho^2\frac{\partial^2}{\partial\rho^2}+\rho\frac{\partial}{\partial\rho}\right)\psi(\rho)=\lambda\psi(\rho) \tag{C.1}$$

Changing variables by taking $\rho = e^u \to u = \ln(\rho)$, we have the derivative operators

$$\frac{\partial}{\partial\rho}=\frac{\partial}{\partial u}\frac{1}{\rho} \quad \text{and} \quad \frac{\partial^2}{\partial\rho^2}=\frac{\partial^2}{\partial u^2}\frac{1}{\rho^2}+\frac{\partial}{\partial u}\frac{1}{\rho^2} \tag{C.2}$$

Substituting Eq.(C.2) into Eq.(C.1) converts the differential equation into a much familiar form

$$-\left(\frac{\partial^2}{\partial u^2}\right)\psi(u)=\lambda\psi(u) \ \text{ with solutions } \ \psi(u)=A\sin(\sqrt{\lambda}u)=A\sin(\sqrt{\lambda}\ln(\rho)). \tag{C.3}$$

With boundary conditions $A\sin(\sqrt{\lambda}\ln(\rho_1)) = A\sin(\sqrt{\lambda}\ln(\rho_2)) = 0$, we have $\sqrt{\lambda}(\ln(\rho_2)-\ln(\rho_1)) = n\pi$. Thus we have the solution

$$\psi_n(\rho)=A\sin\left[\frac{n\pi\ln(\rho/\rho_1)}{\ln(\rho_2/\rho_1)}\right] \ \text{ with eigenvalues } \ \lambda_n=\frac{n^2\pi^2}{\ln^2(\rho_2/\rho_1)} \tag{C.4}$$

Bibliography

[1] C. Kollath, M. Köhl, T. Giamarchi, *Scanning tunneling microscopy for ultracold atoms*, Phys. Rev. A. **76**, 063602 (2007). doi:10.1103/PhysRevA.76.063602. 1, 7

[2] Y. Sherkunov, B. Muzykantskii, N. d'Ambrumenil, B. D. Simons, *Probing ultracold Fermi atoms with a single ion*, Phys. Rev. A. **79**, 023604 (2009). doi:10.1103/PhysRevA.79.023604. 1, 7

[3] P. Zhang, A. Dalgarno, R. Côté, *Scattering of Yb and Yb$^+$*, Phys. Rev. A **80**, 030703(R) (2009). doi:10.1103/PhysRevA.80.030703. 1, 7

[4] E. Bodo, P. Zhang, A. Dalgarno, *Ultra-cold ion-atom collisions: near resonant charge exchange*, New J. Phys. **10**, 033024 (2008). doi:10.1088/1367-2630/10/3/033024. 1, 7

[5] R. Côté, *From classical mobility to hopping conductivity: Charge hopping in an ultracold gas*, Phys. Rev. Lett. **85**, 5316 (2000). doi:10.1103/PhysRevLett.85.5316. 2, 7

[6] U. Bissbort, D. Cocks, A. Negretti, Z. Idziaszek, T. Calarco, F. Schmidt-Kaler, W. Hofstetter, R. Gerritsma, *Emulating Solid-State Physics with a Hybrid System of Ultracold Ions and Atoms*, Phys. Rev. Lett. **111**, 080501 (2013). doi:10.1103/PhysRevLett.111.080501. 2, 8, 105

[7] M. Müller, S. Diehl, G. Pupillo, P. Zoller, *Engineered Open Systems and Quantum Simulations with Atoms and Ions*, Adv. At. Mol. Opt. Phys. **61**, 1 (2012). arXiv:1203.6595v1 [quant-ph]. 2, 8

[8] L. Ratschbacher, C. Sias, L. Carcagni, J. M. Silver, C. Zipkes, M. Köhl, *Decoherence of a Single-Ion Qubit Immersed in a Spin-Polarized Atomic Bath*, Phys. Rev. Lett. **110**, 160402 (2013). doi:10.1103/PhysRevLett.110.160402. 2, 8

[9] J. Catani, G. Lamporesi, D. Naik, M. Gring, M. Inguscio, F. Minardi, A. Kantian, T. Giamarchi, *Quantum dynamics of impurities in a one-dimensional Bose gas*, Phys. Rev. A **85**, 023623 (2012). doi:10.1103/PhysRevA.85.023623. 2, 8

[10] N. Spethmann, F. Kindermann, S. John, C. Weber, D. Meschede, A. Widera, *Inserting single Cs atoms into an ultracold Rb gas*, App. Phys. B. **106**(3), 513 (2012). doi:10.1007/s00340-011-4868-6. 2, 8

[11] N. Spethmann, F. Kindermann, S. John, C. Weber, D. Meschede, A. Widera, *Dynamics of Single Neutral Impurity Atoms Immersed in an Ultracold Gas*, Phys. Rev. Lett. **109**, 235301 (2012). doi:10.1103/PhysRevLett.109.235301. 2, 8

[12] A. Klein, M. Fleischhauer, *Interaction of impurity atoms in Bose-Einstein condensates*, Phys. Rev. A **71**, 033605 (2005). doi:10.1103/PhysRevA.71.033605. 2, 8

[13] M. Bruderer, W. Bao, D. Jaksch, *Self-trapping of impurities in Bose-Einstein condensates: Strong attractive and repulsive coupling*, Eur. Phys. Lett. **82**, 30004 (2008). doi:10.1209/0295-5075/82/30004. 2, 8

[14] R. M. Kalas, D. Blume, *Interaction-induced localization of an impurity in a trapped Bose-Einstein condensate*, Phys. Rev. A **73**, 043608 (2006). doi:10.1103/PhysRevA.73.043608. 2, 8

[15] J. Goold, H. Doerk, Z. Idziaszek, T. Calarco, T. Busch, *Ion-induced density bubble in a strongly correlated one-dimensional gas*, Phys. Rev. A **81**, 041601(R) (2010). doi:10.1103/PhysRevA.81.041601. 2, 8

[16] J. M. Schurer, P. Schmelcher, A. Negretti, *Ground-state properties of ultracold trapped bosons with an immersed ionic impurity*, Phys. Rev. A **90**, 033601 (2014). doi:10.1103/PhysRevA.90.033601. 2, 8

[17] D. K. K. Lee, J. M. F. Gunn, *Polarons and Bose recondensation: A self-trapping approach*, Phys. Rev. B **46**(1), 301 (1992). doi:10.1103/PhysRevB.46.301. 2, 8

[18] K Sacha, E. Timmermans, *Self-localized impurities embedded in a one-dimensional Bose-Einstein condensate and their quantum SSuctuations*, Phys. Rev. A **73**, 063604 (2006). doi:10.1103/PhysRevA.73.063604. 2, 8

[19] H. Bei-Bing, W. Shao-Long, *Polaron in Bose-Einstein Condensation System*, Chinese Phys. Lett. **26**, 080302 (2009). doi:10.1088/0256-307X/26/8/080302. 2, 8

[20] W. Casteels, J. Tempere, J. T. Devreese, *Polaronic properties of an impurity in a Bose-Einstein condensate in reduced dimensions*, Phys. Rev. A **86**, 043614 (2012). doi:10.1103/PhysRevA.86.043614. 2, 8

[21] L.Ratschbacher, C. Zipkes, C. Sias, M. Köhl, *Controlling chemical reactions of a single particle*, Nature Physics **8**, 649 (2012). doi:10.1038/nphys2373. 5, 10

[22] F. H. J. Hall, P. Eberle, G. Hegi, M. Raoult, M. Aymar, O. Dulieu, S. Willitsch, *Ion-neutral chemistry at ultralow energies: Dynamics of reactive collisions between laser-cooled Ca^+ ions and Rb atoms in an ion-atom hybrid trap*, Mol. Phys. **111**, 2020 (2013). doi:10.1080/00268976.2013.780107.

[23] F. H. J. Hall, S. Willitsch, *Millikelvin Reactive Collisions between Sympathetically Cooled Molecular Ions and Laser-Cooled Atoms in an Ion-Atom Hybrid Trap*, Phys. Rev. Lett. **109**, 233202 (2012). doi:10.1103/PhysRevLett.109.233202.

[24] A. Härter, A. Krükow, A. Brunner, W. Schnitzler, S. Schmid, J. H. Denschlag, *Single Ion as a Three-Body Reaction Center in an Ultracold Atomic Gas*, Phys. Rev. Lett. **109**, 123201 (2012). doi:10.1103/PhysRevLett.109.123201.

[25] A. Härter, A. Krükow, M. Deiß, B. Drews, E. Tiemann, J. H. Denschlag, *Shedding Light on Three-Body Recombination in an Ultracold Atomic Gas*, (2013). arXiv:1301.5518v3 [physics.atom-ph].

[26] A. T. Grier, M. Cetina, F. Oručević, V. Vuletić, *Observation of Cold Collisions between Trapped Ions and Trapped Atoms*, Phys. Rev. Lett. **102**, 223201 (2009). doi:10.1103/PhysRevLett.102.223201.

[27] C. Zipkes, S. Palzer, C. Sias, M. Köhl, *A trapped single ion inside a Bose-Einstein condensate*, Nature. **464**, 388 (2010). doi:10.1038/nature08865. xv, 2, 3, 8, 9, 80, 82, 87, 88, 95, 96

[28] S. Schmid, A. Härter, J.H. Denschlag, *Dynamics of a cold trapped ion in a Bose-Einstein condensate*, Phys. Rev. Lett. **105**, 133202 (2010). doi:10.1103/PhysRevLett.105.133202. 2, 8, 82

[29] A. Härter, A. Krükow, A. Brunner, J.H. Denschlag, *Minimization of ion micromotion using ultracold atomic probes*, App. Phys. Lett. **102**, 221115 (2013). doi:10.1063/1.4809578. xv, 4, 10, 82

[30] A. Härter, J.H. Denschlag, *Cold atom-ion experiments in hybrid traps*, Contem. Phys. **55**(1), 33 (2014). doi:10.1080/00107514.2013.854618. 96

[31] K. Ravi, S. Lee, A. Sharma, G. Werth, S. A. Rangwala, *Cooling and stabilization by collisions in a mixed ion-atom system*, Nature Comm. **3**, 1126 (2012). doi:10.1038/ncomms2131. xv, 4, 10, 80, 82, 87, 96

[32] C. Zipkes, S. Palzer, L. Ratschbacher, C. Sias, M. Köhl, *Cold heteronuclear atom-ion collisions*, Phys. Rev. Lett. **105**, 133201 (2010). doi:10.1103/PhysRevLett.105.133201. 80, 96

[33] S. Lee, K. Ravi, S. A. Rangwala, *Measurement of collisions between rubidium atoms and optically dark rubidium ions in trapped mixtures*, Phys. Rev. A **87**, 052701 (2013). doi:10.1103/PhysRevA.87.052701. 88

[34] F. H. J. Hall, M. Aymar, M. Raoult, O. Dulieu, S. Willitsch, *Light-assisted cold chemical reactions of barium ions with rubidium atoms*, Mol. Phys. **111**, 1683 (2013). doi:10.1080/00268976.2013.770930.

[35] F. H. J. Hall, M. Aymar, N. Bouloufa-Maafa, O. Dulieu, S. Willitsch, *Light-Assisted Ion-Neutral Reactive Processes in the Cold Regime: Radiative Molecule Formation versus Charge Exchange*, Phys. Rev. Lett. **107**, 243202 (2011). doi:10.1103/PhysRevLett.107.243202.

[36] K. Ravi, S. Lee, A. Sharma, G. Werth, S. A. Rangwala, *Combined ion and atom trap for low-temperature ion-atom physics*, App. Phys. B. **107**(4), 971 (2012). doi:10.1007/s00340-011-4726-6. 5, 10

[37] H. Doerk, Z. Idziaszek, T. Calarco, *Atom-ion quantum gate*, Phys. Rev. A. **81**, 012708 (2010). doi:10.1103/PhysRevA.81.012708. 2, 8, 105, 116

[38] Z. Idziaszek, T. Calarco, P. Zoller, *Controlled collisions of a single atom and an ion guided by movable trapping potentials*, Phys. Rev. A. **76**, 033409 (2007). doi:10.1103/PhysRevA.76.033409. 2, 8, 70, 116

[39] M. Krych, Z. Idziaszek, *Controlled collisions of two ultracold atoms in separate harmonic traps*, Phys. Rev. A. **80**, 022710 (2009). doi:10.1103/PhysRevA.80.022710. 2, 8, 105, 116, 117

[40] R. Stock, I. H. Deutsch, E. L. Bolda, *Quantum State Control via Trap-Induced Shape Resonance in Ultracold Atomic Collisions*, Phys. Rev. Lett. **91**, 183201 (2003). doi:10.1103/PhysRevLett.91.183201. 2, 8, 105

[41] T. Calarco, J. I. Cirac, and P. Zoller, *Entangling ions in arrays of microscopic traps*, Phys. Rev. A. **63**, 062304 (2001). doi:10.1103/PhysRevA.63.062304. 117

[42] Z. Idziaszek, T. Calarco, P.S. Julienne, A. Simoni, *Quantum theory of ultracold atom-ion collisions*, Phys. Rev. A **79**, 010702 (2009). doi:10.1103/PhysRevA.79.010702. 3, 8

[43] R. G. DeVoe, *Power-Law Distributions for a Trapped Ion Interacting with a Classical Buffer Gas*, Phys. Rev. Lett. **102**, 063001 (2009). doi:10.1103/PhysRevLett.102.063001.

[44] R. Côté, A. Dalgarno, *Ultracold atom-ion collisions*, Phys. Rev. A **62**, 012709 (2000). doi:10.1103/PhysRevA.62.012709.

[45] M. Krych, W. Skomorowski, F. Pawlowski, R. Moszynski, Z. Idziaszek, *Sympathetic cooling of the Ba$^+$ ion by collisions with ultracold Rb atoms: Theoretical prospects*, Phys. Rev. A **83**, 032723 (2011). doi:10.1103/PhysRevA.83.032723. 80

[46] C. Zipkes, L. Ratschbacher, C. Sias, Köhl, *Kinetics of a single trapped ion in an ultracold buffer gas*, New. J. Phys. **13**, 053020 (2011). doi:10.1088/1367-2630/13/5/053020. 3, 8, 80

[47] M. Krych, Z. Idziaszek, *Quantum analysis of atom-ion sympathetic cooling in the presence of micromotion*, arXiv:1312.0279v2 [cond-mat.quant-gas]. 3, 9, 96, 104

[48] L. H. Nguyen, A. Kalev, M.D. Barrett, B.-G. Englert, *Micromotion in trapped atom-ion systems*, Phys. Rev. A **85**, 052718 (2012). doi:10.1103/PhysRevA.85.052718. 3, 9

[49] M. Cetina, A. T. Grier, V. Vuletić, *Micromotion-Induced Limit to Atom-Ion Sympathetic Cooling in Paul Traps*, Phys. Rev. Lett. **109**, 253201 (2012). doi:10.1103/PhysRevLett.109.253201. 4, 9, 82, 96, 104

[50] K. Chen, S. T. Sullivan, E. R. Hudson, *Neutral Gas Sympathetic Cooling of an Ion in a Paul Trap*, Phys. Rev. Lett. **112**, 143009 (2014). doi:10.1103/PhysRevLett.112.143009. 4, 5, 9, 10, 80, 82, 95, 104

[51] R. J. Cook, D. G. Shankland, A. L. Wells, *Quantum theory of particle motion in a rapidly oscillating field*, Phys. Rev. A **31**(2), 564 (1985). doi:10.1103/PhysRevA.31.564. 3, 9, 95

[52] R. J. Glauber, *Classical Behavior of Systems of Quantum Oscillators*, in Quantum Theory of Optical Coherence: Selected Papers and Lectures, Wiley-VCH Verlag GmbH and Co. KGaA, Weinheim, Germany. (2006). doi:10.1002/9783527610075.ch5. 5, 11, 61, 64, 66, 75, 132

[53] D. Leibfriend, R. Blatt, C. Monroe, D. Wineland, *Quantum dynamics of single trapped ions*, Rev. Mod. Phys. **75**, 281 (2003). doi:10.1103/RevModPhys.75.281. 64, 75, 111, 132, 134

[54] M. Combescure, *A quantum particle in a quadrupole radio-frequency trap*, Ann. Inst. Henri Poincaré, section A, **44**(3), 293 (1986). `http://archive.numdam.org/article/AIHPA_1986__44_3_293_0.pdf`. 64

[55] F. Li, *Quantum motion of a charged particle in a Paul trap*, Phys. Rev. A **47**(6), 4975 (1993). doi:10.1103/PhysRevA.47.4975.

[56] John P. Boyd, *Chebyshev and Fourier Spectral Methods*, Second Revised Edition, Dover Publications, (1999). `http://www-personal.umich.edu/~jpboyd/aaabook_9500may00.pdf`.

[57] J. Q. W. Lo, *Pseudospectral Methods in Quantum and Statistical Mechanics*, Doctoral thesis, Dept. of Chem., University of British Columbia (2008). `http://laplace.physics.ubc.ca/ThesesOthers/Phd/lo.pdf`. 14, 25, 37, 45, 135

[58] H. Alici, *Pseudospectral Methods for Differential Equations: Application to the Schrödinger type eigenvalue problems*, Masters thesis, Dept. of Math., Middle East Technical University (2003). `http://etd.lib.metu.edu.tr/upload/1086198/index.pdf`.

[59] M. Abramowitz, I. A. Stegun, *Handbook of mathematical functions*, 10^{th} Edition, Dover Publications, p.887 (1972). 14

[60] J. Spanier, K. B. Oldham, *An Atlas of Functions*, Hemisphere Publishing Corporation, p.189 (1987). 15

[61] W. E. Byerley, *An Elementary Treatise on Fourier's Series, and Spherical, Cylindrical, and Ellipsoidal Harmonics, with Applications to Problems in Mathematical Physics*, Dover Publishing, New York. p.172 (1959). 19

[62] W. H. Press, S. A. Teukolsky, W. T. Vetterling, B. P. Flannery, *Numerical Recipes in Fortran 77: The Art of Scientific Computing*, 2^{nd} Edition, Cambridge University Press, p.144 (1997). 19

[63] R. A. Gonzalez, J. Eisert, I. Koltracht, M. Neumann, G. Rawitscher, *Integral Equation Method for the Continuous Spectrum Radial Schrödinger Equation*, J. Comp. Phys. **134**(1), 134 (1997). doi:10.1006/jcph.1997.5679. 15

[64] L. Greengard, *Spectral integration and two-point boundary value problems*, SIAM J. Num. Anal. **28**(4), 1071 (1991). doi:10.1137/0728057. 13, 16, 17, 123

[65] L. Greengard, V. Rokhlin, *On the numerical solution of two-point boundary value problems*, Comm. Pure Appl. Math. **44**(4), 419 (1991). doi:10.1002/cpa.3160440403. 13, 16

[66] P. Starr, V. Rokhlin, *On the numerical solution of two-point boundary value problems II*, Comm. Pure Appl. Math. **47**(8), 1117 (1994). doi:10.1002/cpa.3160470806. 16

[67] B. R. Johnson, *The multichannel log-derivative method for scattering calculations*, J. Comp. Phys. **13**(3), 445 (1973). doi:10.1016/0021-9991(73)90049-1. 13

[68] B. R. Johnson, *The log-derivative and renormalized Numerov algorithms*, National Resource for Computation in Chemistry, University of California, Berkeley, NRCC Proceedings **5**, 86 (1979). 13, 21, 22, 123

[69] F. Mrugała, Don Secrest, *The generalized log-derivative method for inelastic and reactive collisions*, Comm. Pure Appl. Math. **78**(10), 5954 (1983). doi:10.1063/1.444610. 21

[70] D. E. Manolopoulos, *An improved log derivative method for inelastic scattering*, J. Chem. Phys. **85**(11), 6425 (1986). doi:10.1063/1.451472.

[71] L.D Thomas, M.H Alexander, B.R Johnson, W.A Lester Jr., J.C Light, K.D McLenithan, G.A Parker, M.J Redmon, T.G Schmalz, D Secrest, R.B Walker, *Comparison of numerical methods for solving the second-order differential equations of molecular scattering theory*, J. Comp. Phys. **41**(2), 407 (1981). doi:10.1016/0021-9991(81)90103-0. 13, 21, 22

[72] Chia-Chun Chou, R. E. Wyatt, *Riccati Differential Equation for Quantum Mechanical Bound States: Comparison of Numerical Integrators*, Int. J. Quantum Chem. **108**(2), 238 (2008). doi:10.1002/qua.21478.

[73] A. Simoni, J-M, Launay, *Application of the spectral element method to the solution of the Schrödinger equation*, private communication (2012).

[74] C. Cheng, Q. H. Liu, J. H. Lee, H. Z. Massoud, *Spectral Element Method for the Schrödinger-Poisson System*, J. Comp. Electronics **3**(3-4), 417 (2004). doi:10.1007/s10825-004-7088-z. 123

[75] E. Polizzi, *A High-Performance Numerical Library for Solving Eigenvalue Problems: FEAST Solver v2.1 User's Guide*, (2012). arXiv:1203.4031v2 [cs.MS].

[76] E. Polizzi, *A Density Matrix-based Algorithm for Solving Eigenvalue Problems*, Phys. Rev. B. **79**, 115112 (2009). doi:10.1103/PhysRevB.79.115112. 13, 29, 108

[77] A. Kuzmin, M. Luisier, O. Schenk, *Fast methods for computing selected elements of the Greens function in massively parallel nanoelectronic device simulations*, Euro-Par 2013 Parallel Processing, LNCS **8097**, F. Wolf, B. Mohr, and D. an Ney (Eds.), Springer-Verlag Berlin Heidelberg, 533-544 (2013). doi:10.1007/978-3-642-40047-6_54. 13, 29, 108

[78] O. Schenk, M. Bollhöfer, R. A. Römer, *On Large-Scale Diagonalization Techniques for the Anderson Model of Localization*, SIAM Rev. **50**(1), 91 (2008). doi:10.1137/070707002. 13, 29, 108

[79] O. Schenk, A. Waechter, M. Hagemann, *Matching-based Preprocessing Algorithms to the Solution of Saddle-Point Problems in Large-Scale Nonconvex Interior-Point Optimization*, J. Comp. Opt. App. **36**(2-3), 321 (2007). doi:10.1007/s10589-006-9003-y.

[80] O. Schenk, K. Gärtner, *Solving unsymmetric sparse systems of linear equations with PARDISO*, Journal of Future Generation Computer Systems, **20**(3), 475 (2004). doi:10.1016/j.future.2003.07.011.

[81] Intel Math Kernel Library 11.3.174 (LAPACK and BLAS) for Linux and Apple OS X. (2011). `https://software.intel.com/en-us/intel-mkl`.

[82] D. Secrest, B. R. Johnson, *Exact Quantum-Mechanical Calculation of a Collinear Collision of a Particle with a Harmonic Oscillator* J. Chem. Phys. **45**, 4556 (1966). doi:10.1063/1.1727537.

[83] B. R. Johnson, D. Secrest, *The Solution of the Nonrelativistic Quantum Scattering Problem without Exchange* J. Math. Phys. **7**, 2187 (1966). doi:10.1063/1.1704905. 13, 29, 108

[84] D. Secrest, *Linear Collision of a Classical Harmonic Oscillator with a Particle at High Energies*, J. Chem. Phys. **51**, 421 (1969). doi:10.1063/1.1671741. 17, 21, 33, 34

33

[85] A. Simoni, J-M, Launay, *Landau Quantization Effects in Ultracold Atom-Ion Collisions*, J. Phys. B: At. Mol. Opt. Phys. **44**, 235201 (2011). doi:10.1088/0953-4075/44/23/235201. 33

49, 97

[86] M. Olshanii, *Atomic Scattering in the Presence of an External Confinement and a Gas of Impenetrable Bosons*, Phys. Rev. Lett. **81**(5), 938 (1998). doi:10.1103/PhysRevLett.81.938. 32, 54

[87] T. Bergeman, M. G. Moore, M. Olshanii, *Atom-Atom Scattering under Cylindrical Harmonic Confinement: Numerical and Analytical Studies of the Confinement Induced Resonances*, Phys. Rev. Lett. **91**(16), 163201 (2003). doi:10.1103/PhysRevLett.91.163201.

[88] J. I. Kim, V. S. Melezhik, P. Schmelcher, *Suppression of Quantum Scattering in Strongly Confined Systems*, Phys. Rev. Lett. **97**, 193203 (2006). doi:10.1103/PhysRevLett.97.193203. 54, 102

[89] B. E. Granger, D. Blume, *Tuning the Interactions of Spin-Polarized Fermions Using Quasi-One-Dimensional Confinement*, Phys. Rev. Lett. **92**, 133202 (2004). doi:10.1103/PhysRevLett.92.133202. 54

[90] L. M. Delves, *Tertiary and General-Order Collisions II*, Nucl. Phys. **20**, 275 (1960). doi:10.1016/0029-5582(60)90174-7. 52, 53

[91] F. T. Smith, *Lifetime Matrix in Collision Theory*, Phys. Rev. **118**(1), 349 (1960). doi:10.1103/PhysRev.118.349. 55, 99

[92] T. T. Wu, M. L. Yu, *Theory and application of Fermi pseudo-potential in one dimension*, J. Math. Phys. **43**, 5949 (2002). doi:10.1063/1.1519940. 50

[93] D. O. Harris, G. G. Engerholm, W. D. Gwinn, *Calculation of Matrix Elements for One-Dimensional Quantum-Mechanical Problems and the Application to Anharmonic Oscillators*, J. Chem. Phys. **43**(5), 1515 (1965). doi:10.1063/1.1696963. 46

[94] A. S. Dickinson, P. R. Certain, *Calculation of Matrix Elements for One-Dimensional Quantum-Mechanical Problems*, J. Chem. Phys. **49**(9), 4209 (1968). doi:10.1063/1.1670738.

[95] P. F. Endres, *Energy Levels of One- and Two-Dimensional Anharmonic Oscillators*, J. Chem. Phys. **47**(2), 798 (1967). doi:10.1063/1.2140500. 46

[96] J. C. Light, I. P. Hamilton, J. V. Lill, *Generalized discrete variable approximation in quantum mechanics*, J. Chem. Phys. **82**(3), 1400 (1985). doi:10.1063/1.448462. 14, 18, 40

[97] J. C. Light, T. Carrington, *Discrete-Variable Representations and their Utilization*, in Advances in Chemical Physics, **114**, 2000 (eds I. Prigogine, S. A. Rice), John Wiley and Sons, Inc., Hoboken, NJ, USA. doi:10.1002/9780470141731.ch4. 14, 18, 40

[98] G. C. Groenenboom, *The Discrete Variable Representation*, Lecture notes, Post graduate course on Theoretical Chemistry and Spectroscopy, Domaine des Mesures, Han-sur-Lesse, Belgium, Dec 10-14 (2001). `http://www.theochem.ru.nl/files/dbase/gcg2001.pdf`. 18

[99] A. Markmann, *Propagation Methods*, Lecture notes for post graduate students (2003). `www.pci.uni-heidelberg.de/tc/usr/andreasm/academic/en_index.html`. 18

[100] D. T. Colbert, W. H. Miller, *A novel discrete variable representation for quantum mechanical reactive scattering via the S-matrix Kohn method*, J. Chem. Phys. **96**(3), 1982 (1992). doi:10.1063/1.462100.

[101] D. J. Griffiths, *Introduction to Electrodynamics*, 4th Ed, Addison-Wesley (2013). 27, 40, 46, 73

[102] F. G. Major, V. N. Gheorghe, G. Werth, *Charged Particle Traps: Physics and Techniques of Charged Particle Confinement*, Springer Berlin Heidelberg (2005). doi:10.1007/b137836. 61

[103] J.I. Cirac, L.J. Garay, R. Blatt, A.S. Parkins, P. Zoller, *Laser cooling of trapped ions: The influence of micromotion*, Phys. Rev. A **49**, 421 (1994). doi:10.1103/PhysRevA.49.421. xvi, xix, 63, 64, 65, 75, 106, 109, 132

[104] D. J. Berkeland, J. D. Miller, J. C. Bergquist, W. M. Itano, D. J. Wineland, *Minimization of ion micromotion in a Paul trap*, J. App. Phys. **83**(10), 5025 (1998). doi:10.1063/1.367318. 2, 8

[105] G. Schrade, P.J. Bardroff, R.J. Glauber, C. Leichtle, V. Yakovlev, W.P. Schleich, *Endoscopy in the Paul trap: The influence of the micromotion*, App. Phys. B **64**(2), 181 (1997). doi:10.1007/s003400050163. 2, 8

[106] P. Schwerdtfeger, *Atomic Static Dipole Polarizabilities*, in Computational Aspects of Electric Polarizability Calculations: Atoms,

Molecules and Clusters, ed. G. Maroulis, IOS Press, Amsterdam, p.1-32 (2006). Updated static dipole polarizabilities are available as pdf file from the CTCP website at Massey University: `http://ctcp.massey.ac.nz/dipole-polarizabilities`.

[107] P. Leibfried, C. Roos, H. Rohde, S. Gulde, A.B. Mundt, M. Lederbauer, F. Schmidt-Kaler, J. Eschner, R. Blatt, *Experiments towards quantum information with trapped calcium ions*, Quantum Electronics and Laser Science Conference 2000 (QELS 2000) Technical Digest, p.178 (2000). 70

[108] T. Busch, B.-G. Englert, K. Rzążewski, M. Wilkens, *Two Cold Atoms in a Harmonic Trap*, Found. Phys. **28**(4), 549 (1998). doi:10.1023/A:1018705520999. 71

[109] B. E. King, C. S. Wood, C. J. Myatt, Q. A. Turchette, D. Leibfried, W. M. Itano, C. Monroe, D. J. Wineland, *Cooling the Collective Motion of Trapped Ions to Initialize a Quantum Register*, Phys. Rev. Lett. **81**, 1525 (1998). doi:10.1103/PhysRevLett.81.1525. xix, 112

[110] J.M. Launay, M. Le Dourneuf, *Hyperspherical description of collinear reactive scattering*, J. Phys. B: At. Mol. Phys. **15**, L455 (1982). doi:10.1088/0022-3700/15/13/008. 109

[111] B. Lepetit, J.M. Launay, M. Le Dourneuf, *Quantum study of electronically non-adiabatic collinear reactions. I. Hyperspherical description of the electronuclear dynamics*, Chem Phys **106**(1), 103 (1986). doi:10.1016/0301-0104(86)87042-2. 113, 121

[112] B. Lepetit, J.M. Launay, M. Le Dourneuf, *Quantum study of electronically non-adiabatic collinear reactions. II. Influence of spin-orbit transitions on the F + HH reaction*, Chem. Phys. **106**(1), 111 (1986). doi:10.1016/0301-0104(86)87043-4.

[113] O. I. Tolstikhin, H. Nakamura, *Hyperspherical elliptic coordinates for the theory of light atom transfer reactions in atom-diatom collisions*, J. Chem. Phys. **108**, 8899 (1998). doi:10.1063/1.476337.

[114] G. V. Milnikova, H. Nakamura, *Use of diabatic basis in the adiabatic-by-sector R-matrix propagation method in time-independent reactive scattering calculations*, Comp. Phys. Comm. **140**(3), 381 (2001). doi:10.1016/S0010-4655(01)00287-9.

[115] B. H. Bransden, C. J. Joachain, *Physics of Atoms and Molecules*, 2nd Ed., Longman Scientific (1990). 113, 121

108

[116] W. Paul, *Electromagnetic traps for charged and neutral particles*, Rev. Mod. Phys. **62**, 531 (1990). doi:10.1103/RevModPhys.62.531.

[117] P. M. Morse, H. Feshbach, *Methods of Theoretical Physics, Part I*, McGraw-Hill Science/Engineering/Math, p.556 (1964). 33, 63, 127

[118] R. Coisson, G. Vernizzi, X. Yang, *Mathieu functions and numerical solutions of the Mathieu equation*, Open-source Software for Scientific Computation (OSSC), 2009 IEEE International Workshop, **3**(10), 18 (2009). doi:10.1109/OSSC.2009.5416839. 128

[119] N. W. McLachlan, *Theory and Application of Mathieu Functions*, Dover Publications, p.10 (1964). 63, 127

[120] F. M. Arscott, *Periodic Differential Equations: An Introduction to Mathieu, Lamé and Allied Functions*, Pergamon Press, p.26 (1964). 63, 127

VU :
Le Directeur de Thèse
(Nom et Prénom)

VU :
Le Responsable de l'École Doctorale

VU pour autorisation de soutenance

Rennes, le

Le Président de l'Université de Rennes 1

Guy Cathelineau

VU après soutenance pour autorisation de publication :

Le Président de Jury,
(Nom et Prénom)